UNIVERSITA' DEGLI STUDI DI PAVIA

FACOLTA' DI INGEGNERIA
DIPARTIMENTO DI INGEGNERIA INDUSTRIALE E DELL'INFORMAZIONE

DOTTORATO DI RICERCA IN BIOINGEGNERIA E BIOINFORMATICA
XXIX CICLO - 2016

SIMULATING THE ELECTROMECHANICAL RESPONSE OF THE CARDIAC TISSUE: INSIGHTS ON PATHOPHYSIOLOGY AND TISSUE ENGINEERING

PhD Thesis by
FABRIZIO DEL BIANCO

Advisor:
Prof. Lorenzo Fassina

Co-advisors:
Prof. Piero Colli Franzone
Prof. Simone Scacchi

PhD Program Chair:
Prof. Riccardo Bellazzi

Abstract (Italiano)

Oggigiorno, una delle principali sfide che i ricercatori devono superare è determinare il modo in cui i dati biologici, resisi disponibili a diverse scale spaziali e temporali (dalla genetica alla fisiologia), possano essere raggruppati al fine di migliorare la conoscenza globale dei fenomeni fisici. La modellistica matematica è una tecnica valida per cercare di espletare questo compito, ma richiede un approccio modulare peculiare della cosiddetta biologia dei sistemi. Ciò significa che nuovi modelli più raffinati e complessi sono costruiti da alcuni più semplici già pubblicati in letteratura e che si occupano della descrizione funzionale di singoli processi biologici. Durante questo processo, si deve conoscere il livello di dettaglio cui si tende e verificare le differenze e somiglianze tra i modelli elementari impiegati (per quanto riguarda equazioni, parametri e unità di misura). Dopo aver sviluppato un nuovo modello, si possono eseguire simulazioni *in silico*. Esse rappresentano una delle tecniche che s'ispirano al principio della sostituzione completa (o almeno parziale) dell'uso degli animali nella ricerca con materiale non senziente. Tale principio fu introdotto da Russell e Burch nel 1959 [185] attraverso il loro concetto delle 3 R (Replacement o sostituzione, Reduction o riduzione e Refinement o perfezionamento) e costituisce ancora oggi una delle idee basilari di molte politiche etiche e legislative.

In particolare, grazie ai recenti progressi nel campo delle tecnologie hardware e software (in termini di dimensioni delle memorie, linguaggi di programmazione, librerie di funzioni e tecniche d'imaging medico), il cuore è diventato l'organo più virtualmente utilizzato per studi computazionali. Modellizzare il suo comportamento può fornire ai ricercatori interessanti risultati sugli effetti di strutture molecolari e meccanismi di recente scoperta (ad esempio, recettori e canali sulla membrana plasmatica o pathway intracellulari) o dare loro l'opportunità di studiare la risposta e l'adattamento dell'organo a stimoli ambientali fisici o chimici. Inoltre, le simulazioni consentono potenzialmente di prevedere il decorso clinico di malattie cardiache o l'esito di specifici trattamenti chirurgici o farmacologici finalizzati alla guarigione del tessuto cardiaco o almeno al mantenimento di un livello accettabile di funzionalità.

Com'è intuibile, i modelli più accurati descrivono matematicamente l'intero comportamento elettromeccanico del cuore, sebbene siano attualmente più un'eccezione che una regola a causa della complessità delle equazioni in gioco. Infatti, essi spiegano sia la propagazione dell'eccitazione elettrica attraverso l'organo, risolvendo una o più equazioni non lineari a derivate parziali di reazione-diffusione, sia la

successiva deformazione meccanica del tessuto cardiaco, risolvendo un sistema di equazioni non lineari nella meccanica del continuo. In particolare, il flusso di corrente avviene attraverso la membrana plasmatica dei singoli cardiomiociti e le giunzioni serrate a bassa resistenza tra gli stessi in seguito all'applicazione di uno stimolo elettrico. Il primo flusso dipende dalle correnti ioniche attraverso diversi canali di membrana, mentre il secondo risente dell'organizzazione delle cellule in fibre e foglietti a livello tissutale. Se lo stimolo è sufficientemente intenso, si scatena un potenziale d'azione e s'innesca il rilascio di calcio dai compartimenti intracellulari. Con un certo ritardo, gli ioni calcio si legano a specifici filamenti sarcomerici e determinano lo sviluppo di forza attiva, fenomeno comunemente chiamato accoppiamento eccitazione-contrazione. L'intera contrazione meccanica considera anche le proprietà materiali passive del tessuto cardiaco definite da diverse strutture proteiche extracellulari o intracellulari, le quali possono organizzarsi secondo l'architettura delle fibre. A sua volta, la contrazione può avere effetti sul legame degli ioni calcio ai sarcomeri, sulla forma del potenziale d'azione e sulle conducibilità elettriche passive mediante meccanismi di feedback meccanico. Pertanto, i modelli elettromeccanici tengono in considerazione l'interazione reciproca tra fenomeni elettrici e meccanici, la quale influenza, com'è noto, l'attività del cuore in condizioni sia fisiologiche sia patologiche. Di conseguenza, il valore dei risultati delle simulazioni derivanti da essi aumenta notevolmente.

Questa tesi desidera essere un contributo nel campo della modellistica cardiaca, sfruttando un modello elettromeccanico fortemente accoppiato per affrontare due temi di notevole rilevanza e innovativi:

- le patologie cardiache, in particolare l'ipertrofia, analizzando il comportamento di strutture con geometria a complessità crescente (fibra, campione di parete e ventricolo);
- l'ingegneria tissutale cardiaca, in particolare le colture *in vitro* progettate per diventare patch impiantabili.

La dissertazione è organizzata come segue.

Il **Capitolo 1** riassume i principali tratti anatomici e fisiologici del tessuto cardiaco dei mammiferi, aggiungendo l'esempio di patologia considerata in questa tesi, cioè l'ipertrofia, ed una breve discussione sulle colture cardiache.

Il **Capitolo 2** descrive in dettaglio il modello elettromeccanico e l'algoritmo più generali impiegati per simulare qualunque struttura cardiaca in questa tesi.

Il **Capitolo 3** riporta i risultati delle simulazioni riguardanti la risposta elettromeccanica di una fibra cardiaca caratterizzata da crescita ipertrofica di tessuto in modo eccentrico mentre è soggetta a diversi protocolli di eccitazione-contrazione; un'analisi sui feedback meccanici è inclusa.

Il **Capitolo 4** tratta la risposta elettromeccanica di un campione di parete cardiaca che si contrae liberamente in condizioni di ipertrofia concentrica, di cui sono analizzati i fenomeni di crescita tissutale e dispersione delle fibre.

Il **Capitolo 5** studia la risposta elettromeccanica di un ventricolo colpito da stenosi aortica e ipertrofia concentrica (caratterizzata da sola crescita tissutale) durante un intero ciclo cardiaco; come nel Capitolo 3, si indaga anche sul ruolo dei feedback meccanici.

Il **Capitolo 6** analizza gli effetti elettromeccanici dettati dalla scelta di una specifica struttura intrinseca ed uno specifico spessore per una coltura cardiaca che si sviluppa in un patch a fini di trapianto.

Il **Capitolo 7** trae le conclusioni generali di questo lavoro.

Tutte le attività di ricerca descritte in questa tesi sono state condotte al Centro di Tecnologie per la Salute (Centre for Health Technologies, C.H.T.) dell'Università di Pavia in collaborazione con il Dipartimento di Matematica di Pavia e il Dipartimento di Matematica dell'Università di Milano, che ha fornito i codici tridimensionali elementari e la piattaforma per eseguire simulazioni in calcolo parallelo all'occorrenza.

In merito all'influenza dei feedback meccanici sull'attività elettrica, i risultati delle simulazioni non mostrano sostanziali differenze quando uno o più di essi è trascurato nel caso di fibre sia sane sia colpite da ipertrofia eccentrica. Tuttavia, differenze rilevanti si ottengono nel caso di ventricoli, in particolare nelle aree attivate più tardivamente. La presenza di un termine convettivo nel modello di reazione-diffusione aumenta la dispersione della ripolarizzazione e della durata del potenziale d'azione nel caso di un ventricolo sano. Inoltre, incrementa i singoli valori di durata del potenziale d'azione. I suoi due ultimi effetti sono presenti anche nel caso di un ventricolo ipertrofico, sebbene in misura minore. Invece la presenza del feedback meccanoelettrico, dovuto alla corrente attraverso i canali di membrana attivati dallo stretch, riduce la dispersione della ripolarizzazione per entrambi i ventricoli e i valori della durata del potenziale d'azione per il solo ventricolo ipertrofico.

Confrontando le risposte elettriche in condizioni sane e patologiche, risulta che una fibra colpita da ipertrofia eccentrica possiede all'incirca lo stesso comportamento di quella sana. Nel caso di un campione di parete o di un ventricolo colpito da ipertrofia concentrica, invece, si ottengono differenze rilevanti. Il campione di parete, caratterizzato in questa tesi da conducibilità che non dipendono dalla crescita, presenta valori più bassi per la durata del potenziale d'azione e per la velocità di conduzione all'epicardio; pertanto, il rischio di promuovere aritmie è più elevato. Invece il ventricolo, caratterizzato da conducibilità dipendenti dalla crescita, ha valori più bassi per il solo potenziale d'azione, mentre la velocità di conduzione è più alta. Per quanto riguarda le risposte

meccaniche, i risultati mostrano che una fibra colpita da ipertrofia eccentrica, rispetto a una sana, sviluppa meno forza durante la sistole isovolumica del ciclo cardiaco, è più contrattile durante la fase di efflusso del sangue e si allunga maggiormente durante il riempimento diastolico. Anche un campione di parete colpito da ipertrofia concentrica che batte liberamente è più contrattile, ma può sviluppare forza in misura maggiore e tali effetti s'intensificano con la dispersione delle fibre. Tuttavia, se si considerano un ciclo cardiaco e una geometria più complessa, come quella di un ventricolo, la contrattilità durante la fase di efflusso non varia significativamente in caso di ipertrofia concentrica, nonostante la forza prodotta si mantenga maggiore per contrastare la stenosi aortica. Inoltre, all'epicardio, dove la crescita è massima, il ventricolo ipertrofico si contrae meno durante la fase di efflusso e si allunga maggiormente durante il riempimento diastolico, sebbene il volume a fine sistole della cavità interna sia simile a quello del caso sano e il volume a fine diastole sia più ridotto di quello sano.

Infine, tramite l'analisi delle colture cardiache, si dimostra l'importanza di riprodurre l'architettura anisotropa e ordinata del tessuto cardiaco e di selezionare un adeguato spessore mentre si progettano patch.

Abstract (English)

Nowadays, one of the main challenges researchers have to overcome is determining the way in which biological data, made available at different spatial and temporal scales (from genetics to physiology), can be grouped together in order to improve the global knowledge of physical phenomena. Mathematical modeling is a valid technique to try to carry out this task, but it needs a modular approach peculiar to the so-called system biology. This means that new more refined and complex models are built upon some simpler ones already published in the literature and dealing with the functional description of individual biological processes. During this process, one must know the level of detail he/she aims at and check the differences and similarities among the employed basic models (as regards equations, parameters and measure units). After developing a new model, *in silico* simulations can be run. They represent one of the techniques complying with the principle of the total (or at least partial) replacement of the use of animals in research with insentient material. This principle was introduced by Russell and Burch in 1959 [185] by their 3Rs concept (Replacement, Reduction and Refinement) and it is still one of the key ideas for many ethical and legislative policies.

In particular, thanks to the recent advancements in the field of hardware and software technologies (in terms of memory sizes, programming languages, libraries of functions and medical imaging techniques), the heart has become the most virtually used organ for computational studies. Modeling its behavior can provide researchers with interesting insights on the effects of recently discovered molecular structures and mechanisms (for instance, receptors and channels on the plasma membrane or intracellular pathways) or give them the opportunity to study the heart response and adaptation to physical or chemical environmental stimuli. Moreover, simulations let virtually predict the clinical course of cardiac diseases or the outcome of specific surgical or pharmacological treatments aimed at healing the cardiac tissue or maintaining an acceptable level of functionality at least.

As one might guess, the most accurate models describe mathematically the whole electromechanical behavior of the heart, though they are currently the exception rather than the rule due to the complexity of equations. Actually, they explain both the propagation of the electrical excitation through the organ, by solving one or more non-linear reaction-diffusion partial differential equations, and the following mechanical deformation of the cardiac tissue, by solving a system of non-linear equations related to continuum mechanics. In particular, the current flow

occurs through the plasma membrane of single cardiomyocytes and the low-resistance gap junctions among them after the delivery of an electrical stimulus. The former flow depends on the ionic currents through different membrane channels, whilst the latter one is affected from the organization of cells into fibers and sheets at the tissue level. If the stimulus is strong enough, an action potential arises and the calcium release from intracellular stores is triggered. With a certain delay, calcium ions bind to specific sarcomere filaments and cause the development of active force, a phenomenon usually called excitation-contraction coupling. The whole mechanical contraction also considers the passive material properties of the cardiac tissue defined by different extracellular or intracellular protein structures, which may arrange themselves according to the fiber architecture. In turn, contraction may have effects on the calcium ions binding to sarcomeres, the shape of the action potential and the electrical passive conductivities by mechanical feedback mechanisms. Therefore, the electromechanical models take into account the mutual interaction between electrical and mechanical phenomena, which is known to affect the heart activity under both physiological and pathological conditions. As a consequence, the relevance of the simulation results deriving from them is dramatically enhanced.

This thesis would like to contribute to the field of cardiac modeling by exploiting a strongly-coupled electromechanical model to face two challenging and innovative topics:

- cardiac pathologies, in particular hypertrophy, by analyzing the behavior of structures with an increasing geometric complexity (fiber, wedge and ventricle);
- cardiac tissue engineering, in particular the *in vitro* cultures designed to become implantable patches.

The dissertation is organized as follows.

Chapter 1 resumes the main anatomical and physiological features of the mammalian cardiac tissue, adding the example of pathology considered in this thesis, i.e. hypertrophy, and a brief discussion on cardiac cultures.

Chapter 2 describes in detail the most general form of the electromechanical model and of the algorithm employed for simulating any cardiac structure in this thesis.

Chapter 3 reports the simulation results about the electromechanical response of a cardiac fiber characterized by eccentric hypertrophic growth while it is subjected to different excitation-contraction protocols; an analysis on the mechanical feedbacks is included.

Chapter 4 deals with the electromechanical response of a cardiac wedge contracting freely under concentric hypertrophic conditions, whose phenomena of tissue growth and fiber dispersion are analyzed.

Chapter 5 studies the electromechanical response of a ventricle affected from aortic stenosis and concentric hypertrophy (characterized by tissue growth only) during an entire cardiac cycle; as in Chapter 3, the role of the mechanical feedbacks is investigated too.

Chapter 6 analyzes the electromechanical effects dictated by the choice of a specific intrinsic structure and thickness for a cardiac culture developing into a patch for transplantation.

Chapter 7 draws the overall conclusions of this work.

All research activities described in this thesis have been carried out at the Centre for Health Technologies (C.H.T.) of the University of Pavia in collaboration with the Department of Mathematics in Pavia and the Department of Mathematics at the University of Milano, which has provided the basic three-dimensional codes and the cluster for performing parallel computing simulations when needed.

As regards the influence of the mechanical feedbacks on the bioelectrical activity, the simulation results show no relevant discrepancies when one or more of them are disregarded in case of both healthy and eccentric hypertrophic fibers. However, significant differences are yielded in case of ventricles, in particular in the latest activated areas. The presence of a convective term in the reaction-diffusion model increases the dispersion of repolarization and of the action potential duration in case of a healthy ventricle. Moreover, it raises the single values of the action potential duration. Its last two effects are also present in case of a hypertrophic ventricle, though to a lesser extent. On the contrary, the presence of the mechanoelectric feedback, due to the stretch-activated membrane channels current, decreases the dispersion of repolarization for both ventricles and the values of the action potential duration for the sole hypertrophic ventricle.

By comparing the electrical responses under healthy and pathological conditions, it turns out that an eccentric hypertrophic fiber displays nearly the same behavior of the healthy one. In case of a concentric hypertrophic wedge or ventricle, some significant discrepancies are found instead. The wedge, characterized in this thesis by conductivities that do not depend on growth, shows lower values for the action potential duration and the conduction velocity on the epicardium; therefore, the risk of promoting arrhythmias is greater. On the contrary, the ventricle, characterized by growth-dependent conductivities, has lower values only for the action potential duration, whilst the conduction velocity is higher.

As far as the mechanical responses are concerned, the results show that an eccentric hypertrophic fiber, compared with a healthy one, develops less force during the isovolumic systole of the cardiac cycle, it is more contractile during the blood efflux phase and it stretches more during the diastolic filling. A freely beating concentric hypertrophic wedge is more contractile too, but it can develop force to a higher extent and these effects

are enhanced with fiber dispersion. However, if a cardiac cycle and a more complex geometry, like the one of a ventricle, are taken into account, the contractility during the efflux phase does not vary significantly in case of concentric hypertrophy, though the developed force keeps higher to counteract aortic stenosis. Moreover, on the epicardium, where growth is maximal, the hypertrophic ventricle contracts less during the efflux phase and it stretches more during the diastolic filling, though the end-systolic volume of the internal cavity is similar to the healthy case and the end-diastolic volume is lower than the healthy one.

At last, by the analysis of cardiac cultures, it is proved that it is important to reproduce the anisotropic and ordered architecture of the cardiac tissue and to select a proper thickness while designing patches.

Contents

1. The cardiac tissue 1
1.1. The heart 1
1.1.1. Basic anatomy 1
1.1.2. The cardiac cycle 4
1.1.3. The Frank-Starling law 5
1.2. General properties of the myocardium 8
1.2.1. Excitability 8
1.2.2. Refractoriness 9
1.2.3. Conductivity 10
1.2.4. Contractility 11
1.3. Example of myocardial pathology: hypertrophy 15
1.4. Cardiac cultures 17

2. The electromechanical framework 19
2.1. Overview 19
2.2. Cell modeling 20
2.2.1. The membrane model 20
2.2.2. The active tension generation model 25
2.3. Tissue modeling 28
2.3.1. The finite elasticity model 28
2.3.2. The reaction-diffusion models 40
2.4. The theory of finite volumetric growth 47
2.5. The discretization of the complete model 50
2.5.1. The space discretization 50
2.5.2. The time discretization 53
2.6. The general algorithm for the resolution of the complete model 57

3. Simulations on an eccentric hypertrophic fiber 61
3.1. Introduction 61
3.2. Methods 63
3.2.1. The mechanical model: implementation of eccentric growth and one-dimensional reformulation 63
3.2.2. The electrophysiological model: one-dimensional reformulation and dependence on eccentric growth 65
3.2.3. Details on the discretization and implementation of the complete model 67
3.2.4. The geometry, growth and electrical stimulation of the fiber 67
3.2.5. The implemented tests 70
3.3. Results and discussion 71
3.3.1. The electrical response 71
3.3.2. The mechanical response 75
3.3.3. Comparison among the *in vitro*, *in silico* and *in vivo* fiber behaviors 81
3.4. Conclusions 82

4. Simulations on a concentric hypertrophic wedge 85
4.1. Introduction 85
4.2. Methods 86
4.2.1. The mechanical model: implementation of concentric growth and fiber dispersion 86
4.2.2. The electrophysiological model: dependence on concentric growth and independence of fiber dispersion 87
4.2.3. Details on the discretization and implementation of the complete model 89
4.2.4. The geometry and electrical stimulation of the wedge 90
4.2.5. Bioelectrical and biomechanical measures and statistics 91
4.3. Results and discussion 93
4.3.1. Qualitative analysis of the electromechanical response 93
4.3.2. Quantitative analysis of the electromechanical response 95
4.4. Conclusions 96

5. Simulations on a concentric hypertrophic ventricle 97
5.1. Introduction 97
5.2. Methods 98
5.2.1. The mechanical model: implementation of concentric growth 99
5.2.2. The electrophysiological model: dependence on concentric growth 99
5.2.3. Details on the discretization and implementation of the complete model 101
5.2.4. The geometry and electrical stimulation of the ventricle 101
5.2.5. The cardiac cycle and growth of the ventricle 102
5.3. Results and discussion 105
5.3.1. The electrical response 105
5.3.2. The mechanical response 123
5.4. Conclusions 132

6. Simulations on a culture 133
6.1. Introduction 133
6.2. Methods 134
6.2.1. The mechanical model: details and remarks 134
6.2.2. The electrophysiological model: details and remarks 135
6.2.3. Details on the discretization and implementation of the complete model 135
6.2.4. The geometry and electrical stimulation of the culture 136
6.2.5. Bioelectrical and biomechanical measures 136
6.2.6. Statistics 137
6.3. Results and discussion 138
6.3.1. Effects of the fiber architecture 138
6.3.2. Effects of thickness 139
6.4. Conclusions 141

7. Overall conclusions 143

References 145

Chapter 1

The cardiac tissue

In this chapter, the main aspects concerning the anatomy and physiology of the mammalian cardiac tissue are briefly reviewed to better understand the electromechanical modeling framework described in Chapter 2. A discussion on hypertrophy is also present as it will be the cardiac pathology considered in this thesis. For an easier understanding, the reference species chosen is the human one, though simulations in Chapter 3, Chapter 4 and Chapter 5 will involve other animals when selecting specific models of electrophysiology and mechanics: the guinea-pig, the mouse and the pig. However, the main qualitative features of the human cardiac tissue can be retrieved in all other mammalian species. Differences may arise only when phenomena are quantitatively described; in particular, in this chapter, all measures refer to the human species again. Moreover, the cardiac tissue is compared with the skeletal one, which is the most similar one in mammals, stressing similarities and differences. A final section is devoted to cardiac cultures, which represent a relatively recent way to study *in vitro* the electromechanical behavior of the cardiac tissue and, mainly, to regenerate infarcted areas in the *in vivo* heart. Simulations on them will be reported in Chapter 6.

1.1. The heart

1.1.1. Basic anatomy

The heart is a pump composed of four chambers [16,30]: two atria in the upper part, separated by the interatrial septum, and two ventricles in the lower part, separated by the interventricular septum (Figure 1.1). Each atrium communicates with its corresponding ventricle by an atrioventricular valve: the bicuspid or mitral valve to the left and the

tricuspid valve to the right. Then, each ventricle is connected to the circulatory system by a semilunar valve: the aortic valve between the left ventricle and the aorta and the pulmonary valve between the right ventricle and the pulmonary artery. The aorta and the pulmonary artery are the first two blood vessels of the systemic circulation (reaching all body tissues) and the pulmonary one (passing through the lungs) respectively. The four pulmonary veins and the two venae cavae, instead, are the terminal vessels of the two previous circulations and they end into the left and right atria respectively. All valves are made of connective tissue covered with endothelial cells and work passively, i.e. they open or close according to the pressure gradient across them that changes during a cardiac cycle as it will be discussed later.

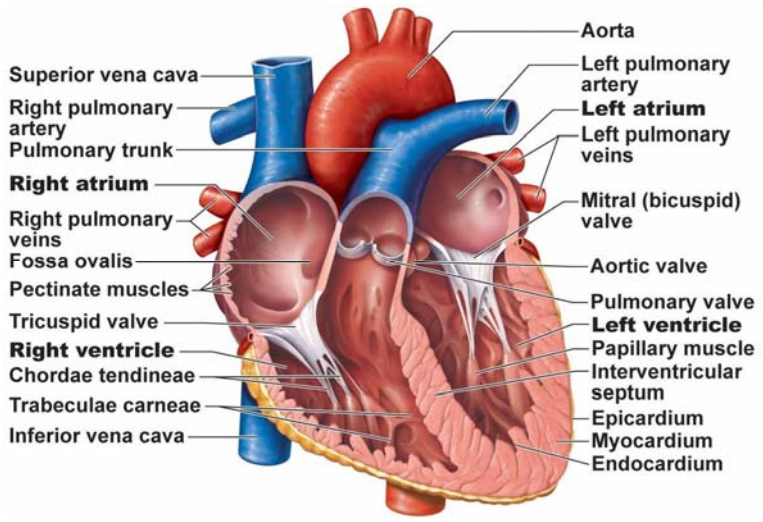

Figure 1.1: Schematic diagram of the heart anatomy (adapted from [85]).

The cardiac wall is formed by:

- the epicardium, which is a thin connective layer covering the external surface of the heart;
- the endocardium, which is a thin endothelial layer covering the internal surface of cardiac chambers;
- the (active) myocardium, which is the muscular tissue between the epicardium and the endocardium and is composed of several layers of parallel and differently oriented cardiomyocytes, forming fibers that rotate from the subepicardial region to the subendocardial one.

The myocardium is also reinforced with connective structures (the elastin and collagen fibers secreted by fibroblasts that form the so-called passive myocardium), among which the most important one is a fibrous ring towards the base of ventricles near the atrioventricular valves.

Moreover, in both ventricles, it is connected to some fusiform papillary muscles (a kind of trabeculae carneae) that ensure the proper closing of the atrioventricular valves during the ventricular systole of the cardiac cycle, when the blood in ventricles may flow into atria again.

There are significant differences regarding the thickness of the myocardium. The atrial walls are largely thinner than the ventricular ones, whereas the left ventricle is about three times thicker than the right one. Actually, the left ventricle must deliver blood with a higher pressure into the systemic circulation, which is far longer than the pulmonary one starting from the right ventricle.

Besides its muscular component, the heart is also characterized by a complex network (of myocardial origin), which is responsible for the generation and propagation of electrical stimuli in the heart. This conduction system groups together the following structures (Figure 1.2):

- the Keith-Flack sinoatrial node located on the posterior part of the right atrium, where the spontaneous and repetitive beating of the heart comes from;
- the Tawara atrioventricular node near the tricuspid valve, which collects the electrical excitation after crossing the atrial musculature and sends it to ventricles with a certain delay (about 170÷200 ms);
- the bundle of His that, starting from the atrioventricular node, runs through the interventricular septum and progressively splits into several smaller and smaller branches (forming the Purkinje network), which transmit the electrical stimulation to ventricular cardiomyocytes from the apex to the base of the heart.

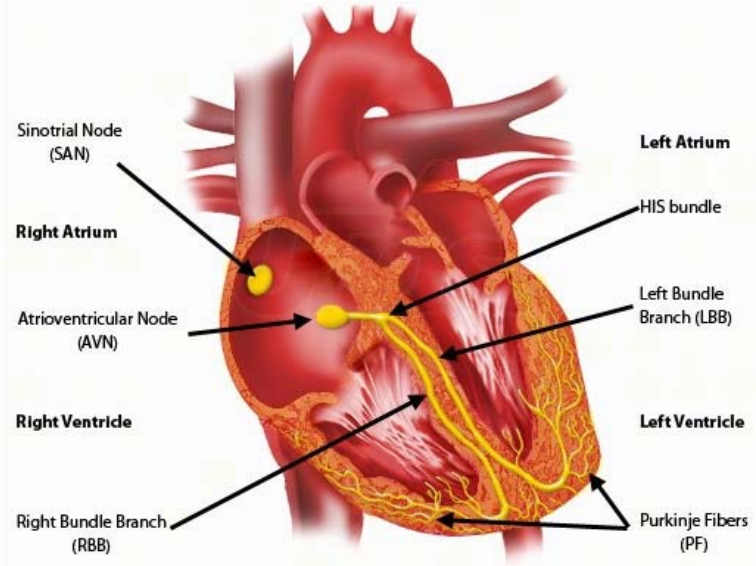

Figure 1.2: Schematic diagram of the heart conduction system (adapted from [86]).

At last, the whole heart is held in a double-walled sac, i.e. the pericardium, made of a parietal layer, which adheres to the mediastinum, and a visceral one, which is fused to the epicardium. The two layers enclose a cavity that contains a mucous fluid avoiding friction during the heart beating.

1.1.2. The cardiac cycle

The propagation of the electrical signal throughout the heart determines an ordered series of mechanical events usually referred to as the cardiac cycle [16,30] (Figure 1.3).

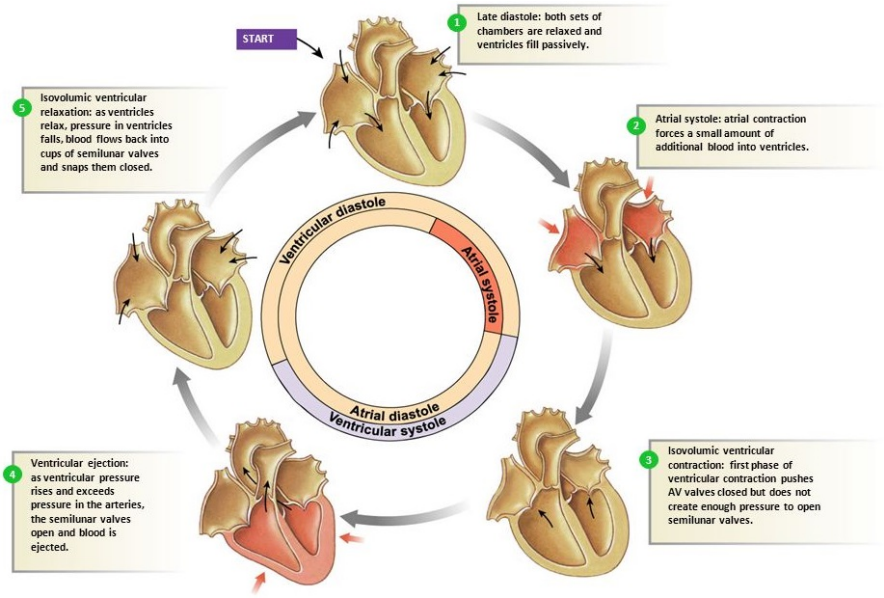

Figure 1.3: Schematic diagram of the cardiac cycle (adapted from [87]).

At the beginning of this cycle, the atrial and ventricular musculatures are completely relaxed, the cardiac chambers are almost filled with blood, the atrioventricular valves are open and the semilunar valves are closed. When the atrial systole arises, a slight increase of pressure in atria and ventricles occurs. Actually, the atrial systole does not last long, the atrial muscular mass is limited and the ventricular chambers have already been passively filled for more than two-thirds of their total capacity at the end of the diastolic phase of the previous cycle. However, thanks to the atrial systole, the volume of each ventricle reaches the end-diastolic volume (120÷130 ml). At the end of the atrial contraction, the sudden deceleration of blood against the ventricular walls causes a whirling motion that tends to close the atrioventricular valves.

In the meanwhile, the electrical excitation has completely propagated from atria to ventricles, leading to the ventricular systole and promoting an abrupt increase of pressure in ventricles that finally seals the

atrioventricular valves. The first phase of the ventricular systole is isovolumic because all valves are closed and the contraction of the ventricular musculature determines an increase of pressure without modifications in volume. It ends when the pressure in ventricles exceeds the one in the aorta and in the pulmonary artery; actually, the semilunar valves open and blood starts to flow into these vessels. This second phase is the ventricular ejection (or blood efflux) and it is characterized by a significant decrease of the ventricular volume up to the end-systolic volume (50÷60 ml) together with, first, an increase and, then, a decrease of pressure.

When the pressure in ventricles gets lower than the one in the aorta and in the pulmonary artery, the semilunar valves shut. The first phase of the ventricular diastole then starts. It is isovolumic since pressure significantly decreases while volume is not affected. When the pressure in ventricles is lower than the one in atria, the atrioventricular valves open and blood from veins starts to flow into ventricles through atria, which have already relaxed during their diastole. Thus, the second phase of the ventricular diastole begins, i.e. the diastolic filling.

The volume and pressure values in ventricles are useful to describe a diagram that summarizes the four just recalled phases of a cardiac cycle, i.e. the isovolumic systole, the ejection or blood efflux, the isovolumic diastole and the diastolic filling (Figure 1.4).

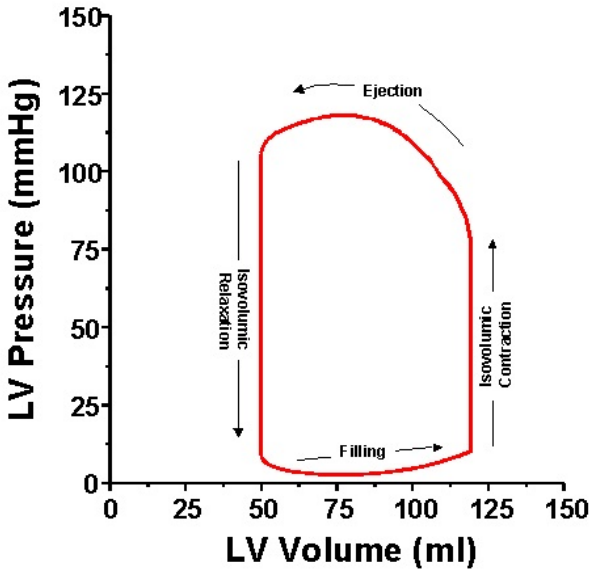

Figure 1.4: Pressure-volume loop of the left ventricle (adapted from [88]).

1.1.3. The Frank-Starling law

The heart must deliver blood to all body tissues by promptly adjusting its cardiac output, defined as the product of the stroke volume, which is the

volume of blood ejected from the left ventricle per beat, i.e. the difference between the end-diastolic volume and the end-systolic one, and the heart rate, when their degree of activity changes from rest to physical exercise and vice versa or under pathological conditions [16,30]. The regulation of the cardiac output can be intrinsic, i.e. related to the heart ability to vary its contraction force, or extrinsic, i.e. achieved via the sympathetic and parasympathetic fibers of the autonomic nervous system or by the hormones flowing through blood, among which the most important ones are the two catecholamines adrenaline and noradrenaline. To meet the aims of this thesis, only the former regulation is discussed.

The heart intrinsic regulation was first discovered by Frank for the isolated frog heart at the end of the 19th century [58], following the first observations made by Cyon, Coats and Bowditch [230], and then formalized by Starling at the beginning of the 20th century [204]. Starling used a specific heart-lungs preparation on a dog (Figure 1.5), where the systemic circulation of the animal was completely replaced with an artificial extracorporeal one, whose mechanical features (for instance, its hydraulic resistance and pressures) could be tuned and which permitted to directly measure the resultant cardiac output. The pulmonary circulation and the lungs of the animal remained active to oxygenate blood. The extracorporeal circulation included: a connecting hose with a manometer that replaced the arterial tree, a compression chamber that simulated the vessel elasticity, a compressible tube that regulated the peripheral resistance, a thermostatic coil that kept blood at body temperature in pipes and a reservoir from which blood came back to the right atrium again.

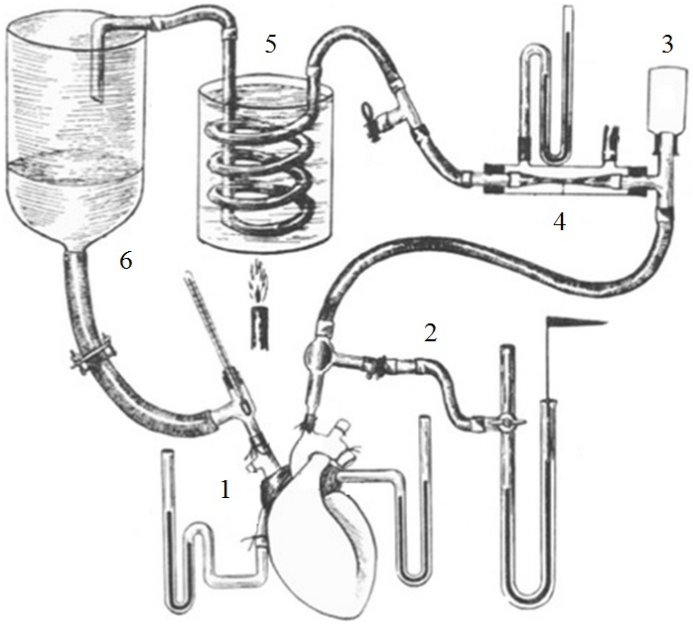

Figure 1.5: Schematic diagram of Starling's heart-lungs preparation on a dog: 1) heart and lungs; 2) connecting hose with manometer; 3) compression chamber; 4) compressible tube; 5) thermostatic coil; 6) reservoir (adapted from [45]).

By moving the reservoir up and down, Starling could modify the blood pressure in the right atrium, thus regulating the diastolic filling of the heart. He remarked that, at a constant heart rate, the cardiac output slightly increased when the arterial pressure was varied (for instance, by raising the circulatory resistance). The output considerably increased, instead, when the venous pressure was raised. This phenomenon proved that the more the ventricular musculature stretched during the diastolic filling the more it contracted during the subsequent systole. Then, Starling stated the following law: the contraction energy of cardiac fibers increases with their initial elongation. This law is valid within a physiological range; actually, if stretching exceeds a certain limit, contraction energy does not increase any longer, but it starts to decrease because the heart failure condition is reached. Therefore, there is an optimal length at which cardiac fibers are able to develop a maximum value of contraction energy. This can be highlighted by a graph where the end-diastolic volume on the abscissa is put in relation with the stroke volume on the ordinate (Figure 1.6). The end-diastolic volume points out the initial length of fibers at the beginning of the cardiac cycle, whereas the stroke volume is an index for the maximum force developed by fibers. Under physiological conditions of rest and physical exercise, the degree of filling is always kept under the previous optimal length value, where the Frank-Starling law is valid. When the blood demand of tissues increases, the vasodilation that occurs in them sends more blood to the right atrium, thus raising the venous pressure and the diastolic filling of ventricles. This automatically causes an increase of the ventricular contraction force and of the stroke volume. Details on the cell mechanisms at the basis of the Frank-Starling law will be given in Chapter 2.

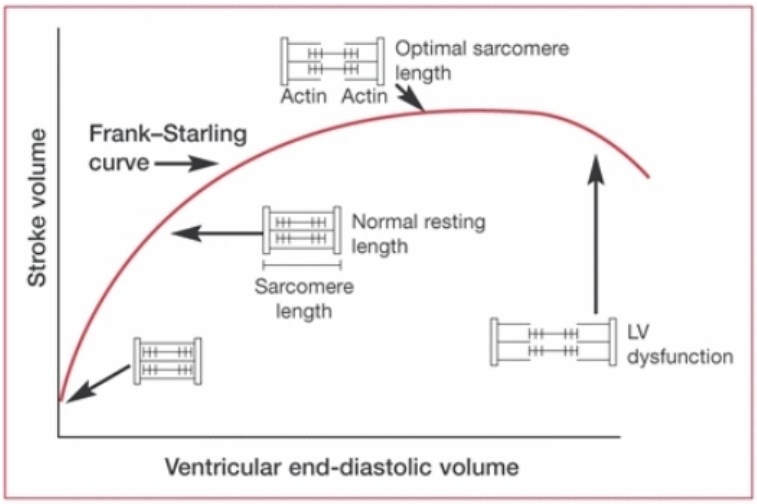

Figure 1.6: Relationship between the ventricular end-diastolic volume and the stroke volume showing the Frank-Starling law [89].

1.2. General properties of the myocardium

From the previous section, it follows that the myocardium is the primary tissue accounting for both the electrical propagation (by the conduction system) and the mechanical contraction (through the active and passive myocardia) of the heart. Since the simulations reported in the next chapters will involve this tissue, further details about its properties are given below [16,30].

1.2.1. Excitability

The myocardium is able to respond to electrical stimuli like the skeletal muscle. If the stimulus is strong enough to exceed a threshold intensity value, it evokes an electrical and mechanical response, otherwise it does not trigger any response. Actually, the stimulus determines a cardiomyocyte activation process characterized by the onset of an electrical phenomenon, called action potential, at the level of the plasma membrane that is followed, with a certain delay, by the mechanical contraction of the cell.

The typical action potential of the human ventricular myocardium is displayed in Figure 1.7 together with its main phases:

1. a depolarization phase, during which the transmembrane potential, i.e. the difference between the intracellular and extracellular potentials, quickly rises from its negative resting value of -80÷-90 mV, crosses 0 mV and reaches a positive peak of about 20÷50 mV;
2. a plateau phase, a quite long period (100÷300 ms) in the human and other mammalian species (except from rats and mice that lack it), during which the transmembrane potential is near 0 mV;
3. a repolarization phase, during which the plasma membrane regains its resting value.

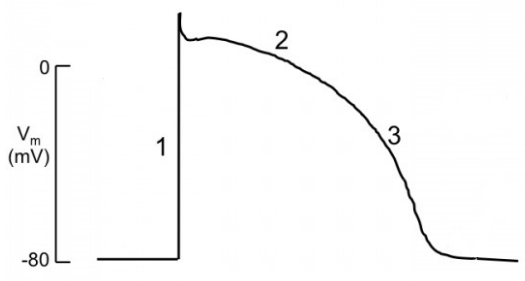

Figure 1.7: Schematic plot of a human ventricular action potential with its phases: 1) depolarization; 2) plateau; 3) repolarization (adapted from [90]).

All previous phases come out from specific ionic phenomena. The depolarization up to the threshold value of about -70 mV induces the opening of the fast sodium channels. These ones bring positive charges inside the myocyte, i.e. an inward current I_{Na} that further depolarizes the membrane, triggering a self-sustained process, until the sign inversion of the transmembrane potential. The plateau is due to the overlap of different ionic events. At the beginning of it, while I_{Na} is extinguishing, some calcium channels, which are activated at about -40 mV, drive an inward current I_{CaL} that is positive again, thus keeping the membrane depolarized. During the plateau, while the I_{CaL} channels are deactivating, the slow delayed rectifier channels carrying an outward potassium current I_{Ks} get open. Therefore, the plateau can be explained in terms of the balance between these two opposite currents. At last, the repolarization up to the resting value is mainly due to the late activation of the rapid delayed rectifiers, which are another kind of potassium channels that, at the end of the plateau, let potassium ions (represented by the current I_{Kr}) leave the myocyte, thus promoting the membrane repolarization till when these channels deactivate.

The presence of the plateau is the main difference between the action potential of cardiomyocytes and the one of skeletal myocytes (if rodents are disregarded). Thus, it may happen that the mechanical contraction starts before the electrical activation ends in cardiac myocytes, whilst it may not in the skeletal ones, where the action potential has already come to an end.

1.2.2. Refractoriness

When the myocardial tissue is electrically excited and an action potential develops, it becomes refractory for a certain period of time, i.e. it is unable to respond to another stimulus. In particular, the whole refractory period is divided into two phases. During the first one, refractoriness is absolute, i.e. no stimuli can elicit a new electrical response independently of their amplitude; this period corresponds to the plateau phase of the action potential. Then, at the beginning of the repolarization phase, refractoriness becomes relative and cardiomyocytes can gradually recover their excitability provided that the second stimulus is sufficiently stronger than the first one.

In skeletal myocytes, the duration of the action potential is limited to some milliseconds, thus the whole refractory period is very short and it terminates immediately after the depolarization of the plasma membrane. In cardiomyocytes, instead, where the action potential can last hundreds of milliseconds, the absolute refractoriness covers most of the contraction period (Figure 1.8). This aspect prevents high-frequency electrical stimuli from causing the merging of subsequent contractions in the myocardium, a phenomenon that may happen in the skeletal muscle instead, giving rise to the so-called muscular tetanus. Therefore, the heart cannot be tetanized.

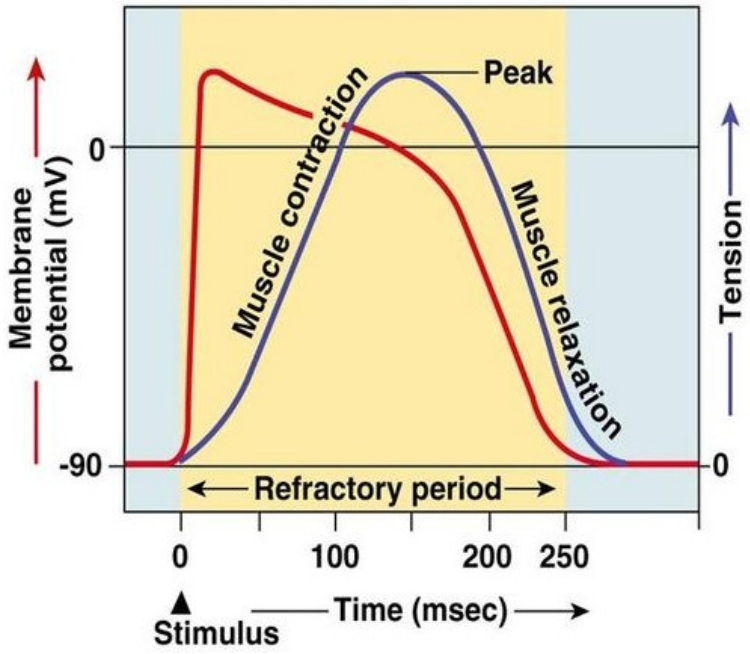

Figure 1.8: Relationship between cardiac refractoriness and contraction (adapted from [91]).

At last, there are significant differences as regards the refractoriness duration throughout the heart. For instance, refractoriness is shorter in the atrial myocardium than in the ventricular one, whilst it is far longer in the atrioventricular node in order to protect ventricles from too frequent stimuli deriving from functional disorders in atria.

1.2.3. Conductivity

Cardiomyocytes are longitudinally and transversely interconnected in order to create a syncytium (Figure 1.9). Connections are characterized by some intercalated discs, where the plasma membranes of two adjacent cells are very close and they may fuse to form gap junctions. This configuration ensures a very low electrical resistance, which fosters the transmission of the action potential from the stimulation point (i.e. the sinoatrial node) to the whole heart. The diffusion of electrotonic currents is strong enough to propagate from the active cells to the resting ones and to elicit new action potentials. The conduction velocity depends on the action potential features (i.e. the intensity of the transmembrane currents) and the geometry of the cardiac network. Moreover, it is usually higher along the major axis of cardiomyocytes than in any transverse direction thanks to the higher concentration of gap junctions and the larger cross-sectional area.

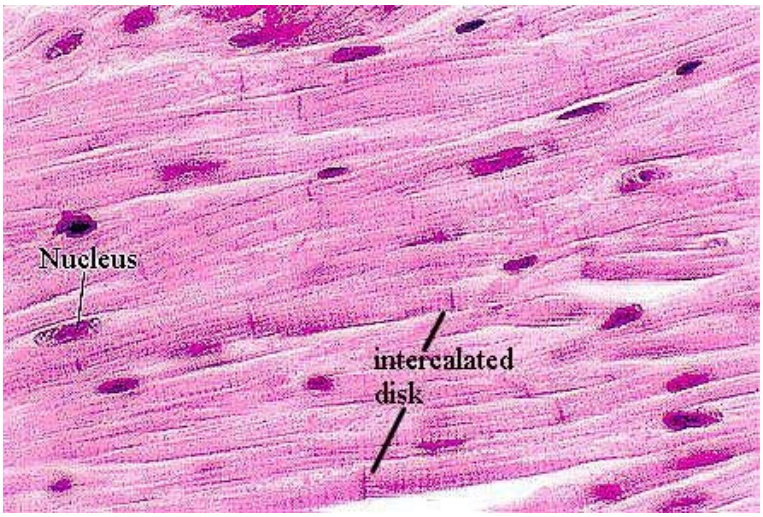

Figure 1.9: Syncytial aspect of the cardiac tissue [92].

Skeletal myocytes, instead, do not show intercalated discs and gap junctions because each of them is isolated and directly driven by the synaptic terminal of a motoneuron after the arrival of an electrical impulse from the central nervous system.

1.2.4. Contractility

The myocardium can contract under electrical stimulation like the skeletal muscle. For both tissues, the concentration of cytoplasmic (or intracellular) calcium must increase in order to elicit the mechanical contraction, though this is achieved in two different ways as it is discussed below.

Both the myocardium and the skeletal muscle have a transverse T-tubule system made of long invaginations of plasma membrane inside cells (Figure 1.10). These structures form diads in cardiomyocytes or triads in skeletal myocytes according to the number of terminal cisternae of the sarcoplasmic reticulum they are in contact with, i.e. one cisterna in the former cells and two cisternae in the latter ones. Thanks to the T-tubules, the electrical activation reaches the deepest areas of cells [17].

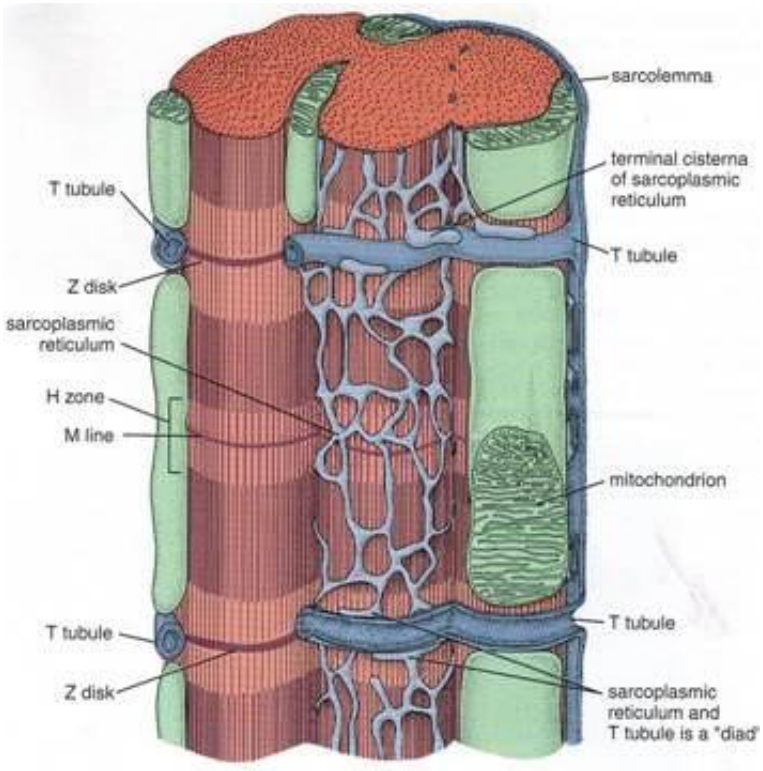

Figure 1.10: Schematic diagram of the T-tubule system in a cardiomyocyte [93].

In cardiomyocytes, the inward calcium current I_{CaL} accompanying the action potential and entering through the L-type channels at the level of the T-tubules triggers a multiplicative phenomenon known as Calcium-Induced Calcium Release (CICR). Actually, starting from a small amount of calcium ions at the level of the plasma membrane, a bigger amount of them is released, through the ryanodine receptors, from the sarcoplasmic reticulum (where they are buffered to the calsequestrin protein) to the dyadic space between the T-tubules and the reticulum first and to the cytoplasm then.

In skeletal myocytes, instead, the calcium release from the sarcoplasmic reticulum occurs thanks to the mechanical opening of some channels driven by a morphological change of the dihydropyridine (DHP) receptors in the T-tubule membrane.

However, after the increase of intracellular calcium, the following mechanism for the development of force is the same in cardiomyocytes and skeletal myocytes and it occurs in sarcomeres [4,68,202].

Sarcomeres show repetitive light and dark stripes (Figure 1.11). They are placed between two dark Z lines that split the light I bands (made of only thin actin filaments) in two halves belonging to two adjacent sarcomeres. The central A band includes thick myosin and thin actin filaments and, in the middle of it, a light H zone with the M line represents the part of thick filaments that is not superimposed by the thin ones.

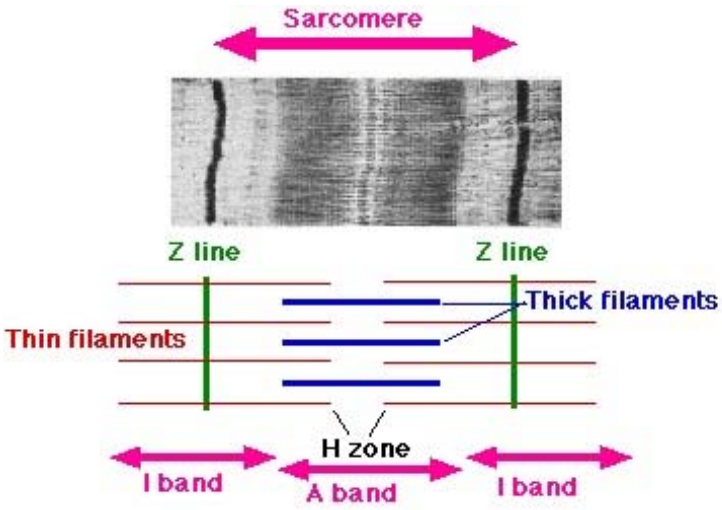

Figure 1.11: Sarcomere aspect through a polarization microscope (top) and schematic diagram of its components (bottom) [94].

A thin filament is a double helix of F-actin, i.e. the polymerized form of the globular protein G-actin that provides the binding sites with myosin (Figure 1.12). It is covered with tropomyosin, a protein with two α-helixes between the two actin helixes, and troponin, which is a complex of three globular units regularly placed along the tropomyosin filament: troponin C (TnC), which includes the binding site with the intracellular calcium, troponin I (TnI), which inhibits the actin-myosin interaction, and troponin T (TnT) that binds TnC, TnI and tropomyosin. In particular, TnC is a long helix with two globular C and N ends. The C end includes the binding sites III and IV that bind calcium and magnesium competitively, but they are saturated under physiological conditions. The N end includes the binding sites I and II for calcium, which are both active for skeletal myocytes, whilst only the site II is active for cardiomyocytes (thus, it controls contraction) due to a high positive charge near the site I that prevents calcium from binding.

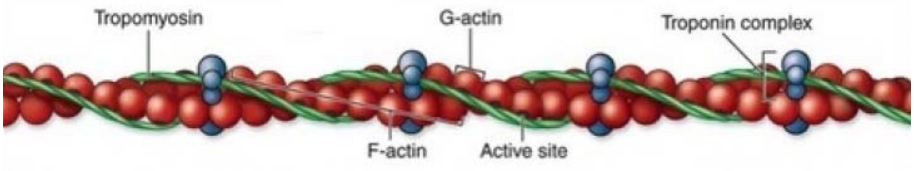

Figure 1.12: Schematic diagram of a thin filament (adapted from [95]).

A thick filament, instead, is made of about 250 myosin molecules with many tails bending outside the filament and ending with a head interacting with actin and ATP (adenosine triphosphate) (Figure 1.13).

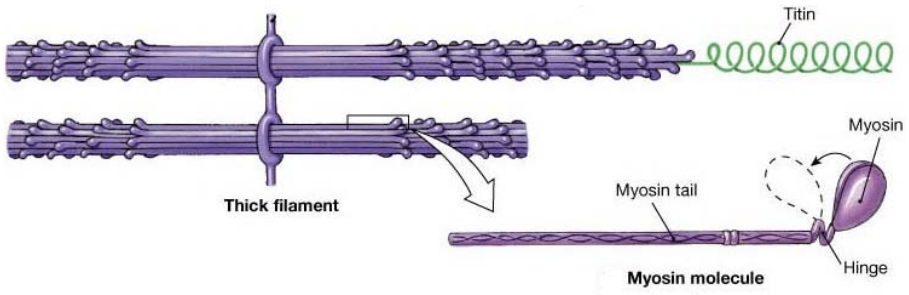

Figure 1.13: Schematic diagram of a thick filament (adapted from [96]).

At rest, the troponin-tropomyosin complex inhibits the actin-myosin interaction. When the intracellular calcium increases, the binding between calcium and TnC shifts tropomyosin, exposing the actin-myosin binding site and allowing the formation of a weak or strong cross-bridge. Myosin releases a phosphate group P_i in order to provide its head with enough energy to rotate and to push the actin filament towards the center of the sarcomere till when ADP (adenosine diphosphate) is released from myosin too. Then, the head separates from actin because it binds to another ATP molecule, it comes back to its original position thanks to the ATP hydrolysis carried out by myosin ATPase and it binds to a new actin molecule. This cycle is followed repeatedly by each myosin molecule in order to develop the contraction force at the cell level (Figure 1.14); as a remark, only strong cross-bridges determine force.

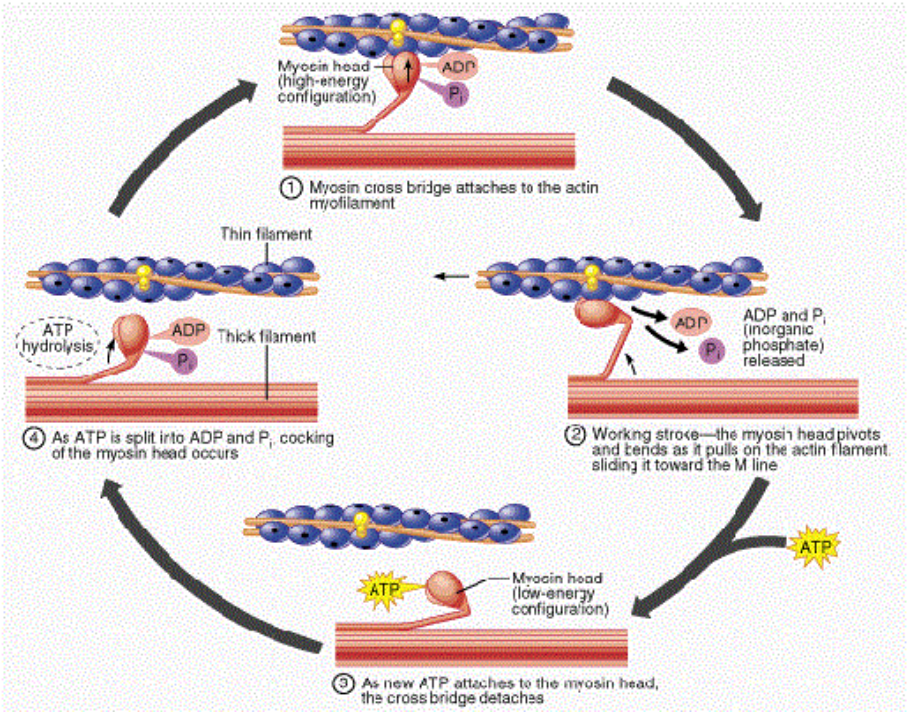

Figure 1.14: Schematic diagram of the actin-myosin interactions during a contraction cycle (adapted from [97]).

The deactivation of the contractile apparatus is similar to the one in the skeletal muscle and it is achieved by bringing back the intracellular calcium concentration to its resting value (<0.1 μM); the remaining intracellular calcium is bound to the calmodulin protein because free calcium is toxic for cells. This is done by a SERCA pump that gathers calcium ions inside the sarcoplasmic reticulum, a plasma membrane sodium/calcium exchanger and a plasma membrane ATP-mediated transport.

At the level of the entire myocardial tissue, contraction is synchronous thanks to its syncytial feature and it cannot be voluntarily modulated. In the skeletal muscle, instead, the developed force can be modulated by the central nervous system thanks to the recruitment of a variable number of motor units. However, the skeletal muscle may be also responsible for involuntary motor acts (the so-called reflexes) in response to environmental stimuli.

1.3. Example of myocardial pathology: hypertrophy

As all other body tissues, the myocardium may be affected from several pathologies that threaten its regular pumping function and may lead to disability and death; more than 25 million people worldwide are affected from heart failure and this figure is expected to increase in the future [152]. In this thesis, the focus is on a recurrent pathology worldwide, i.e. hypertrophy [131,165,205]. Since the heart is part of the cardiovascular system, it may be affected from long-term changes in its mechanical environment and it may adapt to them in time. Hypertrophy is one of these adaptive processes, trying to keep the cardiac output stable by a geometrical remodeling of the organ. Cardiomyocytes grow in size but not in number, thus differencing from hyperplasia, which is another response body tissues may undertake during a maladaptive remodeling. Cells succeed in doing so by carrying out sarcomerogenesis, i.e. by synthetizing and assembling new sarcomere units next to the preexistent ones. Several intracellular signaling pathways come into play during both the transduction of extracellular mechanical stimuli and the subsequent growth [78,106,164,210]. Although hypertrophy may be also a physiological and reversible response, for instance in strength and endurance athletes [50,151,171], it is more often a pathological and irreversible response in people of all ages.

If a chronic volume overload affects the heart (for instance, due to mitral valve regurgitation), the high diastolic strains trigger the development of new sarcomeres in series, which lengthen cells without significant modifications in their cross-sectional area; a length-to-width ratio up to about 11:1 [62] versus a physiological one of 7:1 [63] has been detected. Therefore, ventricles increase their volume, but the wall thickness is

preserved. This kind of cardiac growth is conventionally called eccentric hypertrophy.

On the contrary, a chronic pressure overload (for instance, due to systemic hypertension or aortic valve stenosis) causes high systolic stresses. Cardiomyocytes respond by depositing new sarcomeres in parallel, thus increasing their cross-sectional area, while keeping their length unchanged. The length-to-width ratio can decrease up to 3:1 [146,189]. On the macroscopic scale, this remodeling determines the thickening of ventricular walls without altering the corresponding chamber volumes. This kind of cardiac growth is usually called concentric hypertrophy. Figure 1.15 resumes the effects of the two previous hypertrophic phenotypes on the microscopic scale of a cardiomyocyte and on the macroscopic one of a ventricle.

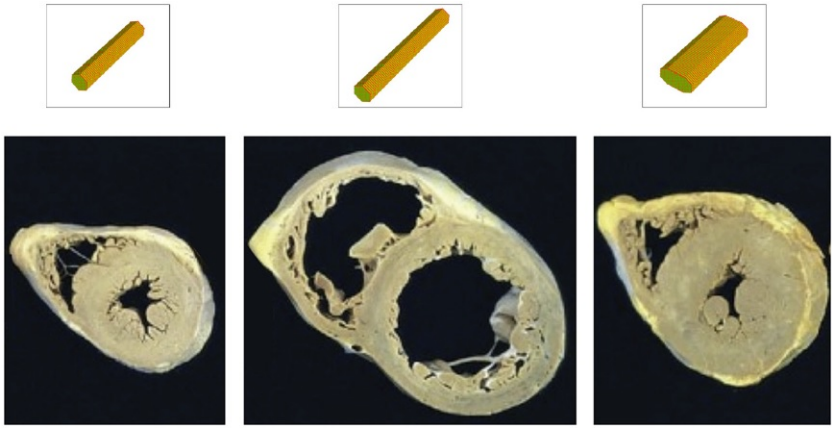

Figure 1.15: Effects of eccentric (middle) and concentric (right) hypertrophy on cardiomyocytes (top) and on ventricles (bottom) compared with the healthy heart (left) (adapted from [66,67]).

However, cardiac growth is not necessarily an ordered phenomenon, especially if it worsens with time and it may lead to severe cardiomyopathies, such as dilated cardiomyopathy DCM, with an eccentric phenotype, and hypertrophic cardiomyopathy HCM with a concentric one [98]. Then, it could be not only a compensatory process, but also the cause of serious ventricular dysfunctions and heart failure. The added sarcomeres may make myocardial fibers lose their structurally rotating architecture, i.e. a fiber dispersion may happen [28,49,209,213]. Moreover, hypertrophy may be accompanied with an increase of fibrosis (additional connective tissue) and an extracellular matrix remodeling [72,78,205].

At last, a hypertrophic phenotype may also derive from one or more well-known inherited genetic defects [145,180]. However, in this thesis, hypertrophy is considered only as an adaptive cardiac response to mechanical alterations in time, thus neglecting any genetic cause.

1.4. Cardiac cultures

Nowadays, cardiac cultures have become a milestone for various researchers involved in discovering the mechanisms of the heart beating thanks to their relatively cheap, easy and reproducible *in vitro* preparation dictated by well-established protocols [188]. They are generally made of cardiomyocytes derived from neonatal hearts through enzymatic digestion or differentiated from embryonic or induced pluripotent stem cells that can proliferate and self-beat on Petri dishes (differently from adult cells that are not able). Since the second half of the 20th century they have formed the basis for physiological and pharmacological studies (e.g., [54,55]) as an effective and safer alternative to the isolation of the *in vivo* heart prescribed by Langendorff in 1898 [134]. Actually, starting from a control culture, one can deliver drugs (for instance, isoproterenol or phenylephrine) or analyze how the propagation of the electrical signal is affected from the way cardiomyocytes are oriented in the space, for instance an isotropic propagation versus an anisotropic one. Moreover, if they are associated with special micromodified substrates or with porous scaffolds and if they are grown together with other cell types (like fibroblasts and endothelial cells) under appropriate mechanical or electrical stimuli in bioreactors, they may develop into functional and viable tissue engineering cardiac patches (monolayered or, better, multilayered). Then, these patches can be grafted onto injured parts of the heart (for instance, infarcted areas), thus promoting a gradual healing [12,25-27,174]. After their transplantation, they must be able to develop enough contractile force and to propagate electrical stimuli in a proper way like the anisotropic surrounding tissue.

Figure 1.16 resumes the most recurrent procedures to build *in vitro* a multilayered cardiac patch. Solutions a) and b) are based on scaffolds. From a physical point of view, scaffolds must be highly porous with adequate pore dimensions promoting the implantation of cells, the diffusion of oxygen and nutrients and the removal of waste products throughout the entire structure. From a chemical point of view, they must be biodegradable, i.e. they must be reabsorbed by the surrounding tissue avoiding any surgical procedure to remove it, and they must have a proper degradation rate in order to ensure that the new tissue will be able to bear a high mechanical load and to propagate electrical signals when it completely degrades. In particular, solution a) is the classical one in tissue engineering based on preformed scaffolds. These ones are first synthetized without cells, which are then seeded just before the culturing process. They are made of only natural materials (for instance, collagen, decellularized extracellular matrixes, fibrinogen or fibroin) or combined with synthetic ones (for instance, polymers of polylactic and polyglycolic acids PLGA). Their main advantage is the high control on the structure, dimensions and orientation of pores, i.e. on the spatial development of cells. Solution b), instead, is represented by hydrogel scaffolds, characterized by a polymeric network with a high amount of water among protein chains. They can trap

cells in this dense network and they can be freely molded by cells themselves. They are liquid outside the body and they become semisolid gels inside thanks to their chemical and physical features and their response to environmental stimuli like temperature and pH; thus, they can be also injected directly inside an infarcted area via a catheter. They are made of fibrin, collagen or chitosan combined with PLGA or polyethylene glycol PEG. At last, solution c) is the most innovative one, i.e. cell-sheet engineering. This is a scaffoldless approach, i.e. no external scaffolds are used because cells are stimulated to produce their own supporting structure. This is achieved thanks to a cell culture surface fixed on a polymeric biomaterial that is sensible to temperature (for instance, poly(N-isopropylacrylamide) PIPAAm). By temperature, cells proliferate, attach to the surface, create interconnections and build their own extracellular matrix. This technique is beneficial because it reduces the number of foreign materials to be grafted *in vivo*, thus limiting immunological issues like rejections. However, similarly to hydrogels, it does not govern the proper spatial distribution and growth of cells owing to their autonomous fabrication of the scaffold.

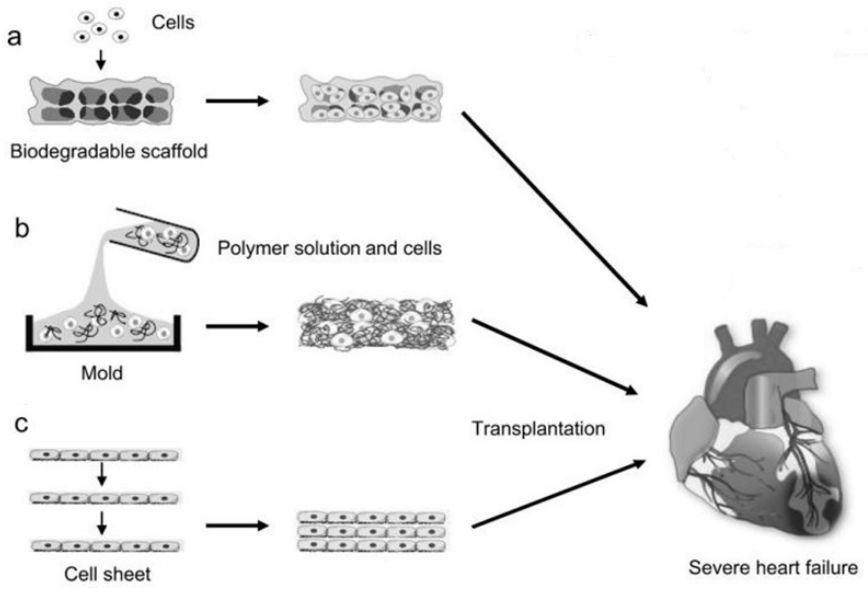

Figure 1.16: Different techniques to build *in vitro* a multilayered cardiac patch for transplantation on the injured heart: a) preformed scaffolds; b) hydrogels; c) scaffoldless approaches (adapted from [196]).

Chapter 2

The electromechanical framework

In this chapter, the general three-dimensional mathematical model of a myocardial tissue structure is developed in order to describe its microscopic and macroscopic electrophysiology and mechanics. A section about tissue growth is also present. The specific models or laws that vary according to the type of simulations carried out will be highlighted in the next chapters instead. Additional details concerning the space and time discretizations of the whole model and the most general algorithm followed to run all simulations are given at the end of this chapter.

2.1. Overview

A complete model of cardiac electromechanics includes three components at least (see an example in Figure 2.1):

- a cell model that describes the main phenomena occurring at the level of a single cardiomyocyte, among which the evolutions of the action potential, ionic currents and intracellular concentrations and the development of contraction force;
- a mechanical model based on finite elasticity, which computes the tissue deformation as a response to the electrical activation by taking into account the passive mechanical properties and the contraction force;
- a reaction-diffusion model, i.e. a Monodomain or Bidomain model, which drives the propagation of the electrical activation throughout the tissue.

In particular, the reaction-diffusion model is connected to the cell model through the transmembrane potential and the ionic currents. The mechanical model is driven by the active tension (or simply by an

intracellular concentration like the calcium one) developed at the cell scale, which acts as an electromechanical coupling variable. Vice versa, it may affect the cell processes by some feedback mechanisms, like the stretch-activated channels in the plasma membrane and the calcium-troponin C binding in sarcomeres. Moreover, it may have effects on the conductivities of the reaction-diffusion model that drive the propagation of the electrical signal. In particular, the influence of mechanics on stretch-activated channels defines the so-called mechanoelectric feedback.

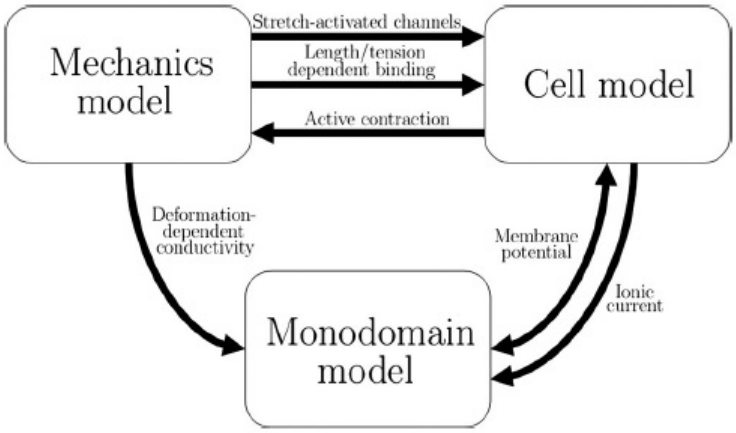

Figure 2.1: Schematic representation of the main components and interactions in a full cardiac electromechanical model [132].

2.2. Cell modeling

2.2.1. The membrane model

As in all excitable cells, the plasma membrane of a cardiomyocyte is a double layer of phospholipids with proteins that can be channels, pumps or exchangers for the selective transport of ions from the extracellular space to the intracellular one and vice versa [36,69,115]. Therefore, the study of the ionic currents flowing through these proteins turns out to be necessary to understand the evolution of the action potential and of the concentration gradients across the membrane. In particular, the main ions driving the electrophysiology of a cardiomyocyte are sodium Na^+, potassium K^+ and calcium Ca^{2+}. Their concentration gradients are held stable by active transport mechanisms that employ the chemical energy from ATP molecules to pump specific ions inside or outside the cell (for instance, the sodium-potassium pump). These active mechanisms counterbalance the passive ionic flows that are simply driven by concentration gradients. The exchangers, instead, are able to remove and attract specific ions without wasting energy.

Due to its function of separating charges, the plasma membrane is generally considered as a capacitor, whose capacitance C_m is expressed as the ratio of the transmembrane charge q to the voltage v

$$C_m = \frac{q}{v}. \tag{2.1}$$

If C_m is constant, the corresponding capacitive current I_{cap} is

$$I_{cap} = \frac{dq}{dt} = C_m \frac{dv}{dt}. \tag{2.2}$$

The previous capacitor is then put in parallel to a resistor (with resistance R_m) representing the sum of all ionic currents I_{ion} (Figure 2.2), thus the conservation law imposes that the sum of I_{cap} and I_{ion} must be equal to the applied stimulation current I_{app}

$$C_m \frac{dv}{dt} + I_{ion} = I_{app}. \tag{2.3}$$

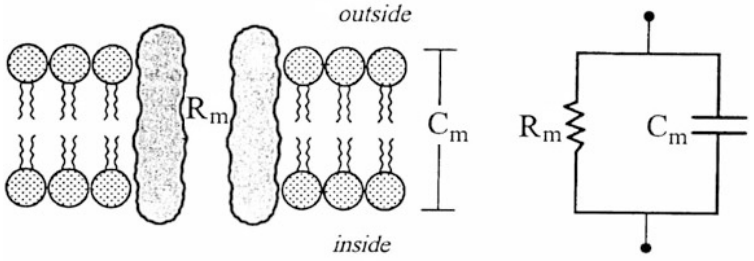

Figure 2.2: General electrical circuit model of the plasma membrane of a cardiomyocyte: R_m is the resistance and C_m is the capacitance (adapted from [36]).

I_{ion} is given by the specific ionic membrane model adopted. Its generic expression in a unit area of membrane surface is the following one

$$I_{ion} = g(v,t)\Phi(v), \tag{2.4}$$

where g(v,t) is the proportion of open channels in a unit area of membrane surface and $\Phi(v)$ is the current-voltage relation of one open channel. $\Phi(v)$ may be linear or non-linear with respect to v. A linear relation may derive from the approximation for long channels of the Poisson-Nernst-Planck (PNP) equation (see [194] for a derivation of the PNP system from the Langevin model of ionic motion)

$$\Phi(v)=\frac{zFD}{L}\frac{c^e-c^i}{E}(v-E)=g_c(v-E), \tag{2.5}$$

where F is the Faraday constant, L is the channel length and, considering an ionic species flowing through that channel, z is its valence, D its diffusion coefficient, c^e and c^i its fixed resting extracellular and intracellular concentrations and $E=RT/(zF)\log(c^e/c^i)$ (with R the gas constant and T the absolute temperature) its Nernst equilibrium (or reversal) potential. The product between the first two ratios is constant and it can be resumed in the channel conductance g_c. On the contrary, a non-linear relation may come from the complementary approximation for short channels of the PNP equation, which gives the so-called Goldman-Hodgkin-Katz (GHK) equation

$$\Phi(v)=\frac{z^2F^2D}{RTL}v\frac{c^i-c^e e^{-\frac{zF}{RT}v}}{1-e^{-\frac{zF}{RT}v}}. \tag{2.6}$$

See [36] for a rigorous derivation of the two previous relations. g(v,t), instead, can be expressed as

$$g(v,t)=\frac{N}{S}=\frac{N_{tot}}{S}\frac{N}{N_{tot}}=\frac{N_{tot}}{S}w, \tag{2.7}$$

where N is the number of open channels, N_{tot} is the total number of membrane channels, S is the membrane surface area and w is the percentage of open channels, also called gating variable. Thus, for a long channel, it derives that

$$I_{ion}=\frac{N_{tot}g_c}{S}w(v-E)=\overline{G}_c w(v-E), \tag{2.8}$$

where $\overline{G}_c$ is the maximum channel conductance per unit area of the membrane surface, whereas, for a short channel, it derives that

$$I_{ion}=\frac{N_{tot}}{S}\frac{z^2F^2D}{RTL}wv\frac{c^i-c^e e^{-\frac{zF}{RT}v}}{1-e^{-\frac{zF}{RT}v}}. \tag{2.9}$$

The evolution of w is described by an ODE (Ordinary Differential Equation)

$$\frac{dw}{dt}=\alpha(1-w)-\beta w, \tag{2.10}$$

where α and β are the transition rate constants (dependent on v) between the closed and open states of a channel made of one protein subunit. By setting $w_\infty=\alpha/(\alpha+\beta)$ and $\tau_w=1/(\alpha+\beta)$, the previous equation can be transformed into

$$\frac{dw}{dt}=\frac{w_\infty-w}{\tau_w}, \tag{2.11}$$

where w_∞ is the equilibrium state and τ_w is the time constant. See [36] for a complete discussion about w when different types of channel structures are accounted for in order to better fit the experimental conductance curves.

Therefore, the general structure of a cardiomyocyte membrane model turns out to be described by the following system of ODEs

$$\begin{cases} C_m\frac{dv}{dt}+I_{ion}(v,\mathbf{w},\mathbf{c})=I_{app} \\ \frac{d\mathbf{w}}{dt}-\mathbf{R}(v,\mathbf{w})=\mathbf{0} \\ \frac{d\mathbf{c}}{dt}-\mathbf{S}(v,\mathbf{w},\mathbf{c})=\mathbf{0} \\ v(0)=v_0, \quad \mathbf{w}(0)=\mathbf{w_0}, \quad \mathbf{c}(0)=\mathbf{c_0}, \end{cases} \tag{2.12}$$

where C_m, I_{ion} and I_{app} are expressed per unit area of the membrane surface and **w** and **c** are two vectors including the gating variables and ionic concentrations. In particular, I_{ion} is described by the following general equation in the remainder of this thesis

$$I_{ion}(v,\mathbf{w},\mathbf{c})=\sum_{k=1}^{N}(G_k(v,\mathbf{c})\prod_{j=1}^{M}w_j^{p_{j_k}}(v-E_k(\mathbf{c})))+I_n(v,\mathbf{w},\mathbf{c}), \tag{2.13}$$

where N is the number of ionic currents, M is the number of gating variables per ionic current, G_k is the membrane conductance and E_k the reversal potential for the k-th current, p_{j_k} are integers that account for the number of subunits of a certain type for each channel and I_n groups together all time-independent ionic currents. The evolution of all w, instead, is represented by the Hodgkin-Huxley formalism [81]

$$\begin{cases} \frac{dw_j}{dt}=R_j(v,\mathbf{w})=\alpha_j(v)(1-w_j)-\beta_j(v)w_j \\ w_j(0)=w_{j,0} \\ \alpha_j,\beta_j>0, \quad 0\le w_j\le 1, \quad j=1,...,M, \end{cases} \tag{2.14}$$

whilst the one for all c is given by

$$\begin{cases} \dfrac{dc_j}{dt} = S_j(v,\mathbf{w},\mathbf{c}) = -\dfrac{I_{c_j}(v,\mathbf{w})A_{cap}}{V_{c_j} z_{c_j} F} \\ c_j(0) = c_{j,0} \\ j = 1,\ldots,S, \end{cases} \tag{2.15}$$

where A_{cap} is the capacitive membrane area, I_{c_j} is the sum of the ionic currents carrying the ion c_j, V_{c_j} is the volume of the compartment where c_j is updated and z_{c_j} is the valence of c_j.

The specific forms of I_{ion} and of the evolutions of w_j and c_j depend on the adopted cardiac plasma membrane model. In the literature, several such models for the ventricular cardiomyocytes of different mammalian species have been published since the first one by Beeler and Reuter in 1977 [14]. In particular, a group of first generation models, like the one just recalled and [141], assumed that the intracellular sodium and potassium concentrations do not vary during an action potential, whereas they described the evolution of the intracellular calcium concentration in a phenomenological way. Then, a group of second generation models were developed, representing the current gold standard (e.g., [18,40,80,105,110,138,139,142-144,160,163,166,197,207,225]). These models do not neglect the ionic concentrations changes in cardiomyocytes because they can affect the shape of the action potential especially at high pacing rates. Moreover, they describe the calcium concentration changes in a more biophysically detailed way by taking into account the Calcium-Induced Calcium Release phenomenon. At last, some of them (e.g., [19,74]) are introducing more and more specific signaling pathways that describe the cardiac cell response to different substrates. In the next chapters, additional details regarding the specific plasma membrane models used for simulations will be reported.

At last, in this thesis, the I_{ion} computed from the adopted plasma membrane model may be summed to a stretch-activated channels current I_{SAC}, which represents a mechanical feedback, in particular a mechanoelectric feedback [124], as it has been recalled at the beginning of this chapter. In the literature, different equations for this current have been developed (e.g., [73,123,212,216]). In this thesis, it is modeled as in [157], i.e. as the sum of non-selective and selective currents $I_{SAC}=I_{SAC,n}+I_{Ko}$. The former current $I_{SAC,n}$ is given by $I_{SAC,n}=I_{SAC,Na}+I_{SAC,K}$, i.e. by the sum of a sodium-related current $I_{SAC,Na}$ and a potassium-related one $I_{SAC,K}$, whereas the second one I_{Ko} is only potassium-related. In more detail, the equations for $I_{SAC,Na}$, $I_{SAC,K}$ and I_{Ko} are

$$I_{SAC,Na}=\bar{G}_{SAC}\gamma_{SL,SAC}\frac{E_R-E_K}{E_{Na}-E_R}(v-E_{Na}),\quad I_{SAC,K}=\bar{G}_{SAC}\gamma_{SL,SAC}(v-E_K),\quad I_{Ko}=\bar{G}_{Ko}\frac{\gamma_{SL,Ko}}{1+e^{\frac{10+v}{45}}}(v-E_K), \tag{2.16}$$

where $\bar{G}_{SAC}=4.13\cdot10^{-3}$ mS/cm^2 and $\bar{G}_{Ko}=1.2\cdot10^{-2}$ mS/cm^2 are the maximum channel conductances per unit area of the membrane surface, $\gamma_{SL,SAC}=10\max(\lambda-1,0)$ and $\gamma_{SL,Ko}=0.7+3\max(\lambda-1,0)$ account for the linear dependence of currents on the stretch λ (as proved experimentally, e.g., in [101,176,178,186,227-229]) and E_R=-10 mV, E_K=-85 mV and E_{Na}=65 mV are the reversal potentials of I_{SAC}, potassium and sodium. Thus, I_{SAC} is active only when $\lambda>1$ according to the experimental results reported in the literature (e.g., [124]).

2.2.2. The active tension generation model

After the electrical activation and the increase of intracellular calcium, a cardiomyocyte develops its force and contracts thanks to its sarcomere apparatus. As regards the development of force, the models in the literature differ according to the level of detail reached while implementing the series of events occurring during a contraction cycle. The simplest ones describe it in a phenomenological way, thus using some macroscopic variables or functions that do not correspond to real entities but have the same dynamics and effect on the development of force (e.g., [65,119,140,154,182]). They are composed of a limited number of ODEs coupled with the previous cell electrophysiological model (2.12) and depending only on the transmembrane potential, intracellular calcium concentration or a time delay variable with respect to the electrical activation. Biochemically detailed models, instead, may help researchers get relevant insights into the actin-myosin interactions especially under non-physiological conditions, when tuning specific parameters may be necessary to simulate the effects of a pathology in a more proper way (e.g., [107,108,133,156,177,187,193,211,224]). They may include only ODEs or couple them with some algebraic equations and even one or more partial differential equations (PDEs), if spatial issues during the mutual sliding between thick and thin filaments (for instance, the myofilament lattice spacing, i.e. the ordered structure of such filaments) are taken into account. However, to be suitable for simulations at higher dimensions (1D, 2D and 3D) than the one of a single cell (0D) in terms of computational time and memory size at each time step, the level of detail in their equations must be reduced, while still including the main phenomena characterizing a contraction cycle. Therefore, some processes are described in a phenomenological way again. The full general form of such a model (employed in this thesis) is given by the following system made of Differential-Algebraic Equations (DAEs), i.e. including a limited number of ODEs, which describe the biochemical events during a contraction cycle,

and an algebraic equation that computes the force or active tension T_a (if expressed per unit area of the cell cross-section)

$$\begin{cases} \dfrac{d\mathbf{a}}{dt} - \mathbf{G}\left(\mathbf{a}, [Ca^{2+}]_i, \lambda, \dfrac{d\lambda}{dt}\right) = 0 \\ \mathbf{a}(0) = \mathbf{a_0} \\ T_a = h(\mathbf{a}, \lambda), \end{cases} \tag{2.17}$$

where **a** is a vector of physical and phenomenological differential variables, $[Ca^{2+}]_i$ is the intracellular calcium concentration computed from the previous membrane model, λ is the stretch already introduced for the stretch-activated channels current and computed from the tissue finite elasticity model (see below) and $d\lambda/dt$ is the corresponding stretch rate.

In particular, the role of λ and $d\lambda/dt$ in modulating T_a represents another mechanical influence on the cell model (in addition to the stretch-activated channels) acting on the calcium-troponin C binding in sarcomeres and recalled at the beginning of this chapter. Moreover, the dependence on λ accounts for the Frank-Starling law at the cell level. The two main aspects underlying this law are the degree of overlap between thick and thin filaments and the myofilament sensitivity to calcium ions [59,125,199]. Indeed, the former directly determines the availability of cross-bridges, whilst the latter may cause an increase of tension by an increase of stretch without a corresponding rise in intracellular calcium. Both of them are phenomenologically represented in (2.17) by a scaling factor for T_a and a change in the intracellular calcium required for the half-maximal tension generation respectively. Nevertheless, the way in which the myofilament calcium sensitivity is regulated is still debated. A possible mechanism is the thin filament cooperativity, by which the first generated strong cross-bridges enhance the formation of many other ones through a further shift of tropomyosin along actin and an increase of the apparent affinity of troponin C for calcium. The model in (2.17) captures this cooperativity using two standard equations for the calcium binding and cross-bridge formation with a Hill curve as their steady state solution. Another two factors may be the myofilament lattice spacing and the elastic protein titin in sarcomeres. The former is compressed when the cell is stretched, thus making thick and thin filaments closer and promoting the formation of new strong cross-bridges. The latter is the main determinant of the passive longitudinal and radial tensions at sarcomere lengths below the optimum value for tension; actually, it binds to myosin at the A band and to actin at the Z line. However, both previous factors are disregarded in (2.17) and in this thesis accordingly. The dependence of (2.17) on $d\lambda/dt$, instead, is included through a phenomenological fading memory model [107], which is the time representation of the frequency response of muscles studied by sinusoidal analysis experiments.

To better understand such a discussion, the general system (2.17) is now replaced by the specific model by Land [133], which will be employed in all next chapters

$$
\begin{cases}
\dfrac{dTRPN}{dt}=k_{TRPN}\left(\left(\dfrac{[Ca^{2+}]_i}{[Ca^{2+}]_{T50}}\right)^{n_{TRPN}}(1\text{-}TRPN)\text{-}TRPN\right)\\
[Ca^{2+}]_{T50}=[Ca^{2+}]^{ref}_{T50}(1+\beta_1(\lambda\text{-}1))\\
\dfrac{dXB}{dt}=k_{XB}\left(\sqrt{\left(\dfrac{TRPN}{TRPN_{50}}\right)^{n_{XB}}}(1\text{-}XB)\text{-}\dfrac{1}{\sqrt{\left(\dfrac{TRPN}{TRPN_{50}}\right)^{n_{XB}}}}XB\right)\\
h(\lambda)=\max(0,h_2(\min(\lambda,1.2)))\\
h_2(\lambda)=1+\beta_0(\lambda+\min(\lambda,0.87)\text{-}1.87)\\
\dfrac{dQ_i}{dt}=A_i\dfrac{d\lambda}{dt}\text{-}\alpha_i Q_i \qquad i=1,2\\
g(Q)=\begin{cases}\dfrac{aQ+1}{1\text{-}Q} & Q\le 0\\ \dfrac{1+(a+2)Q}{1+Q} & Q>0\end{cases}\\
Q=\sum_{i=1}^{2}Q_i\\
TRPN(0)=TRPN_0\\
XB(0)=XB_0\\
Q_i(0)=Q_{i,0} \qquad i=1,2\\
T_a=T_{ref}g(Q)h(\lambda)XB,
\end{cases}
\tag{2.18}
$$

where TRPN is the fraction of regulatory TnC (troponin C) sites bound to calcium, k_{TRPN} is the unbinding rate of calcium from TnC, $[Ca^{2+}]_{T50}$ is the calcium concentration needed for a 50% bound TnC at steady state (i.e. the intracellular calcium required for the half-maximal tension generation), n_{TRPN} is the Hill coefficient for the cooperative binding of calcium to TnC, $[Ca^{2+}]^{ref}_{T50}$ is $[Ca^{2+}]_{T50}$ at resting sarcomere length (i.e. the myofilament sensitivity to calcium ions), β_1 is the magnitude of length-dependent activation effects, XB is the fraction of actively cycling cross-bridges, k_{XB} is the breaking rate of cross-bridges, $TRPN_{50}$ is the 50% bound TnC at steady state, n_{XB} is the Hill coefficient for the cooperative cross-bridge formation, $h(\lambda)$ and $h_2(\lambda)$ are two scaling factors limiting and regulating the myofilament overlap, β_0 is the magnitude of myofilament overlap effects, Q_i are the fading memory model variables, A_i and α_i are the corresponding parameters, $g(Q)$ is the velocity-dependent effect on active tension and T_{ref}

is the reference tension at resting sarcomere length. As a remark, this model is a reformulation of the one by Niederer [156] based upon the model by Rice [177].

2.3. Tissue modeling

2.3.1. The finite elasticity model

The most common framework to describe the macroscopic cardiac mechanics is the theory of large deformations of continuous solids [82], which involves non-rigid bodies (the relative distance among their points may change in time) characterized by a well-defined shape and volume (differently from fluids, which have a volume but not a shape, or gases that have neither of them) and defined through a continuous region, often a subset of the $\mathbb{R}^3$ space where continuous and differentiable functions and other mathematical operators can be suitably applied. According to this theory, a mechanical model is built on three elements:

- kinematics, i.e. the study of the body deformation;
- equilibrium, i.e. the study of the static and dynamic equilibrium conditions for the whole body or some of its subsets;
- constitutive law, i.e. the bond between kinematics and equilibrium variables.

As regards kinematics, the reference configuration for a body is denoted by $\Omega_0 \subset \mathbb{R}^3$ and it is generally considered to be the undeformed configuration, whereas the current configuration is denoted by $\Omega(t) \subset \mathbb{R}^3$ and it represents the deformed configuration at each time step. A body point in Ω_0 is described through the position vector $\mathbf{X}=(X_1,X_2,X_3)^T$, whilst a body point in $\Omega(t)$ is defined by the position vector $\mathbf{x}=(x_1,x_2,x_3)^T$. In the remainder of this paragraph, the indexes appearing in the indicial notation of equations will have the values 1, 2 and 3 for a general three-dimensional body. Moreover, from now on, capital indexes will be used for the variables defined in Ω_0 and small indexes for those defined in $\Omega(t)$; the same convention will be applied to the initial letters of the mathematical operators gradient and divergence.

Let ϕ be the deformation map between Ω_0 and $\Omega(t)$ (Figure 2.3)

$$\mathbf{x}(\mathbf{X},t)=\phi(\mathbf{X},t) \qquad x_i=\phi_i(\mathbf{X},t). \tag{2.19}$$

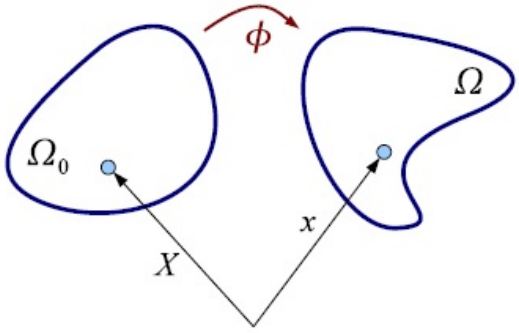

Figure 2.3: Role of the deformation map ϕ between the reference configuration Ω_0 and the current one Ω [11].

The map ϕ must respect the boundary conditions and the continuity of the body. Therefore, it is assumed to be continuous, differentiable with differentiable derivatives (C^2) and invertible (by which the body breaking is avoided). Thanks to the invertibility requirement, in addition to (2.19), it can be written

$$\mathbf{X}=\phi^{-1}(\mathbf{x},t) \qquad X_i=(\phi^{-1})_i(\mathbf{x},t). \tag{2.20}$$

Consequently, one can select either **X** or **x** as the independent variable. If **X** is chosen, a material (or Lagrangian) description, suitable for solid mechanics (like in this thesis), is adopted, otherwise, if **x** is chosen, a spatial (or Eulerian) description, suitable for fluid mechanics, is used.

Focusing on the elementary neighborhood of a material point, a Taylor series of ϕ can be written and stopped at the first-order term in order to define the deformation gradient tensor **F** through the expression

$$\mathbf{F}(\mathbf{X},t)=\mathbf{Grad}\ \phi(\mathbf{X},t) \qquad F_{iJ}=\frac{\partial \phi_i}{\partial X_J} \tag{2.21}$$

or, if ϕ coincides with **x**,

$$\mathbf{F}(\mathbf{X},t)=\mathbf{Grad}\ \mathbf{x}(\mathbf{X},t) \qquad F_{iJ}=\frac{\partial x_i}{\partial X_J}. \tag{2.22}$$

Through **F**, an infinitesimal vector **dX** with its origin in **X** is transformed into the infinitesimal vector **dx** with the origin in **x** (Figure 2.4)

$$\mathbf{dx}=\mathbf{F}\mathbf{dX} \qquad dx_i=F_{iJ}dX_J. \tag{2.23}$$

This means that **F** includes all information related to the local strain in an infinitesimal neighborhood of each body point.

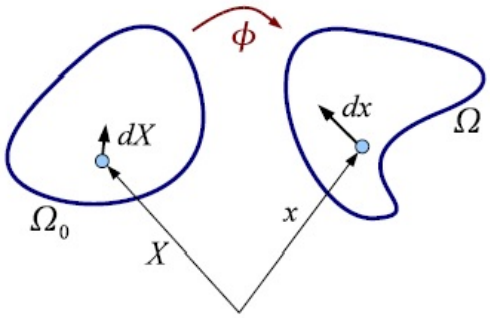

Figure 2.4: Role of the tensor **F** between the infinitesimal vectors **dX** in Ω_0 and **dx** in Ω [11].

Another common kinematic measure is the right Cauchy-Green deformation tensor **C**, which is directly obtained from **F** as

$$\mathbf{C}=\mathbf{F}^T\mathbf{F} \qquad C_{IJ}=F_{aI}F_{aJ}. \tag{2.24}$$

Each tensor like **F** admits the so-called polar decomposition

$$\mathbf{F}=\mathbf{R}\mathbf{U}, \qquad \text{with} \quad \mathbf{R}^T\mathbf{R}=\mathbf{I}, \quad \mathbf{z}^T\mathbf{U}\mathbf{z}>0, \quad \forall \mathbf{z}\in\mathbb{R}^3, \quad \mathbf{z}\neq\mathbf{0}, \tag{2.25}$$

i.e. **F** is the product between an orthogonal rotation tensor **R** and a symmetric and positive definite strain tensor **U**; in particular, **R** acts on a vector in the reference configuration by modifying only its direction, whilst **U** acts on the same vector but it modifies its length independently of any rigid motion. Therefore, **C** can be also written as

$$\mathbf{C}=\mathbf{U}^2. \tag{2.26}$$

However, neither **F** nor **C** are suitable strain measures because both of them are equal to the identity tensor **I** in the reference configuration, whilst one would expect that strain is equal to the zero tensor **0**. Hence, a more realistic strain measure is given by the Green-Lagrange strain tensor **E**

$$\mathbf{E}=\frac{1}{2}(\mathbf{C}-\mathbf{I}) \qquad E_{IJ}=\frac{1}{2}(C_{IJ}-I_{IJ}), \tag{2.27}$$

which is symmetric like **C** and equal to **0** in the reference configuration.

The deformation can be also described through the vector field of displacements **u**, which is defined as the difference between the current position and the reference one (Figure 2.5)

$$\mathbf{u}(\mathbf{X},t)=\mathbf{x}(\mathbf{X},t)-\mathbf{X}=\begin{cases}u_1(X_1,X_2,X_3,t)\\ u_2(X_1,X_2,X_3,t)\\ u_3(X_1,X_2,X_3,t),\end{cases} \tag{2.28}$$

thus

$$\mathbf{x}(\mathbf{X},t)=\phi(\mathbf{X},t)=\mathbf{X}+\mathbf{u}(\mathbf{X},t). \tag{2.29}$$

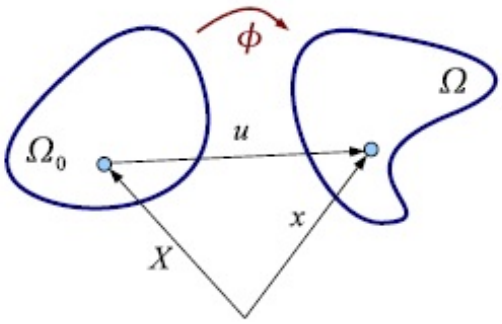

Figure 2.5: Displacement **u** of a point between Ω_0 and Ω [11].

The previous variables written with respect to ϕ can be now expressed in terms of **u**, i.e.

$$\mathbf{F}=\frac{\partial \mathbf{x}}{\partial \mathbf{X}}=\frac{\partial}{\partial \mathbf{X}}(\mathbf{X}+\mathbf{u})=\mathbf{I}+\mathbf{J} \quad \text{with} \quad \mathbf{J}=\mathbf{Grad\ u} \qquad J_{iJ}=\frac{\partial u_i}{\partial X_J}, \tag{2.30}$$

where the tensor **J** is the displacement jacobian, and

$$\begin{aligned}&\mathbf{C}=\mathbf{F}^T\mathbf{F}=\mathbf{I}+\mathbf{J}+\mathbf{J}^T+\mathbf{J}^T\mathbf{J}\\ &\mathbf{E}=\frac{1}{2}(\mathbf{C}-\mathbf{I})=\frac{1}{2}(\mathbf{J}+\mathbf{J}^T)+\frac{1}{2}\mathbf{J}^T\mathbf{J}=\mathbf{E_1}+\mathbf{E_2},\end{aligned} \tag{2.31}$$

where $\mathbf{E_1}$ is the so-called small strain tensor (it is the linear component of **E**) and $\mathbf{E_2}$ is the so-called local rotation tensor (it is the non-linear component of **E** that is neglected under the hypothesis of small displacements).

The map ϕ also affects the volumes of parallelepipeds defined by three vectors in the reference configuration (Figure 2.6). It can be proved that the volume change is equal to

$$\frac{dv}{dV}=\det(\mathbf{F})=J, \tag{2.32}$$

where dv is the infinitesimal current parallelepiped volume and dV is the corresponding reference one. Biological tissues, like the cardiac one, are quasi-incompressible materials, thus one could impose the total incompressibility by setting

$$J=1. \tag{2.33}$$

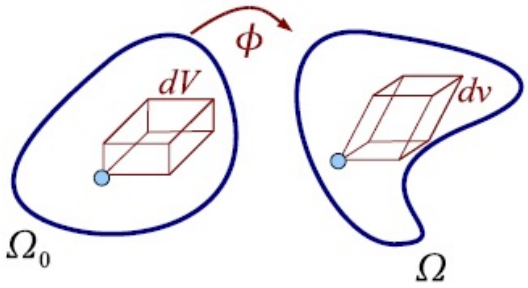

Figure 2.6: Role of ϕ when a parallelepiped volume dV changes into dv [11].

As far as equilibrium is concerned, it must be recalled that the mechanical accelerations in the cardiac tissue are very small, hence inertial effects can be neglected and a quasi-static regime can be considered. Such a regime is then defined by an axiom, which states that, for each time instant t, a deformable body is in equilibrium if and only if the resultants of forces **r** and of moments of forces **m** on the whole body are zero vectors. This must be valid on each subset P of the body itself too, i.e.

$$\begin{cases} \mathbf{r}(P)=\mathbf{0} & \forall P \subseteq \Omega(t) \\ \mathbf{m}(P)=\mathbf{0} & \forall P \subseteq \Omega(t). \end{cases} \tag{2.34}$$

This means that, for each time instant t,

$$\begin{cases} \int_P \mathbf{b}(t)\, dv+\int_{\partial P} \mathbf{t_n}(t)\, da=\mathbf{0} & \forall P \subseteq \Omega(t) \\ \int_P \mathbf{x}\times\mathbf{b}(t)\, dv+\int_{\partial P} \mathbf{x}\times\mathbf{t_n}(t)\, da=\mathbf{0} & \forall P \subseteq \Omega(t), \end{cases} \tag{2.35}$$

where $\mathbf{b}(t)$ is the resultant of forces per unit volume of the whole body $\Omega(t)$ and $\mathbf{t_n}(t)$ is the normal component of forces per unit area of the surface of the subset P with respect to the outward normal **n** from P (see Figure 2.7 for the whole body and Figure 2.8 for two of its subsets).

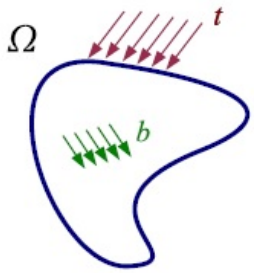

Figure 2.7: Interactions between the external environment and the body Ω: **b** are the forces per unit volume of Ω and **t** are the normal forces per unit area of the surface of Ω [11].

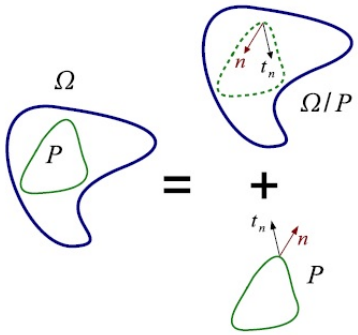

Figure 2.8: Interactions between two internal subsets P and Ω/P of the body Ω: **n** is the outward normal to P and $\mathbf{t_n}$ is the normal of forces per unit area of the surface of P [11].

It can be proved that the first equation of (2.35) is the global integral formulation of the corresponding local differential formulation of the linear momentum balance (first equation of (2.34))

$$\mathbf{div}\ \boldsymbol{\sigma}(\mathbf{x},t)+\mathbf{b}(t)=\mathbf{0} \qquad \sigma_{ij,j}+b_i=0, \tag{2.36}$$

where $\boldsymbol{\sigma}$ is the Cauchy stress tensor that, through the Cauchy tetrahedron proof, is equal to

$$\boldsymbol{\sigma}=\sum_{i=1}^{3}\mathbf{t}_{e_i}\otimes\mathbf{e}_i, \tag{2.37}$$

where $\mathbf{t}_{e_i}$ is the traction vector acting on the tetrahedron face with normal $\mathbf{e_i}$ (unit vector along the i-th reference axis). In particular, the (i,j)-th element of $\boldsymbol{\sigma}$ is the i-th component of the traction vector acting on the face with normal vector $\mathbf{e_j}$. Thus, $\boldsymbol{\sigma}$ holds all information related to the local stress state, i.e. the forces per unit area of the current configuration that act

on this configuration in each point. Actually, starting from $\boldsymbol{\sigma}$, the traction vector $\mathbf{t_n}$ acting on any surface with normal vector $\mathbf{n}$ can be computed

$$\mathbf{t_n}=\boldsymbol{\sigma}\mathbf{n} \qquad t_{n,i}=\sigma_{ij}n_j. \tag{2.38}$$

Similarly, the second equation of (2.35) is the global integral formulation of the corresponding local differential formulation of the angular momentum balance (second equation of (2.34))

$$\boldsymbol{\sigma}=\boldsymbol{\sigma}^T \qquad \sigma_{ij}=\sigma_{ji}, \tag{2.39}$$

i.e. $\boldsymbol{\sigma}$ is a symmetric tensor.

So far, the equilibrium conditions have been written with respect to the current configuration and they have been defined in terms of geometrical variables related to the current configuration again (like $\mathbf{n}$), which represents the natural configuration where equilibrium holds. Nevertheless, thanks to the invertibility of the map ϕ, one can also write:

- equilibrium equations related to the current configuration in terms of geometrical variables related to the reference configuration;
- equilibrium equations related to the reference configuration in terms of geometrical variables related to the same reference configuration.

Following the first idea, it can be proved that the first Piola-Kirchhoff stress tensor $\mathbf{P}$ derives

$$\mathbf{P}(\mathbf{X},t)=J\boldsymbol{\sigma}\mathbf{F}^{-T} \tag{2.40}$$

with local equilibrium equations

$$\begin{cases} \mathbf{Div}\ \mathbf{P}+J\mathbf{b}=\mathbf{0} & P_{iJ,J}+Jb_i=0 \\ \mathbf{P}\mathbf{F}^T=\mathbf{F}\mathbf{P}^T & P_{iJ}F_{aJ}=F_{aJ}P_{iJ}, \end{cases} \tag{2.41}$$

i.e. $\mathbf{P}$ is not a symmetric tensor. Analogously to $\boldsymbol{\sigma}$, the (i,J)-th element of $\mathbf{P}$ is the i-th component of the traction vector acting on the face with normal vector $\mathbf{e_J}$ (unit vector along the J-th reference axis). Hence, the elements of $\mathbf{P}$ are the forces per unit area of the reference configuration that act on the current configuration in each point. Actually, starting from $\mathbf{P}$, the traction vector $\mathbf{t_N}$ acting on any surface with normal vector $\mathbf{N}$ can be computed

$$\mathbf{t_N}=\mathbf{P}\mathbf{N} \qquad t_{N,i}=P_{iJ}N_J. \tag{2.42}$$

On the contrary, following the second idea, the second Piola-Kirchhoff stress tensor $\mathbf{S}$ derives

$$\mathbf{S}(\mathbf{X},t)=J\mathbf{F}^{-1}\boldsymbol{\sigma}\mathbf{F}^{-T}. \tag{2.43}$$

Noting that $\mathbf{P}=\mathbf{FS}$ and replacing this relation in the first equation of (2.41), the following local equilibrium equations hold

$$\begin{cases} \mathbf{Div}(\mathbf{FS})+J\mathbf{b}=\mathbf{0} & (F_{iJ}S_{JI})_{,J}+Jb_i=0 \\ \mathbf{S}=\mathbf{S}^T & S_{IJ}=S_{JI}, \end{cases} \tag{2.44}$$

i.e. $\mathbf{S}$ is a symmetric tensor like $\boldsymbol{\sigma}$. Analogously to $\boldsymbol{\sigma}$ and $\mathbf{P}$, the (I,J)-th element of $\mathbf{S}$ is the I-th component of the traction vector acting on the face with normal vector $\mathbf{e_J}$. Hence, the elements of $\mathbf{S}$ are the forces per unit area of the reference configuration that act on this configuration in each point. Actually, starting from $\mathbf{S}$, the traction vector $\mathbf{S_N}$ acting on every surface with normal vector $\mathbf{N}$ can be computed

$$\mathbf{S_N}=\mathbf{SN} \qquad S_{N,I}=S_{IJ}N_J. \tag{2.45}$$

In this thesis, $\mathbf{S}$ is adopted because a Lagrangian approach is followed.

The equilibrium equation that is valid for each point $\mathbf{X}$ of the reference configuration is

$$\sum_{N,M=1}^{3}\frac{\partial}{\partial X_M}(F_{iN}S_{NM})=0, \tag{2.46}$$

i.e. $\mathbf{b}$ is the zero vector because no volume forces act on the mechanically insulated body. Then, the boundary $\partial\Omega_0$ is also split into two different components, i.e. $\partial\Omega_0{}^D$, where Dirichlet boundary conditions on displacements hold, and $\partial\Omega_0{}^N$, where Neumann boundary conditions on the external tractions applied to the body are given. The general form of the previous boundary conditions is

$$\begin{cases} x_i(\mathbf{X},t)=\widetilde{x}_i(\mathbf{X},t) & \mathbf{X}\in\partial\Omega_0{}^D \\ \sum_{N,M=1}^{3}F_{iN}S_{NM}N_M=b_i(\mathbf{X},t) & \mathbf{X}\in\partial\Omega_0{}^N, \end{cases} \tag{2.47}$$

where $\tilde{\mathbf{x}}(\mathbf{X},t)$ is a fixed position vector. Moreover, the following initial conditions at time t=0 are added

$$\mathbf{x}(\mathbf{X},t_0)=\mathbf{x_0}(\mathbf{X}). \tag{2.48}$$

Due to the rotation of cardiac fibers in the radial layers from the epicardium to the endocardium (Paragraph 1.1.1), it is suitable to employ a right-handed triplet of orthonormal axes in each point $\mathbf{x}$ of the current configuration with $\mathbf{a_f}(\mathbf{x})$ (or $\mathbf{f}(\mathbf{x})$) representing the local fiber direction, $\mathbf{a_s}(\mathbf{x})$

(or $\mathbf{s}(\mathbf{x})$) the sheet direction (perpendicular to $\mathbf{a_f}(\mathbf{x})$ and pointing in the radial direction) and $\mathbf{a_n}(\mathbf{x})$ (or $\mathbf{n}(\mathbf{x})$) the sheet-normal direction orthogonal to $\mathbf{a_f}(\mathbf{x})$ and $\mathbf{a_s}(\mathbf{x})$. Figure 2.9 shows the corresponding directions $\widehat{\mathbf{a}_\mathbf{f}}(\mathbf{X})$ (or $\mathbf{f_0}(\mathbf{X})$), $\widehat{\mathbf{a}_\mathbf{s}}(\mathbf{X})$ (or $\mathbf{s_0}(\mathbf{X})$) and $\widehat{\mathbf{a}_\mathbf{n}}(\mathbf{X})$ (or $\mathbf{n_0}(\mathbf{X})$) in each point $\mathbf{X}$ of the reference configuration.

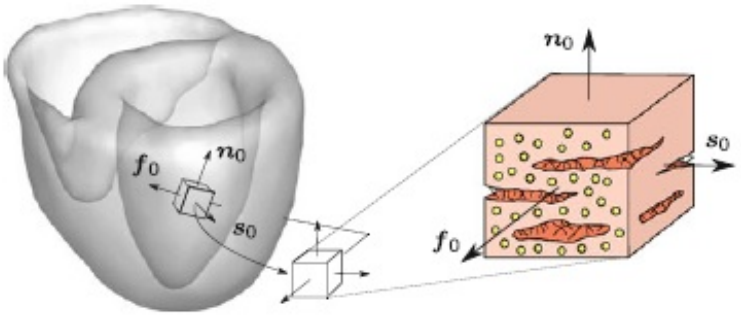

Figure 2.9: Reference system in a point $\mathbf{X}$ of the reference configuration Ω_0: $\mathbf{f_0}$ is the fiber direction, $\mathbf{s_0}$ is the sheet direction and $\mathbf{n_0}$ is the sheet-normal direction [175].

Following the classical and widely used active stress approach (e.g., [65,119,153,154,162,170,215]) instead of the more recent active strain one (first developed in [31] and then used in, e.g., [8,159,181]), $\mathbf{S}$ is the sum of an active component $\mathbf{S^{act}}$, biochemically developed at the cell scale and dependent on the active tension T_a (Paragraph 2.2.2), and a passive elastic one $\mathbf{S^{pas}}$ due to the extracellular matrix elements, among which the collagen and elastin fibers (Paragraph 1.1.1)

$$\mathbf{S}=\mathbf{S^{act}}+\mathbf{S^{pas}}. \tag{2.49}$$

To derive a proper expression for $\mathbf{S^{act}}$ as a function of T_a, it must be recalled that T_a is defined in terms of the current configuration, i.e. it is expressed per unit deformed area. Moreover, T_a is a scalar and not a tensor. Therefore, first, the active Cauchy stress tensor $\boldsymbol{\sigma}^{\mathbf{act}}$ must be computed as

$$\boldsymbol{\sigma}^{\mathbf{act}}=J^{-1}T_a\mathbf{a_f}\otimes\mathbf{a_f}, \tag{2.50}$$

where it is supposed that the active tension develops only along the fiber direction (e.g., [170,223]). Then, the unit vector for this direction turns out to be $\mathbf{a_f}(\mathbf{x})=\mathbf{F}\widehat{\mathbf{a}_\mathbf{f}}/\left\|\mathbf{F}\widehat{\mathbf{a}_\mathbf{f}}\right\|=\mathbf{F}\widehat{\mathbf{a}_\mathbf{f}}/\sqrt{\widehat{\mathbf{a}_\mathbf{f}}^{\mathrm{T}}\mathbf{C}\widehat{\mathbf{a}_\mathbf{f}}}$. Thus, it immediately follows that

$$\mathbf{a}_f \otimes \mathbf{a}_f = \frac{\mathbf{F}\widehat{\mathbf{a}_f} \otimes \mathbf{F}\widehat{\mathbf{a}_f}}{\left\|\mathbf{F}\widehat{\mathbf{a}_f}\right\|^2} = \frac{\mathbf{F}\widehat{\mathbf{a}_f}\widehat{\mathbf{a}_f}^T\mathbf{F}^T}{\widehat{\mathbf{a}_f}^T\mathbf{C}\widehat{\mathbf{a}_f}}. \tag{2.51}$$

At last, by using (2.43), the corresponding active second Piola-Kirchhoff stress tensor $\mathbf{S}^{act}$ turns out to be

$$\mathbf{S}^{act} = J\mathbf{F}^{-1}\boldsymbol{\sigma}^{act}\mathbf{F}^{-T} = \frac{T_a}{\widehat{\mathbf{a}_f}^T\mathbf{C}\widehat{\mathbf{a}_f}}\widehat{\mathbf{a}_f} \otimes \widehat{\mathbf{a}_f} \qquad S^{act}_{MN} = \frac{T_a}{\widehat{\mathbf{a}_f}^T\mathbf{C}\widehat{\mathbf{a}_f}}(\widehat{\mathbf{a}_f} \otimes \widehat{\mathbf{a}_f})_{MN}. \tag{2.52}$$

Writing $\boldsymbol{\sigma}^{act}$ as in (2.50) and $\mathbf{S}^{act}$ as in (2.52) is the most common way found in the literature (e.g., [38,39,51,52,116,154,167,168]), though Humphrey states in his book [104] that

$$\boldsymbol{\sigma}^{act} = T_a\mathbf{a}_f \otimes \mathbf{a}_f, \tag{2.53}$$

thus

$$\mathbf{S}^{act} = J\mathbf{F}^{-1}\boldsymbol{\sigma}^{act}\mathbf{F}^{-T} = \frac{JT_a}{\widehat{\mathbf{a}_f}^T\mathbf{C}\widehat{\mathbf{a}_f}}\widehat{\mathbf{a}_f} \otimes \widehat{\mathbf{a}_f}. \tag{2.54}$$

In this dissertation, the expression (2.52) is used. Moreover, since in the remainder of this thesis it is assumed that the stretch λ, introduced in Paragraph 2.2.1 for the stretch-activated channels current and Paragraph 2.2.2 for the active tension, occurs along $\widehat{\mathbf{a}_f}$, its expression is the following one

$$\lambda = \sqrt{\widehat{\mathbf{a}_f}^T\mathbf{C}\widehat{\mathbf{a}_f}}. \tag{2.55}$$

To derive a general form for $\mathbf{S}^{pas}$, a constitutive law must be introduced instead. It describes some intrinsic qualities of a simple material, i.e. of a material with a response that is function of only local variables, disregarding all dependences on other points and possible temperature excursions during its deformation (isothermal processes). Moreover, a constitutive law must satisfy two requirements:

- the independence of the observer (or material response objectivity), i.e. the constitutive law must not be affected from any change in the point of view of an observer (or, equivalently, from any rigid motion superimposed on the body deformation);
- the material symmetry, i.e. the constitutive law must take into account some particular intrinsic structures of a material (for instance, a group of aligned fibers) that make it symmetric.

The first requirement can be met by postulating a hyperelastic (or Green) material. This one ensures the existence of a scalar strain energy function W, dependent on **F** (through **C** or **E**), by which **σ** can be expressed by the following formula for a compressible material

$$J\boldsymbol{\sigma}=\mathbf{F}\frac{\partial W}{\partial \mathbf{F}}=\mathbf{F}\frac{\partial W}{\partial \mathbf{E}}\frac{\partial \mathbf{E}}{\partial \mathbf{C}}\frac{\partial \mathbf{C}}{\partial \mathbf{F}}=\mathbf{F}\frac{\partial W}{\partial \mathbf{E}}\mathbf{F}^{T} \tag{2.56}$$

or by the following formula for an incompressible one (for which (2.33) is valid too)

$$\boldsymbol{\sigma}=\mathbf{F}\frac{\partial W}{\partial \mathbf{F}}-p\mathbf{I}=\mathbf{F}\frac{\partial W}{\partial \mathbf{E}}\frac{\partial \mathbf{E}}{\partial \mathbf{C}}\frac{\partial \mathbf{C}}{\partial \mathbf{F}}-p\mathbf{I}=\mathbf{F}\frac{\partial W}{\partial \mathbf{E}}\mathbf{F}^{T}-p\mathbf{I}, \tag{2.57}$$

where p is a Lagrange multiplier representing the hydrostatic pressure. Therefore, by using (2.43) and (2.56), $\mathbf{S}^{\mathbf{pas}}$ for a compressible material turns out to be

$$\mathbf{S}^{\mathbf{pas}}=\frac{\partial W}{\partial \mathbf{E}} \qquad S^{pas}_{MN}=\frac{1}{2}\left(\frac{\partial W}{\partial E_{MN}}+\frac{\partial W}{\partial E_{NM}}\right), \tag{2.58}$$

whereas, by using (2.57) and (2.27), the corresponding equation for an incompressible material becomes

$$\mathbf{S}^{\mathbf{pas}}=\frac{\partial W}{\partial \mathbf{E}}-p(\mathbf{I}+2\mathbf{E})^{-1}=\frac{\partial W}{\partial \mathbf{E}}-p\mathbf{C}^{-1} \qquad S^{pas}_{MN}=\frac{1}{2}\left(\frac{\partial W}{\partial E_{MN}}+\frac{\partial W}{\partial E_{NM}}\right)-p(\mathbf{C}^{-1})_{MN}. \tag{2.59}$$

The second requirement is met by the specific strain energy function W used. In the literature, many functions have been developed for the adult cardiac tissue. The early ones considered the myocardium as a linear isotropic material (see [102,226] for a review on these works) or they proposed elementary non-linear relations (e.g., [47]), but they failed. Then, authors started to introduce anisotropy by assuming the myocardium as a non-linear transversely isotropic material, i.e. composed of an isotropic matrix with a preferred direction $\widehat{\mathbf{a}_{\mathbf{f}}}(\mathbf{X})$ determined by the aligned fibers and equal mechanical responses along the transverse directions $\widehat{\mathbf{a}_{\mathbf{s}}}(\mathbf{X})$ and $\widehat{\mathbf{a}_{\mathbf{n}}}(\mathbf{X})$ (e.g., [41,70,84,102,103,119]). One of them [109] also added a viscoelastic component to W, which depends on the application rate of external loads, because the loading and unloading curves during *in vitro* tests show a little hysteresis. However, more and more researchers (e.g., [42,83,107,191]) are modeling the myocardium as an orthotropic material, i.e. with different mechanical responses along each direction, as from more recent experiments (e.g., [48,137]). In this thesis, Chapter 3, Chapter 4 and Chapter 5 will include both transversely isotropic and orthotropic laws for the adult myocardium, whereas Chapter 6 will involve only the isotropic

one for the neonatal myocardium. The viscoelasticity and the further existence of a residual stress in the unloaded myocardium will be neglected in all simulations. Further details regarding the specific laws employed will be given in each chapter. Figure 2.10 clearly shows the just recalled anisotropic, non-linear and slightly viscoelastic response of a typical myocardial tissue sample under uniaxial shear stress tests.

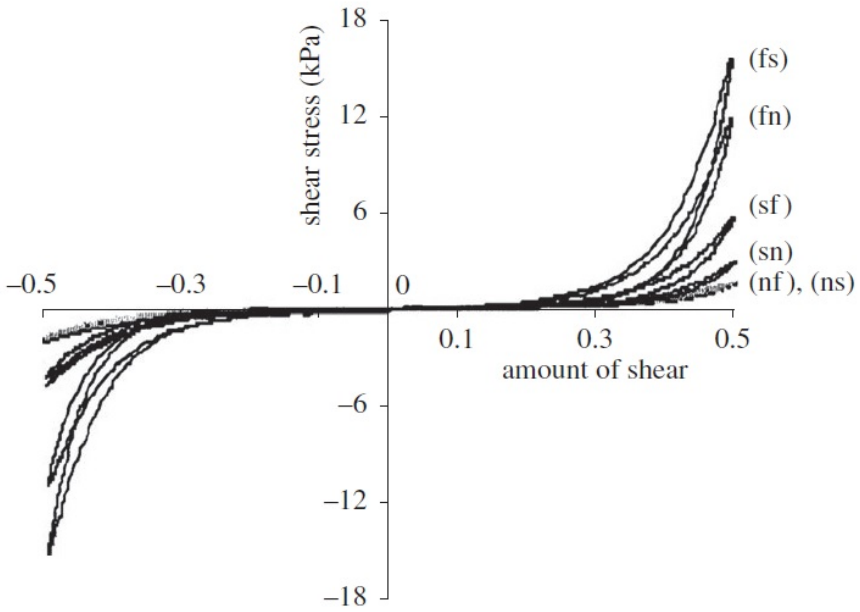

Figure 2.10: Loading and unloading curves during uniaxial shear stress tests on a cubic sample of pig ventricular myocardium; the (i,j)-th curve stands for the stress along the j-th direction in the (i,j)-th plane, i.e. the fs plane (defined by $\mathbf{a_f}$ and $\mathbf{a_s}$), the fn plane (defined by $\mathbf{a_f}$ and $\mathbf{a_n}$) and the sn plane (defined by $\mathbf{a_s}$ and $\mathbf{a_n}$) [83].

A final remark is about the incompressibility constraint. Sometimes, it is replaced by a quasi-incompressibility one, represented by the tensor $\mathbf{S^{qi}}$, in order to reduce the computational cost of simulations and to let the cardiac tissue modify its shape more freely during its contraction and relaxation processes. Therefore, $\mathbf{S^{pas}}$ for a quasi-incompressible material becomes

$$\mathbf{S}^{pas}=\frac{\partial W}{\partial \mathbf{E}}+\mathbf{S}^{qi}=\frac{\partial W}{\partial \mathbf{E}}+\frac{\partial W^{qi}}{\partial \mathbf{E}} \qquad S^{pas}_{MN}=\frac{1}{2}\left(\frac{\partial W}{\partial E_{MN}}+\frac{\partial W}{\partial E_{NM}}\right)+\frac{1}{2}\left(\frac{\partial W^{qi}}{\partial E_{MN}}+\frac{\partial W^{qi}}{\partial E_{NM}}\right), \quad (2.60)$$

where W^{qi} is a volume change penalization term that is characterized by the expression [215]

$$W^{qi}=K(J-1)^2, \quad (2.61)$$

where K is the so-called bulk modulus parameter, when it is used for the simulations in this thesis.

2.3.2. The reaction-diffusion models

The most thorough model of macroscopic electrical excitation propagation is the Bidomain one [36]. A heuristic derivation of it based on the concept of interpenetrating domains [192] is here reviewed.

The cardiac tissue is considered as formed by two ohmic conducting media (the intracellular and extracellular spaces) that are split by a continuous distributed and active plasma membrane (Figure 2.11). These two media are characterized by the anisotropic conductivity tensors $\mathbf{D_i}$ and $\mathbf{D_e}$ respectively, which are inhomogeneous functions of space and take into account the local changes in conductivities due to the syncytial structure of the myocardium, i.e. they are affected from the way cardiac fibers are organized and from the presence of more or fewer gap junctions and higher or lower cross-sectional areas according to the end-to-end or side-to-side connections among cells (Paragraph 1.2.3).

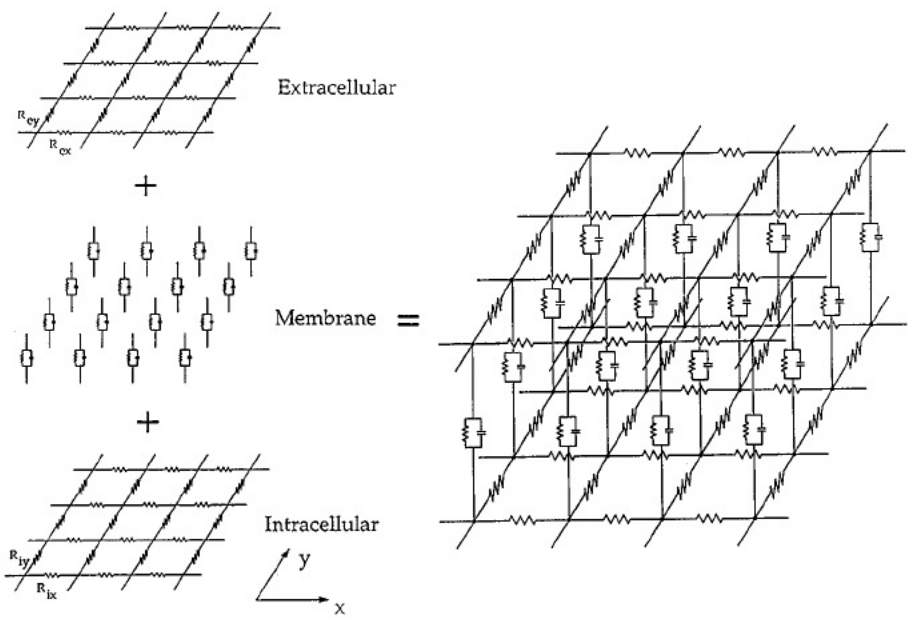

Figure 2.11: General electrical circuit model for the Bidomain representation of the cardiac tissue: R_{ix}, R_{iy}, R_{ex} and R_{ey} are the intra- and extracellular resistances along the x and y axes [190].

Let $\sigma_f^{i,e}$, $\sigma_s^{i,e}$ and $\sigma_n^{i,e}$ be the conductivity coefficients in the intra- and extracellular media of the current tissue configuration $\Omega(t)$ and measured along the corresponding directions $\mathbf{a_f}$, $\mathbf{a_s}$ and $\mathbf{a_n}$. They may depend on the position $\mathbf{x}$ according to the local state of the cardiac tissue. Nevertheless,

they are assumed constant in the remainder of this chapter for an easier understanding of the general model. Hence, $\mathbf{D_i}$ and $\mathbf{D_e}$ are given by

$$\mathbf{D}_{i,e}(\mathbf{x})=\sigma_f^{i,e}\mathbf{a}_f(\mathbf{x})\otimes\mathbf{a}_f(\mathbf{x})+\sigma_s^{i,e}\mathbf{a}_s(\mathbf{x})\otimes\mathbf{a}_s(\mathbf{x})+\sigma_n^{i,e}\mathbf{a}_n(\mathbf{x})\otimes\mathbf{a}_n(\mathbf{x}) \tag{2.62}$$

or alternatively, thanks to the orthonormality of $\mathbf{a_f}$, $\mathbf{a_s}$ and $\mathbf{a_n}$ (i.e. $\mathbf{a}_f(\mathbf{x})\otimes\mathbf{a}_f(\mathbf{x})+\mathbf{a}_s(\mathbf{x})\otimes\mathbf{a}_s(\mathbf{x})+\mathbf{a}_n(\mathbf{x})\otimes\mathbf{a}_n(\mathbf{x})=\mathbf{I}$),

$$\mathbf{D}_{i,e}(\mathbf{x})=\sigma_f^{i,e}\mathbf{I}+(\sigma_s^{i,e}-\sigma_f^{i,e})\mathbf{a}_s(\mathbf{x})\otimes\mathbf{a}_s(\mathbf{x})+(\sigma_n^{i,e}-\sigma_f^{i,e})\mathbf{a}_n(\mathbf{x})\otimes\mathbf{a}_n(\mathbf{x}) \tag{2.63}$$

or again

$$\mathbf{D}_{i,e}(\mathbf{x})=\sigma_s^{i,e}\mathbf{I}+(\sigma_f^{i,e}-\sigma_s^{i,e})\mathbf{a}_f(\mathbf{x})\otimes\mathbf{a}_f(\mathbf{x})+(\sigma_n^{i,e}-\sigma_s^{i,e})\mathbf{a}_n(\mathbf{x})\otimes\mathbf{a}_n(\mathbf{x}). \tag{2.64}$$

In case of transversely isotropic tissues, $\sigma_n^{i,e}=\sigma_s^{i,e}$ holds, thus

$$\mathbf{D}_{i,e}(\mathbf{x})=\sigma_s^{i,e}\mathbf{I}+(\sigma_f^{i,e}-\sigma_s^{i,e})\mathbf{a}_f(\mathbf{x})\otimes\mathbf{a}_f(\mathbf{x}). \tag{2.65}$$

By imposing the current conservation law on a volume surrounding $\mathbf{x}$, i.e. the flux leaving the intracellular volume must be equal to the flux reaching the extracellular one and both of them must correspond to the transmembrane current per unit volume across the plasma membrane i_m, it derives that, taking the limit as the volume tends to zero,

$$\mathrm{div}\mathbf{J}_e(\mathbf{x},t)=-\mathrm{div}\mathbf{J}_i(\mathbf{x},t)=i_m, \tag{2.66}$$

where $\mathbf{J}_{i,e}=-\mathbf{D}_{i,e}\mathbf{grad}\ u_{i,e}$ are the local average intracellular and extracellular current densities per unit area of the intracellular and extracellular media and i_m is equal to $i_m=\chi I_m=c_m dv/dt+i_{ion}(v,\mathbf{w},\mathbf{c})$, where χ is the ratio of surface membrane area per tissue volume and $c_m=\chi C_m$ and $i_{ion}=\chi I_{ion}$ are the membrane capacitance and ionic current per unit volume. Therefore, the Bidomain model can be described through a system made of two parabolic reaction-diffusion partial differential equations coupled with two systems made of ordinary differential equations for M gating variables and S ionic concentrations. Given the applied intracellular and extracellular currents per unit volume $i_{app}^{i,e}:\Omega\times(0,T)\to\mathbb{R}$ and initial conditions $v_0:\Omega\to\mathbb{R}$, $\mathbf{w_0}:\Omega\to\mathbb{R}^M$ and $\mathbf{c_0}:\Omega\to\mathbb{R}^S$, find the intracellular and extracellular potentials $u_{i,e}:\Omega\times(0,T)\to\mathbb{R}$, the transmembrane potential $v=u_i-u_e:\Omega\times(0,T)\to\mathbb{R}$, the gating variables $\mathbf{w}:\Omega\times(0,T)\to\mathbb{R}^M$ and the ionic concentrations $\mathbf{c}:\Omega\times(0,T)\to\mathbb{R}^S$ such that

$$\begin{cases} c_m \dfrac{\partial v}{\partial t} - \mathrm{div}(\mathbf{D_i}\mathbf{grad}\ u_i) + i_{ion}(v,\mathbf{w},\mathbf{c}) + i_{SAC}(v,\mathbf{c},\lambda) = i^i_{app} & \text{in} \quad \Omega\times(0,T) \\ -c_m \dfrac{\partial v}{\partial t} - \mathrm{div}(\mathbf{D_e}\mathbf{grad}\ u_e) - i_{ion}(v,\mathbf{w},\mathbf{c}) - i_{SAC}(v,\mathbf{c},\lambda) = i^e_{app} & \text{in} \quad \Omega\times(0,T) \\ \dfrac{\partial \mathbf{w}}{\partial t} - \mathbf{R}(v,\mathbf{w}) = 0 & \text{in} \quad \Omega\times(0,T) \\ \dfrac{\partial \mathbf{c}}{\partial t} - \mathbf{S}(v,\mathbf{w},\mathbf{c}) = 0 & \text{in} \quad \Omega\times(0,T) \\ \mathbf{n}^T\mathbf{D}_{i,e}\mathbf{grad}\ u_{i,e} = 0 & \text{on} \quad \partial\Omega\times(0,T) \\ v(\mathbf{x},0) = v_0(\mathbf{x}), \quad \mathbf{w}(\mathbf{x},0) = \mathbf{w_0}(\mathbf{x}), \quad \mathbf{c}(\mathbf{x},0) = \mathbf{c_0}(\mathbf{x}) & \text{in} \quad \Omega, \end{cases} \tag{2.67}$$

where the stretch-activated channels current i_{SAC} is included and the boundary $\partial\Omega$ is assumed insulated.

The previous system, which coincides with the classical Bidomain model used during those simulations taking into account only the electrical activity of the cardiac tissue, is posed on the current configuration Ω. This is required when the Bidomain model is strongly coupled with a mechanical model (e.g., [1,8,37,39,43,65,117,118,154,167,170,182,223]), as in this thesis, otherwise, if a weak coupling is considered, the Bidomain model is posed on the reference configuration Ω_0 (e.g., [120,155]). Therefore, in the former case, when the Bidomain model is reformulated on Ω_0 following a Lagrangian framework, it becomes dependent on the deformation gradient $\mathbf{F}$ as it is proved herein. Let $V(\mathbf{X},t)=v(\mathbf{x},t)$ be the transmembrane potential referred to the reference configuration Ω_0. Considering that $\partial V/\partial t=\partial v/\partial t+\mathbf{grad}\ v\cdot\partial\mathbf{x}/\partial t$, $\mathrm{div}\,\mathbf{f}=J^{-1}\mathrm{Div}(J\mathbf{F}^{-1}\mathbf{f})$ and $\mathbf{grad}\ f=\mathbf{F}^{-T}\mathbf{Grad}\ f$, where $\mathbf{f}$ is a general vector field and f is a general scalar field, the following formulation holds. Given the applied intracellular and extracellular currents per unit undeformed volume $i^{i,e}_{app}:\Omega_0\times(0,T)\to\mathbb{R}$ and the applied initial conditions $V_0:\Omega_0\to\mathbb{R}$, $\mathbf{w_0}:\Omega\to\mathbb{R}^M$ and $\mathbf{c_0}:\Omega\to\mathbb{R}^S$, find the intracellular and extracellular potentials $U_{i,e}:\Omega_0\times(0,T)\to\mathbb{R}$, the transmembrane potential $V=U_i-U_e:\Omega_0\times(0,T)\to\mathbb{R}$, the gating variables $\mathbf{w}:\Omega\times(0,T)\to\mathbb{R}^M$ and the ionic concentrations $\mathbf{c}:\Omega\times(0,T)\to\mathbb{R}^S$ such that

$$\begin{cases} c_m\left(\frac{\partial V}{\partial t}-\mathbf{F}^{-T}\mathbf{Grad}\,V\cdot\frac{\partial \mathbf{x}}{\partial t}\right)-J^{-1}\mathrm{Div}\left(J\mathbf{F}^{-1}\mathbf{D}_i\mathbf{F}^{-T}\mathbf{Grad}\,U_i\right)+i_{ion}(V,\mathbf{w},\mathbf{c})+i_{SAC}(V,\mathbf{c},\lambda)=i^i_{app} & \text{in } \Omega_0\times(0,T) \\ -c_m\left(\frac{\partial V}{\partial t}-\mathbf{F}^{-T}\mathbf{Grad}\,V\cdot\frac{\partial \mathbf{x}}{\partial t}\right)-J^{-1}\mathrm{Div}\left(J\mathbf{F}^{-1}\mathbf{D}_e\mathbf{F}^{-T}\mathbf{Grad}\,U_e\right)-i_{ion}(V,\mathbf{w},\mathbf{c})-i_{SAC}(V,\mathbf{c},\lambda)=i^e_{app} & \text{in } \Omega_0\times(0,T) \\ \frac{\partial \mathbf{w}}{\partial t}-\mathbf{R}(V,\mathbf{w})=0 & \text{in } \Omega_0\times(0,T) \\ \frac{\partial \mathbf{c}}{\partial t}-\mathbf{S}(V,\mathbf{w},\mathbf{c})=0 & \text{in } \Omega_0\times(0,T) \\ \mathbf{N}^T\mathbf{F}^{-1}\mathbf{D}_{i,e}\mathbf{F}^{-T}\mathbf{Grad}\,U_{i,e}=0 & \text{on } \partial\Omega_0\times(0,T) \\ V(\mathbf{X},0)=V_0(\mathbf{X}) \quad \text{in } \Omega_0, \quad \mathbf{w}(\mathbf{x},0)=\mathbf{w}_0(\mathbf{x}), \quad \mathbf{c}(\mathbf{x},0)=\mathbf{c}_0(\mathbf{x}) & \text{in } \Omega, \end{cases} \tag{2.68}$$

where c_m, i_{ion}, i_{SAC} are defined per unit undeformed volume, $\mathbf{F}$ is the deformation gradient tensor and $c_m\mathbf{F}^{-T}\mathbf{Grad}\,V\cdot\partial\mathbf{x}/\partial t$ is a convective term depending on the tissue deformation rate $\partial\mathbf{x}/\partial t$; this convective term together with the dependence of the diffusive term on $\mathbf{F}$ represent two geometric feedbacks on the electrical propagation that add to the mechanoelectric feedback by the stretch-activated channels already introduced in this chapter. As a remark, if one already wrote the convective term in the current configuration Ω, then such a term would cancel when pulling back to the reference configuration Ω_0. Although this last situation sounds more physically correct in case of moving particles, in this thesis the Bidomain model is written in Ω (so the convective term appears in Ω_0) since it is still not sure if the same approach is valid for a moving activation wavefront among cells, which shift only around their reference positions; a detailed comparison with experimental data should define the correct way to proceed.

For the computation of the product $\mathbf{F}^{-1}\mathbf{D}_{i,e}\mathbf{F}^{-T}$, (2.64) must be recalled. Moreover, the following consideration holds. In the reference configuration Ω_0, the unit vector $\widehat{\mathbf{a}_n}$ is given by

$$\widehat{\mathbf{a}_n}=\widehat{\mathbf{a}_f}\times\widehat{\mathbf{a}_s}, \tag{2.69}$$

whereas, in the current configuration Ω,

$$\mathbf{a}_n=\frac{\mathbf{F}\widehat{\mathbf{a}_f}\times\mathbf{F}\widehat{\mathbf{a}_s}}{\|\mathbf{F}\widehat{\mathbf{a}_f}\times\mathbf{F}\widehat{\mathbf{a}_s}\|}. \tag{2.70}$$

Since $\mathbf{Au}\times\mathbf{Av}=\det(\mathbf{A})\mathbf{A}^{-T}(\mathbf{u}\times\mathbf{v})$, where $\mathbf{A}$ is a general tensor field and $\mathbf{u}$ and $\mathbf{v}$ are two general vector fields, then $\mathbf{F}\widehat{\mathbf{a}_f}\times\mathbf{F}\widehat{\mathbf{a}_s}=J\mathbf{F}^{-T}(\widehat{\mathbf{a}_f}\times\widehat{\mathbf{a}_s})=J\mathbf{F}^{-T}\widehat{\mathbf{a}_n}$,

$$\mathbf{a}_n = \frac{\mathbf{F}^{-T}\widehat{\mathbf{a}}_n}{\| \mathbf{F}^{-T}\widehat{\mathbf{a}}_n \|} \tag{2.71}$$

and

$$\mathbf{a}_n \otimes \mathbf{a}_n = \frac{\mathbf{F}^{-T}\widehat{\mathbf{a}}_n \otimes \mathbf{F}^{-T}\widehat{\mathbf{a}}_n}{\widehat{\mathbf{a}}_n^T \mathbf{C}^{-1}\widehat{\mathbf{a}}_n}. \tag{2.72}$$

Therefore, the product $\mathbf{F}^{-1}\mathbf{D}_{i,e}\mathbf{F}^{-T}$ for an orthotropic tissue can be computed as

$$(\mathbf{F}^{-1}\mathbf{D}_{i,e}\mathbf{F}^{-T})(\mathbf{X}) = \sigma_s^{i,e}\mathbf{C}^{-1}(\mathbf{X}) + (\sigma_f^{i,e} - \sigma_s^{i,e})\frac{\widehat{\mathbf{a}}_f(\mathbf{X}) \otimes \widehat{\mathbf{a}}_f(\mathbf{X})}{\widehat{\mathbf{a}}_f^T(\mathbf{X})\mathbf{C}(\mathbf{X})\widehat{\mathbf{a}}_f(\mathbf{X})} + (\sigma_n^{i,e} - \sigma_s^{i,e})\frac{\mathbf{C}^{-1}(\mathbf{X})\widehat{\mathbf{a}}_n(\mathbf{X}) \otimes \mathbf{C}^{-1}(\mathbf{X})\widehat{\mathbf{a}}_n(\mathbf{X})}{\widehat{\mathbf{a}}_n^T(\mathbf{X})\mathbf{C}^{-1}(\mathbf{X})\widehat{\mathbf{a}}_n(\mathbf{X})}, \tag{2.73}$$

which, for a transversely isotropic one, reduces to

$$(\mathbf{F}^{-1}\mathbf{D}_{i,e}\mathbf{F}^{-T})(\mathbf{X}) = \sigma_s^{i,e}\mathbf{C}^{-1}(\mathbf{X}) + (\sigma_f^{i,e} - \sigma_s^{i,e})\frac{\widehat{\mathbf{a}}_f(\mathbf{X}) \otimes \widehat{\mathbf{a}}_f(\mathbf{X})}{\widehat{\mathbf{a}}_f^T(\mathbf{X})\mathbf{C}(\mathbf{X})\widehat{\mathbf{a}}_f(\mathbf{X})}. \tag{2.74}$$

The resolution of the Bidomain model requires a high computational time and memory size mainly due to the small space and time steps (of the order of 0.1 mm and 0.01 ms respectively) necessary for the correct simulation of the excitation process, which is characterized by an about 0.5-mm-wide and 1-ms-long propagating layer. This represents a tremendous drawback especially for large scale simulations at the ventricle scale. Therefore, some less demanding approximations are made from the Bidomain model, among which the Monodomain one [36]. In the following, the derivation of this model is briefly resumed.

Let $\mathbf{J}_{tot} = \mathbf{J}_i + \mathbf{J}_e$ be the total current flux in the intracellular and extracellular media and $\mathbf{D}_{tot} = \mathbf{D}_i + \mathbf{D}_e$ the conductivity tensor of the bulk medium. Substituting $u_i = v + u_e$ into $\mathbf{J}_{tot} = -\mathbf{D}_i \mathbf{grad}\, u_i - \mathbf{D}_e \mathbf{grad}\, u_e$ and solving for u_e, it follows that

$$\mathbf{grad}\, u_e = -\mathbf{D}_{tot}^{-1}\mathbf{D}_i \mathbf{grad}\, v - \mathbf{D}_{tot}^{-1}\mathbf{J}_{tot}. \tag{2.75}$$

Therefore, the second equation of the Bidomain system (2.67) can be rewritten as

$$-c_m \frac{\partial v}{\partial t} - \mathrm{div}(\mathbf{D}_e\mathbf{D}_{tot}^{-1}\mathbf{D}_i \mathbf{grad}\, v) + \mathrm{div}(\mathbf{D}_e^{-1}\mathbf{D}_{tot}^{-1}\mathbf{J}_{tot}) - i_{ion}(v,\mathbf{w},\mathbf{c}) = i_{app}^e. \tag{2.76}$$

Using the second alternative expression for the conductivity tensor (2.63), it derives that

$$\mathbf{D_e D_{tot}}^{-1}=\mu_f^e\mathbf{I}+(\mu_s^e-\mu_f^e)\mathbf{a_s}\otimes\mathbf{a_s}+(\mu_n^e-\mu_f^e)\mathbf{a_n}\otimes\mathbf{a_n}, \quad (2.77)$$

where $\mu_{f,s,n}^e=\sigma_{f,s,n}^e/(\sigma_{f,s,n}^e+\sigma_{f,s,n}^i)$. If the conductivity coefficients are constant, the following expression can be written

$$\mathrm{div}(\mathbf{D_e D_{tot}}^{-1}\mathbf{J_{tot}})=\mu_f^e\mathrm{div}\,\mathbf{J_{tot}}+(\mu_s^e-\mu_f^e)\mathrm{div}(\mathbf{a_s a_s}^T\mathbf{J_{tot}})+(\mu_n^e-\mu_f^e)\mathrm{div}(\mathbf{a_n a_n}^T\mathbf{J_{tot}}), \quad (2.78)$$

which immediately turns into

$$\mathrm{div}(\mathbf{D_e D_{tot}}^{-1}\mathbf{J_{tot}})=\mu_f^e(i_{app}^i+i_{app}^e)+(\mu_s^e-\mu_f^e)\mathrm{div}(\mathbf{a_s a_s}^T\mathbf{J_{tot}})+(\mu_n^e-\mu_f^e)\mathrm{div}(\mathbf{a_n a_n}^T\mathbf{J_{tot}}) \quad (2.79)$$

because it holds that $\mathrm{div}\,\mathbf{J_{tot}}=i_{app}^i+i_{app}^e$. From (2.75), it follows that $-\mathbf{D_e D_{tot}}^{-1}\mathbf{D_i}\mathbf{grad}\ v=\mathbf{D_e D_{tot}}^{-1}\mathbf{J_{tot}}+\mathbf{D_e}\mathbf{grad}\ u_e$, thus

$$-\mathbf{n}^T\mathbf{D_e D_{tot}}^{-1}\mathbf{D_i}\mathbf{grad}\ v=\mathbf{n}^T\mathbf{D_e D_{tot}}^{-1}\mathbf{J_{tot}}+\mathbf{n}^T\mathbf{D_e}\mathbf{grad}\ u_e. \quad (2.80)$$

By employing (2.77), the first term on the right-hand side of the last equation becomes

$$\mathbf{n}^T(\mathbf{D_e D_{tot}}^{-1}\mathbf{J_{tot}})=\mu_f^e\mathbf{n}^T\mathbf{J_{tot}}+(\mu_s^e-\mu_f^e)(\mathbf{n}^T\mathbf{a_s})(\mathbf{a_s}^T\mathbf{J_{tot}})+(\mu_n^e-\mu_f^e)(\mathbf{n}^T\mathbf{a_n})(\mathbf{a_n}^T\mathbf{J_{tot}}). \quad (2.81)$$

From the insulating conditions $\mathbf{n}^T\mathbf{J_i}=\mathbf{n}^T\mathbf{J_e}=0$, it follows that $\mathbf{n}^T\mathbf{J_{tot}}=0$, which means that $\mathbf{J_{tot}}$ is tangent to $\partial\Omega$. If cardiac fibers are tangent to $\partial\Omega$ too, $\mathbf{n}^T\mathbf{a_n}=0$ and $\mathbf{a_s}^T\mathbf{J_{tot}}=0$. By replacing these conditions in (2.80) and (2.81), then (2.81) itself gives

$$\mathbf{n}^T\mathbf{D_e D_{tot}}^{-1}\mathbf{D_i}\mathbf{grad}\ v=0. \quad (2.82)$$

Since for media having an equal anisotropic ratio, i.e. $\sigma_f^e/\sigma_f^i=\sigma_s^e/\sigma_s^i=\sigma_n^e/\sigma_n^i$, it holds that $\mu_f^e=\mu_s^e=\mu_n^e$, the two terms in (2.79) representing the projection of $\mathbf{J_{tot}}$ along the orthogonal directions to fibers $\mathbf{a_s}^T\mathbf{J_{tot}}$ and $\mathbf{a_n}^T\mathbf{J_{tot}}$ are zero, obtaining $\mathrm{div}(\mathbf{D_e D_{tot}}^{-1}\mathbf{J_{tot}})\approx\mu_f^e(i_{app}^i+i_{app}^e)$. By replacing this approximation in (2.76) and taking into account the boundary condition (2.82), the Monodomain model can be written. It is a system made of only one parabolic reaction-diffusion partial differential equation for v coupled with the two previous systems made of ordinary differential equations for the gating variables and ionic concentrations

$$\begin{cases} c_m \dfrac{\partial v}{\partial t} - \mathrm{div}(\mathbf{D}\,\mathbf{grad}\ v) + i_{ion}(v,\mathbf{w},\mathbf{c}) + i_{SAC}(v,\mathbf{c},\lambda) = i_{app}^m & \text{in } \Omega\times(0,T) \\ \dfrac{\partial \mathbf{w}}{\partial t} - \mathbf{R}(v,\mathbf{w}) = 0 & \text{in } \Omega\times(0,T) \\ \dfrac{\partial \mathbf{c}}{\partial t} - \mathbf{S}(v,\mathbf{w},\mathbf{c}) = 0 & \text{in } \Omega\times(0,T) \\ \mathbf{n}^T\mathbf{D}\,\mathbf{grad}\ v = 0 & \text{on } \partial\Omega\times(0,T) \\ v(\mathbf{x},0) = v_0(\mathbf{x}), \quad \mathbf{w}(\mathbf{x},0) = \mathbf{w_0}(\mathbf{x}), \quad \mathbf{c}(\mathbf{x},0) = \mathbf{c_0}(\mathbf{x}) & \text{in } \Omega, \end{cases} \tag{2.83}$$

where $\mathbf{D}$ is the conductivity tensor equal to $\mathbf{D}=\mathbf{D_e}\mathbf{D_{tot}}^{-1}\mathbf{D_i}$ and i_{app}^m is the applied stimulation current equal to $i_{app}^m=(i_{app}^i\sigma_f^e - i_{app}^e\sigma_f^i)/(\sigma_f^e+\sigma_f^i)$. However, analogously to $\mathbf{D_{i,e}}$, $\mathbf{D}$ is computed in simulations as

$$\mathbf{D}(\mathbf{x})=\sigma_f\mathbf{a_f}(\mathbf{x})\otimes\mathbf{a_f}(\mathbf{x})+\sigma_s\mathbf{a_s}(\mathbf{x})\otimes\mathbf{a_s}(\mathbf{x})+\sigma_n\mathbf{a_n}(\mathbf{x})\otimes\mathbf{a_n}(\mathbf{x}), \tag{2.84}$$

where $\sigma_f=(\sigma_f^i\sigma_f^e)/(\sigma_f^i+\sigma_f^e)$, $\sigma_s=(\sigma_s^i\sigma_s^e)/(\sigma_s^i+\sigma_s^e)$ and $\sigma_n=(\sigma_n^i\sigma_n^e)/(\sigma_n^i+\sigma_n^e)$, or alternatively as before

$$\mathbf{D}(\mathbf{x})=\sigma_f\mathbf{I}+(\sigma_s-\sigma_f)\mathbf{a_s}(\mathbf{x})\otimes\mathbf{a_s}(\mathbf{x})+(\sigma_n-\sigma_f)\mathbf{a_n}(\mathbf{x})\otimes\mathbf{a_n}(\mathbf{x}) \tag{2.85}$$

or again

$$\mathbf{D}(\mathbf{x})=\sigma_s\mathbf{I}+(\sigma_f-\sigma_s)\mathbf{a_f}(\mathbf{x})\otimes\mathbf{a_f}(\mathbf{x})+(\sigma_n-\sigma_s)\mathbf{a_n}(\mathbf{x})\otimes\mathbf{a_n}(\mathbf{x}). \tag{2.86}$$

In case of transversely isotropic tissues, $\sigma_n=\sigma_s$ holds, thus

$$\mathbf{D}(\mathbf{x})=\sigma_s\mathbf{I}+(\sigma_f-\sigma_s)\mathbf{a_f}(\mathbf{x})\otimes\mathbf{a_f}(\mathbf{x}). \tag{2.87}$$

The previous Monodomain system is valid for the current configuration Ω, thus it must be rewritten in the reference configuration Ω_0 for a Lagrangian description. Following the same procedure for the Bidomain model, it can be rewritten as

$$\begin{cases} c_m\left(\frac{\partial V}{\partial t}-\mathbf{F}^{-T}\mathbf{Grad}\,V\cdot\frac{\partial \mathbf{x}}{\partial t}\right)-J^{-1}\mathrm{Div}\left(J\mathbf{F}^{-1}\mathbf{D}\mathbf{F}^{-T}\mathbf{Grad}\,V\right)+i_{ion}(V,\mathbf{w},\mathbf{c})+i_{SAC}(V,\mathbf{c},\lambda)=i_{app}^{m} & \text{in } \Omega_0\times(0,T) \\ \frac{\partial \mathbf{w}}{\partial t}-\mathbf{R}(v,\mathbf{w})=0 & \text{in } \Omega\times(0,T) \\ \frac{\partial \mathbf{c}}{\partial t}-\mathbf{S}(v,\mathbf{w},\mathbf{c})=0 & \text{in } \Omega\times(0,T) \\ \mathbf{N}^{T}\mathbf{F}^{-1}\mathbf{D}\mathbf{F}^{-T}\mathbf{Grad}\,V=0 & \text{on } \partial\Omega_0\times(0,T) \\ V(\mathbf{X},0)=V_0(\mathbf{X}) \text{ in } \Omega_0,\quad \mathbf{w}(\mathbf{x},0)=\mathbf{w}_0(\mathbf{x}),\quad \mathbf{c}(\mathbf{x},0)=\mathbf{c}_0(\mathbf{x}) & \text{in } \Omega \end{cases} \tag{2.88}$$

For the computation of the product $\mathbf{F}^{-1}\mathbf{D}\mathbf{F}^{-T}$, similar equations to the Bidomain formulation hold, i.e.

$$(\mathbf{F}^{-1}\mathbf{D}\mathbf{F}^{-T})(\mathbf{X})=\sigma_s\mathbf{C}^{-1}(\mathbf{X})+(\sigma_f-\sigma_s)\frac{\hat{\mathbf{a}}_f(\mathbf{X})\otimes\hat{\mathbf{a}}_f(\mathbf{X})}{\hat{\mathbf{a}}_f^{T}(\mathbf{X})\mathbf{C}(\mathbf{X})\hat{\mathbf{a}}_f(\mathbf{X})}+(\sigma_n-\sigma_s)\frac{\mathbf{C}^{-1}(\mathbf{X})\hat{\mathbf{a}}_n(\mathbf{X})\otimes\mathbf{C}^{-1}(\mathbf{X})\hat{\mathbf{a}}_n(\mathbf{X})}{\hat{\mathbf{a}}_n^{T}(\mathbf{X})\mathbf{C}^{-1}(\mathbf{X})\hat{\mathbf{a}}_n(\mathbf{X})} \tag{2.89}$$

for an orthotropic tissue and

$$(\mathbf{F}^{-1}\mathbf{D}\mathbf{F}^{-T})(\mathbf{X})=\sigma_s\mathbf{C}^{-1}(\mathbf{X})+(\sigma_f-\sigma_s)\frac{\hat{\mathbf{a}}_f(\mathbf{X})\otimes\hat{\mathbf{a}}_f(\mathbf{X})}{\hat{\mathbf{a}}_f^{T}(\mathbf{X})\mathbf{C}(\mathbf{X})\hat{\mathbf{a}}_f(\mathbf{X})} \tag{2.90}$$

for a transversely isotropic one.

2.4. The theory of finite volumetric growth

The three-dimensional model introduced so far is here slightly modified to include tissue growth, which will be analyzed in Chapter 3, Chapter 4 and Chapter 5.

Following [179], a quite recurrent framework researchers refer to is the continuum theory of finite volumetric growth; see [9,20,135,149] for extensive reviews on the state of the art of different modeling approaches to growth related not only to the heart [15,66,67,121,136,175] but also to other soft and hard biological structures, such as bones (e.g., [127,128,169,206,219]), arteries (e.g., [2,3,7,79,129,214]), skin (e.g., [32,201,208,231,232]) and tumors (e.g., [5,6,10,33,172]). This framework is characterized by the multiplicative decomposition of the deformation gradient tensor $\mathbf{F}$ into an elastic part $\mathbf{F}^{e}$ and a growth part $\mathbf{F}^{g}$

$$\mathbf{F}=\mathbf{F}^{e}\mathbf{F}^{g}, \tag{2.91}$$

which defines an intermediate growth configuration Ω_g (Figure 2.12). This new configuration is incompatible, i.e. equilibrium cannot be enforced

because, differently from $\mathbf{F}$, neither $\mathbf{F}^{\mathbf{e}}$ nor $\mathbf{F}^{\mathbf{g}}$ can be derived from a vector field.

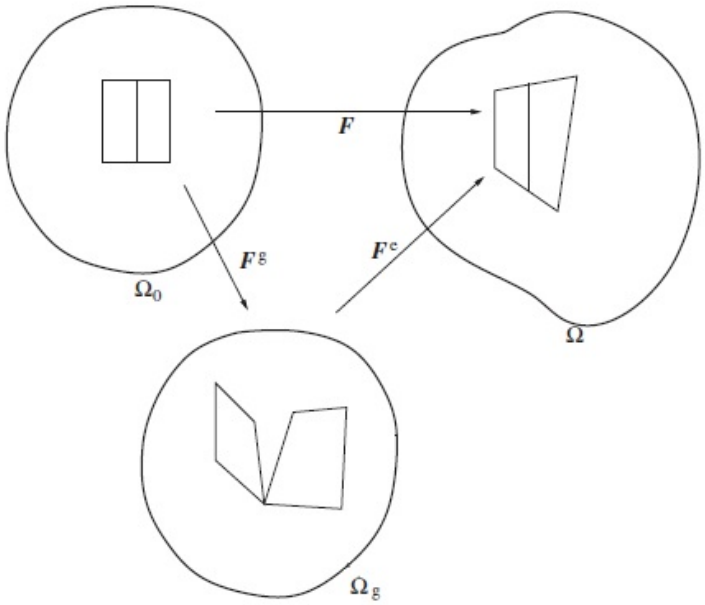

Figure 2.12: Multiplicative decomposition $\mathbf{F}=\mathbf{F}^{\mathbf{e}}\mathbf{F}^{\mathbf{g}}$ between the reference configuration Ω_0, the intermediate growth configuration Ω_g and the current configuration Ω (adapted from [9]).

By rewriting equation (2.91) with respect to $\mathbf{F}^{\mathbf{e}}$

$$\mathbf{F}^{\mathbf{e}}=\mathbf{F}(\mathbf{F}^{\mathbf{g}})^{-1}, \tag{2.92}$$

it immediately follows from (2.24) that the elastic part $\mathbf{C}^{\mathbf{e}}$ of the right Cauchy-Green deformation tensor $\mathbf{C}$ is

$$\mathbf{C}^{\mathbf{e}}=(\mathbf{F}^{\mathbf{e}})^{\mathrm{T}}\mathbf{F}^{\mathbf{e}}, \tag{2.93}$$

from which the elastic part $\mathbf{E}^{\mathbf{e}}$ of the Lagrange-Green strain tensor $\mathbf{E}$ is directly derived (as in (2.27))

$$\mathbf{E}^{\mathbf{e}}=\frac{1}{2}(\mathbf{C}^{\mathbf{e}}-\mathbf{I}). \tag{2.94}$$

By using (2.49), the elastic part $\mathbf{S}^{\mathbf{e}}$ of the total second Piola-Kirchhoff stress tensor $\mathbf{S}$ is computed as

$$\mathbf{S}^{\mathbf{e}}=\mathbf{S}^{\mathbf{e,act}}+\mathbf{S}^{\mathbf{e,pas}}. \tag{2.95}$$

The elastic active component $\mathbf{S}^{\mathbf{e,act}}$ is related to the cell active tension T_a that is supposed to develop only along the fiber direction, i.e. from (2.52)

$$\mathbf{S}^{\mathbf{e,act}}=\frac{T_a}{\widehat{\mathbf{a}_f}^{T}\mathbf{C}^{\mathbf{e}}\widehat{\mathbf{a}_f}}\widehat{\mathbf{a}_f}\otimes\widehat{\mathbf{a}_f}, \tag{2.96}$$

where T_a is computed through the previously recalled model by Land, which can be now summarized in the following way (similarly to (2.17))

$$\begin{cases}\dfrac{\partial \mathbf{a}}{\partial t}-\mathbf{G}\left(\mathbf{a},[Ca^{2+}]_i,\lambda^e,\dfrac{d\lambda^e}{dt}\right)=0 & \text{in} \quad \Omega_0\times(0,T)\\ \mathbf{a}(\mathbf{X},0)=\mathbf{a_0}(\mathbf{X}) & \text{in} \quad \Omega_0\\ T_a=h(\mathbf{a},\lambda^e) & \text{in} \quad \Omega_0\times(0,T),\end{cases} \tag{2.97}$$

where λ^e and $d\lambda^e/dt$ are the elastic stretch and stretch rate. The variables λ^e and $d\lambda^e/dt$ are used instead of the total ones λ and $d\lambda/dt$ because growth is carried out by adding new sarcomeres in cardiomyocytes rather than lengthening or widening the preexistent ones (as observed in [136] or inferred from [175]). In particular, from (2.55) λ^e is given by

$$\lambda^e=\sqrt{\widehat{\mathbf{a}_f}^{T}\mathbf{C}^{\mathbf{e}}\widehat{\mathbf{a}_f}}, \tag{2.98}$$

which is also used to compute the stretch-activated channels current I_{SAC} (2.16) by the new factors

$$\gamma_{SL,SAC}=10\max\left(\lambda^e-1,0\right),\quad \gamma_{SL,Ko}=0.7+3\max\left(\lambda^e-1,0\right). \tag{2.99}$$

If the cardiac tissue is modeled as a compressible material, the elastic passive component $\mathbf{S}^{\mathbf{e,pas}}$ is related only to a strain energy function W (as in (2.58))

$$\mathbf{S}^{\mathbf{e,pas}}=\frac{\partial W}{\partial \mathbf{E}^{\mathbf{e}}}, \tag{2.100}$$

otherwise, if it is incompressible, $\mathbf{S}^{\mathbf{e,pas}}$ is related to an incompressibility term too (as in (2.59))

$$\mathbf{S}^{\mathbf{e,pas}}=\frac{\partial W}{\partial \mathbf{E}^{\mathbf{e}}}-p(\mathbf{C}^{\mathbf{e}})^{-1}. \tag{2.101}$$

After computing the elastic part $\mathbf{S}^{\mathbf{e}}$, the total $\mathbf{S}$ can be derived as

$$\mathbf{S}=J^g(\mathbf{F}^{\mathbf{g}})^{-1}\mathbf{S}^{\mathbf{e}}(\mathbf{F}^{\mathbf{g}})^{-T}, \tag{2.102}$$

where $J^g=\det(\mathbf{F}^g)$, from the intermediate growth configuration Ω_g to the reference one Ω_0. Then, the total $\mathbf{S}$ enters the quasi-static equilibrium condition (2.46).

The growth tensor $\mathbf{F}^g$ is assumed to be symmetric and it is given the following generic equation that takes into account the orthotropic nature of the cardiac tissue [66,67]

$$\mathbf{F}^g=\theta_f \widehat{\mathbf{a}_f} \otimes \widehat{\mathbf{a}_f}+\theta_s \widehat{\mathbf{a}_s} \otimes \widehat{\mathbf{a}_s}+\theta_n \widehat{\mathbf{a}_n} \otimes \widehat{\mathbf{a}_n}, \tag{2.103}$$

where θ_f, θ_s and θ_n are the growth parameters along $\widehat{\mathbf{a}_f}$, $\widehat{\mathbf{a}_s}$ and $\widehat{\mathbf{a}_n}$ that usually depend on time and space; they take the value 1 in the plain elastic case, they are smaller than 1 for shrinkage and they are larger than 1 for growth. Details on the way they evolve or not during growth and of the specific equations used for $\mathbf{F}^g$ will be given in Chapter 3, Chapter 4 and Chapter 5, where some other parameters belonging to the three-dimensional model will be affected from growth too.

2.5. The discretization of the complete model

The space and time discretizations of all previous equations are necessary to implement the electromechanical model in a computational code for simulations.

2.5.1. The space discretization

In the literature, many space discretization procedures can be retrieved, such as finite differences, first- or high-order finite elements, finite volumes, non-conforming finite elements and adaptive remeshing techniques. In this thesis, the whole electromechanical model is spatially discretized by first-order finite elements [22].

The discretization of the Bidomain and Monodomain models is based on the Galerkin procedure [60] applied to the variational formulations of these models. Actually, their forms in (2.67) and (2.83) are similar to the Poisson parabolic equation with a symmetric anisotropic diffusive tensor $\mathbf{D}(\mathbf{x})=\mathbf{D}(\mathbf{x})^T$

$$\frac{\partial u}{\partial t}-\mathrm{div}(\mathbf{D}\mathbf{grad}\ u)=f \qquad \text{in} \quad \Omega\times(0,T), \tag{2.104}$$

where u is the Poisson variable (it would be the transmembrane potential v) and $f(\mathbf{x},t)$ is the constant term (it would be $i_{app}^{i,e,m}-i_{ion}(v,\mathbf{w},\mathbf{c})-i_{SAC}(v,\mathbf{c},\lambda)$). Leaving out here the entire Galerkin procedure, in the following, the final finite-element discretization of the previous models is reported directly. Let

T^h be a uniform mesh of the current configuration $\Omega(t)$ and W^h the corresponding finite-element space. By selecting a finite-element basis φ_i for W^h and a suitable quadrature rule, the discretization of the first two equations of the Bidomain system (2.67) turns out to be [36]

$$\begin{cases} c_m \mathbf{M}\dfrac{\partial \mathbf{v}_h}{\partial t}+\mathbf{A_i u}_{i,h}+\mathbf{Mi}_{\mathbf{ion},h}(\mathbf{v}_h,\mathbf{w}_h,\mathbf{c}_h)+\mathbf{Mi}_{\mathbf{SAC},h}(\mathbf{v}_h,\mathbf{c}_h,\boldsymbol{\lambda}_h)=\mathbf{Mi}^{\mathbf{i}}_{\mathbf{app},h} \\ -c_m \mathbf{M}\dfrac{\partial \mathbf{v}_h}{\partial t}+\mathbf{A_e u}_{e,h}-\mathbf{Mi}_{\mathbf{ion},h}(\mathbf{v}_h,\mathbf{w}_h,\mathbf{c}_h)-\mathbf{Mi}_{\mathbf{SAC},h}(\mathbf{v}_h,\mathbf{c}_h,\boldsymbol{\lambda}_h)=\mathbf{Mi}^{\mathbf{e}}_{\mathbf{app},h}, \end{cases} \tag{2.105}$$

where $\mathbf{u}_{i,h}$, $\mathbf{u}_{e,h}$, $\mathbf{v}_h=\mathbf{u}_{i,h}-\mathbf{u}_{e,h}$, $\mathbf{w}_h$, $\mathbf{c}_h$, $\boldsymbol{\lambda}_h$, $\mathbf{i}_{\mathbf{ion},h}$, $\mathbf{i}_{\mathbf{SAC},h}$ and $\mathbf{i}^{\mathbf{i,e}}_{\mathbf{app},h}$ are the finite-element approximations (vectors of nodal values) of u_i, u_e, v, $\mathbf{w}$, $\mathbf{c}$, λ, i_{ion}, i_{SAC} and $i^{i,e}_{app}$, whereas $\mathbf{M}$ is the mass matrix and $\mathbf{A_{i,e}}$ are the stiffness matrixes defined in the following way

$$\mathbf{M}=\{m_{rs}=\int_\Omega \varphi_r\varphi_s d\Omega\}, \qquad \mathbf{A_{i,e}}=\{a^{i,e}_{rs}=\int_\Omega (\mathbf{grad}\ \varphi_r)^T \mathbf{D_{i,e}}\mathbf{grad}\ \varphi_s d\Omega\}. \tag{2.106}$$

The previous system can be alternatively written in a compact form as

$$c_m\widetilde{\mathbf{M}}\frac{\partial}{\partial t}\begin{pmatrix}\mathbf{u}_{i,h}\\ \mathbf{u}_{e,h}\end{pmatrix}+\widetilde{\mathbf{A}}\begin{pmatrix}\mathbf{u}_{i,h}\\ \mathbf{u}_{e,h}\end{pmatrix}+\begin{pmatrix}\mathbf{Mi}_{\mathbf{ion},h}(\mathbf{v}_h,\mathbf{w}_h,\mathbf{c}_h)+\mathbf{Mi}_{\mathbf{SAC},h}(\mathbf{v}_h,\mathbf{c}_h,\boldsymbol{\lambda}_h)\\ -\mathbf{Mi}_{\mathbf{ion},h}(\mathbf{v}_h,\mathbf{w}_h,\mathbf{c}_h)-\mathbf{Mi}_{\mathbf{SAC},h}(\mathbf{v}_h,\mathbf{c}_h,\boldsymbol{\lambda}_h)\end{pmatrix}=\begin{pmatrix}\mathbf{Mi}^{\mathbf{i}}_{\mathbf{app},h}\\ \mathbf{Mi}^{\mathbf{e}}_{\mathbf{app},h}\end{pmatrix}, \tag{2.107}$$

where

$$\widetilde{\mathbf{M}}=\begin{bmatrix}\mathbf{M} & -\mathbf{M}\\ -\mathbf{M} & \mathbf{M}\end{bmatrix}, \qquad \widetilde{\mathbf{A}}=\begin{bmatrix}\mathbf{A_i} & \mathbf{0}\\ \mathbf{0} & \mathbf{A_e}\end{bmatrix}. \tag{2.108}$$

The first equation of the Monodomain system (2.83) becomes, instead, [36]

$$c_m\mathbf{M}\frac{\partial \mathbf{v}_h}{\partial t}+\mathbf{A}\mathbf{v}_h+\mathbf{Mi}_{\mathbf{ion},h}(\mathbf{v}_h,\mathbf{w}_h,\mathbf{c}_h)+\mathbf{Mi}_{\mathbf{SAC},h}(\mathbf{v}_h,\mathbf{c}_h,\boldsymbol{\lambda}_h)=\mathbf{Mi}^{\mathbf{m}}_{\mathbf{app},h}, \tag{2.109}$$

where $\mathbf{i}^{\mathbf{m}}_{\mathbf{app},h}$ is the finite-element approximation of i^m_{app} and the stiffness matrix $\mathbf{A}$ is

$$\mathbf{A}=\{a_{rs}=\int_\Omega (\mathbf{grad}\ \varphi_r)^T \mathbf{D}\mathbf{grad}\ \varphi_s d\Omega\}. \tag{2.110}$$

Then, (2.105) or (2.109) are coupled with the approximations of the gating variables and ionic concentrations systems [36]

$$\begin{cases} \dfrac{\partial \mathbf{w}_h}{\partial t} - \mathbf{R}(\mathbf{v}_h, \mathbf{w}_h) = \mathbf{0} \\ \dfrac{\partial \mathbf{c}_h}{\partial t} - \mathbf{S}(\mathbf{v}_h, \mathbf{w}_h, \mathbf{c}_h) = \mathbf{0}. \end{cases} \tag{2.111}$$

Similarly, in a Lagrangian setting, the first two equations of the Bidomain system (2.68) turn out to be

$$\begin{cases} c_m \left(\mathbf{M} \dfrac{\partial \mathbf{V}_h}{\partial t} + \mathbf{A}_c \dfrac{\partial \mathbf{x}_h}{\partial t} \right) + \mathbf{J}^{-1} \mathbf{A}_i \mathbf{U}_{i,h} + \mathbf{M} \mathbf{i}_{ion,h}(\mathbf{V}_h, \mathbf{w}_h, \mathbf{c}_h) + \mathbf{M} \mathbf{i}_{SAC,h}(\mathbf{V}_h, \mathbf{c}_h, \boldsymbol{\lambda}_h) = \mathbf{M} \mathbf{i}^{i}_{app,h} \\ -c_m \left(\mathbf{M} \dfrac{\partial \mathbf{V}_h}{\partial t} + \mathbf{A}_c \dfrac{\partial \mathbf{x}_h}{\partial t} \right) + \mathbf{J}^{-1} \mathbf{A}_e \mathbf{U}_{e,h} - \mathbf{M} \mathbf{i}_{ion,h}(\mathbf{V}_h, \mathbf{w}_h, \mathbf{c}_h) - \mathbf{M} \mathbf{i}_{SAC,h}(\mathbf{V}_h, \mathbf{c}_h, \boldsymbol{\lambda}_h) = \mathbf{M} \mathbf{i}^{e}_{app,h}, \end{cases} \tag{2.112}$$

where $\mathbf{x}_h$ is the finite-element approximation of $\mathbf{x}$, $\mathbf{A}_{i,e}$ have now the following structure

$$\mathbf{A}_{i,e} = \{ a^{i,e}_{rs} = \int_{\Omega_0} J(\mathbf{Grad}\ \varphi_r)^T \mathbf{F}^{-1} \mathbf{D}_{i,e} \mathbf{F}^{-T} \mathbf{Grad}\ \varphi_s \, d\Omega_0 \} \tag{2.113}$$

and $\mathbf{A}_c$ is another stiffness matrix defined by

$$\mathbf{A}_c = \{ a^{c}_{rs} = \int_{\Omega_0} \mathbf{F}^{-T} \mathbf{Grad}\ \varphi_s \varphi_r \, d\Omega_0 \}. \tag{2.114}$$

The previous system can be written in a compact form again as

$$c_m \left(\widetilde{\mathbf{M}} \frac{\partial}{\partial t} \begin{pmatrix} \mathbf{U}_{i,h} \\ \mathbf{U}_{e,h} \end{pmatrix} + \mathbf{A}_c \frac{\partial \mathbf{x}_h}{\partial t} \right) + \mathbf{J}^{-1} \widetilde{\mathbf{A}} \begin{pmatrix} \mathbf{U}_{i,h} \\ \mathbf{U}_{e,h} \end{pmatrix} + \begin{pmatrix} \mathbf{M} \mathbf{i}_{ion,h}(\mathbf{V}_h, \mathbf{w}_h, \mathbf{c}_h) + \mathbf{M} \mathbf{i}_{SAC,h}(\mathbf{V}_h, \mathbf{c}_h, \boldsymbol{\lambda}_h) \\ -\mathbf{M} \mathbf{i}_{ion,h}(\mathbf{V}_h, \mathbf{w}_h, \mathbf{c}_h) - \mathbf{M} \mathbf{i}_{SAC,h}(\mathbf{V}_h, \mathbf{c}_h, \boldsymbol{\lambda}_h) \end{pmatrix} = \begin{pmatrix} \mathbf{M} \mathbf{i}^{i}_{app,h} \\ \mathbf{M} \mathbf{i}^{e}_{app,h} \end{pmatrix}. \tag{2.115}$$

The first equation of the Monodomain system (2.88) becomes, instead,

$$c_m \left(\mathbf{M} \frac{\partial \mathbf{V}_h}{\partial t} + \mathbf{A}_c \frac{\partial \mathbf{x}_h}{\partial t} \right) + \mathbf{J}^{-1} \mathbf{A} \mathbf{V}_h + \mathbf{M} \mathbf{i}_{ion,h}(\mathbf{V}_h, \mathbf{w}_h, \mathbf{c}_h) + \mathbf{M} \mathbf{i}_{SAC,h}(\mathbf{V}_h, \mathbf{c}_h, \boldsymbol{\lambda}_h) = \mathbf{M} \mathbf{i}^{m}_{app,h}, \tag{2.116}$$

where $\mathbf{A}$ is now

$$\mathbf{A} = \{ a_{rs} = \int_{\Omega_0} J(\mathbf{Grad}\ \varphi_r)^T \mathbf{F}^{-1} \mathbf{D} \mathbf{F}^{-T} \mathbf{Grad}\ \varphi_s \, d\Omega_0 \}. \tag{2.117}$$

Then, (2.112) or (2.116) are coupled with the approximations of the gating variables and ionic concentrations systems (2.111) again.

Analogously, the first and third equation of the active tension generation system (2.17), now written in a three-dimensional setting like in (2.97), are discretized in the following way

$$\begin{cases} \dfrac{\partial \mathbf{a}_h}{\partial t} - \mathbf{G}\left(\mathbf{a}_h, [\mathbf{Ca}^{2+}]_{i,h}, \boldsymbol{\lambda}_h, \dfrac{d\boldsymbol{\lambda}_h}{dt} \right) = \mathbf{0} \\ \mathbf{T}_{a,h} = \mathbf{h}(\mathbf{a}_h, \boldsymbol{\lambda}_h), \end{cases} \tag{2.118}$$

where $\mathbf{a}_h$, $[\mathbf{Ca}^{2+}]_{i,h}$, $d\boldsymbol{\lambda}_h/dt$ and $\mathbf{T}_{a,h}$ are the finite-element approximations of $\mathbf{a}$, $[Ca^{2+}]_i$, $d\boldsymbol{\lambda}/dt$ and T_a.

Since the non-linear equilibrium equation of the mechanical model is solved by means of the iterative Newton-Raphson algorithm, a residual vector $\mathbf{F}_{mec}$ and a jacobian matrix $\mathbf{J}_{mec} = \partial \mathbf{F}_{mec} / \partial \mathbf{x}$ are computed for a generic iteration as

$$\begin{aligned} \mathbf{F}_{mec} &= \{ f_s = \sum_{r=1}^{n_{p,mec}} \mathbf{x}_r \int_{\Omega_0} (\mathbf{Grad}\, \varphi_r)^T \mathbf{S} \mathbf{Grad}\, \varphi_s d\Omega_0 \} \\ \mathbf{J}_{mec} &= \{ j_{rs} = \int_{\Omega_0} (\mathbf{Grad}\, \varphi_r)^T \mathbf{S} \mathbf{Grad}\, \varphi_s d\Omega_0 \} + \sum_{l=1}^{n_{p,mec}} \mathbf{x}_l \int_{\Omega_0} (\mathbf{Grad}\, \varphi_r)^T \frac{\partial \mathbf{S}}{\partial \mathbf{x}} \mathbf{Grad}\, \varphi_s \mathbf{Grad}\, \varphi_l d\Omega_0 \}, \end{aligned} \tag{2.119}$$

where $n_{p,mec}$ is the number of nodes of the employed mechanical mesh. The variation of coordinates $\Delta\mathbf{x}$ is then obtained from the resolution of the linearized system

$$\mathbf{J}_{mec}(\mathbf{x}) \Delta\mathbf{x} = -\mathbf{F}_{mec}(\mathbf{x}) \tag{2.120}$$

in all points $\mathbf{x}$ where a Dirichlet boundary condition is not assigned.

In conclusion, the electrical equations are solved on a mesh with a uniform spacing Δh_{el}, whereas the mechanical ones together with the active tension generation system on a coarser mesh with a uniform spacing Δh_{mec} because the quasi-static tissue deformation turns out to be much slower than the electrical propagation.

2.5.2. The time discretization

As for the space discretization, one can find several techniques to perform the time discretization of a model in the literature like explicit, implicit or semi-implicit methods and splitting operators. However, in the remainder of this paragraph, only the procedures employed for the simulations in this thesis will be recalled.

The discretization of the Bidomain and Monodomain models is achieved via the Godunov splitting [64] or a decoupled semi-implicit method [36].

The former is part of the so-called splitting methods. These ones separate the diffusive term, which describes the propagation of the electrical signal in a tissue through the conductivity tensor $\mathbf{D}$, from the non-linear reaction one i_{ion} that accounts for the time evolution of the ionic concentrations and gating variables belonging to a plasma membrane

model. In this way, the time updating of variables gets easier because different numerical schemes can be applied to the two previous terms. However, the accuracy of results is threatened due to the lack of simultaneous dependences among the model variables. In particular, the Godunov splitting includes two subsequent steps. First, starting from the values for $\mathbf{v}^{n_{el}}$, $\mathbf{w}^{n_{el}}$ and $\mathbf{c}^{n_{el}}$ at the previous electrical time step $t^{n_{el}}$ (and the value of $\boldsymbol{\lambda}^{n_{mec}}$ at the previous mechanical time step $t^{n_{mec}}$ for the stretch-activated channels current), the new values $\mathbf{w}^{n_{el}+1}$ and $\mathbf{c}^{n_{el}+1}$ at the current time step $t^{n_{el}+1}$ are found and a temporary value $\mathbf{v}^{n_{el}+1,*}$ is computed by solving the system of ODEs (written in the discretized space without the subscript h for sake of clearness)

$$\begin{cases} c_m \dfrac{d\mathbf{v}}{dt} + \mathbf{i}_{ion}(\mathbf{v},\mathbf{w},\mathbf{c}) + \mathbf{i}_{SAC}(\mathbf{v},\mathbf{c},\boldsymbol{\lambda}) = \mathbf{0} \\ \dfrac{d\mathbf{w}}{dt} - \mathbf{R}(\mathbf{v},\mathbf{w}) = \mathbf{0} \\ \dfrac{d\mathbf{c}}{dt} - \mathbf{S}(\mathbf{v},\mathbf{w},\mathbf{c}) = \mathbf{0}. \end{cases} \tag{2.121}$$

In particular, in this thesis, the explicit Forward Euler method is used to solve the first equation and the system of ionic concentrations, whereas the implicit Rush-Larsen scheme [184] is applied to the system of gating variables (see below for the general formulation of both methods). Then, from the just computed $\mathbf{v}^{n_{el}+1,*}$, the new values at $t^{n_{el}+1}$ for $\mathbf{u}_i^{n_{el}+1}$ and $\mathbf{u}_e^{n_{el}+1}$ in case of the Bidomain model or for $\mathbf{v}^{n_{el}+1}$ in case of the Monodomain one are found by solving the corresponding system of PDEs, i.e.

$$\begin{cases} c_m \mathbf{M} \dfrac{d\mathbf{v}}{dt} + \mathbf{A}_i \mathbf{u}_i = \mathbf{M}\mathbf{i}_{app}^{i} \\ -c_m \mathbf{M} \dfrac{d\mathbf{v}}{dt} + \mathbf{A}_e \mathbf{u}_e = \mathbf{M}\mathbf{i}_{app}^{e} \end{cases} \tag{2.122}$$

or

$$c_m \mathbf{M} \frac{d\mathbf{v}}{dt} + \mathbf{A}\mathbf{v} = \mathbf{M}\mathbf{i}_{app}^{m}. \tag{2.123}$$

In a Lagrangian framework, the previous two systems and equation become

$$\begin{cases} c_m \dfrac{d\mathbf{V}}{dt} + \mathbf{i}_{ion}(\mathbf{V},\mathbf{w},\mathbf{c}) + \mathbf{i}_{SAC}(\mathbf{V},\mathbf{c},\boldsymbol{\lambda}) = \mathbf{0} \\ \dfrac{d\mathbf{w}}{dt} - \mathbf{R}(\mathbf{v},\mathbf{w}) = \mathbf{0} \\ \dfrac{d\mathbf{c}}{dt} - \mathbf{S}(\mathbf{v},\mathbf{w},\mathbf{c}) = \mathbf{0} \end{cases} \tag{2.124}$$

for the first step and

$$\begin{cases} c_m \left(\mathbf{M} \dfrac{d\mathbf{V}}{dt} + \mathbf{A}_c \dfrac{d\mathbf{x}}{dt} \right) + \mathbf{J}^{-1} \mathbf{A}_i \mathbf{U}_i = \mathbf{M} \mathbf{i}_{app}^i \\ -c_m \left(\mathbf{M} \dfrac{d\mathbf{V}}{dt} + \mathbf{A}_c \dfrac{d\mathbf{x}}{dt} \right) + \mathbf{J}^{-1} \mathbf{A}_e \mathbf{U}_e = \mathbf{M} \mathbf{i}_{app}^e \end{cases} \tag{2.125}$$

or

$$c_m \left(\mathbf{M} \frac{d\mathbf{V}}{dt} + \mathbf{A}_c \frac{d\mathbf{x}}{dt} \right) + \mathbf{J}^{-1} \mathbf{A} \mathbf{V} = \mathbf{M} \mathbf{i}_{app}^m \tag{2.126}$$

for the second one.

The latter method, the semi-implicit one, is based on an implicit treatment of the diffusive term and of the resolution of the ODE system of gating variables (by the Backward Euler method or the Rush-Larsen scheme respectively in this thesis), whereas an explicit method (the Forward Euler method in this thesis) is used for solving the ODE system of ionic concentrations. Two steps are required by this method too. During the first one, starting from the values for $\mathbf{v}^{n_{el}}$, $\mathbf{w}^{n_{el}}$ and $\mathbf{c}^{n_{el}}$ at $t^{n_{el}}$, the values $\mathbf{w}^{n_{el}+1}$ and $\mathbf{c}^{n_{el}+1}$ at $t^{n_{el}+1}$ are computed by solving

$$\begin{cases} \mathbf{w}^{n_{el}+1} - \Delta t_{el} \mathbf{R}(\mathbf{v}^{n_{el}}, \mathbf{w}^{n_{el}+1}) = \mathbf{w}^{n_{el}} \\ \mathbf{c}^{n_{el}+1} = \mathbf{c}^{n_{el}} + \Delta t_{el} \mathbf{S}(\mathbf{v}^{n_{el}}, \mathbf{w}^{n_{el}+1}, \mathbf{c}^{n_{el}}), \end{cases} \tag{2.127}$$

where $\Delta t_{el} = t^{n_{el}+1} - t^{n_{el}}$ is the electrical time-step size. During the second one, in case of the Bidomain model, the new $\mathbf{u}^{n_{el}+1} = (\mathbf{u}_i^{n_{el}+1}, \mathbf{u}_e^{n_{el}+1})$ is found by solving the linear system

$$\mathbf{A}_{bid} \mathbf{u}^{n_{el}+1} = \tilde{\mathbf{F}}, \tag{2.128}$$

where

$$\mathbf{A_{bid}}=\frac{c_m}{\Delta t_{el}}\widetilde{\mathbf{M}}+\widetilde{\mathbf{A}}=\frac{c_m}{\Delta t_{el}}\begin{bmatrix}\mathbf{M} & \mathbf{-M}\\ \mathbf{-M} & \mathbf{M}\end{bmatrix}+\begin{bmatrix}\mathbf{A_i} & \mathbf{0}\\ \mathbf{0} & \mathbf{A_e}\end{bmatrix} \tag{2.129}$$

and

$$\widetilde{\mathbf{F}}=\begin{pmatrix}\mathbf{M}[-\mathbf{i}_{\mathbf{ion}}(\mathbf{v}^{n_{el}},\mathbf{w}^{n_{el}+1},\mathbf{c}^{n_{el}+1})-\mathbf{i}_{\mathbf{SAC}}(\mathbf{v}^{n_{el}},\mathbf{c}^{n_{el}+1},\boldsymbol{\lambda}^{n_{mec}})+\mathbf{i}_{\mathbf{app}}^{\mathbf{i},n_{el}+1}]\\ \mathbf{M}[\mathbf{i}_{\mathbf{ion}}(\mathbf{v}^{n_{el}},\mathbf{w}^{n_{el}+1},\mathbf{c}^{n_{el}+1})+\mathbf{i}_{\mathbf{SAC}}(\mathbf{v}^{n_{el}},\mathbf{c}^{n_{el}+1},\boldsymbol{\lambda}^{n_{mec}})+\mathbf{i}_{\mathbf{app}}^{\mathbf{e},n_{el}+1}]\end{pmatrix}. \tag{2.130}$$

In case of the Monodomain model, instead, during the second step, the new $\mathbf{v}^{n_{el}+1}$ is found by solving the linear system

$$\mathbf{A_{mon}}\mathbf{v}^{n_{el}+1}=\widetilde{\mathbf{F}}, \tag{2.131}$$

where

$$\mathbf{A_{mon}}=\frac{c_m}{\Delta t_{el}}\mathbf{M}+\mathbf{A} \tag{2.132}$$

and

$$\widetilde{\mathbf{F}}=\mathbf{M}[-\mathbf{i}_{\mathbf{ion}}(\mathbf{v}^{n_{el}},\mathbf{w}^{n_{el}+1},\mathbf{c}^{n_{el}+1})-\mathbf{i}_{\mathbf{SAC}}(\mathbf{v}^{n_{el}},\mathbf{c}^{n_{el}+1},\boldsymbol{\lambda}^{n_{mec}})+\mathbf{i}_{\mathbf{app}}^{\mathbf{m},n_{el}+1}]. \tag{2.133}$$

In a Lagrangian framework again, during the second step, the new $\mathbf{U}^{n_{el}+1}=(\mathbf{U}_{\mathbf{i}}^{n_{el}+1},\mathbf{U}_{\mathbf{e}}^{n_{el}+1})$ is found by solving the following linear system for the Bidomain model

$$\mathbf{A_{bid}}\mathbf{U}^{n_{el}+1}=\widetilde{\mathbf{F}}, \tag{2.134}$$

where the constant term is now

$$\widetilde{\mathbf{F}}=\begin{pmatrix}\mathbf{M}[-\mathbf{i}_{\mathbf{ion}}(\mathbf{V}^{n_{el}},\mathbf{w}^{n_{el}+1},\mathbf{c}^{n_{el}+1})-\mathbf{i}_{\mathbf{SAC}}(\mathbf{V}^{n_{el}},\mathbf{c}^{n_{el}+1},\boldsymbol{\lambda}^{n_{mec}})+\mathbf{i}_{\mathbf{app}}^{\mathbf{i},n_{el}+1}]-\frac{c_m}{\Delta t_{mec}}\mathbf{A_c}[\mathbf{x}^{n_{mec}+1}-\mathbf{x}^{n_{mec}}]\\ \mathbf{M}[\mathbf{i}_{\mathbf{ion}}(\mathbf{V}^{n_{el}},\mathbf{w}^{n_{el}+1},\mathbf{c}^{n_{el}+1})+\mathbf{i}_{\mathbf{SAC}}(\mathbf{V}^{n_{el}},\mathbf{c}^{n_{el}+1},\boldsymbol{\lambda}^{n_{mec}})+\mathbf{i}_{\mathbf{app}}^{\mathbf{e},n_{el}+1}]+\frac{c_m}{\Delta t_{mec}}\mathbf{A_c}[\mathbf{x}^{n_{mec}+1}-\mathbf{x}^{n_{mec}}]\end{pmatrix} \tag{2.135}$$

and $\Delta t_{mec}=t^{n_{mec}+1}-t^{n_{mec}}$ is the mechanical time-step size, i.e. the difference between the current and previous mechanical time steps $t^{n_{mec}+1}$ and $t^{n_{mec}}$ that is taken bigger than (or equal to) Δt_{el} due to the quasi-static mechanical response. The new $V^{n_{el}+1}$ for the Monodomain model, instead, is found by solving the new linear system

$$\mathbf{A_{mon}}\mathbf{V}^{n_{el}+1}=\tilde{\mathbf{F}}, \tag{2.136}$$

where

$$\tilde{\mathbf{F}}=\mathbf{M}[-\mathbf{i_{ion}}(\mathbf{V}^{n_{el}},\mathbf{w}^{n_{el}+1},\mathbf{c}^{n_{el}+1})-\mathbf{i_{SAC}}(\mathbf{V}^{n_{el}},\mathbf{c}^{n_{el}+1},\boldsymbol{\lambda}^{n_{mec}})+\mathbf{i}_{app}^{m,n_{el}+1}]-\frac{c_m}{\Delta t_{mec}}\mathbf{A_c}[\mathbf{x}^{n_{mec}+1}-\mathbf{x}^{n_{mec}}]. \tag{2.137}$$

As it has already been recalled, for both the Godunov splitting and the semi-implicit method, the ODE system of ionic concentrations is solved by means of the explicit Forward Euler method, which can be written as

$$\mathbf{c}^{n_{el}+1}=\mathbf{c}^{n_{el}}+\Delta t_{el}\mathbf{S}(\mathbf{v}^{n_{el}},\mathbf{w}^{n_{el}+1},\mathbf{c}^{n_{el}}). \tag{2.138}$$

The ODE system of gating variables is solved, instead, by the implicit Rush-Larsen scheme, which ensures the stability for Hodgkin-Huxley-type gates by assuming that the opening and closing probabilities of channels at $t^{n_{el}+1}$ are approximatively constant and equal to the corresponding ones at $t^{n_{el}}$

$$\mathbf{w}^{n_{el}+1}=\mathbf{w}_\infty(\mathbf{v}^{n_{el}})-e^{-\frac{\Delta t_{el}}{\boldsymbol{\tau}_w(\mathbf{v}^{n_{el}})}}(\mathbf{w}_\infty(\mathbf{v}^{n_{el}})-\mathbf{w}^{n_{el}}), \tag{2.139}$$

where $\mathbf{w}_\infty$ and $\boldsymbol{\tau}_\mathbf{w}$ are the equilibrium state and time constant (2.11) that depend on $\mathbf{v}^{n_{el}}$.

As regards the active tension generation system, the first and third equation are generally discretized by means of the Backward Euler method in this way

$$\begin{cases}\mathbf{a}^{n_{mec}+1}-\Delta t_{mec}\mathbf{G}\left(\mathbf{a}^{n_{mec}+1},[\mathbf{Ca}^{2+}]_\mathbf{i}^{n_{el}+1},\boldsymbol{\lambda}^{n_{mec}+1},\dfrac{\boldsymbol{\lambda}^{n_{mec}+1}-\boldsymbol{\lambda}^{n_{mec}}}{\Delta t_{mec}}\right)=\mathbf{a}^{n_{mec}}\\ \mathbf{T}_\mathbf{a}^{n_{mec}+1}=\mathbf{h}(\mathbf{a}^{n_{mec}+1},\boldsymbol{\lambda}^{n_{mec}+1}).\end{cases} \tag{2.140}$$

However, the non-linear equations appearing in this system are discretized by means of the Forward Euler method in order to avoid further Newton-Raphson algorithms for their resolution, thus limiting the computational time while keeping the numerical schema stable. Additional details on the updating of this system will be given in the next section.

2.6. The general algorithm for the resolution of the complete model

The general algorithm followed to solve the complete electromechanical model during all simulations is shown in Figure 2.13. A deeper explanation

is given in the remainder of this section, whereas further details on the specific procedures implemented during each group of simulations will be reported in the next chapters.

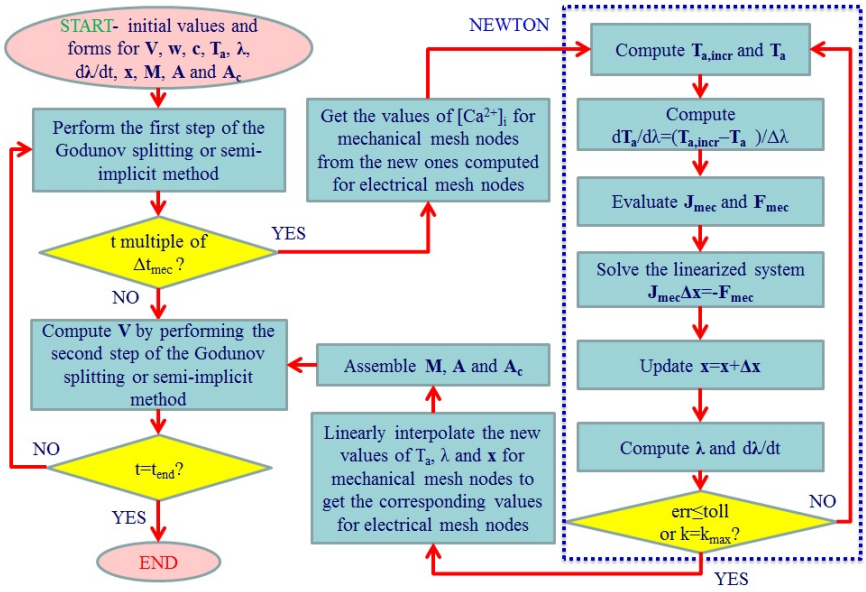

Figure 2.13: General algorithm for the resolution of the electromechanical model during all simulations (see text for details).

First, assign the initial values to all differential variables, i.e. V, **w** and **c**, and the initial values to T_a, λ and dλ/dt in all nodes belonging to the electrical and mechanical meshes. Moreover, initialize coordinates **x** and compute the initial forms of the matrixes **M**, **A** and $\mathbf{A_c}$.

Then, for $t=0:\Delta t_{el}:t_{end}$, do the following steps.

1. Perform the first step of the Godunov splitting or semi-implicit method in all electrical mesh nodes, i.e. solve the systems of the ionic concentrations **c** and gating variables **w** and, in case of the former technique, the equation in terms of the transmembrane potential V without the diffusive term too.
2. If $t=i*\Delta t_{mec}$ with i=1,2,3…, then do the following steps.
   2.1. Select the values of the intracellular calcium concentration $[Ca^{2+}]_i$ belonging to those electrical mesh nodes that coincide with the mechanical ones.
   2.2. Apply the Newton-Raphson algorithm till when the error $err=\left\|\mathbf{F_{mec}}(\mathbf{x}^k)\right\|$ (computed from the mechanical mesh nodes where a Dirichlet boundary condition is not assigned) is lower than a tolerance value toll or the number of iterations k is equal to a maximum value k_{max}.

2.2.1. Solve the active tension generation system with $[Ca^{2+}]_i$, the stretch $\lambda(\mathbf{x}^k)$, and stretch rate $d\lambda/dt(\mathbf{x}^k)$ as its inputs in order to compute $\mathbf{a}^{k+1}$ and $T_a^{k+1}(\mathbf{x}^k)$.

2.2.2. Solve again the active tension generation system with the same inputs as before but with $\lambda(\mathbf{x}^k)$ and $d\lambda/dt(\mathbf{x}^k)$ raised by a small $\Delta\lambda=10^{-8}$ in order to compute $T_{a,incr}^{k+1}(\mathbf{x}^k)$.

2.2.3. Compute $dT_a(\mathbf{x}^k)/d\lambda=(T_{a,incr}^{k+1}(\mathbf{x}^k)-T_a^{k+1}(\mathbf{x}^k))/\Delta\lambda$.

2.2.4. Evaluate $\mathbf{F_{mec}}(\mathbf{x}^k)$ by computing $\mathbf{S}(\mathbf{x}^k)$ with $T_a^{k+1}(\mathbf{x}^k)$ as input.

2.2.5. Evaluate $\mathbf{J_{mec}}(\mathbf{x}^k)$ by computing $\mathbf{S}(\mathbf{x}^k)$ and $\partial\mathbf{S}(\mathbf{x}^k)/\partial\mathbf{x}^k$ with $T_a^{k+1}(\mathbf{x}^k)$ and $dT_a(\mathbf{x}^k)/d\lambda$ as inputs.

2.2.6. Compute the variation of coordinates $\Delta\mathbf{x}^k$ by solving the linearized system (2.120) for all nodes without a Dirichlet boundary condition.

2.2.7. Update coordinates $\mathbf{x}^{k+1}=\mathbf{x}^k+\Delta\mathbf{x}^k$.

2.2.8. Compute the new values $\lambda(\mathbf{x}^{k+1})$ and $d\lambda(\mathbf{x}^{k+1})/dt=(\lambda(\mathbf{x}^{k+1})-\lambda(\mathbf{x}))/\Delta t_{mec}$ with $\lambda(\mathbf{x})$ equal to the stretch at time $t^{n_{mec}}$.

2.3. Linearly interpolate the new values of $\mathbf{x}$, $T_a(\mathbf{x})$ and $\lambda(\mathbf{x})$ in all mechanical mesh nodes to get the corresponding ones in all electrical mesh nodes.

2.4. Assemble the new matrixes $\mathbf{M}$, $\mathbf{A}$ and $\mathbf{A_c}$.

3. Compute the new values for the transmembrane potential V in all electrical mesh nodes by performing the second step of the Godunov splitting or semi-implicit method.

Therefore, the cell component of active tension generation has not been solved together with the plasma membrane model. This latter feature is peculiar to the so-called fixed method (see, e.g., [120,155,200]), according to which the new computed value for the active tension T_a keeps constant during the resolution of the mechanical deformation by the Newton-Raphson algorithm. In this thesis, an update approach [158] is followed instead, thus the new value of active tension must be continuously updated during each iteration of the previous algorithm by solving a differential-algebraic equation together with the stretch λ and the stretch rate $d\lambda/dt$. Actually, it has been proved that the dependence of the active tension on the stretch and stretch rate makes the algorithm more unstable if its value is kept fixed. A predictor-corrector splitting between the differential electrical component and the algebraic mechanical one cannot be done, i.e. the electrical and mechanical problems cannot be solved sequentially and separated from each other, but the electromechanical coupling carried out by the active tension must be treated in a strong way. This means that the non-linear system deriving from the discretization of the quasi-static elastic model must be solved implicitly by the Newton-Raphson algorithm,

involving both the passive tensor and the active one (with the jacobian matrix $\mathbf{J_{mec}}$ computed analytically for the passive component and approximately for the active one).

Chapter 3

Simulations on an eccentric hypertrophic fiber

In this chapter, the finite-element strongly-coupled electromechanical model introduced in Chapter 2 is applied to a one-dimensional myocardial ventricular fiber affected from eccentric hypertrophy that undertakes different types of contraction according to well-known protocols. First, the three-dimensional model including tissue growth is properly reduced to the one-dimensional case. Then, the typical isometric, afterloaded isotonic and quick-release tests that are made *in vitro* on cardiac muscles are run *in silico*. This is done to investigate the influence of the geometric feedbacks, i.e. the conductivity and convection ones, and of the mechanoelectric feedback due to stretch-activated channels on the electrical current flow model written in the reference configuration and to study the electrical and mechanical responses of that fiber. Since there are no experimental studies run on eccentric hypertrophic fibers in the literature, the simulation results reported in this chapter turn out to be innovative in predicting their electromechanical behavior.

3.1. Introduction

As it has been recalled in Section 1.3, eccentric hypertrophy may be a heart response to a chronic volume overload caused by different factors, such as mitral regurgitation. This yields a dilation of ventricles with a negligible wall thinning. Actually, the high diastolic wall strains developing in such an environment lead to the serial deposition of new sarcomere units inside cells without significant changes in their cross-sectional area. Eccentric hypertrophy may also be the phenotype deriving from genetic mutations that affect the correct encoding of some cytoskeletal proteins.

In the literature, there are a few recent studies dealing with the mathematical modeling of eccentric hypertrophy in the whole heart (e.g., [15,66,67,121,136]). However, they have mainly focused on the mechanical activity of hypertrophic hearts, disregarding the coupling with a model of bioelectrical activity, except from [15,136]. The latter ones do not take into account any mechanical feedback though.

The focus of this chapter, instead, is the cardiac elementary anatomical structure, i.e. the fiber, whose contraction and relaxation processes are associated with the pumping function of the heart. In the literature, many models referring to the electromechanics of ventricular fibers have been proposed. They have been either lumped parameter models, like the ones derived from the original Hill three-element model of skeletal muscle (e.g., [113,114,130,161,217]), or continuous electromechanical models for one- or three-dimensional fibers (e.g., [158,223]), which have only focused on free-loaded or isometric contractions. However, experimental studies with *in vivo* ventricular myocardium fibers have never been performed, whereas there exist many *in vitro* and involving papillary muscles (Paragraph 1.1.1) due to their tendon ends (like the ones of skeletal muscles) that help their fixing on a measurement apparatus [147]. Since they are made up with the same cardiomyocytes [56] and they have the same long and thin shape, papillary muscles are traditionally taken as a model of ventricular fibers [21,44,46,75,111,147,148,161,203]. Therefore, various experimental protocols have been proposed and applied on papillary muscles in the literature to replicate the *in vivo* behavior of the myocardium (e.g., [13,21,23,24,44,46,57,75,111,122,147,148,161,203]). In doing so, for instance, researchers have often proved the existence of the Frank-Starling law of the heart (Paragraph 1.1.3).

The novelty of this chapter is the development of a finite-element strongly-coupled electromechanical model that is able to investigate both the electrical and mechanical activities of eccentric hypertrophic ventricular fibers. Three classical *in vitro* protocols, i.e. the isometric, afterloaded isotonic and quick-release ones, which are known to reproduce the different types of contraction and relaxation during the four phases of a cardiac cycle (the isovolumic systole, the blood efflux, the isovolumic diastole and the diastolic filling) are implemented. The whole model consists of a zero-dimensional cardiomyocyte model of bioelectrical activity, calcium dynamics and active tension generation and a one-dimensional mechanical model of finite elasticity coupled with the Monodomain reaction-diffusion equation written in the current fiber configuration and describing the electrical current flow. As it is discussed in Paragraph 2.3.2, in a Lagrangian framework, the corresponding Monodomain equation written in the reference configuration includes two types of geometric feedback: the conductivity feedback, i.e. the influence of the deformation gradient on the conductivity tensor, and the convection feedback, by introducing a dependence on the deformation rate. Moreover, the mechanoelectric feedback represented by the influence of stretch-activated membrane channels on the ionic current is taken into account. In

the literature, there are already several studies on the impact of mechanical feedbacks on the bioelectrical activity under physiological and pathological conditions (e.g., [38,39,112,114,116,117,130,150,154,167,168,217,222]). However, no previous works have investigated the effects of all previous mechanical influences in case of both healthy and eccentric hypertrophic fibers. Therefore, this is the first problem faced in this chapter by considering isometric contractions. Then, the remainder of this chapter aims at studying the electromechanical behavior of fibers contracting under not only isometric but also afterloaded isotonic and quick-release conditions, by employing some classical measures and curves found in the literature of *in vitro* and *in silico* studies. For the first time, hypertrophic alterations are added both at the level of a single cardiomyocyte and at the level of the entire fiber and for both electrical and mechanical activities. Moreover, the effects of the mechanical feedback induced by a finite growth and of the changes in cardiomyocyte size on the propagation of the electrical signal are considered.

3.2. Methods

The adopted full cell model includes the bioelectrical activity and calcium dynamics model by Faber-Rudy [53] for the guinea-pig and the active tension generation model by Land [133] for the mouse. Despite the different species, the Land model is already calibrated at the same physiological temperature of 37°C of the Faber-Rudy model and it is able to catch the fast relaxation kinetics at that temperature, so its parameters are not modified. Then, this cell model is coupled with a quasi-static finite elasticity model and a Monodomain model.

3.2.1. The mechanical model: implementation of eccentric growth and one-dimensional reformulation

In a three-dimensional framework, to characterize eccentric hypertrophy, the general equation (2.103) for $\mathbf{F}^{\mathbf{g}}$ is simplified as in [15,66,67,136] to represent the cardiomyocytes elongation due to the serial deposition of new sarcomeres, i.e.

$$\mathbf{F}^{\mathbf{g}}=\mathbf{I}+(\theta_f-1)\widehat{\mathbf{a}_\mathbf{f}}\otimes\widehat{\mathbf{a}_\mathbf{f}}, \tag{3.1}$$

where $\widehat{\mathbf{a}_\mathbf{f}}$ is the unit vector for the local fiber direction in the reference configuration Ω_0 and θ_f is the growth parameter along the fiber, which depends on time and space varying typically between 1 and 2 in those computational studies dealing with eccentric hypertrophy in a ventricular model.

Then, in this chapter, for W the orthotropic law proposed in [83] is adopted. For a transverse isotropic structure like the fiber, it simplifies into

$$W=\frac{a}{2b}e^{b(I_1^e-3)}+\frac{a_1}{2b_1}(e^{b_f(I_{4f}^e-1)^2}-1)+\frac{a_s}{2b_s}(e^{b_s(I_{4s}^e-1)^2}-1), \tag{3.2}$$

where a, b, a_f, b_f, a_s and b_s are fixed parameters taken from [220], which fitted the experimental data from [48] about the passive properties of the porcine myocardium, whilst $I_1^e=\mathbf{C}^e:\mathbf{I}$, $I_{4f}^e=\widehat{\mathbf{a}_f}^T\mathbf{C}^e\widehat{\mathbf{a}_f}$ and $I_{4s}^e=\widehat{\mathbf{a}_s}^T\mathbf{C}^e\widehat{\mathbf{a}_s}$ are the elastic invariants [15,82] ($\widehat{\mathbf{a}_s}$ is the unit vector for the local sheet direction that is orthogonal to $\widehat{\mathbf{a}_f}$ in the reference configuration).

Following [170,223], the cardiac domain is assumed to be composed of fibers parallel to $\mathbf{X_1}=(1,0,0)^T$, hence $\widehat{\mathbf{a}_f}=(1,0,0)^T$ and $\widehat{\mathbf{a}_s}=(0,0,1)^T$. Thus, the analytical expression of $\mathbf{S^{e,act}}$ simplifies into

$$\mathbf{S}^{\mathbf{e,act}}=\frac{T_a}{C_{11}^e}\mathbf{X_1}\mathbf{X_1}^T \qquad S_{MN}^{e,act}=\frac{T_a}{C_{11}^e}\delta_{M1}\delta_{N1}, \tag{3.3}$$

where M,N=1,2,3 and δ_{ij} are the Kronecker symbols. Then, since the behavior of a single fiber must be modeled, it is assumed that $x_i(\mathbf{X},t)=x_i(X_i,t)$ for i=1,2,3 in order to reduce (3.2) to the one-dimensional case keeping into account the three-dimensional properties of the fiber; such a procedure is suggested in [223], whilst another one is proposed in [29]. In this case, $\mathbf{F^e}$, $\mathbf{C^e}$, $\mathbf{E^e}$ and $\mathbf{S^e}$ become diagonal tensors. In particular, considering only $\mathbf{S^{e,pas}}$, it can be written as

$$S_{MM}^{e,pas}=\frac{\partial W}{\partial E_{MM}^e}-\frac{p}{2E_{MM}^e+1}, \qquad S_{MN}^{e,pas}=0 \quad \text{if} \quad M\neq N. \tag{3.4}$$

If the traction exerted by the load acts only in the direction of the fiber, then $S_{22}^{e,pas}=S_{33}^{e,pas}=0$. Considering that soft tissues (like the fiber in this chapter) may be characterized by relevant volume changes during growth, the incompressibility constraint (2.33) is set only on the elastic part of the deformation [175], i.e. $J^e=\det(\mathbf{F^e})=1$, which, in terms of E_{MM}^e, is written as

$$(2E_{11}^e+1)(2E_{22}^e+1)(2E_{33}^e+1)=1. \tag{3.5}$$

At last, an equation for $S_{11}^{e,pas}$ as a function of E_{11}^e is written following the procedure suggested in [223],

$$S_{11}^{e,pas}=\frac{\partial W}{\partial E_{11}^e}-\frac{p}{2E_{11}^e+1}=ae^{b(I_1^e-3)}+2a_fe^{b_f(I_{4f}^e-1)^2}(I_{4f}^e-1)-\frac{p}{2E_{11}^e+1}. \tag{3.6}$$

In particular, while deriving the expression for p in (3.6), E^e_{22} is taken equal to E^e_{33} because the fiber is a transversely isotropic structure.

Since a one-dimensional framework is used in the remainder of this chapter, the following identities hold

$$\begin{aligned} &X=X_1, \quad x=x_1, \quad x(X,t):\Omega_0=[0,L_0]\rightarrow\Omega(t)=[0,L(t)],\\ &F=F_{11}, \quad C=C_{11}, \quad E=E_{11}, \quad S=S^{act}_{11}+S^{pas}_{11} \end{aligned} \tag{3.7}$$

and

$$F^e=F^e_{11}, \quad F^g=F^g_{11}, \quad C^e=C^e_{11}, \quad E^e=E^e_{11}, \quad S^e=S^{e,act}_{11}+S^{e,pas}_{11}, \tag{3.8}$$

where

$$S^{e,act}_{11}=\frac{T_a}{C^e_{11}}. \tag{3.9}$$

After computing the elastic part S^e, the total S can be derived as

$$S=S^e\frac{1}{\theta_f}, \tag{3.10}$$

which is the simplified one-dimensional form of the corresponding three-dimensional pull-back equation (2.102).

Then, the scalar S enters the quasi-static equilibrium condition written in Ω_0 for the one-dimensional fiber

$$\frac{d(FS)}{dX}=0, \tag{3.11}$$

which is closed by suitable boundary conditions described later.

At last, the active tension T_a in (3.9) is computed through the model by Land (2.97), where $[Ca^{2+}]_i$ is the intracellular calcium concentration from the bioelectrical activity and calcium dynamics model by Faber-Rudy and λ^e is given by

$$\lambda^e=\sqrt{C^e_{11}}=F^e_{11}. \tag{3.12}$$

3.2.2. The electrophysiological model: one-dimensional reformulation and dependence on eccentric growth

The Monodomain model coupled with the Faber-Rudy one is adopted for electrophysiology in this chapter. Taking into account the incompressibility

constraint $J^e=\det(\mathbf{F}^e)=1$, it follows that $J=\det(\mathbf{F})=J^eJ^g=\theta_f$. By assuming homogeneous electrical properties across the fiber too, the full three-dimensional electrophysiological model in the reference configuration Ω_0 (2.88) can be reduced to

$$\begin{cases} c_m\left(\frac{\partial V}{\partial t}-\frac{1}{F}\frac{\partial V}{\partial X}\frac{\partial x}{\partial t}\right)-\frac{1}{\theta_f}\frac{\partial}{\partial X}\left(\theta_f\frac{\sigma_f}{F^2}\frac{\partial V}{\partial X}\right)+i_{ion}(V,\mathbf{w},\mathbf{c})+i_{SAC}(V,\mathbf{c},\lambda^e)=i_{app}^m & \text{in } \Omega_0\times(0,T) \\ \frac{\partial \mathbf{w}}{\partial t}-\mathbf{R}(v,\mathbf{w})=0 & \text{in } \Omega\times(0,T) \\ \frac{\partial \mathbf{c}}{\partial t}-\mathbf{S}(v,\mathbf{w},\mathbf{c})=0 & \text{in } \Omega\times(0,T) \\ \frac{\partial V}{\partial X}=0 & \text{on } \partial\Omega_0\times(0,T) \\ V(X,0)=V_0(X) & \text{in } \Omega_0,\ \mathbf{w}(x,0)=\mathbf{w}_0(x),\ \mathbf{c}(x,0)=\mathbf{c}_0(x) \text{ in } \Omega \end{cases} \tag{3.13}$$

where $\mathbf{w}$ and $\mathbf{c}$ contain the gating variables and ionic concentrations belonging to the Faber-Rudy model and c_m is the membrane capacitance, σ_f the fiber electrical conductivity coefficient, i_{ion} the total ionic current, i_{SAC} the stretch-activated channels current (where the dependence on λ is replaced by the one on λ^e) and i_{app}^m the applied current stimulus all expressed per unit length of the undeformed fiber.

The conductivity coefficient σ_f in (3.13) is written as (Paragraph 2.3.2)

$$\sigma_f=\frac{\sigma_f^i\sigma_f^e}{\sigma_f^i+\sigma_f^e}, \tag{3.14}$$

where σ_f^e is the extracellular conductivity with a conservative value of 2 mS/cm (e.g., [36]), whilst σ_f^i is the intracellular one computed as [76,183]

$$\sigma_f^i=\frac{1}{r_{cyt}+\frac{r_{junct}}{L_{cell}}}, \tag{3.15}$$

where r_{cyt} and r_{junct} are the cytoplasmic and gap junction resistivities and $L_{cell}=\theta_f L_{cell,healthy}$ is the cardiomyocytes length (with $L_{cell,healthy}$ the length value from the original Faber-Rudy membrane model, i.e. 0.01 cm). The values $r_{cyt}=150\ \Omega\cdot$cm and $r_{junct}=1.5\ \Omega\cdot$cm^2 from [198] are used to obtain a value of 3 mS/cm for σ_f^i [36] if $\theta_f=1$, which, together with the conservative one chosen for c_m (1 μF/cm), ensures a conduction velocity between 0.06 and 0.07 cm/ms in case of the healthy fiber. Moreover, the same variable L_{cell} is computed as before when solving the Faber-Rudy membrane model related to the single cardiomyocyte; this, in turn, affects the geometric

plasma membrane area $A_{geo}=2\pi R_{cell}^2+2\pi R_{cell}L_{cell}$ (where R_{cell} is the cardiomyocytes radius, i.e. 0.0011 cm), the capacitive one $A_{cap}=2A_{geo}$ and the cell volume $V_{cell}=\pi R_{cell}^2 L_{cell}$.

As in Paragraph 2.3.2, the second term in the first equation of (3.13) contains a convective term depending on F and on the fiber deformation rate $\partial x/\partial t$, whereas the third term is only dependent on F; these two geometric feedbacks are the convection and conductivity ones respectively. Moreover, the membrane current i_{SAC}, depending on the elastic stretch λ^e, points out the addition of stretch-activated channels to the original Faber-Rudy model, which define the mechanoelectric feedback acting only when $\lambda^e>1$.

3.2.3. Details on the discretization and implementation of the complete model

A uniform mesh of 100 linear finite elements (defining a spacing $\Delta h_{el}=0.1$ mm) and a constant time step $\Delta t_{el}=0.05$ ms are used for the electrical components, whereas 50 linear finite elements (defining a spacing $\Delta h_{mec}=0.2$ mm) and a constant time step $\Delta t_{mec}=1$ ms (if not otherwise specified) are used for the mechanical ones. Moreover, a Godunov splitting is employed to perform the time discretization of the model.

Simulations are run in Matlab®.

3.2.4. The geometry, growth and electrical stimulation of the fiber

The reference fiber is a one-dimensional rod with a uniform cross-section and a reference length L_0 of 1 cm (Figure 3.1, panel A). Its initial length changes according to the type of fiber, i.e. it is equal to 1 cm for the healthy fiber and about 1.95 cm for the hypertrophic one, which is obtained at the end of five beats by following the two experimentally validated assumptions recalled in [136]. The first one is that an appreciable growth can be detected only after many heartbeats. Thus, its timing is slower than the contraction-relaxation processes characterizing a single cardiac cycle and the growth tensor $\mathbf{F^g}$ can be considered a time constant during this cycle. The second one is that the mechanical stimuli inducing growth span over an entire cycle rather than limiting to specific phases, hence the cardiomyocytes response is affected from the overall time-varying stress or strain signals (for instance, in terms of their means or maximum values). No cardiac cycle phases are implemented at the level of the fiber for simplicity. For each beat, the fiber is first stretched at its right end by a load equal to 6 kPa, which should simulate the rise in ventricular end-diastolic pressure from a healthy value of 2 kPa due to an increase of atrial pressure during mitral regurgitation. Then, it is excited for 1 ms by a

current stimulus i_{app}^{m} of 250 mA/cm towards its left end (that is always fixed) in order to contract and relax without modifying its length. At last, at the end of the beat, the fiber can grow. In the literature, there are two approaches for updating tissue growth, i.e. the fixed reference configuration method or the updated reference configuration one (see [126] for a comparison between them). In this chapter, the former one is adopted. Thus, first, after the fiber unloading, the local increments for θ_f between the beats n and n+1, i.e. $\theta_{f,*}$, are computed by

$$\theta_{f,*}=1+k(\theta_{f,n})(\overline{\lambda_n^e}-\overline{\lambda_h^e}). \tag{3.16}$$

Here, k is a rate-limiting function with the expression

$$k=\frac{1}{\tau}\left(\frac{\theta_f^{max}-\theta_{f,n}}{\theta_f^{max}-1}\right)^{\gamma}, \tag{3.17}$$

where τ and γ are the sarcomere deposition time and non-linearity (with values 0.2 and 1 respectively) and θ_f^{max} is the maximum limit for θ_f (with a value of 4 to increase growth). The growth criterion $\overline{\lambda_n^e}-\overline{\lambda_h^e}$, instead, is given by the deviation of the local time-averaged elastic stretch during the beat n from the local time-averaged homeostatic set point value dictated by a healthy simulation with a preload equal to 2 kPa. Then, the new local values for θ_f at the beat n+1, i.e. $\theta_{f,n+1}$, are computed from the product of $\theta_{f,*}$ with $\theta_{f,n}$, which represents the cumulative growth of all previous beats up to the beat n. At last, the new unloaded growth configuration for the fiber is found by solving the equilibrium equation (3.11) with $\theta_{f,n+1}$ as input.

Panel B of Figure 3.1 displays the resultant spatial distribution of θ_f at the end of the fifth beat on the reference configuration. The resultant inhomogeneity of such a distribution mainly derives from the isometric beat performed before triggering growth, which has been found to enhance differences in local growth better than an isotonic one with a constant applied load. Due to the fact that both fiber ends are fixed, a more inhomogeneous distribution of $\overline{\lambda_n^e}$ values (driving fiber growth) comes out. The nodes closer to the left end, which are the first activated ones, contract to a lesser extent, hence they show more positive $\overline{\lambda_n^e}$ values, whilst the ones closer to the right end, which are activated later, contract to a higher extent, thus they exhibit less positive $\overline{\lambda_n^e}$ values. Actually, the former nodes develop a lower value of active tension T_a due to the lower values of λ_n^e before their contraction compared with the latter nodes, which develop a higher value of T_a because the λ_n^e values are raised by the preceding contraction of the leftmost nodes.

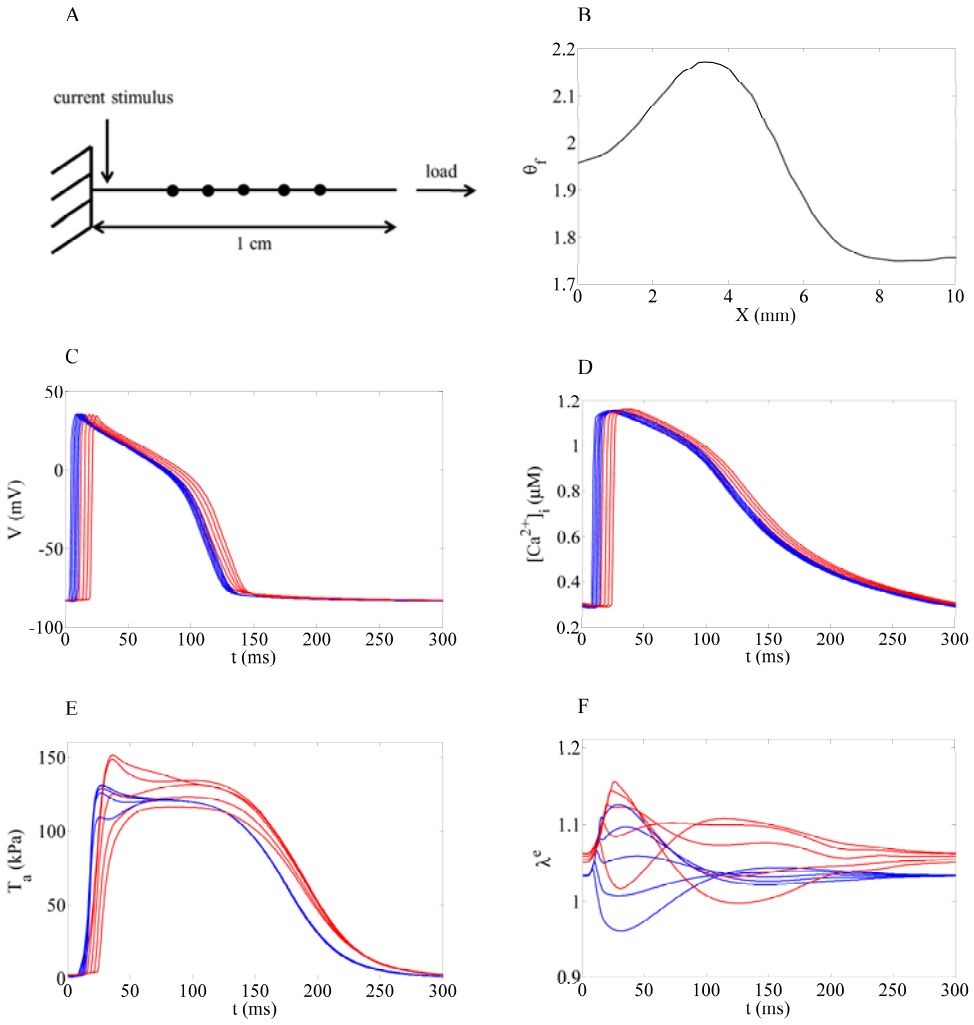

Figure 3.1: A) reference configuration between 0 and 1 cm for the healthy and hypertrophic fibers. The left end is always kept fixed, whilst the right one can be subjected to a load. The current stimulus is given at the left end. B) spatial distribution of the growth parameter θ_f shown in the reference configuration (see text for details on its derivation). C-F) time evolutions of the transmembrane potential V (C), intracellular calcium concentration $[Ca^{2+}]_i$ (D), active tension T_a (E) and elastic stretch λ^e (F), all referring to five equally-spaced nodes (denoted by dots and selected at 3, 4, 5, 6 and 7 mm from the left end in A)) during an isometric simulation with a preload equal to 4 kPa and involving the healthy (blue) or hypertrophic (red) fiber.

Even for the protocols applied in the remainder of this chapter, the current stimulus is delivered to the left end and then propagates towards the right end in order to better simulate the *in vivo* propagation of current stimuli along fibers. This aspect is visible in panels C-F of Figure 3.1, which represent the time evolutions of the transmembrane potential V, intracellular calcium concentration $[Ca^{2+}]_i$, active tension T_a and elastic stretch λ^e in five equally-spaced nodes along the healthy and hypertrophic fibers (denoted by dots and chosen at 3, 4, 5, 6 and 7 mm from the left end in panel A) in case of isometric simulations with a preload equal to 4 kPa.

Actually, with this point stimulation protocol, an action potential propagating wavefront along the fiber is generated, unlike the usual *in vitro* experiments, where the entire fiber is stimulated simultaneously.

3.2.5. The implemented tests

In this chapter, three types of tests are implemented: isometric tests, afterloaded isotonic tests and quick-release tests.

At the beginning of all protocols, a specific preload is applied to the right end of the fiber to stretch it passively; a preload is so called because it is applied to the muscle prior to its contraction [203]. Then, the fiber is fixed at the right end and five isometric beats are run to reach a steady state for that preload. The final values for nodal stretches, coordinates and all Faber-Rudy-Land model variables are saved and represent the initial conditions for all tests made later. The stretch rate is set to zero for all nodes because the fiber stops after its stretching.

For the isometric tests, only another isometric twitch is run. This kind of test is useful to characterize *in vitro* the passive and active responses of a muscle due to changes in its length (e.g., [75,111,203]). Moreover, it is usually employed *in silico* to analyze the electrical response of fibers (e.g., [114,130,217]).

The afterloaded isotonic tests, instead, consider a muscle that, after being stretched by a preload, contracts against a variable afterload (e.g., [23,75,161,203]). To implement these tests, the right end is automatically fixed solely as long as the fiber does not contract. Thus, an initial isometric contraction phase occurs before becoming purely isotonic as soon as the developed tension (i.e. the reaction at the left end of the fiber) equals the applied load. In experimental studies, this load is the sum of the previous preload and another externally applied afterload, which is so called because it is sensed after the onset of fiber contraction [203]. However, the *in silico* protocol proposed in this chapter automatically sets a unique afterload, which virtually includes the preload and the afterload, by the following procedure. First, an isometric twitch is run after the preloading phase. Then, the range between the maximum and the minimum values of the developed tension is equally divided in ten parts, obtaining a constant increment step. At last, starting from the minimum value, the afterload is raised by this constant step in an iterative way, resulting in many isotonic tests that start from the same initial conditions assigned to the isometric twitch. When the afterload is too heavy, i.e. it is equal to the maximum value of the developed tension, then the last isotonic test becomes totally isometric. A simulation with a zero afterload is run for each preload too.

The quick-release tests are similar to the afterloaded isotonic ones apart from the fact that the transition from the isometric contraction to the isotonic one is externally enforced by removing the stop that fixes the free end of a muscle at a certain time (e.g., [23,161]). They have been developed to overcome the problem of a not equal level of muscle

activation when isotonic contractions start during the afterloaded isotonic tests. For the simulations reported in this chapter, the fiber is allowed to contract isotonically only when it develops the maximum tension due to a specific initial length; thus, the initial isometric contraction is prolonged to elicit at the same time all subsequent isotonic contractions for different afterloads. A simulation with a zero afterload is eventually performed again.

3.3. Results and discussion

3.3.1. The electrical response

The electrical responses of healthy and hypertrophic fibers are compared by means of isometric tests.

The first issue is the analysis of the relevance of the mechanical feedbacks in the Monodomain model of electrophysiology (3.13). For both healthy and hypertrophic fibers, the following simulations are run: i) a simulation with the conductivity feedback (COND); ii) a simulation with the conductivity and convection feedbacks (COND+CONV); iii) a simulation with the conductivity and mechanoelectric feedbacks (COND+SAC); iv) a simulation with all three feedbacks (COND+CONV+SAC). For these simulations, Δt_{mec} is chosen equal to Δt_{el} in order to improve the accuracy of results.

Figure 3.2 and Figure 3.3 report the resulting spatial distributions (shown in the reference configuration) of the activation time AT, repolarization time RT, corresponding action potential duration APD=RT-AT and propagation (or conduction) velocity v_{prop} for the healthy and hypertrophic fibers respectively under all simulated conditions. In this chapter, AT is defined as the time instant when V exceeds the threshold value of -40 mV, RT is defined as the time instant when V becomes less than its 90% repolarization value of -76.5 mV and v_{prop} is computed as the ratio of the coordinate of each node at the moment of its electrical activation to its activation time. From a visual inspection, it appears that the AT of the healthy fiber is not affected at all. A maximum discrepancy of only 2 ms is present at the right end of the hypertrophic fiber instead. As regards both RT and APD, a systematic but slight difference is found along the entire healthy fiber between the COND or COND+CONV case and the COND+SAC or COND+CONV+SAC one. A similar difference is detected for APD only in case of the hypertrophic fiber. By computing dispersions as the differences between the maximum and minimum values in Figure 3.2 and Figure 3.3, Table 3.1 shows that negligible differences among the four cases characterize AT, RT and APD for both fibers; actually, they are lower than 2 ms in case of the healthy fiber and lower than or equal to 3 ms in case of the hypertrophic one. Moreover, from Figure 3.2 and Figure 3.3

again, v_{prop} for both fibers turns out not to be strongly affected from mechanical feedbacks.

Table 3.2 reports the relative errors computed for AT, RT and APD between the COND+CONV+SAC case (that represents the most complete model) and the other ones. For both fibers, the convection feedback determines the smallest error on AT, whilst the mechanoelectric feedback has the same effect on RT and APD. Therefore, the convection feedback tends to prevail during the activation phase, so does the mechanoelectric one during the repolarization phase. However, although errors get higher with the hypertrophic fiber, they remain too small to be evident.

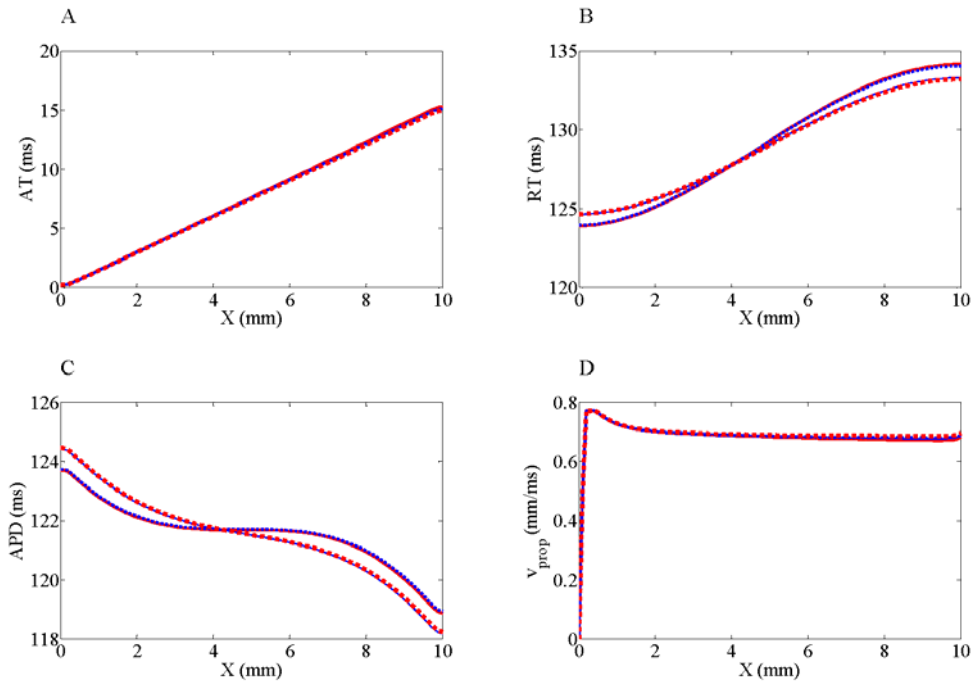

Figure 3.2: Spatial distributions of electrical variables shown in the reference configuration in case of isometric simulations with a preload equal to 4 kPa and involving the healthy fiber: activation time AT (A), repolarization time RT (B), action potential duration APD (C) and propagation velocity v_{prop} (D). The different curves belong to a simulation with the conductivity feedback alone (red, continuous) or together with the convection feedback (blue, dotted), the mechanoelectric feedback (blue, continuous) or both of them (red, dotted).

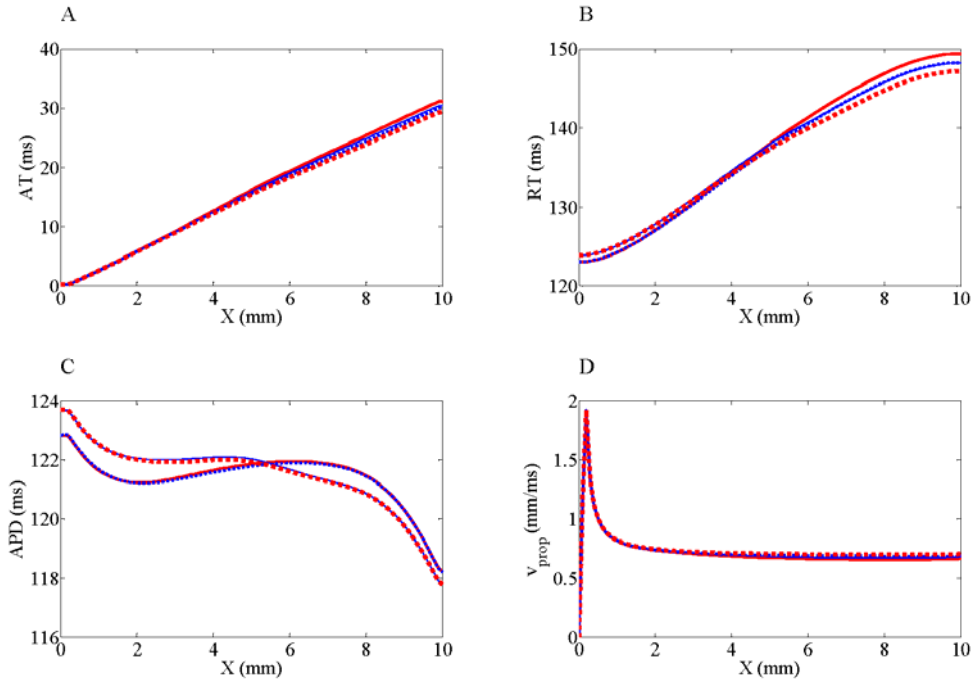

Figure 3.3: Spatial distributions of electrical variables shown in the reference configuration in case of isometric simulations with a preload equal to 4 kPa and involving the hypertrophic fiber. Same format as in Figure 3.2.

Table 3.1: Dispersions (differences between the maximum and minimum values) in ms of the activation time AT, repolarization time RT and action potential duration APD in case of isometric simulations with a preload equal to 4 kPa and involving the healthy (A) or hypertrophic (B) fiber. Simulations may include the conductivity feedback alone (COND) or together with the convection feedback (COND+CONV), the mechanoelectric feedback (COND+SAC) or both of them (COND+CONV+SAC).

A

	HEALTHY			
	COND	COND+CONV	COND+SAC	COND+CONV+SAC
AT dispersion	15.06	14.88	14.92	14.75
RT dispersion	10.22	10.09	8.66	8.53
APD dispersion	4.84	4.80	6.26	6.22

B

	HYPERTROPHIC			
	COND	COND+CONV	COND+SAC	COND+CONV+SAC
AT dispersion	30.99	29.86	30.26	29.20
RT dispersion	26.39	25.22	24.38	23.29
APD dispersion	4.62	4.66	5.89	5.92

Table 3.2: Relative errors of the activation time AT, repolarization time RT and action potential duration APD in case of isometric simulations with a preload equal to 4 kPa and involving the healthy (A) or hypertrophic (B) fiber. All errors are computed with respect to the associated reference variable belonging to a simulation with all mechanical feedbacks, i.e. the conductivity, convection and mechanoelectric ones. The symbol * denotes a simulation disregarding the convection and mechanoelectric feedbacks (COND), the sole mechanoelectric feedback (COND+CONV) or the sole convection feedback (COND+SAC).

A

	HEALTHY		
	* = COND	* = COND+CONV	* = COND+SAC
$\|\|AT_*-AT_{REF}\|\|_2/\|\|AT_{REF}\|\|_2$	$1.73\cdot10^{-2}$	$7.90\cdot10^{-3}$	$9.37\cdot10^{-3}$
$\|\|RT_*-RT_{REF}\|\|_2/\|\|RT_{REF}\|\|_2$	$4.81\cdot10^{-3}$	$4.41\cdot10^{-3}$	$4.14\cdot10^{-4}$
$\|\|APD_*-APD_{REF}\|\|_2/\|\|APD_{REF}\|\|_2$	$4.16\cdot10^{-3}$	$4.26\cdot10^{-3}$	$2.85\cdot10^{-4}$

B

	HYPERTROPHIC		
	* = COND	* = COND+CONV	* = COND+SAC
$\|\|AT_*-AT_{REF}\|\|_2/\|\|AT_{REF}\|\|_2$	$5.88\cdot10^{-2}$	$1.91\cdot10^{-2}$	$3.77\cdot10^{-2}$
$\|\|RT_*-RT_{REF}\|\|_2/\|\|RT_{REF}\|\|_2$	$1.03\cdot10^{-2}$	$5.70\cdot10^{-3}$	$5.00\cdot10^{-3}$
$\|\|APD_*-APD_{REF}\|\|_2/\|\|APD_{REF}\|\|_2$	$4.82\cdot10^{-3}$	$4.81\cdot10^{-3}$	$4.78\cdot10^{-4}$

In the remainder of this chapter, the effects of all feedbacks are always included. Therefore, to better compare the electrical responses of healthy and hypertrophic fibers, panels A and B of Figure 3.4 collect the spatial distributions of APD and v_{prop} for the COND+CONV+SAC case. From panel A, it turns out that the decreasing trend of APD for the hypertrophic fiber is less linear than the one for the healthy fiber, but the overall dispersion is not significantly affected. From panel B, hypertrophy does not alter v_{prop}. Moreover, panels C and D display the time evolutions of the transmembrane potential V in those nodes where the maximum and minimum values for the growth parameter θ_f are detected compared with the corresponding time evolutions of the healthy case. Similarly, panels A and B of Figure 3.6 show the same evolutions for the hypertrophic fiber (with different local values for θ_f) compared with the ones for the case with all local θ_f values equal to the mean of their distribution along the fiber (Figure 3.1, panel B). No significant differences in terms of APD are found in both figures again.

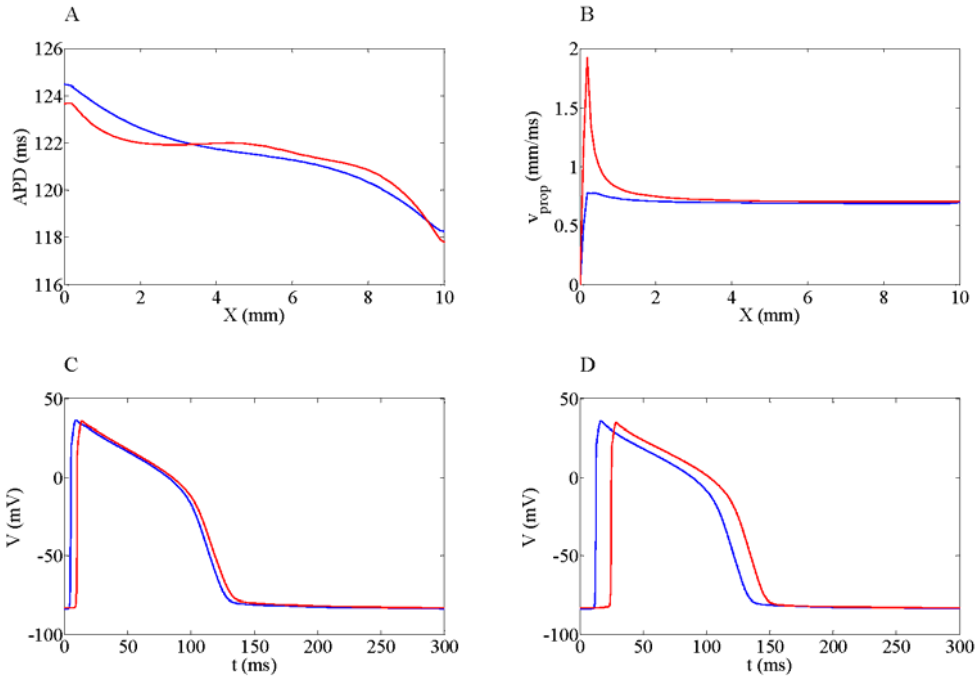

Figure 3.4: Electrical responses of the healthy (blue) and hypertrophic (red) fibers in case of isometric simulations with a preload equal to 4 kPa and all mechanical feedbacks. A-B) spatial distributions of the action potential duration APD (A) and propagation velocity v_{prop} (B) shown in the reference configuration. C-D) time evolutions of the transmembrane potential V in the nodes with the maximum (C) and minimum (D) values for θ_f in case of the hypertrophic fiber compared with the corresponding evolutions of the healthy case.

Therefore, the electrical results achieved by isometric tests suggest that eccentric hypertrophy does not raise the risk of inducing arrhythmogenic phenomena at the level of a single ventricular fiber, which are more likely to be fostered by a reduced propagation velocity and action potential duration instead (see, e.g., [36] for a discussion and a series of examples about reentry phenomena, which lie at the basis of arrhythmias, in the three-dimensional case of a slab or a ventricle).

3.3.2. The mechanical response

The mechanical responses of healthy and hypertrophic fibers are studied by means of isometric, afterloaded isotonic and quick-release tests.

As regards the isometric tests, panel A of Figure 3.5 shows the time evolutions of the tension T developed by the healthy and hypertrophic fibers at the left end after their electrical stimulation when the preload is varied (0, 1, 2, 3 or 4 kPa). The peak values of curves get higher and higher as the preload increases, but they decrease with hypertrophy. Panel B reports the length-tension relationships, where the tensions before and after

the electrical stimulation are represented as function of the increments in muscle length ΔL, caused by the applied preloads. The length-tension relationships are the corresponding curves at the fiber scale of the relationships at the ventricle scale between the end-diastolic volume and the stroke volume or the peak value of pressure developed during the isovolumic systole. Again, the peak value for the tension developed after the electrical stimulation T_{max} decreases owing to the pathology. This result suggests that, in a three-dimensional environment, eccentric hypertrophic ventricles may develop a lower pressure during their isovolumic systole. Moreover, if the same preload is taken into account in panel B, it appears that the hypertrophic fiber gets more stretched than the healthy one during the preloading phase according to panel F of Figure 3.1, where the values of λ^e are generally higher for the former fiber. This phenomenon is peculiar to cardiac fibers that are more likely to cause ventricular dilation during the diastolic filling, thus leading to a higher end-diastolic volume. Interestingly, both previous results are obtained without altering the mechanical parameters belonging to the strain energy function in (3.2). Moreover, for the hypertrophic fiber, the previous decrease in T_{max}, which includes both active and passive components, occurs while the active tension T_a in panel E of Figure 3.1 increases due to the higher values of λ^e. However, in panel B of Figure 3.5, for all fibers, a higher preload determines a higher peak of isometric tension (defining a positive slope), which proves the implementation of the Frank-Starling law in the adopted excitation-contraction model [133]. Then, similarly to APD, panels C and D of Figure 3.5 display the time evolutions of the elastic stretch λ^e where the maximum and minimum values for the growth parameter θ_f are found, comparing them with the healthy case. Moreover, panels C and D of Figure 3.6 display the same evolutions for the hypertrophic fiber (with different local values for θ_f) compared with the ones for the case with a constant θ_f equal to the mean value along the fiber. From both figures, it appears that, where θ_f is maximum (panel C), contraction is depressed. Conversely, where θ_f is minimum (panel D), contraction is enhanced. This proves that the more growth gets heterogeneous along the fiber the more the resulting mechanical response during the isovolumic systole of the cardiac cycle gets heterogeneous too.

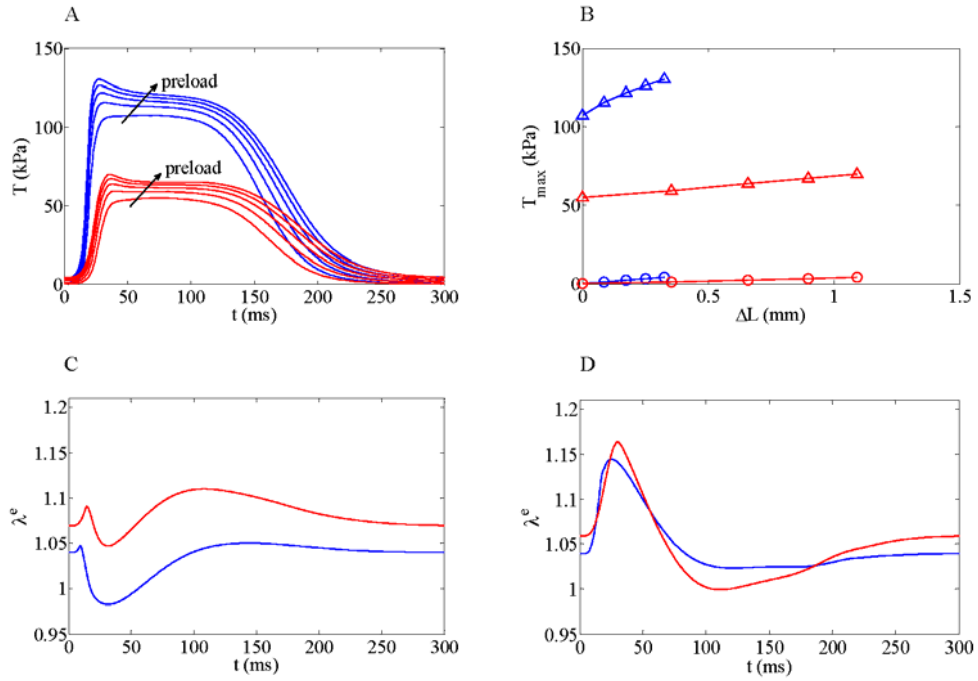

Figure 3.5: Mechanical responses of the healthy (blue) and hypertrophic (red) fibers in case of isometric simulations. A) time evolutions of the tension T developed by the two fibers after their electrical stimulation for increasing preloads (0, 1, 2, 3 or 4 kPa). B) corresponding length-tension relationships. ΔL on the abscissa is the increment in fiber length from the initial value according to the type of fiber, whereas T_{max} on the ordinate is the maximum value for the tensions developed before (circles) and after (triangles) the electrical stimulation. C-D) time evolutions of the elastic stretch λ^e in the nodes with the maximum (C) and minimum (D) values for θ_f in case of the hypertrophic fiber compared with the corresponding evolutions of the healthy case.

As a final remark, it has to be noted that a load (i.e. the preload) must be assigned as an input to the implemented isometric tests because only in this way a length change can be elicited during the computation of the mechanical deformation, whereas the *in vitro* isometric experiments can receive a length change as their input thanks to the attached lever, being able to give a tension as their output [57,111,203]. Despite this limitation, results are the same because a length-tension relationship is univocally determined.

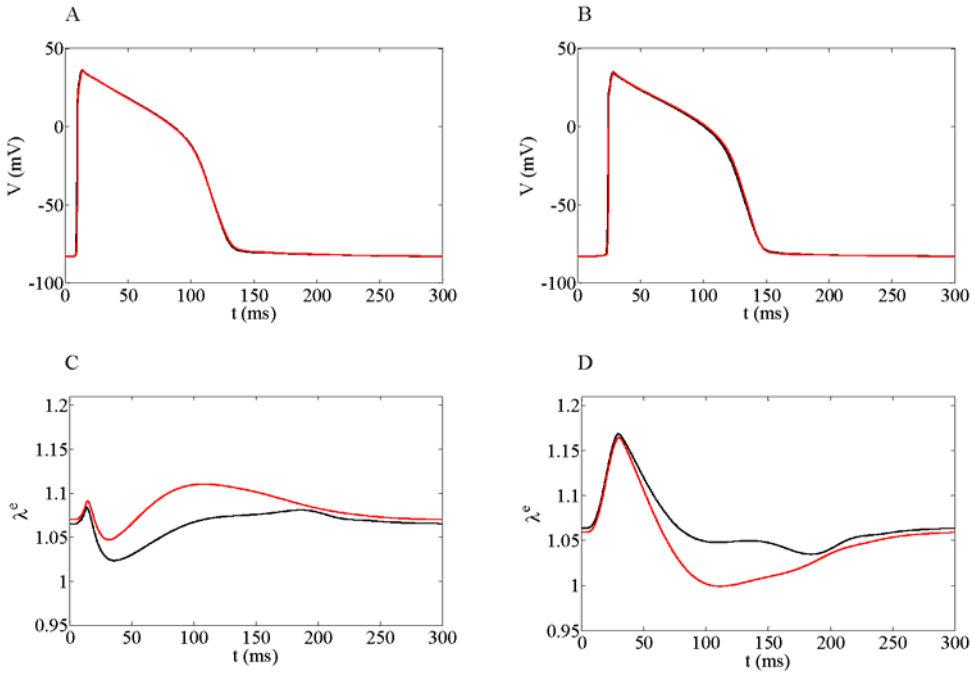

Figure 3.6: Time evolutions of electrical and mechanical variables in the nodes with the maximum (A-C) and minimum (B-D) values for θ_f in case of the hypertrophic fiber with an inhomogeneous growth (red) compared with the ones in the same nodes for the fiber with a homogeneous growth (black), i.e. with all local θ_f values equal to their mean along the fiber: A-B) transmembrane potential V; C-D) elastic stretch λ^e. These results belong to isometric simulations with a preload equal to 4 kPa and all mechanical feedbacks.

As far as the afterloaded isotonic and quick-release tests are concerned, panel A of Figure 3.7 illustrates an example of the time evolutions of the tension T developed by the two fibers during the afterloaded isotonic contractions with a preload equal to 4 kPa, whereas panel B depicts the corresponding time evolutions of the fiber length L. Panels A and B of Figure 3.8, instead, show the corresponding time evolutions during the quick-release contractions under the same preload.

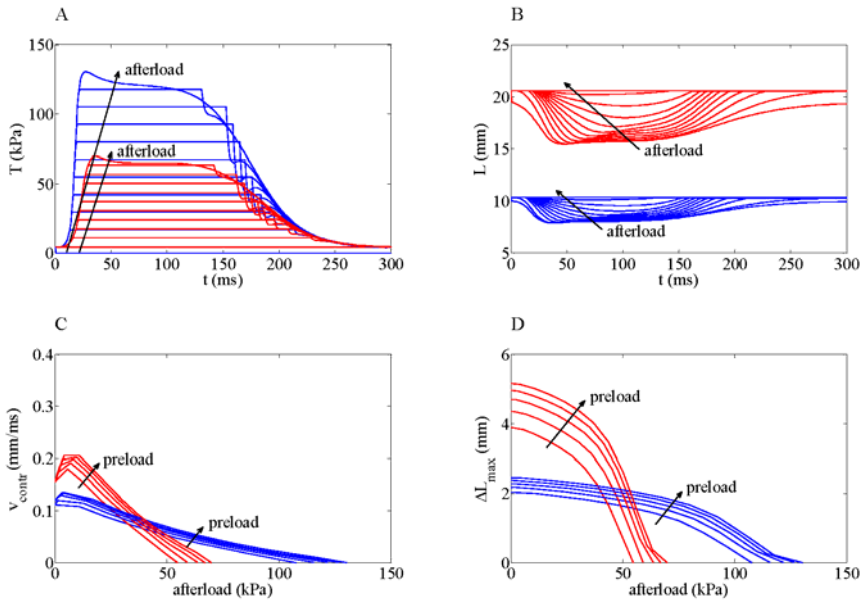

Figure 3.7: Mechanical responses of the healthy (blue) and hypertrophic (red) fibers in case of afterloaded isotonic simulations. A) time evolutions of the tension T developed by the two fibers after their electrical stimulation with a preload equal to 4 kPa and afterloads ranging from the minimum to the maximum value of T. B) corresponding time evolutions of the fiber length L. C) tension-velocity curves for increasing preloads (0, 1, 2, 3 or 4 kPa). The afterloads on the abscissa are equal to the tensions developed by the two fibers during their isotonic phase. The isotonic contraction velocities v_{contr} are taken positive. D) corresponding maximum shortenings ΔL_{max}.

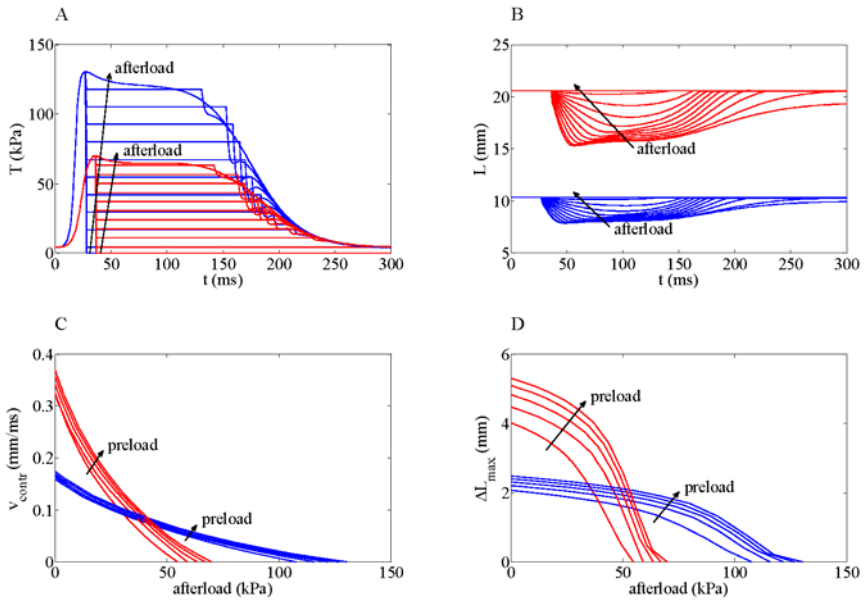

Figure 3.8: Mechanical responses of the healthy (blue) and hypertrophic (red) fibers in case of quick-release simulations. Same format as in Figure 3.7.

As it can be seen from panels A and B of Figure 3.7, during an afterloaded isotonic test, fiber shortening does not start immediately apart from the case of an afterload that is zero or equal to the minimum value of the tension developed during the initial isometric twitch. It requires a certain amount of time to develop sufficient tension during an initial isometric phase; this one lasts more ms for heavier and heavier afterloads. Only when the developed tension equals the load, contraction becomes really isotonic and the muscle can modify its length; first, the muscle contracts, then it relaxes under the effect of the same afterload. The bigger the afterload is the more limited the extent of contraction results. Moreover, the isotonic phase becomes shorter and shorter as the afterload increases, but it can last more than the corresponding isometric twitch. When the fiber length reaches its original value at the end of the preloading phase, relaxation becomes isometric; the afterload is removed and the right end is fixed. Eventually, isometric relaxation lasts till the end time of the simulation. In panel A, the bigger the afterload is the more an initial rapid decay of tension occurs, whereas the following exponential decay is slower and it is very similar to the relaxation of the isometric twitch, so it is independent of the applied afterload [24].

From panels A and B of Figure 3.8, instead, it is evident that, during a quick-release test, the initial isometric contraction lasts the same amount of time for all afterloads, in particular the time needed to reach the peak value for tension at a given initial length. Then, the stop is removed and contraction becomes isotonic, letting the muscle modify its length. There is a rapid transient directly after the release (not present in the afterloaded isotonic length curves), which is followed by a muscle contraction at a quite constant velocity since the fiber length linearly decreases for about 20-30 ms after the release (see panel B). Again, the bigger the afterload is the more limited the extent of contraction results. Then, till the end of the simulation, the isotonic contraction and relaxation and the isometric relaxation are similar to the corresponding phases during the afterloaded isotonic tests.

By considering all preloads from 0 to 4 kPa, tension-velocity relationships are derived from both afterloaded isotonic and quick-release tests (panels C of Figure 3.7 and Figure 3.8). The afterloads on the abscissa correspond to the developed tensions during the isotonic phase, whereas the contraction velocities v_{contr} on the ordinate (taken positive) are computed from the constant slopes of the length curves in time as soon as the two fibers start to contract isotonically [23,75,161,203]. In particular, when the afterload is zero, the initial reduction of the fiber length up to the rest value within the first ms in panel B of Figure 3.7 must be neglected for the measurement of the isotonic contraction velocity. From both afterloaded isotonic and quick-release tests, tension-velocity curves shift upwards and rightwards as the preload increases; this result displays the Frank-Starling law again. Now, it has to be remarked that, during an *in vitro* experiment, too small values for the afterload cannot be chosen [23,75,161,203]. On the contrary, *in silico* simulations permit to do that, so the values for the

corresponding velocities can be computed, even for the ones at a zero afterload, which are often estimated by extrapolation of the tension-velocity equation to a zero afterload [23,57,75,161,203]. Such a procedure often computes contraction velocity values at a zero afterload that may not coincide for all curves. In case of the simulations reported in this chapter, these values are the same during the afterloaded isotonic tests, whilst they change during the quick-release ones. This different result may come out from the nature of the test itself. On one hand, the afterloaded isotonic test is the protocol that mimics best the *in vivo* transition from the isometric contraction to the isotonic one. On the other hand, the quick-release test is the one that most approaches the *in vitro* experiments run on tetanized skeletal muscles, to which cardiac fibers are often compared; actually, although the heart cannot be tetanized, researchers try to reach an equally-activated muscle state by making constant the time during contraction at which the isotonic contraction velocity is measured. This discrepancy may lead to tension-velocity relationships that are not similar to Hill hyperbolas [77] (especially for small afterloads as in this chapter) when they are derived from afterloaded isotonic tests, whilst they could be entirely fitted to hyperbolas in case of quick-release tests. Nevertheless, from both tests, higher values of contraction velocity are reached by the hypertrophic fiber at smaller afterloads (and at a zero one accordingly), whereas lower values are found at bigger afterloads. The same trend characterizes the maximum shortenings ΔL_{max} (that are nearly the same for both tests too) during the isotonic phase under each applied afterload in panels D of Figure 3.7 and Figure 3.8. The two previous results point out that, in case of small afterloads (for example, when the aortic resistance to blood flow is physiological), eccentric hypertrophy may determine greater volume variations for a three-dimensional ventricle during the systolic blood efflux phase of the cardiac cycle.

Therefore, if taken altogether, the mechanical results from the isometric, afterloaded isotonic and quick-release tests suggest a pressure-volume loop for eccentric hypertrophic ventricles that enlarges over volumes and is more likely to shrink over pressures.

3.3.3. Comparison among the *in vitro*, *in silico* and *in vivo* fiber behaviors

Despite all previous results, it must be noted that the *in vitro* tests on papillary muscles are not able to simulate the real sequence of events that characterize the dynamics of ventricular fibers during a cardiac cycle.

In a typical pressure-volume diagram of the *in vivo* mammalian ventricle (Paragraph 1.1.2), all transitions among phases are determined by pressure differences between the ventricle and an artery (the aortic or pulmonary one) or between the atrium and the ventricle. During the *in vitro* afterloaded isotonic experiments on papillary muscles, whose protocol is the closest to mimic the *in vivo* reality in comparison with the isometric

and the quick-release ones, the transition between the isometric contraction and the isotonic one takes place when the muscle tension is equal to the applied afterload, which is the analogue for the aortic or pulmonary artery pressure at the fiber scale. However, the transition between the isotonic relaxation and the isometric one is not governed by loads, but it occurs when the fiber length reaches its original value after the preloading phase. For the *in silico* simulations run in this chapter, the first transition is performed by looking at the fiber length again, i.e. the fiber starts to contract isotonically when the new length computed from the mechanical deformation is lower than the initial length attained by the preload. In this way, the force equilibrium between the fiber tension and the applied afterload necessary to perform the transition is not externally enforced, but it is automatically reached by the implemented protocols.

During the *in vivo* functioning, the pressure in the aorta or in the pulmonary artery changes during the isotonic contraction of ventricles, in particular it rises due to the blood filling of those arteries, till when the semilunar valve closes. The *in vitro* experiments and *in silico* simulations are characterized, instead, by a constant afterload that does not let fiber tension vary too during the isotonic contraction and relaxation. So, the same value of tension is achieved both at the beginning and at the end of the isotonic contraction, a situation that does not happen *in vivo* since the ventricular pressure is usually higher at the end of this phase than at the beginning.

Another important difference between the *in vivo* and *in vitro*/*in silico* cardiac cycles is the time order of the different phases. In intact hearts, the isotonic relaxation comes after the isometric one since the isovolumic diastole anticipates the diastolic filling, during which the venous blood pressure drives the lengthening of ventricular fibers. During the *in vitro* experiments and *in silico* simulations, instead, the isotonic relaxation comes before the isometric one, which only starts when the fiber length reaches its initial value after the preloading phase. Moreover, an analogue for the diastolic filling is absent during the entire afterloaded isotonic test because it is replaced by the initial preloading phase that stretches fibers according to the applied preload. However, the tension-velocity relationships are meaningful because they are built from the values recorded at the beginning of the isotonic contraction, which follows the isometric one like during the *in vivo* functioning.

3.4. Conclusions

In this chapter, a one-dimensional strongly-coupled model has been developed to simulate the electromechanical activity of a ventricular fiber affected from eccentric hypertrophy while it contracts according to different protocols. In the literature, there are no experimental data for eccentric hypertrophic fibers, thus the simulation results of this chapter have tried to fill this lack of information. Hypertrophy has been

implemented both in the electrophysiological model and in the mechanical one to better analyze the full electromechanical response of contracting fibers. First, the effects of the geometric feedbacks and of the mechanoelectric one on the electrical response of both healthy and hypertrophic fibers have been investigated. Then, by including all previous feedbacks, the electrical and mechanical responses of such fibers have been compared too. To achieve this aim, the same preloads (from 0 to 4 kPa) have been applied to both fibers as it would be done during *in vitro* experiments, though the corresponding diastolic fillings for the *in vivo* heart are different.

Future simulations may include the effects of eccentric growth at a molecular level through one or more genetic defects, which could not preserve the shape of the action potential due to modifications involving the total number of membrane channels.

Chapter 4

Simulations on a concentric hypertrophic wedge

In this chapter, the three-dimensional electromechanical model introduced in Chapter 2 is used to simulate the response of a cardiac ventricular wedge affected from concentric hypertrophy and contracting freely. To achieve this aim, the previous model includes concentric hypertrophy both at the level of a single cardiomyocyte and at the one of the entire tissue (as in Chapter 3 for eccentric hypertrophy). In particular, two increasing stages of severity are considered: a first stage characterized by the sole growth of the cardiac tissue and a second one with the further spatial dispersion of fibers that may originate from hypertrophy. An initial single beat is simulated to show qualitative differences characterizing the electrograms and the mechanical trajectories of some epicardial markers. Then, the electrical and mechanical responses are quantitatively studied by means of some macroscopic measures computed over a higher number of markers and beats. The results in this chapter may provide researchers with new challenging results for future work.

4.1. Introduction

Like the corresponding eccentric phenotype, concentric hypertrophy may be a physiological adaptive response of some athletes to effort, but it is more often a pathological remodeling caused by a long-term pressure overload inside ventricles. Actually, the activation of specific signaling pathways leads to a progressive intracellular deposition of new sarcomere units in parallel to the preexistent ones, causing thickened ventricular walls without significant alterations in cardiomyocytes length. Moreover, growth may be accompanied by some changes in the overall myocardial structure

to accommodate for the increase in pressure or volume in ventricles. One of such alterations is a higher angular dispersion of fibers.

Therefore, the aim of this chapter is to study how growth and fiber dispersion characterizing concentric hypertrophy correlate with changes in the electromechanical response of a simulated ventricular wedge, which should represent a portion of the cardiac wall with a simplified geometry. The adopted strongly-coupled electromechanical model joins together an electrophysiological model, an active tension generation model and a finite elasticity model. By following the same framework of finite growth already applied to eccentric hypertrophy in Chapter 3, hypertrophic conditions are properly added to the healthy model. No genetic defects are included and the wedge contracts without any constraints or loads applied on it, hence it is not subjected to any phase of the cardiac cycle. Nevertheless, previous *in silico* studies (e.g., [51,61,66,67,121,175,195]) have investigated the effects of growth and fiber dispersion separately. Here, both effects are grouped together instead, trying to better elucidate the hypertrophic consequences on cardiac electromechanics.

4.2. Methods

The same model of bioelectrical activity, calcium dynamics and active tension generation, i.e. the Faber-Rudy-Land model [53,133], introduced in Chapter 3 is adopted for a single cardiomyocyte. Then, a quasi-static finite elastic model and a Bidomain or Monodomain model are added. Only those modifications needed to consider the growth and fiber dispersion related to concentric hypertrophy rather than to the eccentric one are discussed below.

4.2.1. The mechanical model: implementation of concentric growth and fiber dispersion

Concentric growth is introduced by writing the growth tensor $\mathbf{F}^{\mathbf{g}}$ as in [15,66,67,175] to model the cardiomyocytes thickening due to the parallel deposition of new sarcomeres

$$\mathbf{F}^{\mathbf{g}}=\mathbf{I}+(\theta_s-1)\widehat{\mathbf{a}_s}\otimes\widehat{\mathbf{a}_s}, \tag{4.1}$$

where $\widehat{\mathbf{a}_s}$ is the unit vector for the local sheet direction in the reference configuration Ω_0 and θ_s is the corresponding growth parameter, which is assumed to be constant in time and space in this chapter.

The elastic active component $\mathbf{S}^{\mathbf{e,act}}$ of the total elastic stress tensor $\mathbf{S}^{\mathbf{e}}$ is expressed as [51,61]

$$\mathbf{S}^{e,act}=T_a\left(\frac{k_f}{1-2k_f}(\mathbf{C}^e)^{-1}+\frac{1-3k_f}{1-2k_f}\frac{1}{\widehat{\mathbf{a}_f}^T\mathbf{C}^e\widehat{\mathbf{a}_f}}\widehat{\mathbf{a}_f}\otimes\widehat{\mathbf{a}_f}\right), \tag{4.2}$$

where k_f is a fiber dispersion parameter that is taken constant in space and time like θ_s.

The passive myocardium is modeled as an almost incompressible orthotropic material. Hence, $\mathbf{S}^{e,pas}$ is derived from an orthotropic strain energy function W, in particular the one by Holzapfel [83] introduced and reduced to the transversely isotropic case in Chapter 3, that includes a volumetric term (as in (2.60))

$$W=\frac{a}{2b}e^{b(I_1^e-3)}+\frac{a_f}{2b_f}(e^{b_f(I_{4f}^e-1)^2}-1)+\frac{a_s}{2b_s}(e^{b_s(I_{4s}^e-1)^2}-1)+\frac{a_{fs}}{2b_{fs}}(e^{b_{fs}(I_{8s}^e)^2}-1)+c(\sqrt{\det(\mathbf{C}^e)}-1)^2, \tag{4.3}$$

where a_{fs}, b_{fs} and c are three further fixed parameters taken from [220] and [215], whilst $I_1^e=\mathbf{C}^e:\mathbf{I}$, $I_{4f}^e=k_fI_1^e+(1-3k_f)\widehat{\mathbf{a}_f}^T\mathbf{C}^e\widehat{\mathbf{a}_f}$, $I_{4s}^e=\widehat{\mathbf{a}_s}^T\mathbf{C}^e\widehat{\mathbf{a}_s}$ and $I_{8fs}^e=\widehat{\mathbf{a}_f}^T\mathbf{C}^e\widehat{\mathbf{a}_s}$ are the elastic invariants, among which I_{4f}^e includes the dependence on k_f again [51,61,82,175].

4.2.2. The electrophysiological model: dependence on concentric growth and independence of fiber dispersion

Both the Bidomain (2.68) and Monodomain (2.88) models are used in this chapter together with the Faber-Rudy one in order to model electrophysiology. However, both the convective term and the stretch-activated channels current are here disregarded. Hence, the Bidomain and Monodomain systems read as follows

$$\begin{cases} c_m\dfrac{\partial V}{\partial t}-J^{-1}\mathrm{Div}(J\mathbf{F}^{-1}\mathbf{D}_i\mathbf{F}^{-T}\mathbf{Grad}\,U_i)+i_{ion}(V,\mathbf{w},\mathbf{c})=i_{app}^i & \text{in } \Omega_0\times(0,T)\\ -c_m\dfrac{\partial V}{\partial t}-J^{-1}\mathrm{Div}(J\mathbf{F}^{-1}\mathbf{D}_e\mathbf{F}^{-T}\mathbf{Grad}\,U_e)-i_{ion}(V,\mathbf{w},\mathbf{c})=i_{app}^e & \text{in } \Omega_0\times(0,T)\\ \dfrac{\partial \mathbf{w}}{\partial t}-\mathbf{R}(v,\mathbf{w})=0 & \text{in } \Omega\times(0,T)\\ \dfrac{\partial \mathbf{c}}{\partial t}-\mathbf{S}(v,\mathbf{w},\mathbf{c})=0 & \text{in } \Omega\times(0,T)\\ \mathbf{N}^T\mathbf{F}^{-1}\mathbf{D}_{i,e}\mathbf{F}^{-T}\mathbf{Grad}\,U_{i,e}=0 & \text{on } \partial\Omega_0\times(0,T)\\ V(\mathbf{X},0)=V_0(\mathbf{X}) \text{ in } \Omega_0, \quad \mathbf{w}(\mathbf{x},0)=\mathbf{w_0}(\mathbf{x}), \quad \mathbf{c}(\mathbf{x},0)=\mathbf{c_0}(\mathbf{x}) & \text{in } \Omega, \end{cases} \tag{4.4}$$

$$\begin{cases} c_m \dfrac{\partial V}{\partial t} - J^{-1}\mathrm{Div}(J\mathbf{F}^{-1}\mathbf{D}\mathbf{F}^{-T}\mathbf{Grad}\ V) + i_{ion}(V,\mathbf{w},\mathbf{c}) = i_{app}^{m} & \text{in } \Omega_0\times(0,T) \\ \dfrac{\partial \mathbf{w}}{\partial t} - \mathbf{R}(v,\mathbf{w}) = 0 & \text{in } \Omega\times(0,T) \\ \dfrac{\partial \mathbf{c}}{\partial t} - \mathbf{S}(v,\mathbf{w},\mathbf{c}) = 0 & \text{in } \Omega\times(0,T) \\ \mathbf{n}^T\mathbf{F}^{-1}\mathbf{D}\mathbf{F}^{-T}\mathbf{Grad}\ V = 0 & \text{on } \partial\Omega_0\times(0,T) \\ V(\mathbf{X},0) = V_0(\mathbf{X}) & \text{in } \Omega_0, \quad \mathbf{w}(\mathbf{x},0) = \mathbf{w_0}(\mathbf{x}), \quad \mathbf{c}(\mathbf{x},0) = \mathbf{c_0}(\mathbf{x}) \quad \text{in } \Omega. \end{cases} \tag{4.5}$$

The ratio of surface membrane area per tissue volume χ appearing in the products $c_m=\chi C_m$ and $i_{ion}=\chi I_{ion}$ is computed as $\chi=\sqrt{2(B_{cell}^{\ 2}+C_{cell}^{\ 2})}/(B_{cell}C_{cell})$ to take into account the resultant elliptical cross-section of a concentric hypertrophic cell originally modeled as a cylinder. Actually, B_{cell}, which is the cell semi-major axis along $\widehat{\mathbf{a}_s}$, is defined as $B_{cell}=\theta_s R_{cell}$ (where R_{cell} is the cell radius from the Faber-Rudy model), thus it depends on the growth parameter θ_s; the cell semi-minor axis C_{cell} is kept equal to R_{cell} instead. However, χ is divided by 2 to make its value closer to the conservative one of 1000 cm^{-1} [36] in case of the healthy wedge. The same values for B_{cell} and C_{cell} are used when solving the Faber-Rudy model for a single cardiomyocyte so that the cell geometric area $A_{geo}=2\pi B_{cell}C_{cell}+\pi\sqrt{2(B_{cell}^{\ 2}+C_{cell}^{\ 2})}L_{cell}$ (where L_{cell} is the cell length from the Faber-Rudy model), the cell capacitive membrane area $A_{cap}=2A_{geo}$ and the cell volume $V_{cell}=\pi B_{cell}C_{cell}L_{cell}$ are affected accordingly. The conductivity coefficients defining $\mathbf{D_i}$, $\mathbf{D_e}$ and $\mathbf{D}$ do not depend on growth and are taken from [39] for the case of an orthotropic electrical propagation. Moreover, they do not depend on fiber dispersion as it is proved herein in case of the Monodomain model for simplicity. If fiber dispersion is introduced only along the local fiber direction $\mathbf{a_f}$ in the current configuration Ω, then, similarly to [51] for the active second Piola-Kirchhoff stress tensor, the conductivity tensor $\mathbf{D}$ should be written as

$$\mathbf{D}(\mathbf{x})=\sigma_f\left(\frac{k_f}{1-2k_f}\mathbf{I}+\frac{1-3k_f}{1-2k_f}\mathbf{a_f}(\mathbf{x})\otimes\mathbf{a_f}(\mathbf{x})\right)+\sigma_s\mathbf{a_s}(\mathbf{x})\otimes\mathbf{a_s}(\mathbf{x})+\sigma_n\mathbf{a_n}(\mathbf{x})\otimes\mathbf{a_n}(\mathbf{x}). \tag{4.6}$$

If $\mathbf{v}$ denotes the unit vector normal to the excitation wavefront, the propagation velocity along $\mathbf{v}$ turns out to be proportional to $\sqrt{\mathbf{v}^T\mathbf{D}\mathbf{v}}$. This last quadratic form is equal to

$$\mathbf{v}^T\mathbf{D}\mathbf{v}=\sigma_f\left(\frac{k_f}{1-2k_f}+\frac{1-3k_f}{1-2k_f}\right)(\mathbf{v}^T\mathbf{a_f})^2+\sigma_s(\mathbf{v}^T\mathbf{a_s})^2+\sigma_n(\mathbf{v}^T\mathbf{a_n})^2, \tag{4.7}$$

which, for $\mathbf{v}=\mathbf{a_f},\mathbf{a_s},\mathbf{a_n}$, gives

$$\mathbf{v}^T\mathbf{D}\mathbf{v}=\sigma_f\left(\frac{k_f}{1-2k_f}+\frac{1-3k_f}{1-2k_f}\right)=\sigma_f,\quad \mathbf{v}^T\mathbf{D}\mathbf{v}=\sigma_f\frac{k_f}{1-2k_f}+\sigma_s,\quad \mathbf{v}^T\mathbf{D}\mathbf{v}=\sigma_f\frac{k_f}{1-2k_f}+\sigma_n. \tag{4.8}$$

Hence, σ_s and σ_n increase by $\sigma_f k_f/(1-2k_f)$, which does not make sense. Actually, the way the conductivity tensors are built in the Monodomain and Bidomain models requires the knowledge of all local directions $\mathbf{a_f}$, $\mathbf{a_s}$ and $\mathbf{a_n}$ simultaneously, thus a change in any of these directions affects the remaining ones. As regards mechanics, instead, since the strain-energy function is built upon some invariants that do not interact with one another, a single direction can be dispersed and the corresponding contribution to the energy function can be modified without altering the other ones. The proper formulation of $\mathbf{D}$ in Ω to solve the previous problem is

$$\mathbf{D}(\mathbf{x})=\sigma_f\left(\frac{k_f}{1-2k_f}\mathbf{I}+\frac{1-3k_f}{1-2k_f}\mathbf{a_f}(\mathbf{x})\otimes\mathbf{a_f}(\mathbf{x})\right)+\left(\sigma_s-\sigma_f\frac{k_f}{1-2k_f}\right)\mathbf{a_s}(\mathbf{x})\otimes\mathbf{a_s}(\mathbf{x})+\left(\sigma_n-\sigma_f\frac{k_f}{1-2k_f}\right)\mathbf{a_n}(\mathbf{x})\otimes\mathbf{a_n}(\mathbf{x}), \tag{4.9}$$

from which $\mathbf{v}^T\mathbf{D}\mathbf{v}$ gives, for $\mathbf{v}=\mathbf{a_f},\mathbf{a_s},\mathbf{a_n}$,

$$\mathbf{v}^T\mathbf{D}\mathbf{v}=\sigma_f\left(\frac{k_f}{1-2k_f}+\frac{1-3k_f}{1-2k_f}\right)=\sigma_f,\quad \mathbf{v}^T\mathbf{D}\mathbf{v}=\sigma_f\frac{k_f}{1-2k_f}+\sigma_s-\sigma_f\frac{k_f}{1-2k_f}=\sigma_f,\quad \mathbf{v}^T\mathbf{D}\mathbf{v}=\sigma_f\frac{k_f}{1-2k_f}+\sigma_n-\sigma_f\frac{k_f}{1-2k_f}=\sigma_n. \tag{4.10}$$

However, if (4.9) is rewritten by replacing $\mathbf{a_s}(\mathbf{x})\otimes\mathbf{a_s}(\mathbf{x})$ with $\mathbf{I}-\mathbf{a_f}(\mathbf{x})\otimes\mathbf{a_f}(\mathbf{x})-\mathbf{a_n}(\mathbf{x})\otimes\mathbf{a_n}(\mathbf{x})$ and rearranging the resultant terms, then it follows that

$$\mathbf{D}(\mathbf{x})=\sigma_s\mathbf{I}+(\sigma_f-\sigma_s)\mathbf{a_f}(\mathbf{x})\otimes\mathbf{a_f}(\mathbf{x})+(\sigma_n-\sigma_s)\mathbf{a_n}(\mathbf{x})\otimes\mathbf{a_n}(\mathbf{x}) \tag{4.11}$$

like the case without dispersion (2.86). In any case, future computational and experimental studies are needed to investigate and model accurately fiber dispersion in a continuous framework that couples mechanics with electrophysiology.

4.2.3. Details on the discretization and implementation of the complete model

The electrical components of the model are approximated on a uniform mesh of 200 × 200 × 50 trilinear finite elements (yielding a mesh size

Δh_{el}=0.1 mm) and using a constant time step Δt_{el}=0.05 ms. The mechanical components, instead, are approximated on a uniform coarser mesh of 40 × 40 × 10 trilinear finite elements (yielding a mesh size Δh_{mec}=0.5 mm) and using a constant time step Δt_{mec}=1 ms. The time discretization is carried out by a decoupled semi-implicit method.

Simulations are run on the Linux cluster of the Department of Mathematics of the University of Milan [99]. The electromechanical code is written in FORTRAN 90 and parallelized by means of PETSc libraries from the Argonne National Laboratory [100].

4.2.4. The geometry and electrical stimulation of the wedge

The ventricular wedge is modeled as a slab with the reference configuration in Figure 4.1. Growth is introduced by choosing θ_s=2 [67], whereas fiber dispersion is obtained by setting k_f=0.0886 [51]; the healthy values are 1 and 0 respectively. In particular, θ_s=2 means that the initial thickness of the hypertrophic wedge is twice bigger than the one of the healthy wedge. The endocardium is kept fixed to avoid any rigid motion. Fibers rotate linearly and in a counterclockwise fashion from the epicardium (-45°) to the endocardium (+45°).

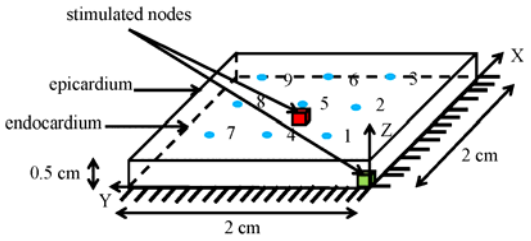

Figure 4.1: Reference configuration for the ventricular wedge. A 2 cm × 2 cm × 0.5 cm slab with a fixed endocardium is adopted. The green cube of nodes is given the first electrical stimulus necessary for the initial qualitative analysis of the electromechanical response of the wedge, whilst the red one is given the other electrical stimuli necessary for the quantitative analysis. Nine points (denoted by numbered blue spots) belonging to a uniform 3 × 3 grid central to the epicardium are chosen for the qualitative analysis.

Two different clusters of nodes located on the endocardium are delivered electrical stimuli. The green cube of nodes in Figure 4.1 is given one current stimulus i_{app}^{e} with amplitude equal to 250 mA/cm^3 and duration 1 ms to compare qualitatively the epicardial electrograms close to and far from the stimulation site and the epicardial trajectories in case of healthy and hypertrophic wedges. The red cube, instead, is given a sequence of ten current stimuli i_{app}^{m} with amplitude equal to 250 mA/cm^3, duration 1 ms and

basic cycle length 300 ms to compare quantitatively the macroscopic bioelectrical and biomechanical measures listed below.

4.2.5. Bioelectrical and biomechanical measures and statistics

During the quantitative analysis of the electromechanical response of the wedge, the transmembrane potential values V(t) and (x(t),y(t),z(t)) coordinates are saved in 121 nodes of a uniform 11 × 11 grid on the epicardium (in the following called markers); see Figure 4.2 for an example of the time evolution of V and the trajectory described in the XY plane.

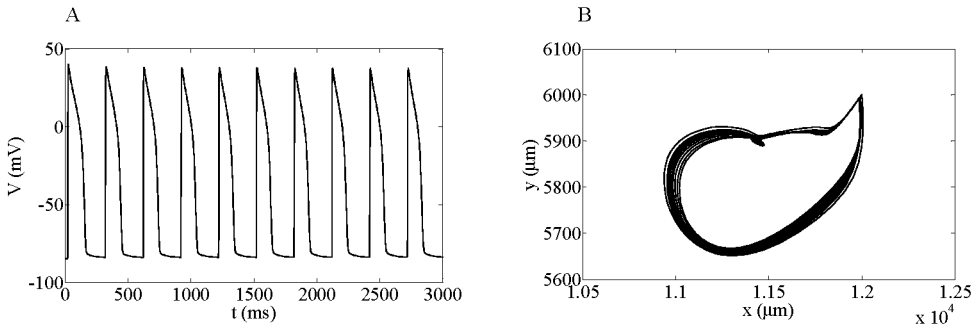

Figure 4.2: Typical simulation results for a marker: A) time evolution of the transmembrane potential V; B) trajectory in the XY plane.

The previous simulation results are postprocessed by using two algorithms implemented in Matlab® to derive the following bioelectrical and biomechanical measures for each marker.

As regards the electrical activity, first, the activation and repolarization times are computed from the time evolution of the transmembrane potential like the one in panel A of Figure 4.2. The activation times are defined as the time delays between the moments when the transmembrane potential exceeds the threshold value of -40 mV and the ones when the corresponding stimulus is delivered to the red cluster in Figure 4.1. The repolarization times, instead, are defined as the time delays between the moments when the transmembrane potential reaches its 90% repolarization value (-76.5 mV) and the ones when the corresponding stimulus is delivered as before. Then, the action potential durations APD_i are computed as the differences between the repolarization and activation times and their mean gives the mean action potential duration APD_{mean}

$$APD_{mean} = \frac{1}{N_b} \sum_{i=1}^{N_b} APD_i, \tag{4.12}$$

where N_b is the total number of considered beats. Moreover, the mean conduction velocity is estimated in the following way. First, for each beat i,

the (x,y,z) coordinates of a marker at the moment of its electrical activation are detected and its distance from the central node of the red cluster in the bottom layer (that is fixed during all simulations) is computed. Then, the value of the conduction velocity CV_i is achieved by dividing this distance with respect to the activation time. Again, by taking the mean over all beats, the mean conduction velocity CV_{mean} is obtained

$$CV_{mean} = \frac{1}{N_b} \sum_{i=1}^{N_b} CV_i. \tag{4.13}$$

For the mechanical activity, an already published algorithm developed for *in vitro* experimental results on cultures [54] is employed starting from the trajectory described by each marker in the XY plane like the one in panel B of Figure 4.2. Briefly, first, the values for the velocities along the X and Y axes $v_{x,m}=(x_{m+1}-x_m)/\Delta t_{mec}$ and $v_{y,m}=(y_{m+1}-y_m)/\Delta t_{mec}$, where $(x_{m+1}-x_m)$ and $(y_{m+1}-y_m)$ are the displacements along the X and Y axes for m=1,…,M-1 and M is the number of time steps, are derived. Then, for the beat i, the contractility CT_i is computed by identifying the velocity vector $\mathbf{v}=(v_x,v_y)^T$ with the highest magnitude during the corresponding contraction phase and the mean contractility over all beats CT_{mean} is defined as

$$CT_{mean} = \frac{1}{N_b} \sum_{i=1}^{N_b} CT_i. \tag{4.14}$$

Moreover, the mean contraction force CF_{mean} is derived as

$$CF_{mean} = \frac{1}{M} \sum_{m=1}^{M-1} |\mathbf{CF}_m|, \tag{4.15}$$

where $\mathbf{CF}_m$ is a force whose expression can be derived using the Hamiltonian mechanics

$$\mathbf{CF}_m = -(\nabla_{\mathbf{x}} \mathbf{v})^T \mathbf{v}. \tag{4.16}$$

Therefore, the mass of the epicardium is neglected because it is a constant among simulations (CF_{mean} is actually normalized).

Finally, the 121 values for APD_{mean}, CV_{mean}, CT_{mean} and CF_{mean} belonging to the healthy case (in the following called H) and to the hypertrophic ones with only growth (G) or together with fiber dispersion (G+FD) are statistically compared by means of the one-way ANOVA and LSD test with a significance level of 0.05.

4.3. Results and discussion

4.3.1. Qualitative analysis of the electromechanical response

Figure 4.3 displays the extracellular potentials U_e (or unipolar electrograms EGs) in nine nodes of a uniform 3 × 3 grid central to the epicardium (the blue spots in Figure 4.1) for the healthy wedge and the hypertrophic ones with only growth or together with fiber dispersion. In the healthy wedge, the EGs located in the early excited and repolarized epicardial area show a deep Q wave in the local QRS complex followed by a positive T wave. When the epicardium is half excited and half repolarized, the EGs at sites on this boundary exhibit positive R and negative S waves with about the same amplitude followed by biphasic T waves. Finally, large R and negative T waves indicate a late excitation and repolarization. These EG morphologies are in agreement with those measured and simulated after a local stimulation in dogs [35]. When growth is incorporated, in the early excited and repolarized epicardial sites, the EGs display a local QRS complex with Q and S waves of the same amplitude and large R waves followed by multiphasic T waves. Conversely, in the late excited and repolarized sites, the EGs exhibit large R waves followed by negative T waves as in the healthy wedge. In those sites excited when the epicardium is half activated and half repolarized, the EGs show R and S waves with the same amplitude and biphasic T waves similarly to the healthy case again. The presence of fiber dispersion does not change further the morphology of EGs.

However, the trajectories described by the nine nodes in the XY plane in Figure 4.4 enlarge not only with growth but also with fiber dispersion. This means that the ventricular wedge requires more and more energy to beat and overcome its maladaptive remodeling.

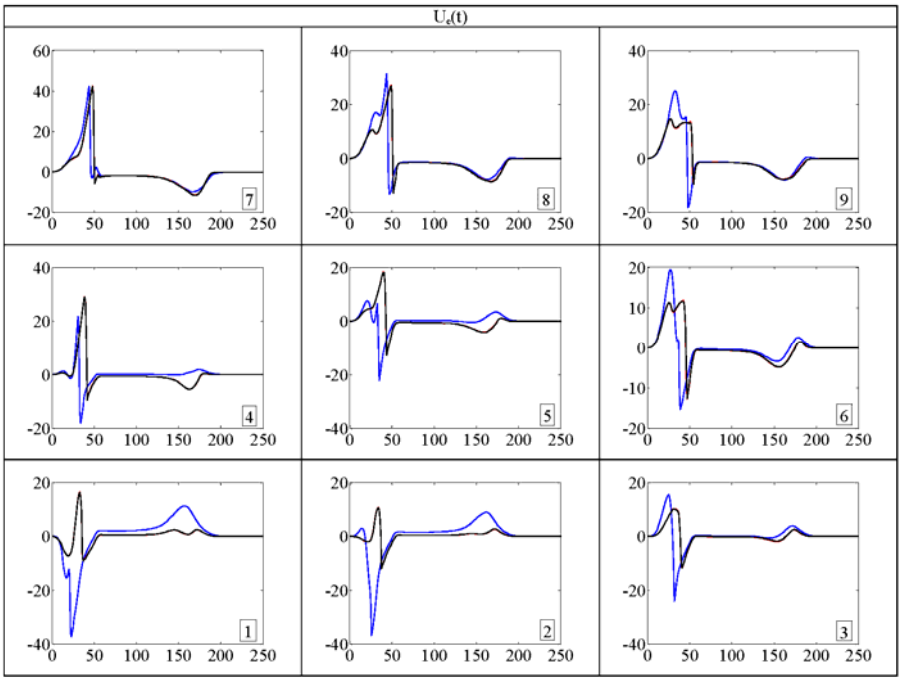

Figure 4.3: Electrograms U_e computed in the nine selected nodes of Figure 4.1 for the healthy case (blue), the hypertrophic one with only growth (red) and the one with growth and fiber dispersion (black); all values on the abscissa are in ms, whereas the ones on the ordinate are in mV.

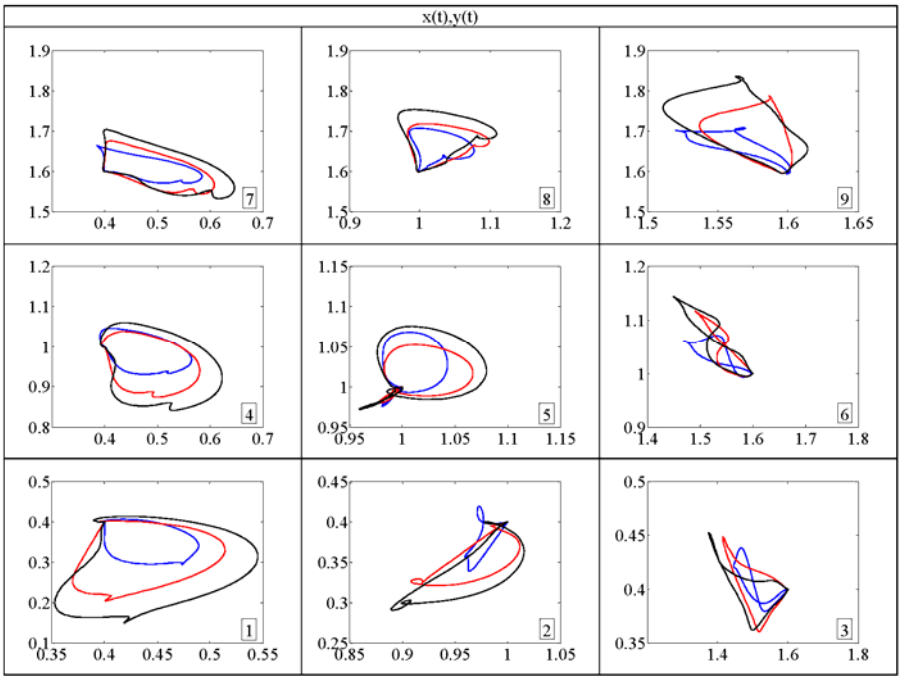

Figure 4.4: Trajectories in the XY plane computed in the nine selected nodes of Figure 4.1 for the healthy case (blue), the hypertrophic one with only growth (red) and the one with growth and fiber dispersion (black); all values are in cm.

4.3.2. Quantitative analysis of the electromechanical response

Panel A of Figure 4.5 reports significant differences ($p<0.05$) of APD_{mean} between the H case and the G or G+FD ones. Again, as regards CV_{mean}, there are significant differences ($p<0.05$) between the H case and the G or G+FD ones in panel B. All remaining differences in Figure 4.5 are insignificant ($p>0.05$). In particular, simulation results suggest that growth, both with and without fiber dispersion, is responsible for a slight decrease of APD_{mean} (about 6 ms). Moreover, growth strongly decreases CV_{mean}. Both previous effects raise the risk of inducing arrhythmogenic phenomena in a thickened cardiac wall.

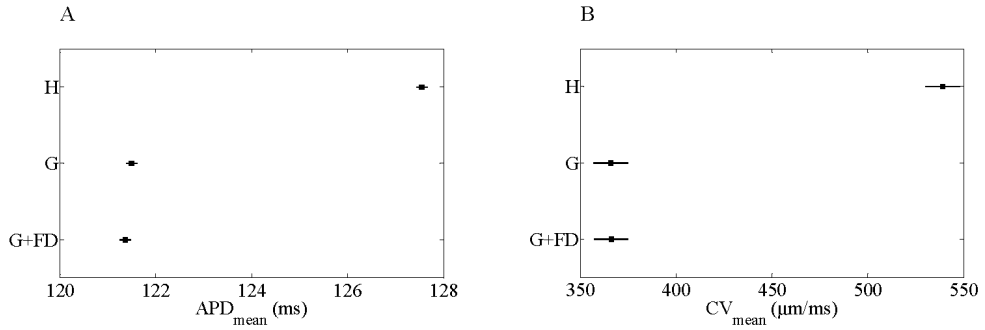

Figure 4.5: Statistical results for the bioelectrical activity of the healthy wedge (H) and of the two hypertrophic ones with only growth (G) or with fiber dispersion too (G+FD): A) mean action potential duration APD_{mean}; B) mean conduction velocity CV_{mean}. The horizontal bars are the 95% confidence intervals for the differences between means according to the LSD test.

Panel A of Figure 4.6 shows significant differences ($p<0.05$) of CT_{mean} among all cases. Considering CF_{mean}, there is a significant difference ($p<0.05$) between the H or G case and the G+FD one in panel B. Again, all other differences in Figure 4.6 are insignificant ($p>0.05$). In particular, both growth and fiber dispersion cause an increase of CT_{mean} and CF_{mean}. This means that the ventricular wall requires more energy to beat and develops more force to keep on pumping blood efficiently [205] in accordance with the widening of trajectories in the XY plane in Figure 4.4.

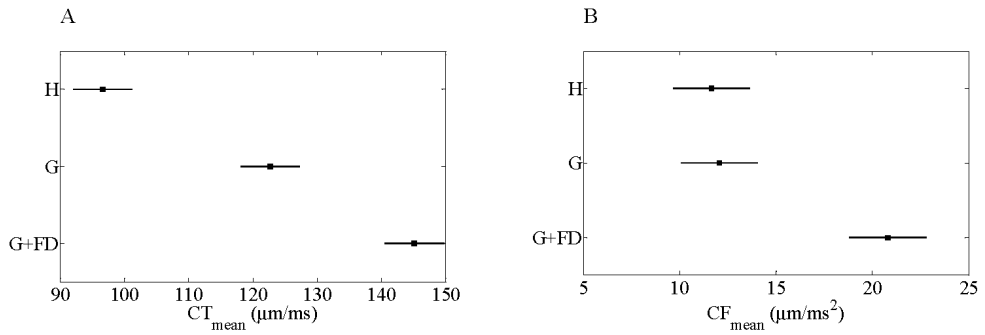

Figure 4.6: Statistical results for the biomechanical activity of the healthy wedge (H) and of the two hypertrophic ones with only growth (G) or with fiber dispersion too (G+FD): A) mean contractility CT_{mean}; B) mean contraction force CF_{mean}. The horizontal bars are the 95% confidence intervals for the differences between means according to the LSD test.

4.4. Conclusions

The aim of this chapter has been to get insights into the electromechanical behavior of the cardiac wall when growth and fiber dispersion are accounted for during concentric hypertrophy. A ventricular wedge has been modeled as a 3D slab including the main features of the wall structure, such as the transmural rotation of fibers and the orthotropic mechanical and electrical properties. The dependence of the electrical response on the mechanical deformation through the tensor **F** in the diffusive terms of (4.4) and (4.5) has been included too, though the convective term and the stretch-activated channels current have been disregarded.

In this chapter, cardiomyocytes have been assumed to preserve an organized contractile apparatus under hypertrophic conditions, i.e. with sarcomeres still made of correctly-polymerized actin and myosin fibers locally oriented along a preferential direction. Therefore, the phenomenological description of growth and fiber dispersion in (4.1), (4.2) and (4.3) in terms of the parameters θ_s and k_f has been adopted. Moreover, the interstitial fibrosis due to the proliferation of fibroblasts that often accompanies myocyte hypertrophy has not been considered. At last, the structure of the T-tubule system acting upon the calcium-induced calcium release phenomenon has not been altered, though experimental evidence points out morphological changes during concentric hypertrophy [71].

Future investigations may include a non-uniform and time-dependent growth and fiber dispersion and other phenotypic features related to concentric hypertrophy in order to analyze their additional effects on the electromechanical response of the wedge.

Chapter 5

Simulations on a concentric hypertrophic ventricle

In this chapter, a cardiac ventricle affected from concentric hypertrophy is studied while it is subjected to an entire cardiac cycle. Similarly to Chapter 4, the hypertrophic phenotype is properly implemented at the microscopic level of a cardiomyocyte and at the macroscopic one of the tissue, starting from the three-dimensional electromechanical model in Chapter 2 again. Only growth is considered, disregarding any spatial dispersion of fibers, but the case with aortic stenosis (causing hypertrophy) and without growth is taken into account too. The electrical response is investigated through activation, repolarization and action potential duration maps, by including the analysis of the effects of the mechanical feedbacks as in Chapter 3. Moreover, the electrograms related to specific nodes of the ventricle are displayed. The mechanical response is studied by means of pressure-volume loops and the same kinematic and dynamic measures of Chapter 4, i.e. the contractility and contraction force. Furthermore, the maps of the principal cardiac strains both at end systole and at end diastole are reported. Thus, the simulation results reported in this chapter contribute to better forecast the electromechanical effects of concentric hypertrophy on a whole ventricle.

5.1. Introduction

As it has already been recalled in Chapter 1 and Chapter 4, concentric hypertrophy is one of the phenotypes developing in the heart when an excessive load characterizes the closed loop of blood circulation. It may represent an athlete's response during an intensive and prolonged training or a pathological remodeling due to aortic stenosis for instance. A parallel deposition of new sarcomere units inside cardiomyocytes is peculiar to this

phenotype, thus increasing the cross-sectional area of cells and determining a thickening of the cardiac wall. Moreover, it may be the expression of genetic mutations encoding for some sarcolemmal and cytoskeletal proteins.

Similarly to Chapter 3 for eccentric hypertrophy, there are already a few studies in the literature aimed at modeling concentric hypertrophy at the level of a ventricle (e.g., [15,66,67,121,175]). The first works focused only on the mechanical activity of hypertrophic hearts, whilst the most recent ones are including a model of bioelectrical activity too. However, the influence of mechanical feedbacks on the cardiac electrical activity has not been studied yet.

The novelty of this chapter is the analysis of the electromechanical activity of concentric hypertrophic ventricles by a finite-element strongly-coupled electromechanical model. The model is composed of a zero-dimensional cardiomyocyte model of bioelectrical activity, calcium dynamics and active tension generation and a three-dimensional mechanical model of finite elasticity coupled with the Bidomain reaction-diffusion equation describing the electrical current flow. The Bidomain equation is written in the reference configuration, thus including the two geometric feedbacks of conductivity and convection. The mechanoelectric feedback carried out by stretch-activated membrane channels is taken into account too. First, the effects of these mechanical feedbacks on the bioelectrical activity of both a healthy and a hypertrophic ventricle are investigated. Then, the electromechanical behavior of such ventricles is studied. In particular, to attain a proper initial configuration for the hypertrophic ventricle, aortic stenosis is implemented in a cardiac cycle and the corresponding consequent maladaptive growth process is triggered. Hypertrophic modifications are applied to each single cardiomyocyte and the whole ventricle as regards both electrophysiology and mechanics. Moreover, the hypertrophic case is compared with the stenotic one without growth in order to find out to which extent growth counteracts the effects of aortic stenosis as never done before.

5.2. Methods

Once again, the Faber-Rudy-Land model [53,133] is used for the bioelectrical activity, calcium dynamics and active tension generation of a cardiomyocyte. A quasi-static finite elasticity model and a Bidomain model are employed too. Even if most of the equations related to concentric growth have already been reported in Chapter 4, some of them are collected below again for sake of clearness.

5.2.1. The mechanical model: implementation of concentric growth

The parallel deposition of sarcomeres occurring during concentric hypertrophy is represented by the following expression for $\mathbf{F}^{\mathbf{g}}$ [15,66,67,175]

$$\mathbf{F}^{\mathbf{g}}=\mathbf{I}+(\theta_s-1)\widehat{\mathbf{a}_s}\otimes\widehat{\mathbf{a}_s}, \tag{5.1}$$

where $\widehat{\mathbf{a}_s}$ is the unit vector for the local sheet direction in the reference configuration Ω_0 and θ_s is the corresponding local growth parameter. Differently from Chapter 4 and similarly to Chapter 3 in case of eccentric hypertrophy, θ_s is not assumed constant in space and time in this chapter.

The elastic active component $\mathbf{S}^{\mathbf{e,act}}$ of the total elastic stress tensor $\mathbf{S}^{\mathbf{e}}$ is defined as

$$\mathbf{S}^{\mathbf{e,act}}=\frac{T_a}{\widehat{\mathbf{a}_f}^{T}\mathbf{C}^{\mathbf{e}}\widehat{\mathbf{a}_f}}\widehat{\mathbf{a}_f}\otimes\widehat{\mathbf{a}_f}, \tag{5.2}$$

where $\widehat{\mathbf{a}_f}$ is the unit vector for the local fiber direction in Ω_0; hence, fiber dispersion is disregarded in this chapter.

As in Chapter 4, the elastic passive component $\mathbf{S}^{\mathbf{e,pas}}$ comes from the orthotropic strain energy function W by Holzapfel [83], including a volumetric term too,

$$W=\frac{a}{2b}e^{b(I_1^e-3)}+\frac{a_f}{2b_f}(e^{b_f(I_{4f}^e-1)^2}-1)+\frac{a_s}{2b_s}(e^{b_s(I_{4s}^e-1)^2}-1)+\frac{a_{fs}}{2b_{fs}}(e^{b_{fs}(I_{8fs}^e)^2}-1)+c(\sqrt{\det(\mathbf{C}^e)}-1)^2, \tag{5.3}$$

where the parameters a, b, a_f, b_f, a_s, b_s, a_{fs}, b_{fs} and c are taken from [220] and [215], but the elastic invariants are now $I_1^e=\mathbf{C}^e:\mathbf{I}$, $I_{4f}^e=\widehat{\mathbf{a}_f}^{T}\mathbf{C}^e\widehat{\mathbf{a}_f}$, $I_{4s}^e=\widehat{\mathbf{a}_s}^{T}\mathbf{C}^e\widehat{\mathbf{a}_s}$ and $I_{8fs}^e=\widehat{\mathbf{a}_f}^{T}\mathbf{C}^e\widehat{\mathbf{a}_s}$ [82,175], thus fiber dispersion is not included again.

5.2.2. The electrophysiological model: dependence on concentric growth

The most complete form of the Bidomain system (2.68), including all mechanical feedbacks, is used for the simulations run in this chapter together with the Faber-Rudy model

$$\begin{cases} c_m\left(\dfrac{\partial V}{\partial t}-\mathbf{F}^{-T}\mathbf{Grad}\,V\cdot\dfrac{\partial \mathbf{x}}{\partial t}\right)-J^{-1}\mathrm{Div}(J\mathbf{F}^{-1}\mathbf{D}_i\mathbf{F}^{-T}\mathbf{Grad}\,U_i)+i_{ion}(V,\mathbf{w},\mathbf{c})+i_{SAC}(V,\mathbf{c},\lambda^e)=i^i_{app} & \text{in } \Omega_0\times(0,T)\\ -c_m\left(\dfrac{\partial V}{\partial t}-\mathbf{F}^{-T}\mathbf{Grad}\,V\cdot\dfrac{\partial \mathbf{x}}{\partial t}\right)-J^{-1}\mathrm{Div}(J\mathbf{F}^{-1}\mathbf{D}_e\mathbf{F}^{-T}\mathbf{Grad}\,U_e)-i_{ion}(V,\mathbf{w},\mathbf{c})-i_{SAC}(V,\mathbf{c},\lambda^e)=i^e_{app} & \text{in } \Omega_0\times(0,T)\\ \dfrac{\partial \mathbf{w}}{\partial t}-\mathbf{R}(V,\mathbf{w})=0 & \text{in } \Omega\times(0,T)\\ \dfrac{\partial \mathbf{c}}{\partial t}-\mathbf{S}(V,\mathbf{w},\mathbf{c})=0 & \text{in } \Omega\times(0,T)\\ \mathbf{N}^T\mathbf{F}^{-1}\mathbf{D}_{i,e}\mathbf{F}^{-T}\mathbf{Grad}\,U_{i,e}=0 & \text{on } \partial\Omega_0\times(0,T)\\ V(\mathbf{X},0)=V_0(\mathbf{X}) & \text{in } \Omega_0,\ \mathbf{w}(\mathbf{x},0)=\mathbf{w}_0(\mathbf{x}),\ \mathbf{c}(\mathbf{x},0)=\mathbf{c}_0(\mathbf{x}) \text{ in } \Omega \end{cases} \tag{5.4}$$

As in Chapter 4, the ratio χ in $c_m=\chi C_m$, $i_{ion}=\chi I_{ion}$ and $i_{SAC}=\chi I_{SAC}$ is computed as $\chi=\sqrt{2(B_{cell}^2+C_{cell}^2)}/(B_{cell}C_{cell})$, where $B_{cell}=\theta_s R_{cell}$ is the semi-major axis along $\widehat{\mathbf{a}_s}$ (with R_{cell} the cell radius from the Faber-Rudy model) and $C_{cell}=R_{cell}$ the semi-minor axis. Then, χ is divided by 2 to make its value closer to the conservative one of 1000 cm^{-1} in case of the healthy ventricle again. The orthotropic intra- and extracellular conductivity coefficients $\sigma^{i,e}_{f,s,n}$ building up $\mathbf{D_{i,e}}$ have the following expressions or values (in mS/cm) [36,76,183]

$$\begin{aligned} &\sigma^i_f=\frac{1}{r_{cyt}+\dfrac{r_{junct}}{L_{cell}}},\quad \sigma^i_s=\frac{1}{r_{cyt}+\dfrac{r_{junct}L_{cell}}{A_{cell}}},\quad \sigma^i_n=\frac{\sigma^i_s}{10},\\ &\sigma^e_f=2,\quad \sigma^e_s=1.3514,\quad \sigma^e_n=\frac{\sigma^e_s}{2}, \end{aligned} \tag{5.5}$$

where $r_{cyt}=150\ \Omega\cdot$cm and $r_{junct}=1.5\ \Omega\cdot cm^2$ are the cytoplasmic and gap junction resistivities [198], whilst L_{cell} (from the original Faber-Rudy model) and $A_{cell}=\pi B_{cell}C_{cell}$ are the length and cross-sectional area of cardiomyocytes. Hence, differently from Chapter 4, the conductivity coefficients depend on local growth now.

The same variables B_{cell} and C_{cell} are computed as before when solving the Faber-Rudy model related to the single cardiomyocyte; this, in turn, affects the geometric plasma membrane area $A_{geo}=2\pi B_{cell}C_{cell}+\pi\sqrt{2(B_{cell}^2+C_{cell}^2)}L_{cell}$, the capacitive one $A_{cap}=2A_{geo}$ and the cell volume $V_{cell}=\pi B_{cell}C_{cell}L_{cell}$.

5.2.3. Details on the discretization and implementation of the complete model

The space discretization is performed by trilinear finite elements on two hexahedral structured grids, the former with a mesh size Δh_{el}=0.1 mm for the electrical model being a refinement of the latter with a mesh size Δh_{mec}=0.8 mm for the mechanical model. The time discretization is carried out by a decoupled semi-implicit method. A constant time step Δt_{el}=0.05 ms is used for the electrical model, whilst a constant time step Δt_{mec}=0.25 ms is employed for the mechanical one.

As in Chapter 4, simulations are performed on the Linux cluster of the Department of Mathematics of the University of Milan [99]. The electromechanical code is written in FORTRAN 90 and parallelized by means of PETSc libraries from the Argonne National Laboratory [100].

5.2.4. The geometry and electrical stimulation of the ventricle

The reference configuration of the ventricle (the left one) is schematized in panel A of Figure 5.1. It consists of a portion of truncated ellipsoid with the nodes located on the endocardial boundary of its base completely fixed and the other nodes of the base constrained only along the Z axis to avoid rigid motions. Fibers rotate linearly and in a counterclockwise fashion from the epicardium to the endocardium for a total amount of 120°. In general, they are not tangent to the radial sheets of the ventricular wall; actually, they may cross them obliquely, thus defining a non-zero imbrication angle [34]. The pressure boundary conditions imposed by the ventricular deformation and the vascular system are applied to the whole endocardium.

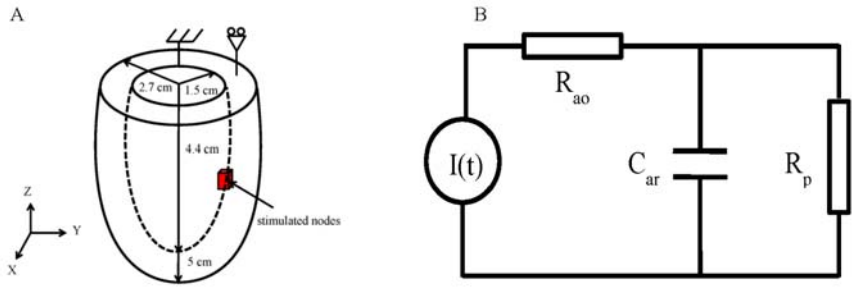

Figure 5.1: A) reference configuration for the healthy and hypertrophic ventricles. The entire base is constrained along the Z axis and the corresponding nodes on the endocardium are constrained along the X and Y axes too. The whole endocardial surface is subjected to pressure. The current stimuli are given towards the center of the ventricle on the anterior view of the endocardium. B) three-element Windkessel model of the circulatory system during the blood efflux phase of the cardiac cycle: the current $I(t)$=-dV/dt stands for the blood flow, C_{ar} is the compliance of the aorta and large elastic arteries, R_{ao} is the characteristic impedance of the aorta and R_p is the peripheral resistance.

Extracellular current stimuli of 250 mA/cm^3 are delivered for 1 ms at a basic cycle length of 400 ms to a small volume of tissue located at the center of the anterior view of the endocardial surface. This point stimulation indicates that the electrical activation of the ventricle via the Purkinje network is disregarded in this chapter for simplicity.

5.2.5. The cardiac cycle and growth of the ventricle

Under healthy conditions or in presence of aortic stenosis, the dynamics of the ventricular pressure P and volume V follow the usual four phases of a cardiac cycle: the isovolumic systole, the blood efflux, the isovolumic diastole and the diastolic filling (Paragraph 1.1.2). Starting from a non-physiological initial phase with a linear increase of pressure from P=0 kPa to P=EDP (with EDP the ventricular end-diastolic pressure), the previous phases are implemented as follows. During the isovolumic systole, which begins when P equals EDP and dV/dt becomes negative (i.e. the ventricle is not inflating anymore), P is computed by employing the iterative relation

$$P_{n+1}=P_n+\frac{V_{n+1}-V_n}{C_{p1}} \tag{5.6}$$

to keep V constant (dV/dt=0 ml/ms), while choosing an adequate value for the penalty parameter C_{p1} for a robust convergence. When P is greater than a prescribed arterial pressure P_{ar}, the blood efflux starts and a three-element Windkessel model (Figure 5.1, panel B) is connected to the ventricle to simulate the circulatory system

$$C_{ar}\frac{dP}{dt}+\frac{P}{R_p}=-\left(1+\frac{R_{ao}}{R_p}\right)\frac{dV}{dt}-C_{ar}R_{ao}\frac{d^2V}{dt^2}, \tag{5.7}$$

where C_{ar} is the compliance of the aorta and large elastic arteries, R_{ao} is the characteristic impedance of the aorta (due to the aortic valve), approximated as a simple resistance, and R_p is the peripheral resistance. This equation is discretized implicitly with respect to P and the resulting term including d^2V/dt^2 is disregarded because it generates instabilities when $R_{ao}\neq 0$ kPa·ms/ml in case of aortic stenosis; nevertheless, R_{ao} is present in the term depending on dV/dt. The ejection phase ends when dV/dt becomes positive (i.e. the ventricle is not deflating anymore). Then, during the isovolumic diastole, an equation similar to (5.6) (with another penalty parameter C_{p2}) holds. At last, when P becomes lower than a prescribed atrial pressure at the end of the atrial diastole P_{at}, the diastolic filling starts. It consists of a linear increase of P up to EDP till the end of the cardiac cycle. Table 5.1 collects the values of all parameters introduced before.

Table 5.1: Values of parameters used for simulating the healthy and stenotic cardiac cycles: end-diastolic pressure EDP; penalty parameter for the isovolumic systole C_{p1}; arterial pressure at the end of the isovolumic systole P_{ar}; compliance of the aorta and large elastic arteries C_{ar}; peripheral resistance R_p; characteristic impedance of the aorta R_{ao}; penalty parameter for the isovolumic diastole C_{p2}; atrial pressure at the end of the atrial diastole P_{at}.

	HEALTHY	STENOTIC
EDP (kPa)	2	2
C_{p1} (ml/kPa)	-2	-2
P_{ar} (kPa)	10	10
C_{ar} (ml/kPa)	1	1
R_p (kPa ms/ml)	80	80
R_{ao} (kPa ms/ml)	0	100
C_{p2} (ml/kPa)	-5	-5
P_{at} (kPa)	1	1

To trigger a concentric growth, a similar procedure to the one suggested in Chapter 3 for eccentric hypertrophy is followed. Therefore, the ventricle is allowed to grow at the end of each cardiac cycle, maintaining its reference configuration. However, in this chapter, the deviation of the time-averaged trace of the elastic Mandel stress tensor $\mathbf{M}^e=\mathbf{C}^e\cdot\mathbf{S}^e$, denoted by $\overline{\mathrm{tr}(\mathbf{M}^e)}$, from the corresponding homeostatic set point value $\overline{\mathrm{tr}(\mathbf{M}^e)_h}$ (given by a healthy simulation), i.e. $\overline{\mathrm{tr}(\mathbf{M}^e)}-\overline{\mathrm{tr}(\mathbf{M}^e)_h}$, represents the mechanical stimulus driving concentric growth in each node. The use of $\mathrm{tr}(\mathbf{M}^e)$ can be found in [66,67], though there are some experimental studies showing that concentric hypertrophy is driven by strain rather than stress similarly to the eccentric one (see [121] for a thorough discussion on this topic). Thus, the local increments for θ_s between the beats n and n+1, i.e. $\theta_{s,*}$, are now given by

$$\theta_{s,*}=1+k(\theta_{s,n})\left(\overline{\mathrm{tr}(\mathbf{M}^e)_n}-\overline{\mathrm{tr}(\mathbf{M}^e)_h}\right) \tag{5.8}$$

in those nodes where $\overline{\mathrm{tr}(\mathbf{M}^e)_n}-\overline{\mathrm{tr}(\mathbf{M}^e)_h}$ is positive, except from the ones on the base because the constraints on displacements provoke higher local stresses that would generate too high values of θ_s compared with the remaining ventricle. In the previous equation, the rate-limiting function k has the expression

$$k=\frac{1}{\tau}\left(\frac{\theta_s^{max}-\theta_{s,n}}{\theta_s^{max}-1}\right)^{\gamma}, \tag{5.9}$$

where τ and γ have the values 1000 and 1 respectively and θ_s^{max} is the maximum limit for θ_s (value of 2).

First, five cardiac cycles are run for the healthy case and the resulting values for $\overline{\mathrm{tr}(\mathbf{M}^e)}_h$ at the fifth cycle are saved. Then, twenty cycles with aortic stenosis and concentric hypertrophy are simulated with $\overline{\mathrm{tr}(\mathbf{M}^e)}_h$ as input and the spatial distribution of θ_s at the end of the twentieth cycle as output. Figure 5.2 displays this distribution on the anterior and posterior views of the epicardium, midmyocardium and endocardium and of two central transmural sections, a horizontal and a vertical one. Growth gets more and more pronounced from the endocardium to the epicardium, where wall stresses are higher [66,67]. As a remark, in the next figures, the two-dimensional distributions of electrical variables will be shown in the same nodes of Figure 5.2.

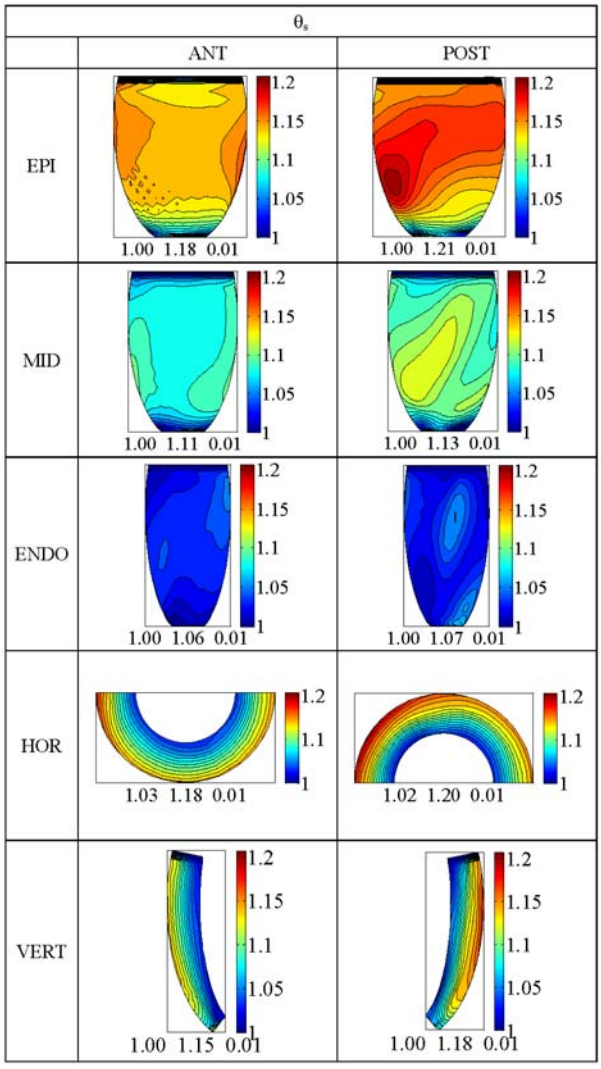

Figure 5.2: Spatial distributions of the growth parameter θ_s in case of the concentric hypertrophic ventricle on the anterior (ANT) and posterior (POST) views of the epicardium (EPI), midmyocardium (MID) and endocardium (ENDO) and of a central horizontal (HOR) and vertical (VERT) transmural section (see text for details on their derivation).

5.3. Results and discussion

5.3.1. The electrical response

An initial analysis on the relevance of the mechanical feedbacks in the Bidomain model of electrophysiology (5.4) is carried out. For both the healthy and hypertrophic ventricle, a cardiac cycle is simulated with: i) the conductivity feedback alone (COND); ii) the conductivity and convection feedbacks (COND+CONV); iii) the conductivity and mechanoelectric feedbacks (COND+SAC); iv) all three feedbacks (COND+CONV+SAC). All these simulations are performed starting from the values of all mechanical and electrical model variables, nodal coordinates, ventricular pressure P and volume derivative dV/dt saved at the end of five cycles run with the healthy or hypertrophic ventricle to reach a steady state. For the hypertrophic case, the values of θ_s saved at the end of the twentieth growth cycle represent further inputs.

Figure 5.3, Figure 5.4 and Figure 5.5 report the epicardial, midmyocardial and endocardial distributions (shown in the reference configuration) of the activation time AT, repolarization time RT and action potential duration APD=RT-AT for the healthy ventricle under all simulated conditions i)-iv). Figure 5.7, Figure 5.8 and Figure 5.9 show the corresponding distributions for the hypertrophic ventricle. Moreover, Figure 5.6 and Figure 5.10 display the horizontal and vertical transmural distributions of APD for both ventricles. In this chapter, AT is the time instant when V exceeds -40 mV and RT is the time instant when V becomes less than its 90% repolarization value (-76.5 mV). For both ventricles, the AT patterns on all anterior views are similar and characterized by a wavefront that, starting from the center of the endocardium where the stimulus is applied, spreads faster along the fibers direction than across them in an ellipsoidal way towards the epicardium, where it tends to become spherical. On the contrary, the AT patterns on all posterior views display a V shape that is distorted by the fibers twist and accentuates from the endocardium to the epicardium, similarly to an apical pacing of a ventricle characterized by a late activation of the base [34]. From a visual inspection, no immediate differences are detectable for both ventricles. By looking at the numbers under the maps, instead, the presence of the convective feedback in the COND+CONV case generates an increase of dispersion, given by the difference between the maximum and minimum values, of about 4 ms with respect to the COND case on the anterior views of the healthy ventricle. However, this reduction is partially cut down by adding the mechanoelectric feedback in the COND+CONV+SAC case (compare the COND and COND+SAC cases too). Such a trend is also present on the posterior views of the epicardium and midmyocardium. On the endocardium, instead, both the convective feedback and the mechanoelectric one cause a decrease of the AT dispersion, which amounts

to nearly 7 ms in the COND+CONV+SAC case. For the hypertrophic ventricle, the convective feedback affects the AT dispersion to a lower extent; actually, its increase is always lower than 2 ms between the COND case and the COND+CONV one. Nevertheless, the mechanoelectric feedback is responsible for a decrease up to about 4 ms on the posterior views between the COND case and the COND+SAC one. As regards RT, no differences are visible at first sight again. However, by looking at the maximum and minimum values, it turns out that the convective feedback determines the greatest variations on the posterior views of the healthy ventricle, especially the endocardial one, where an increase of dispersion of nearly 9 ms can be found between the COND case and the COND+CONV one. The mechanoelectric feedback tends to reduce RT everywhere, mainly on the posterior views again, where a decrease up to 4÷5 ms can be computed for the dispersion on the midmyocardium between the COND case and the COND+SAC one. With the hypertrophic ventricle, the effects of the former feedback vanish, whilst the ones of the latter are still present with the same decrease of dispersion of 4÷5 ms on the midmyocardium. As far as APD is concerned, it immediately appears that, for the healthy ventricle, its values are higher on average on every intramural posterior view where the convective feedback is present. Moreover, there is an increase of dispersion for all distributions between the COND case and the COND+CONV or COND+CONV+SAC one. Actually, for the anterior views, this increase amounts to nearly 13 ms on the epicardium and endocardium and about 9 ms on the midmyocardium. For the posterior views, it reaches about 20 ms on the endocardium, 19 ms on the epicardium and 13÷14 ms on the midmyocardium. The mechanoelectric feedback does not play a significant role instead. For the hypertrophic ventricle, the effects of the convective feedback on the anterior views disappear, whilst the ones on the posterior views are still present, even if to a lesser extent compared with the healthy ventricle. Actually, fewer nodes have a higher value for APD and the increase of dispersion amounts to 6 ms on the epicardium, 3 ms on the midmyocardium and 3÷4 ms on the endocardium. The mechanoelectric feedback tends to reduce APD mainly on the posterior views of the midmyocardium (compare the COND+SAC or COND+CONV+SAC case with the COND or COND+CONV one respectively). Similarly to the intramural distributions, the transmural ones for the healthy ventricle show an increase of the number of nodes with a higher value for APD on all posterior views where the convective feedback is present. Moreover, the dispersion rises on the horizontal and vertical posterior views and on the horizontal anterior view; in particular, shifts of 5÷6 ms characterize the horizontal views and a shift of 10÷11 ms characterize the vertical one. As for the intramural distributions again, no visible differences are introduced by the mechanoelectric feedback. Furthermore, fewer nodes have a higher value for APD when the convective feedback is taken into account for the hypertrophic ventricle. Such a feedback increases the dispersion to a lesser extent than the healthy ventricle, i.e. about 4 ms both on the horizontal and vertical posterior

views. The mechanoelectric feedback slightly reduces the APD values on all posterior views.

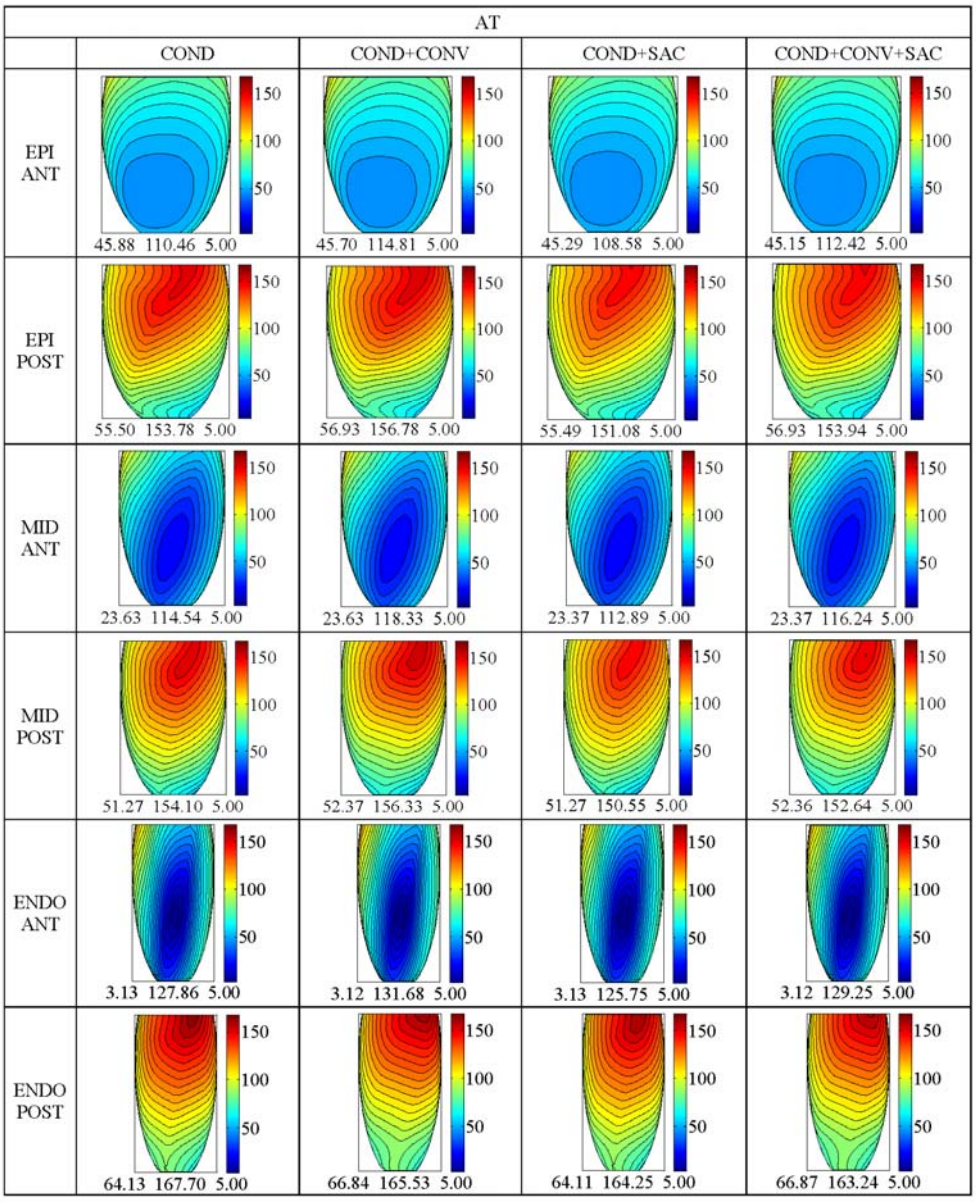

Figure 5.3: Spatial distributions of the activation time AT shown in the reference configuration in case of the healthy ventricle: anterior (ANT) and posterior (POST) views of the epicardium (EPI), midmyocardium (MID) and endocardium (ENDO). Simulations may include the conductivity feedback alone (COND) or together with the convection feedback (COND+CONV), the mechanoelectric feedback (COND+SAC) or both of them (COND+CONV+SAC). The minimum and maximum values and the step (all in ms) of the displayed maps are reported below each panel.

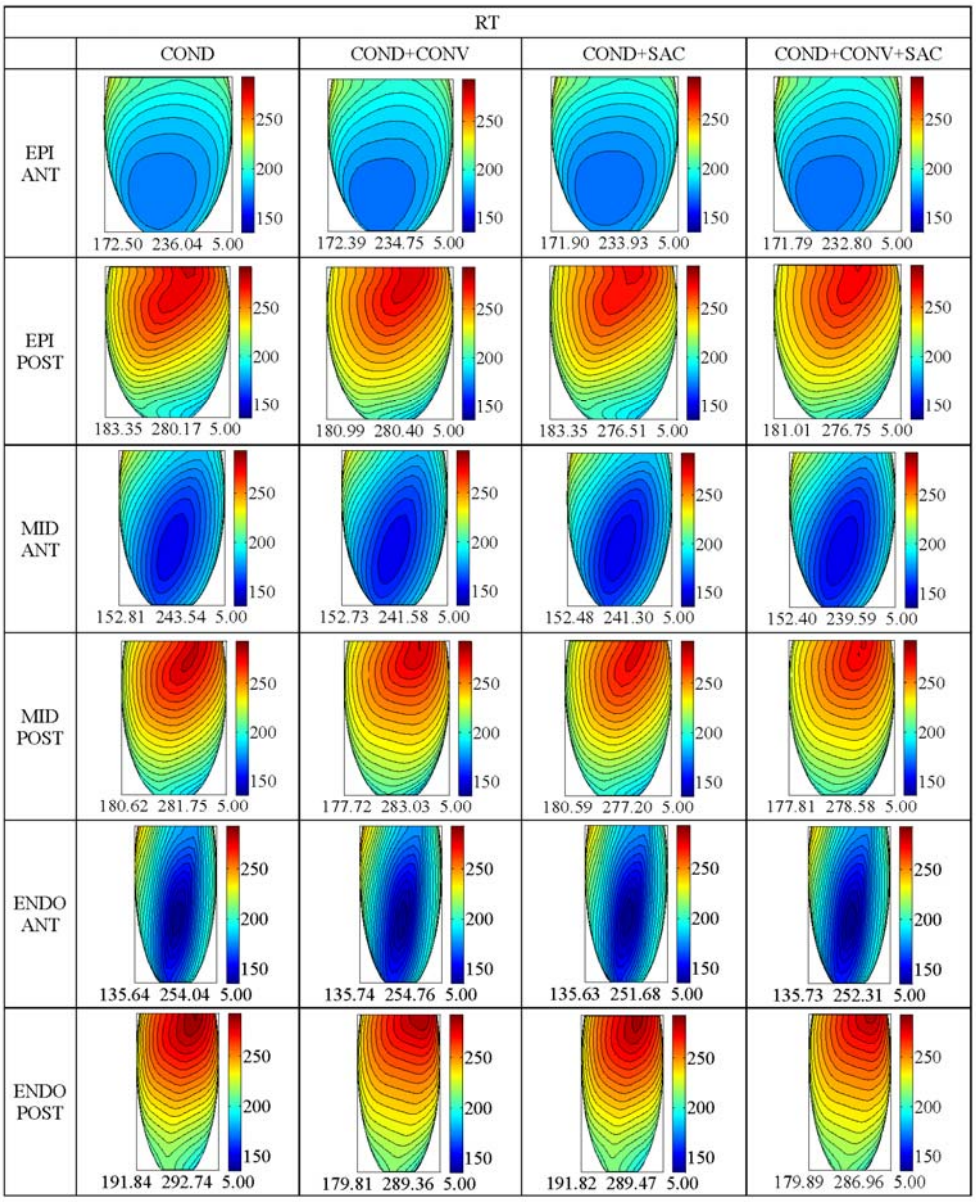

Figure 5.4: Spatial distributions of the repolarization time RT shown in the reference configuration in case of the healthy ventricle. Same format as in Figure 5.3.

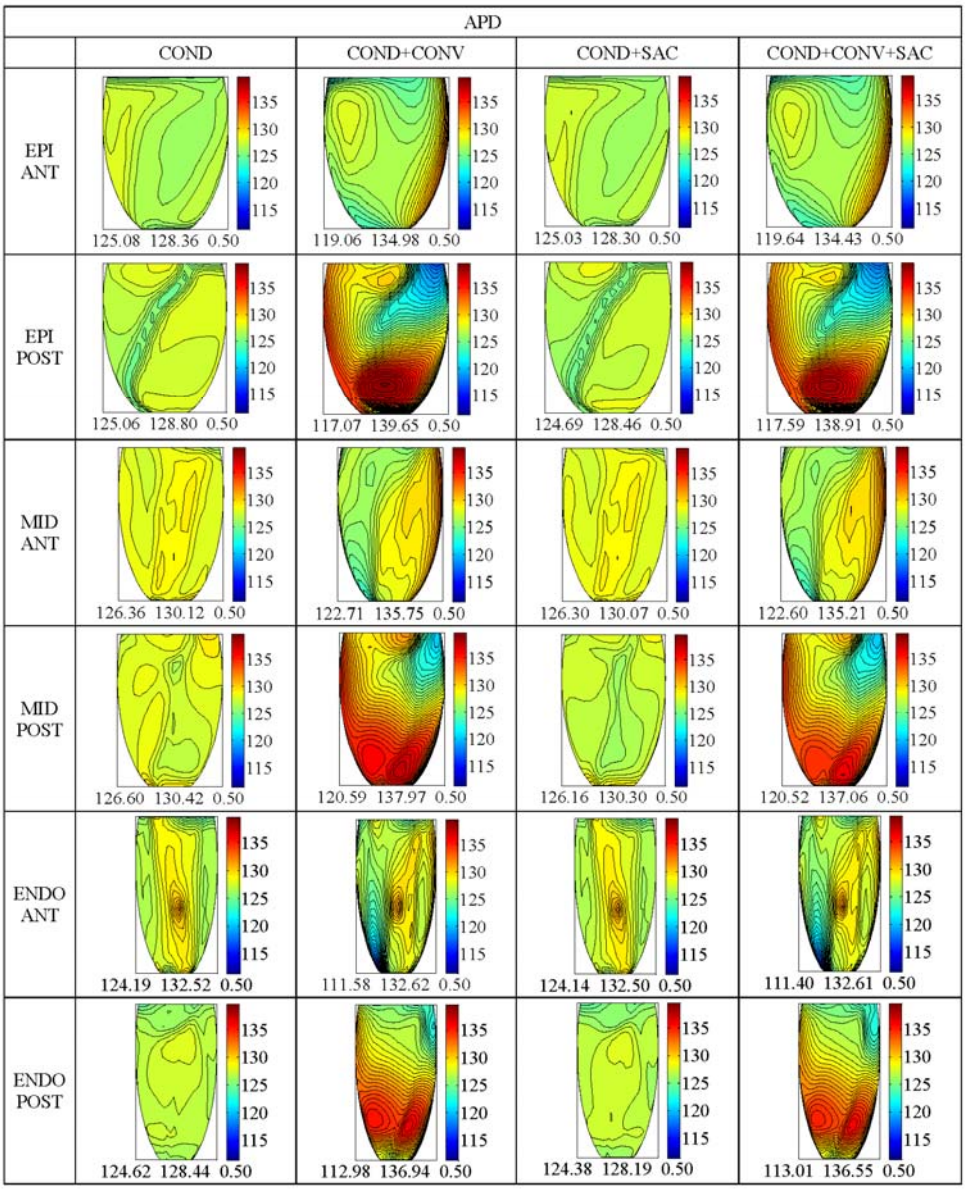

Figure 5.5: Spatial distributions of the action potential duration APD shown in the reference configuration in case of the healthy ventricle. Same format as in Figure 5.3.

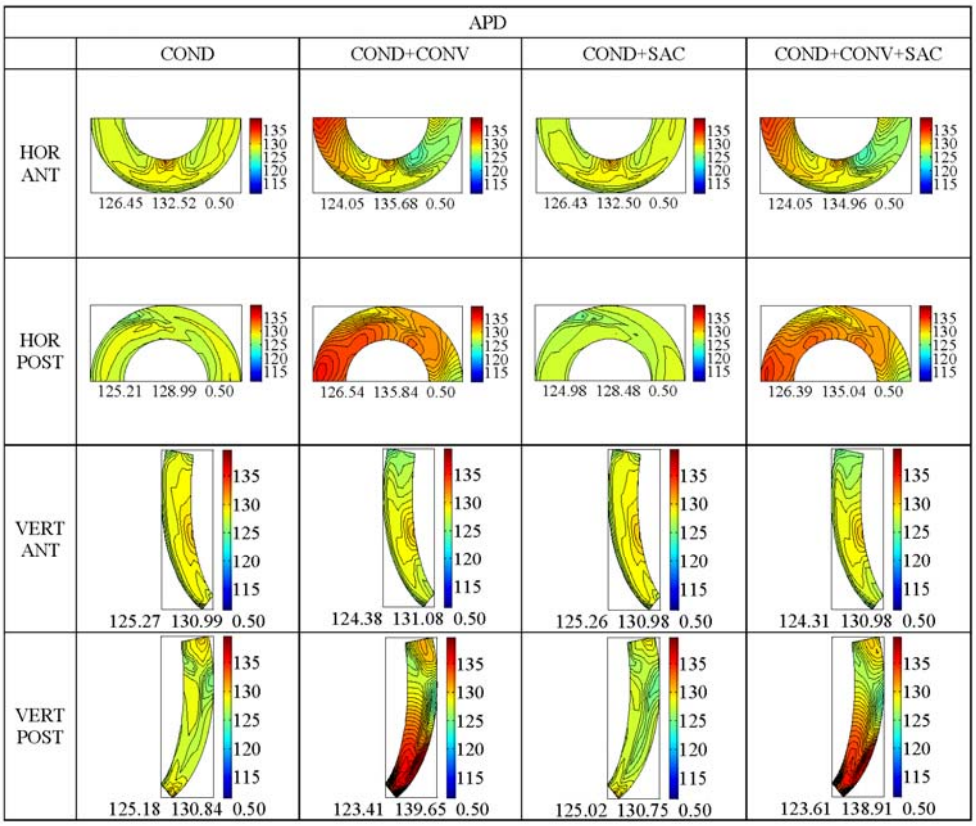

Figure 5.6: Spatial distributions of the action potential duration APD shown in the reference configuration in case of the healthy ventricle: anterior (ANT) and posterior (POST) views of the horizontal (HOR) and vertical (VERT) transmural sections. Simulations may include the conductivity feedback alone (COND) or together with the convection feedback (COND+CONV), the mechanoelectric feedback (COND+SAC) or both of them (COND+CONV+SAC). The minimum and maximum values and the step (all in ms) of the displayed maps are reported below each panel.

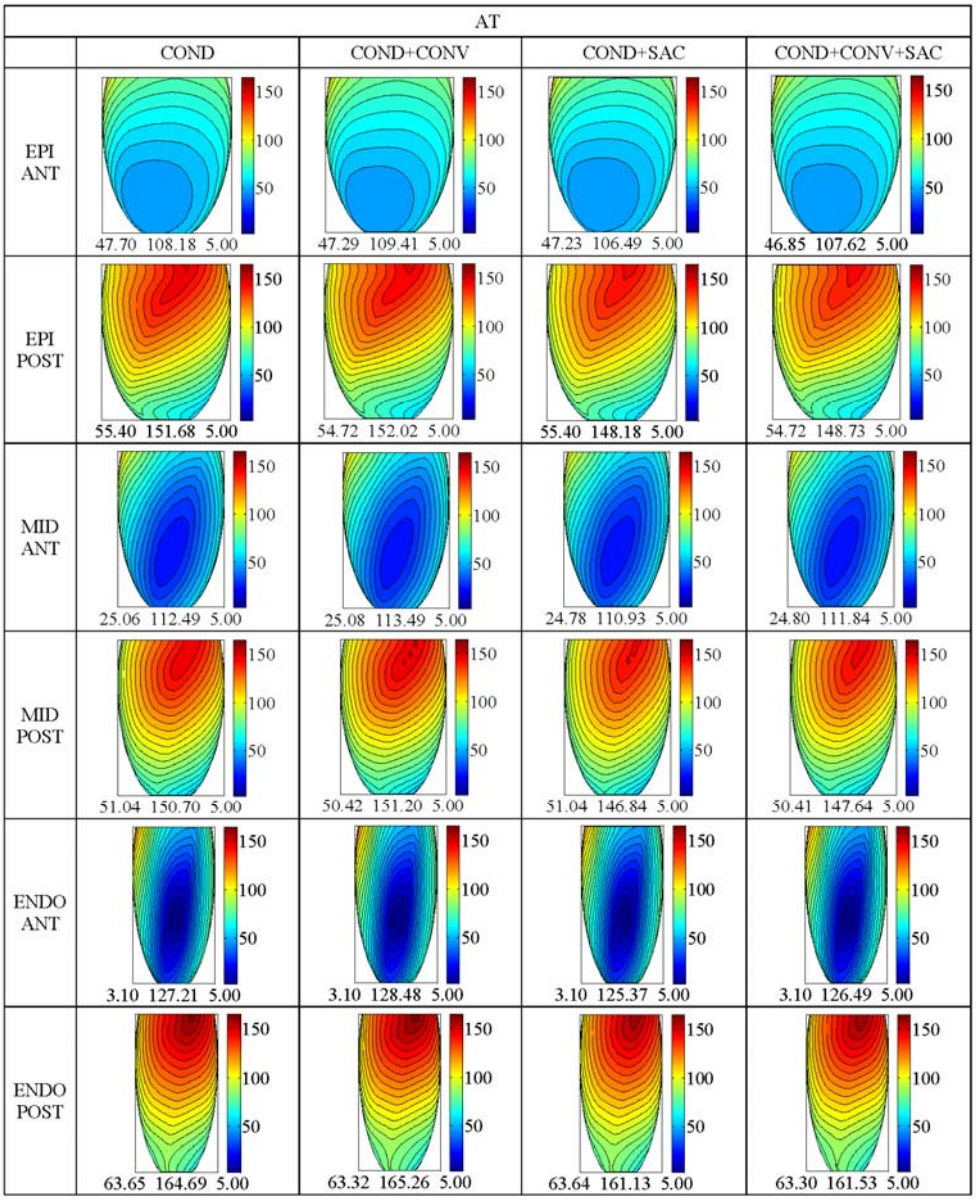

Figure 5.7: Spatial distributions of the activation time AT shown in the reference configuration in case of the hypertrophic ventricle. Same format as in Figure 5.3.

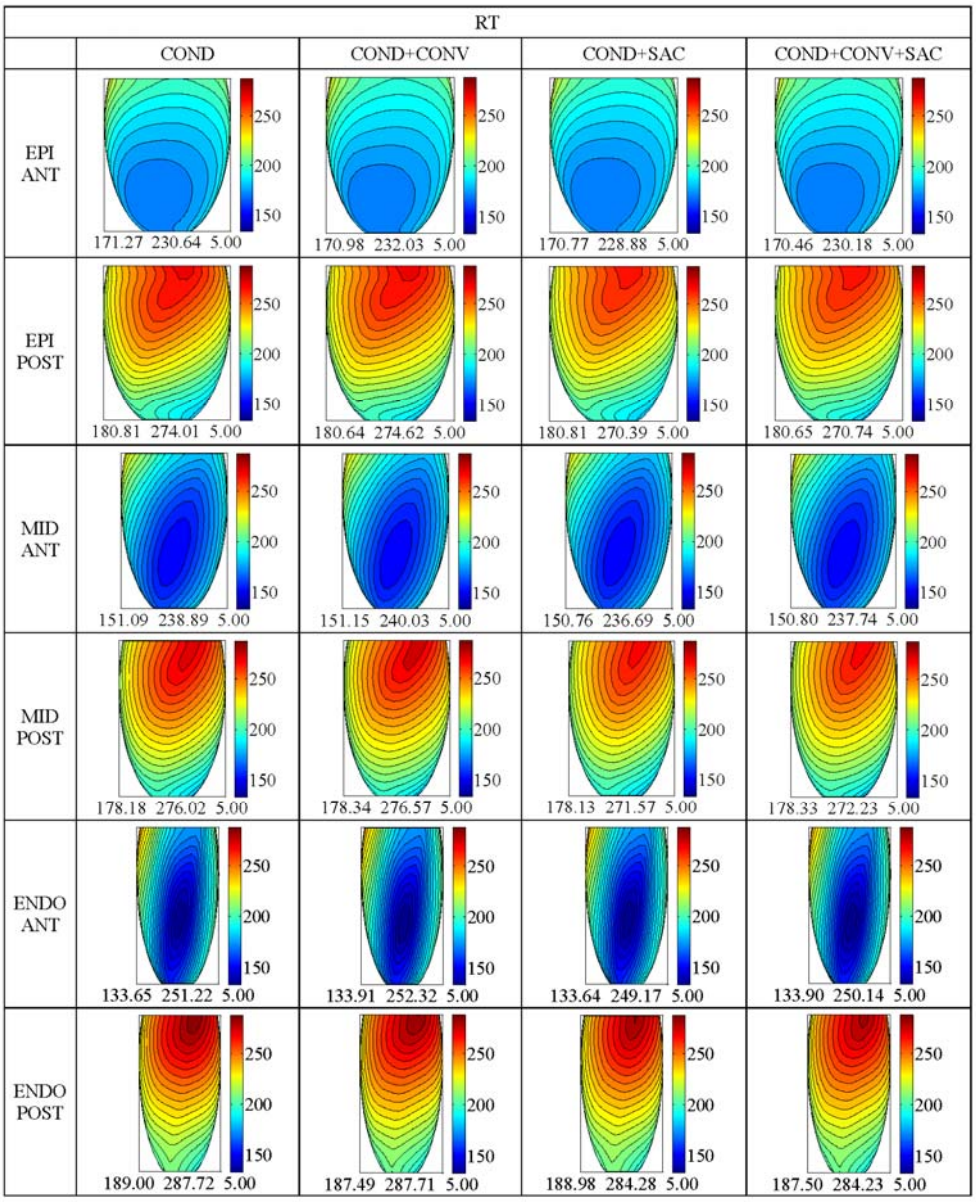

Figure 5.8: Spatial distributions of the repolarization time RT shown in the reference configuration in case of the hypertrophic ventricle. Same format as in Figure 5.3.

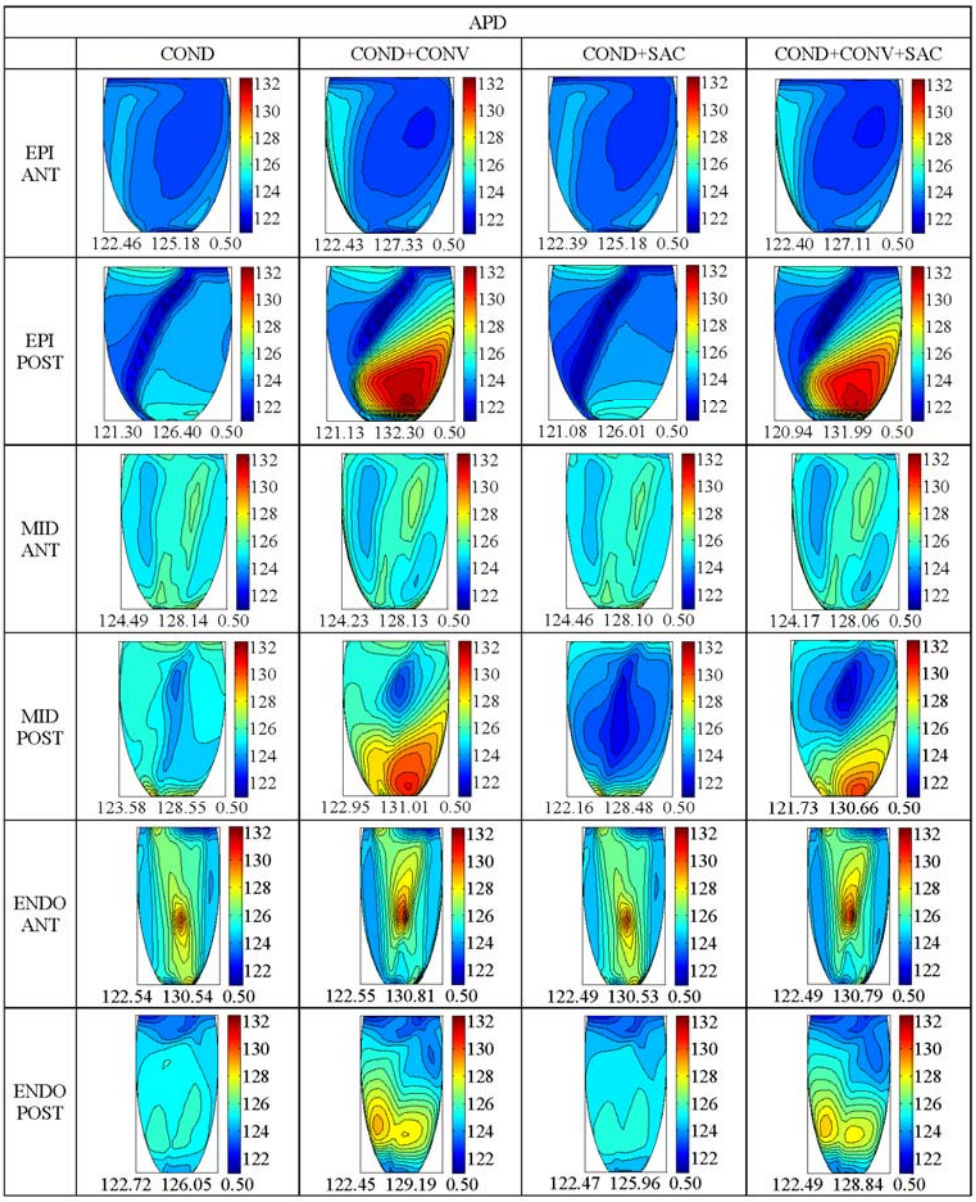

Figure 5.9: Spatial distributions of the action potential duration APD shown in the reference configuration in case of the hypertrophic ventricle. Same format as in Figure 5.3.

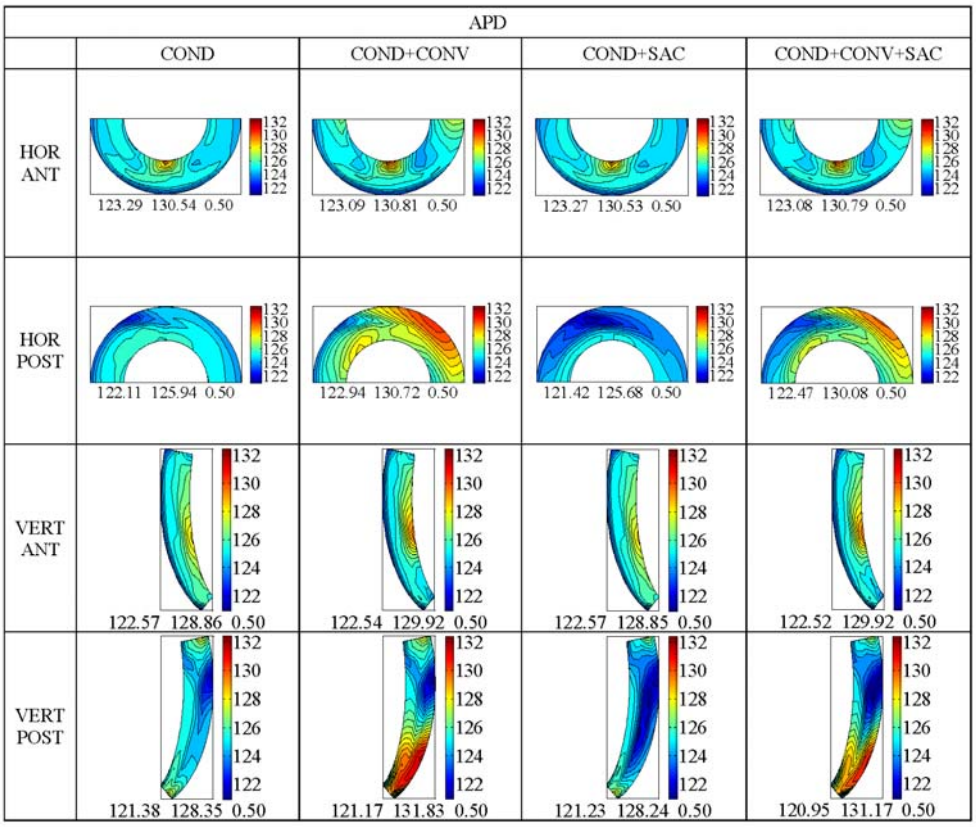

Figure 5.10: Spatial distributions of the action potential duration APD shown in the reference configuration in case of the hypertrophic ventricle. Same format as in Figure 5.6.

The total AT, RT and APD dispersions, i.e. the differences between their maximum and minimum values in the whole ventricle, are reported in Table 5.2. They point out that the total AT dispersion reduces by about 4-5 ms between the COND case and the COND+CONV+SAC one for the healthy ventricle, thus both the convective feedback and the mechanoelectric one are responsible for this decrease. This also happens for the total RT dispersion, which reduces up to nearly 6 ms. The total APD dispersion, instead, rises by about 19÷20 ms when the sole convective feedback is included, whereas the mechanoelectric one has no effects. The total AT and RT dispersions of the hypertrophic ventricle are affected from the sole mechanoelectric feedback, which determines decreases of 3÷4 ms when it is included. As for the healthy ventricle, the convective feedback acts on the total APD dispersion of the hypertrophic one, but it causes an increase of only 2 ms when it is accounted for.

Table 5.3 collects the relative errors for AT, RT and APD between the COND+CONV+SAC case (that is the most complete model) and the other ones. For the healthy ventricle, the convection feedback determines the smallest error on AT, RT and APD. However, for the hypertrophic

ventricle, the convective feedback is predominant for APD only, whilst the mechanoelectric one has the major effect on AT and RT.

Table 5.2: Total dispersions (differences between the maximum and minimum values in the whole ventricle) in ms of the activation time AT, repolarization time RT and action potential duration APD in case of the healthy (A) and hypertrophic (B) ventricles. Simulations may include the conductivity feedback alone (COND) or together with the convection feedback (COND+CONV), the mechanoelectric feedback (COND+SAC) or both of them (COND+CONV+SAC).

A

	HEALTHY			
	COND	COND+CONV	COND+SAC	COND+CONV+SAC
AT dispersion	164.57	162.41	161.12	160.12
RT dispersion	157.10	153.62	153.84	151.23
APD dispersion	8.33	28.07	8.36	27.50

B

	HYPERTROPHIC			
	COND	COND+CONV	COND+SAC	COND+CONV+SAC
AT dispersion	161.58	162.16	158.03	158.43
RT dispersion	154.08	153.80	150.64	150.33
APD dispersion	9.24	11.28	9.46	11.07

Table 5.3: Relative errors of the activation time AT, repolarization time RT and action potential duration APD in case of the healthy (A) and hypertrophic (B) ventricles. All errors are computed with respect to the associated reference variable belonging to a simulation with all mechanical feedbacks, i.e. the conductivity, convection and mechanoelectric ones. The symbol * denotes a simulation disregarding the convection and mechanoelectric feedbacks (COND), the sole mechanoelectric feedback (COND+CONV) or the sole convection feedback (COND+SAC).

A

	HEALTHY		
	* = COND	* = COND+CONV	* = COND+SAC
$\|\|AT_{*}-AT_{REF}\|\|_2 / \|\| AT_{REF} \|\|_2$	$3.71 \cdot 10^{-2}$	$1.77 \cdot 10^{-2}$	$3.30 \cdot 10^{-2}$
$\|\|RT_{*}-RT_{REF}\|\|_2 / \|\| RT_{REF} \|\|_2$	$1.79 \cdot 10^{-2}$	$8.34 \cdot 10^{-3}$	$1.76 \cdot 10^{-2}$
$\|\|APD_{*}-APD_{REF}\|\|_2 / \|\| APD_{REF} \|\|_2$	$3.13 \cdot 10^{-2}$	$3.73 \cdot 10^{-3}$	$3.21 \cdot 10^{-2}$

B

	HYPERTROPHIC		
	* = COND	* = COND+CONV	* = COND+SAC
$\|\|AT_{*}-AT_{REF}\|\|_2 / \|\| AT_{REF} \|\|_2$	$2.10 \cdot 10^{-2}$	$1.70 \cdot 10^{-2}$	$1.33 \cdot 10^{-2}$
$\|\|RT_{*}-RT_{REF}\|\|_2 / \|\| RT_{REF} \|\|_2$	$9.12 \cdot 10^{-3}$	$8.79 \cdot 10^{-3}$	$7.01 \cdot 10^{-3}$
$\|\|APD_{*}-APD_{REF}\|\|_2 / \|\| APD_{REF} \|\|_2$	$1.24 \cdot 10^{-2}$	$4.26 \cdot 10^{-3}$	$1.36 \cdot 10^{-2}$

From now on, the effects of all mechanical feedbacks will be included while comparing the electrical and mechanical responses of healthy and hypertrophic ventricles. Thus, Figure 5.11, Figure 5.12, Figure 5.13, Figure 5.14, Figure 5.15 and Figure 5.16 first collect the epicardial, midmyocardial, endocardial and horizontal and vertical transmural distributions of AT, RT and APD for the COND+CONV+SAC case and both ventricles. The corresponding distributions for the case of aortic stenosis without growth at steady state are also shown. It turns out that the healthy and stenotic cases are almost equal; from a visual inspection, one can only find a slight decrease in APD values on the horizontal views from the former case to the latter one. However, the strongest decrease of AT, RT and APD values occurs with hypertrophy. Moreover, the corresponding dispersions decrease more than increasing; actually, the maximum increments with respect to the healthy case are about 4 ms, about 5 ms and less than 1 ms for AT, RT and APD respectively, whilst the maximum decrements are 6÷7 ms, about 10 ms and about 17 ms. Therefore, although concentric hypertrophy causes a lowering of the action potential duration, it increases the propagation velocity (related to the inverse of the activation time) and does not affect negatively the RT dispersion, thus trying to avoid triggering arrhythmogenic phenomena [36]. The result on propagation velocity differs from the one reported in Chapter 4 for the wedge and it may be due mainly to the fact that the conductivity coefficients are here dependent on local growth.

At last, Figure 5.17 displays the time evolutions of the extracellular potential U_e (or unipolar electrograms) in eighteen nodes located along the middle longitudinal lines of the anterior and posterior views of the epicardium (six nodes), midmyocardium (six nodes) and endocardium (six nodes) near the apex, the center and the base of the healthy, stenotic and hypertrophic ventricles. For all ventricles, there is always a discordance between the polarity of the QRS complex and the one of the T wave, i.e. if the former is positive, then the latter is negative and vice versa. No relevant morphological changes in the QRS complexes, ST segments and T waves are detectable. Some discrepancies are only found in terms of time delays on the posterior views, which are the latest activated areas; the total duration of the response is shortened in accordance with the previous lowering of the action potential duration. Therefore, once again, if local conductivity coefficients change with growth, the activation wavefront and the subsequent repolarization phase are not negatively affected from hypertrophy.

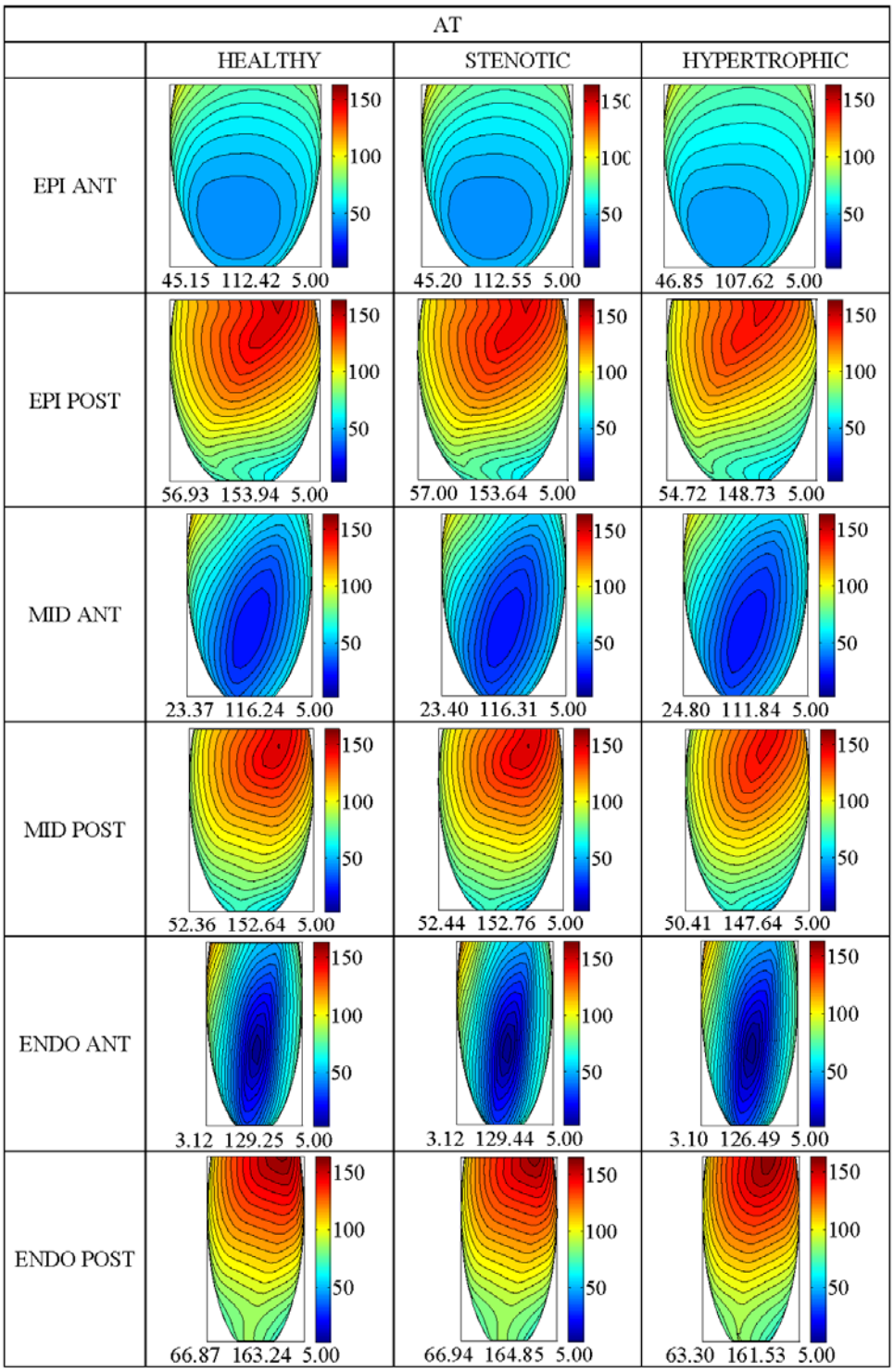

Figure 5.11: Spatial distributions of the activation time AT shown in the reference configuration for the healthy, stenotic and hypertrophic ventricles with all mechanical feedbacks included: anterior (ANT) and posterior (POST) views of the epicardium (EPI), midmyocardium (MID) and endocardium (ENDO). The minimum and maximum values and the step (all in ms) of the displayed maps are reported below each panel.

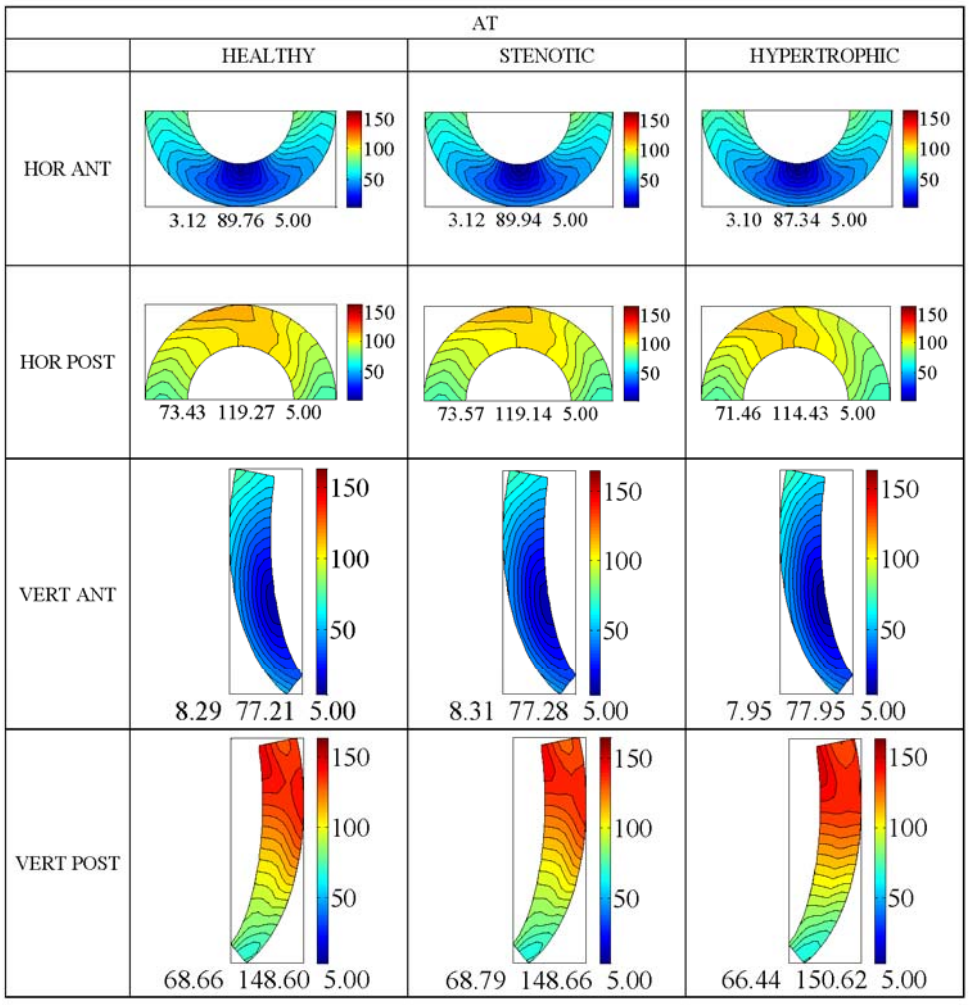

Figure 5.12: Spatial distributions of the activation time AT shown in the reference configuration for the healthy, stenotic and hypertrophic ventricles with all mechanical feedbacks included: anterior (ANT) and posterior (POST) views of the horizontal (HOR) and vertical (VERT) transmural sections. The minimum and maximum values and the step (all in ms) of the displayed maps are reported below each panel.

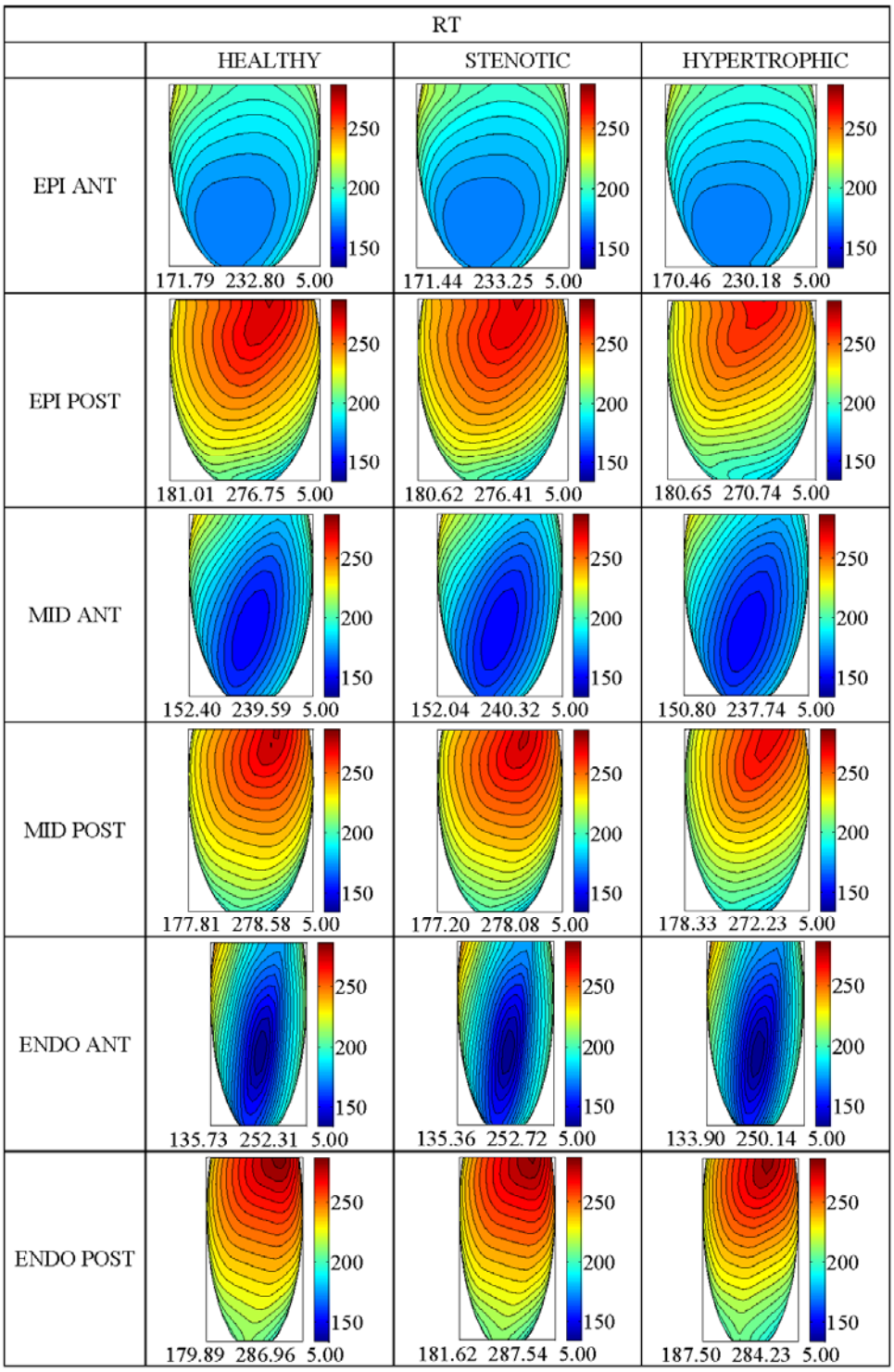

Figure 5.13: Spatial distributions of the repolarization time RT shown in the reference configuration for the healthy, stenotic and hypertrophic ventricles with all mechanical feedbacks included. Same format as in Figure 5.11.

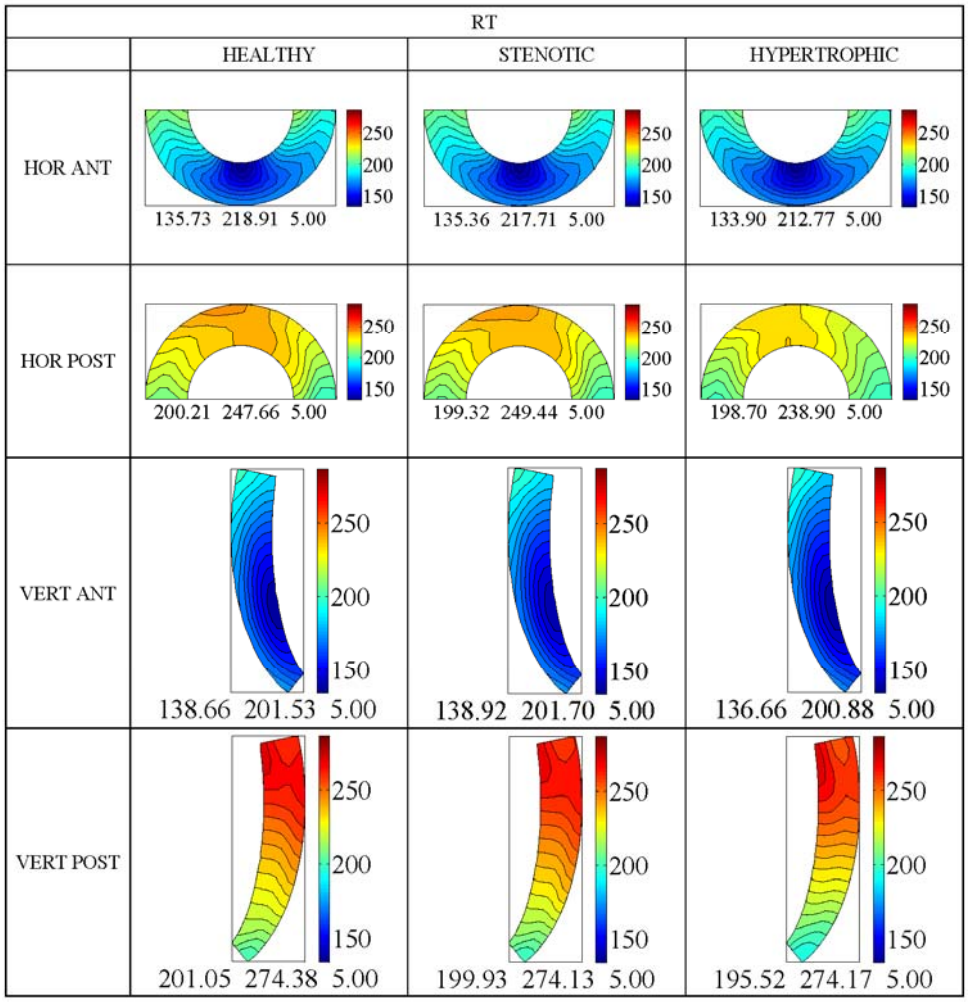

Figure 5.14: Spatial distributions of the repolarization time RT shown in the reference configuration for the healthy, stenotic and hypertrophic ventricles with all mechanical feedbacks included. Same format as in Figure 5.12.

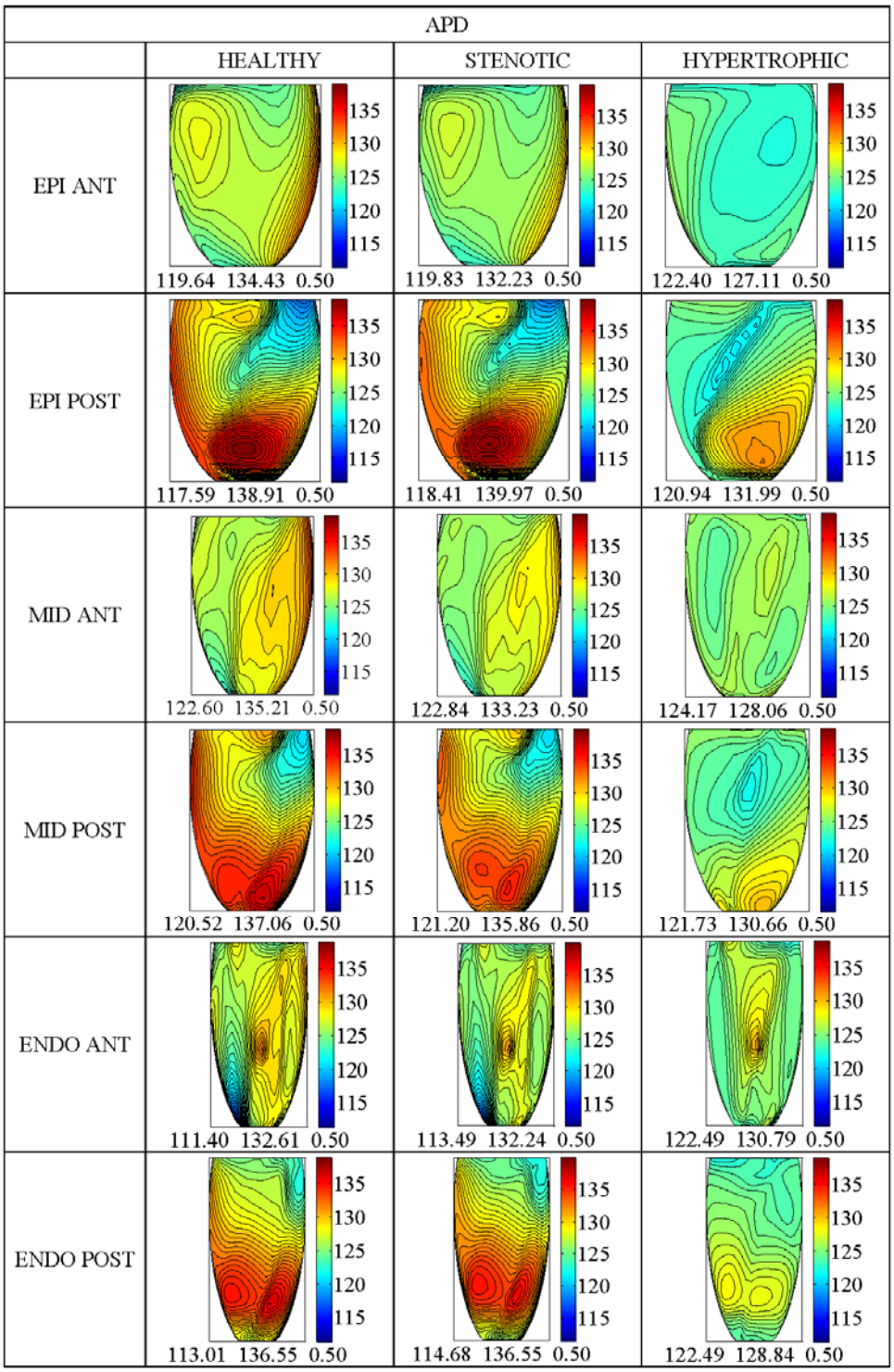

Figure 5.15: Spatial distributions of the action potential duration APD shown in the reference configuration for the healthy, stenotic and hypertrophic ventricles with all mechanical feedbacks included. Same format as in Figure 5.11.

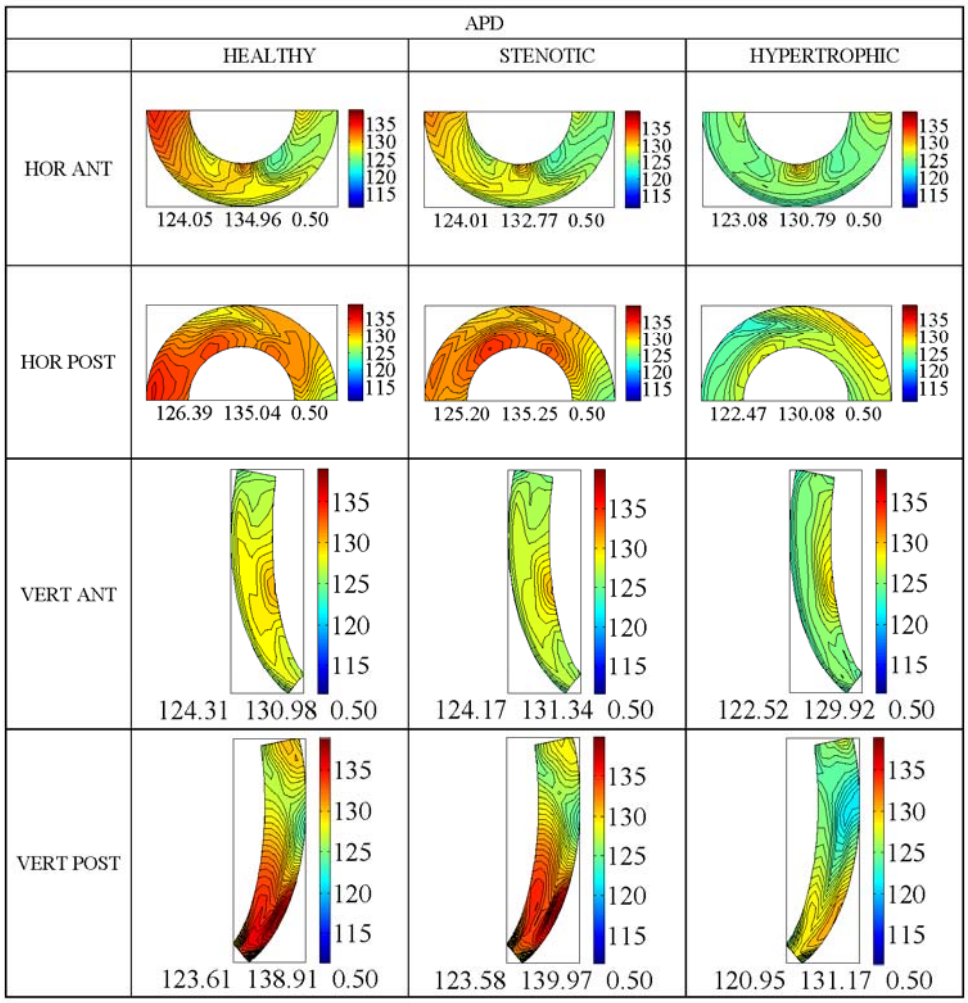

Figure 5.16: Spatial distributions of the action potential duration APD shown in the reference configuration for the healthy, stenotic and hypertrophic ventricles with all mechanical feedbacks included. Same format as in Figure 5.12.

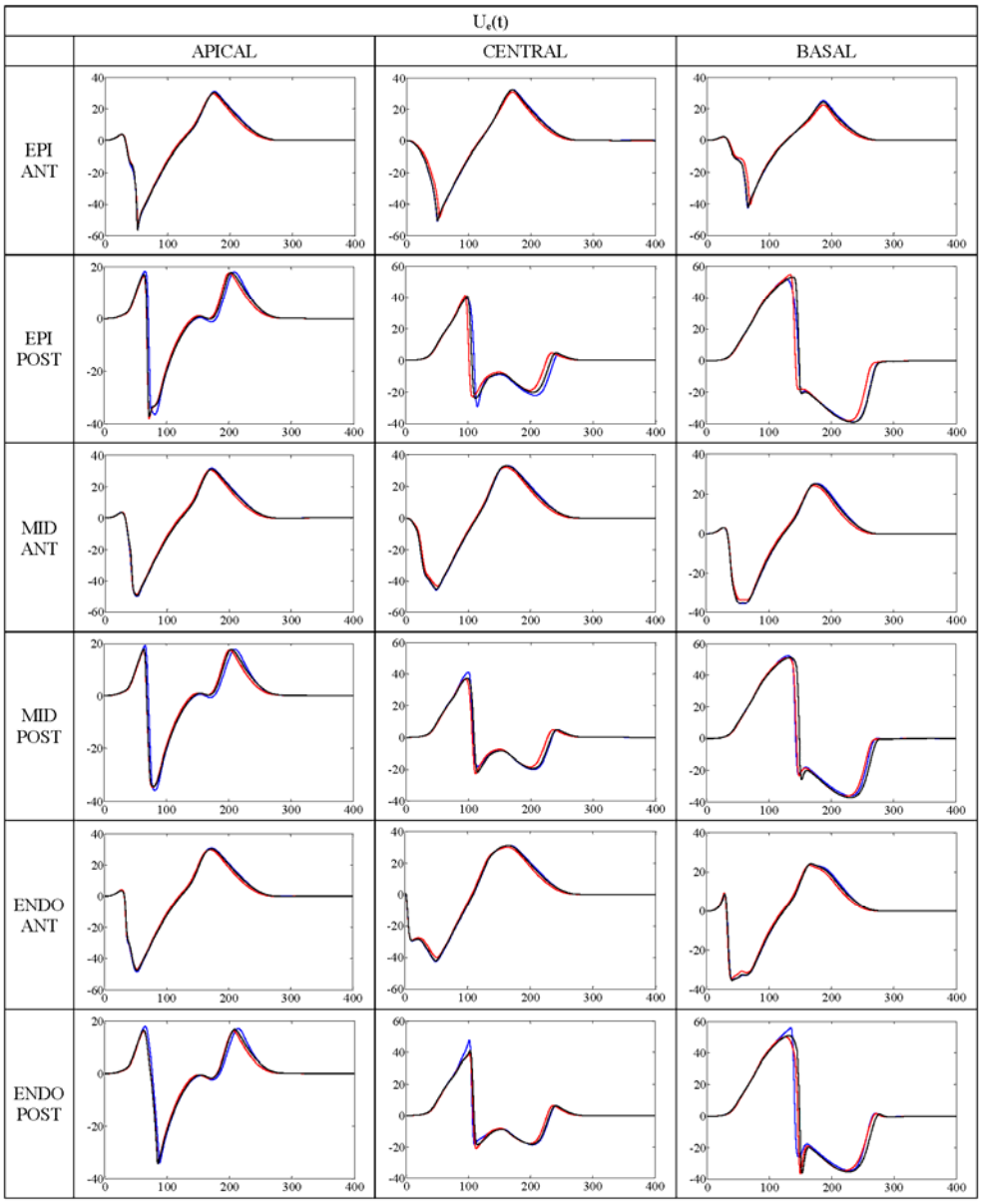

Figure 5.17: Electrograms U_e in eighteen epicardial, midmyocardial and endocardial nodes on the anterior (ANT) and posterior (POST) views near the apex, the center and the base of the healthy (blue), stenotic (black) and hypertrophic (red) ventricles; all values on the abscissa are in ms, whereas the ones on the ordinate are in mV.

5.3.2. The mechanical response

Figure 5.18 shows the steady-state pressure-volume loops related to the healthy, stenotic and hypertrophic ventricles. Compared with the healthy case, the two ventricles affected from aortic stenosis display an increase of pressure during the blood efflux phase due to a higher value of R_{ao}, which acts as an afterload, thus determining a higher end-systolic value for the developed pressure. However, by comparing the stenotic and hypertrophic

cases, it turns out that growth tends to reduce, i.e. normalize, the end-systolic pressure. Moreover, by growth, the ventricle recovers its healthy end-systolic volume, hence counteracting the increase due to stenosis, which limits the ejection of blood. Nevertheless, during the diastolic filling, it cannot reach its healthy end-diastolic volume for a given EDP, which represents the preload [15], thus impairing filling and leading to possible diastolic dysfunction. As a remark, the healthy value for the end-systolic volume may not be recovered if one modified the coefficients of the strain-energy function in (5.3) and/or added fiber dispersion in order to account for a remodeling accompanying hypertrophy too (see, e.g., [51]).

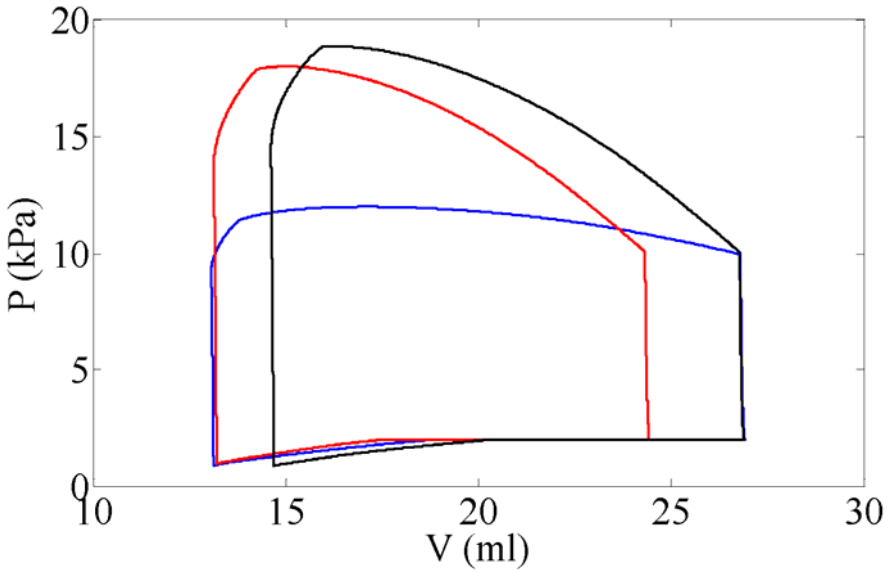

Figure 5.18: Pressure-volume (P-V) loops of the healthy (blue), stenotic (black) and hypertrophic (red) ventricles.

Figure 5.19, Figure 5.20, Figure 5.21, Figure 5.22, Figure 5.23 and Figure 5.24 report the end-systolic and end-diastolic epicardial, midmyocardial, endocardial and horizontal and vertical transmural distributions of the elastic longitudinal strain E^e_{ll}, circumferential strain E^e_{cc} and radial strain E^e_{rr} for the healthy, stenotic and hypertrophic ventricles; the end-diastolic strains for the stenotic case are not displayed because stenosis acts only during the blood efflux phase, hence they would coincide with the healthy ones. The longitudinal strains are directed along the axis tangent to the ventricular surface in each node from the apex to the base and they point out to which extent the ventricles contract/relax along the Z axis. The hypertrophic ventricle shows more positive values for them on the epicardium (where the values for θ_s are maximal) both at end systole and at end diastole compared with the healthy and stenotic ones, meaning that growth makes the epicardial wall contract to a lesser extent during the blood efflux phase and stretch to a higher extent during the diastolic filling.

The circumferential strains lie on the axis tangent to the wall plane in the circumferential direction and they measure the twist of ventricles. More precisely, at end systole, this twist is due to an opposite trend between the anterior and posterior views, which is maximal on the epicardium; one can also guess that ventricles twist clockwise with less positive values on the anterior views, where fibers are more contracted, and more positive values on the posterior views, where fibers are more stretched. Then, by comparing the three ventricles, it turns out that the values of the stenotic ventricle are slightly more positive on all views at end systole compared with the healthy one. The hypertrophic ventricle tends to enhance this trend on the epicardium, whilst it causes the opposite phenomenon on the endocardium, where values get closer to the healthy ones again. Therefore, similarly to the longitudinal strains at end diastole, growth on the epicardium makes fibers on the posterior views stretch to a higher extent during the systolic twist, but, in accordance to the longitudinal strains at end systole, it reduces their contraction on the anterior views. At end diastole, less homogenous and less positive values characterize the hypertrophic ventricle on the endocardium, meaning that it keeps more twisted there. The radial strains are computed along the axis from the endocardium to the epicardium and they quantify the inflation/deflation of the ventricular wall. Their trend is opposite to the one of the longitudinal strains. At end systole, the former ones are more positive on the endocardium and more negative on the epicardium, whilst at end diastole they are more negative everywhere. On the contrary, at end systole the latter ones are more negative on the endocardium and more positive on the epicardium, whereas at end diastole they are more positive everywhere. Then, they are generally less positive for the stenotic ventricle compared with the healthy one on all views at end systole. Hypertrophy emphasizes this trend on the epicardium, pointing out that growth limits the enlargement of the ventricular wall there, while normalizing the values on the endocardium. No differences are detectable at end diastole instead.

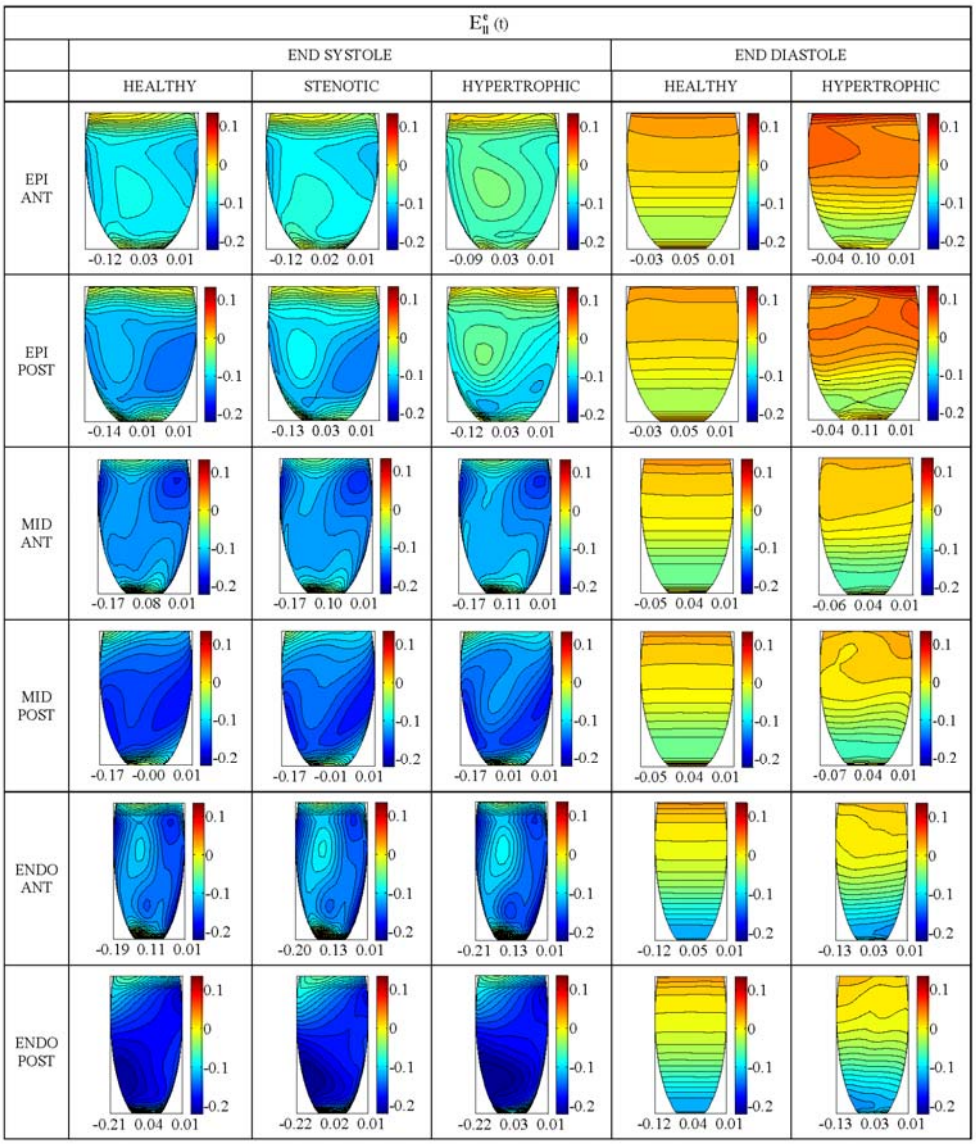

Figure 5.19: End-systolic and end-diastolic spatial distributions of the elastic longitudinal strain E^e_{ll} shown in the reference configuration for the healthy, stenotic and hypertrophic ventricles: anterior (ANT) and posterior (POST) views of the epicardium (EPI), midmyocardium (MID) and endocardium (ENDO). The minimum and maximum values and the step of the displayed maps are reported below each panel.

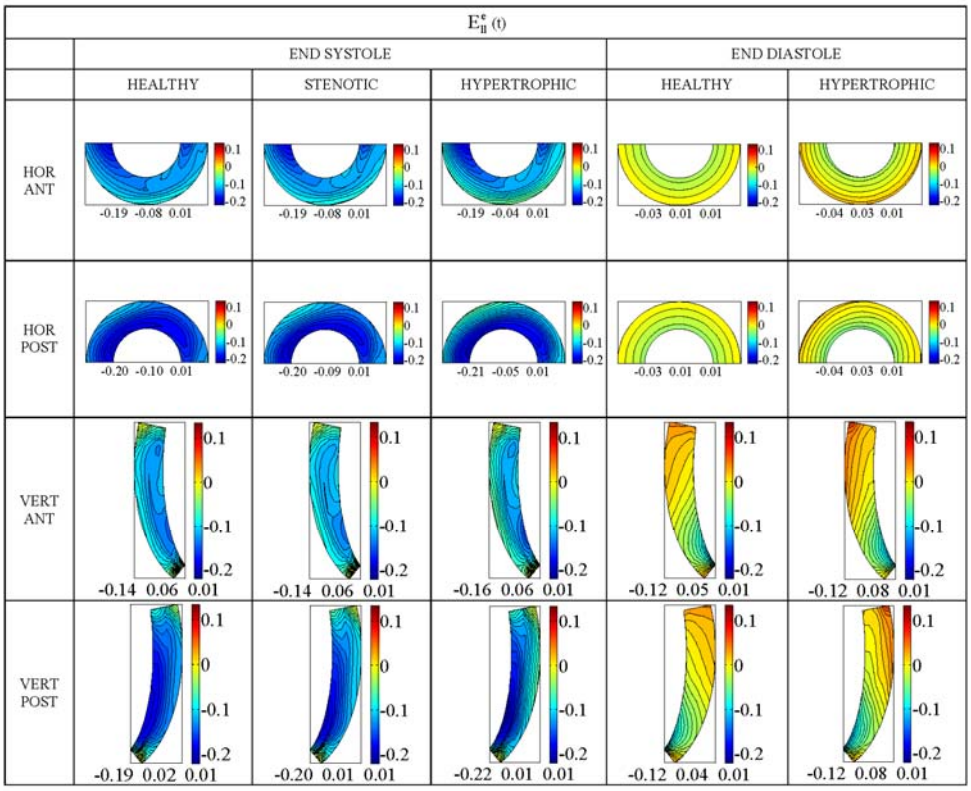

Figure 5.20: End-systolic and end-diastolic spatial distributions of the elastic longitudinal strain E^e_{ll} shown in the reference configuration for the healthy, stenotic and hypertrophic ventricles: anterior (ANT) and posterior (POST) views of the horizontal (HOR) and vertical (VERT) transmural sections. The minimum and maximum values and the step of the displayed maps are reported below each panel.

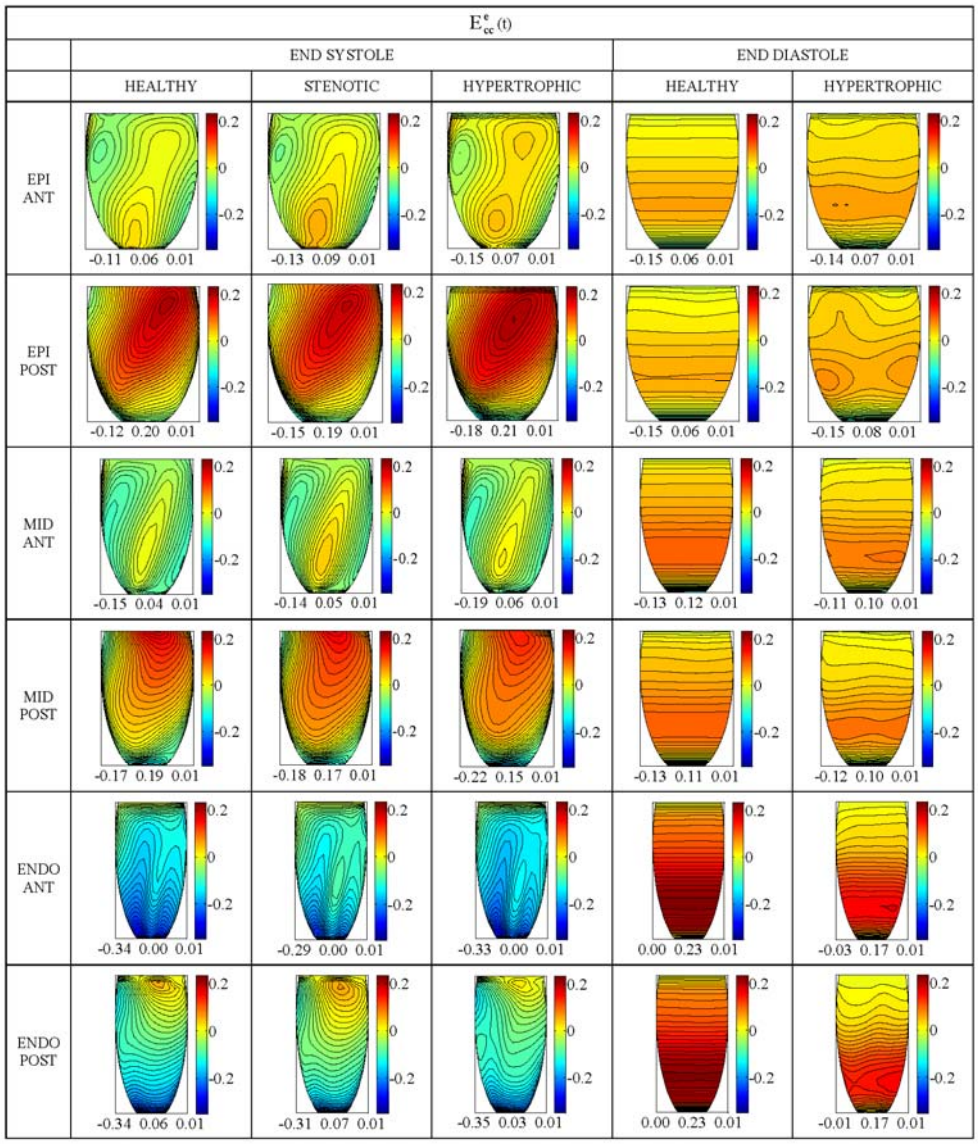

Figure 5.21: End-systolic and end-diastolic spatial distributions of the elastic circumferential strain E^e_{cc} shown in the reference configuration for the healthy, stenotic and hypertrophic ventricles. Same format as in Figure 5.19.

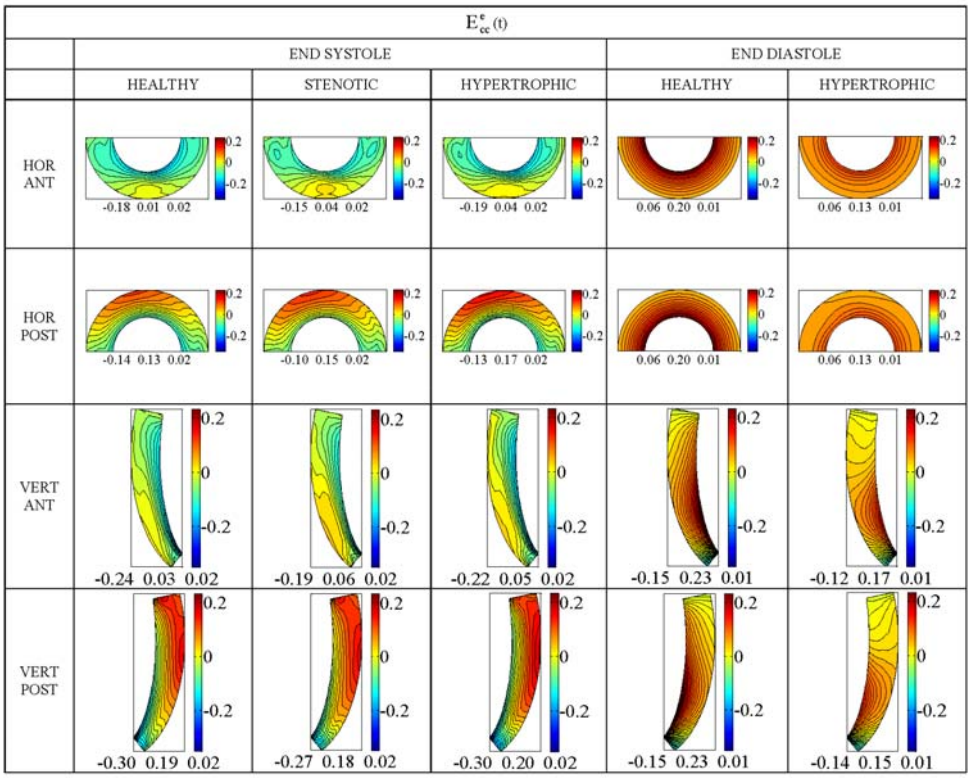

Figure 5.22: End-systolic and end-diastolic spatial distributions of the elastic circumferential strain E^e_{cc} shown in the reference configuration for the healthy, stenotic and hypertrophic ventricles. Same format as in Figure 5.20.

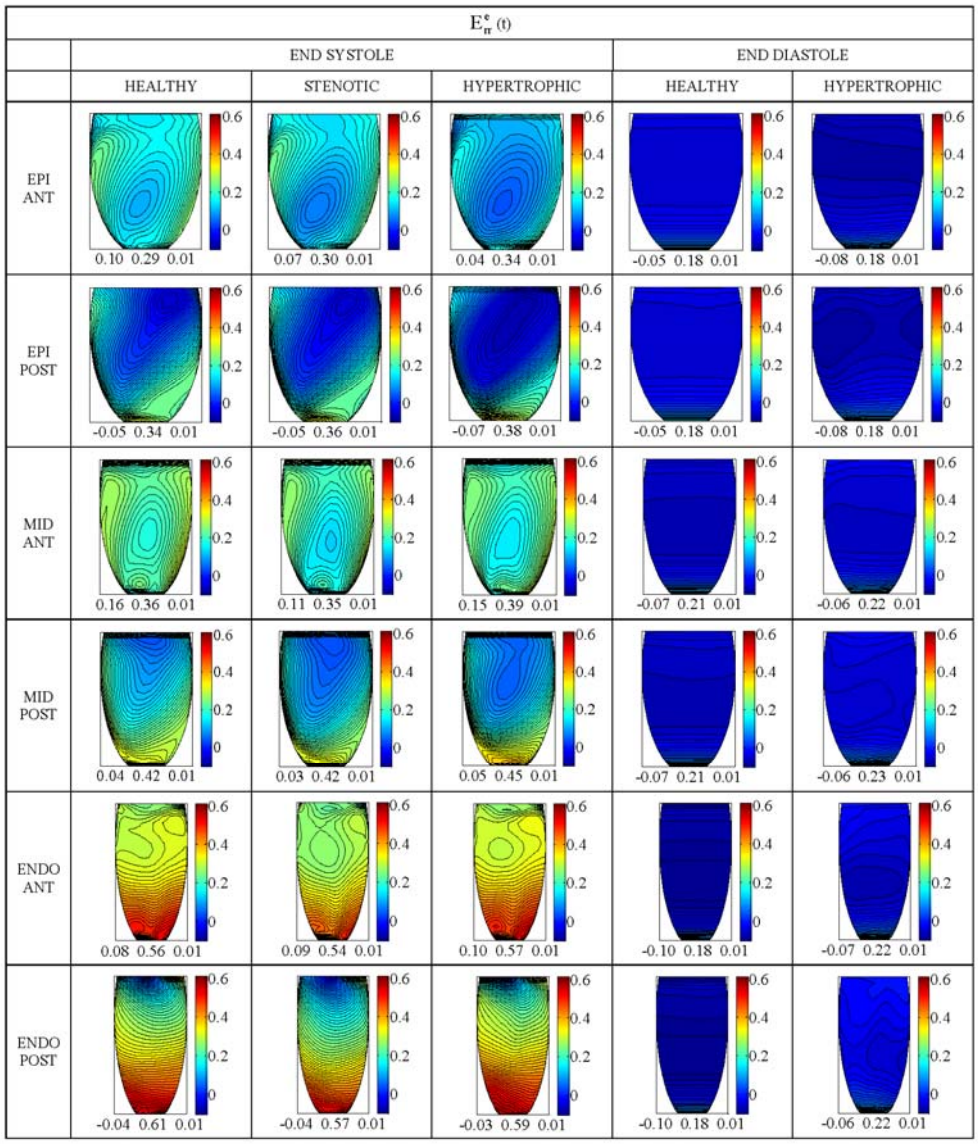

Figure 5.23: End-systolic and end-diastolic spatial distributions of the elastic radial strain E^e_{rr} shown in the reference configuration for the healthy, stenotic and hypertrophic ventricles. Same format as in Figure 5.19.

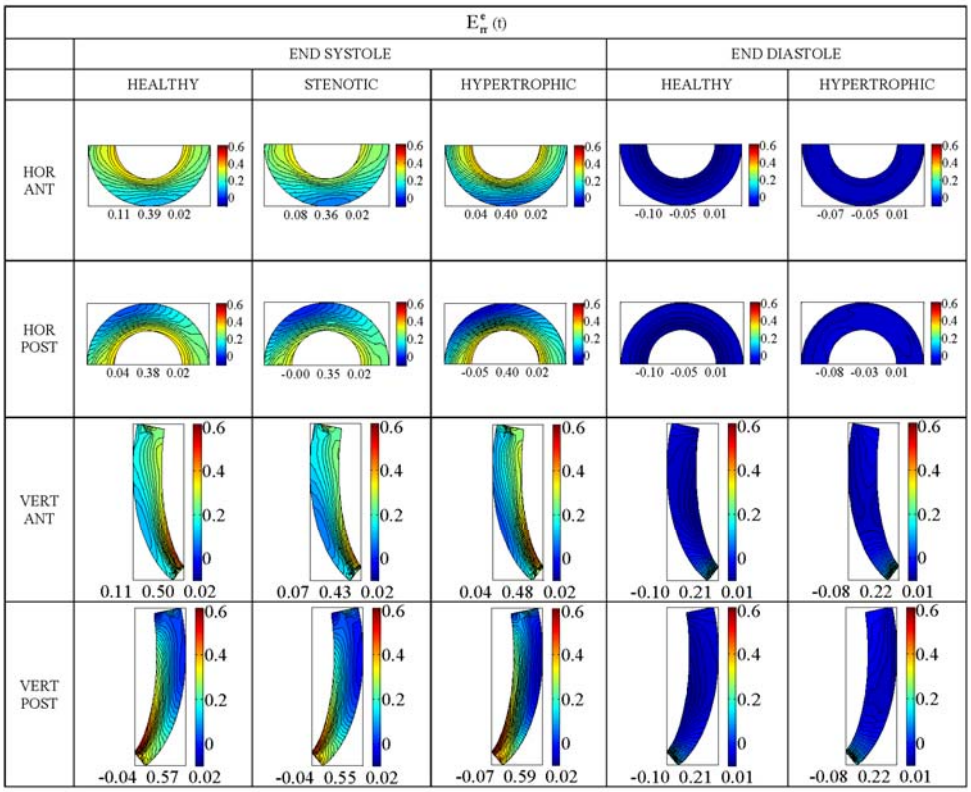

Figure 5.24: End-systolic and end-diastolic spatial distributions of the elastic radial strain E^e_{rr} shown in the reference configuration for the healthy, stenotic and hypertrophic ventricles. Same format as in Figure 5.20.

In addition to loops and strains, the same macroscopic measures introduced in Chapter 4 to describe the mechanical activity of the wedge are here computed again for the ventricle over one cycle, i.e. the mean contractility CT_{mean} (that directly corresponds to the contractility CT in this case) during the blood efflux phase and the mean contraction force CF_{mean}. In particular, the algorithm already described in two dimensions on the XY coordinate plane is extended to the three-dimensional case by computing the displacements $(z_{m+1}\text{-}z_m)$ and contraction velocities $v_{z,m}=(z_{m+1}\text{-}z_m)/\Delta t_{mec}$ along the Z axis too. In this chapter, 216 equidistant nodes are selected as markers on the epicardium. The resulting values for CT and CF_{mean} belonging to a simulation with the healthy (H), stenotic (STEN) or hypertrophic (HYP) ventricle are statistically compared by means of the one-way ANOVA and LSD test with a significance level of 0.05 as in Chapter 4. Figure 5.25 shows these results. It appears that CT does not vary significantly ($p>0.05$) among the three cases. As regards CF_{mean}, instead, there is a significant increase ($p<0.05$) from the H or STEN case to the HYP one, which is in accordance with the trend for the hypertrophic wedge in Chapter 4, pointing out that, by growth, the heart can face the higher internal pressure due to aortic stenosis, while preserving

the end-systolic volume in case of no remodeling. The increase from the H case to the STEN one is insignificant ($p>0.05$) instead.

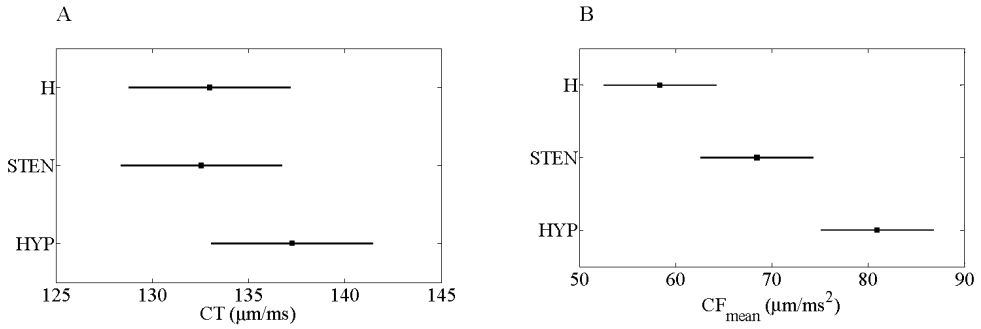

Figure 5.25: Statistical results for the mechanical response of the healthy (H), stenotic (STEN) and hypertrophic (HYP) ventricles: A) contractility CT and B) mean contraction force CF_{mean}. The horizontal bars are the 95% confidence intervals for the differences between means according to the LSD test.

5.4. Conclusions

In this chapter, the electromechanical activity of a concentric hypertrophic ventricle has been simulated during a cardiac cycle. A three-dimensional finite-element strongly-coupled model has been coupled to a simplified model of the circulatory system, including aortic stenosis and a model of concentric growth, whose effects on electrophysiology and mechanics have been taken into account. First, an analysis of the geometric and mechanoelectric feedbacks on the electrical response of healthy and hypertrophic ventricles has been carried out. Then, the electrical and mechanical responses of such ventricles have been studied when all mechanical feedbacks are included; the case with only aortic stenosis without growth has been considered too.

As in Chapter 4, hypertrophic cardiomyocytes have not lost the organization of their sarcomeres, the interstitial fibrosis caused by fibroblasts has been neglected and the T-tubule system has not been remodeled.

In the future, the molecular effects of concentric growth due to specific genetic defects could be implemented in order to study to which extent they further affect the cardiac electromechanical performance. Moreover, the same framework could include fiber dispersion and be applied to eccentric hypertrophy.

Chapter 6

Simulations on a culture

In this chapter, the three-dimensional electromechanical model introduced in Chapter 2 is applied to a cardiac culture that is grown to become a tissue-engineered patch. In particular, the goal of this chapter is to study how the fiber architecture of cultures, i.e. the way cell sarcomeres are locally oriented, and their thickness affect their electromechanical response. The culture is multilayered, i.e. it is made of more than one layer of ventricular cells. Moreover, it can be characterized by four possible architectures consisting of: i) random fibers in all cells; ii) randomly rotating fibers among layers; iii) structurally rotating fibers from the bottom layer to the top one; iv) parallel fibers among layers. First, the effects of the fiber architecture are analyzed, then, after choosing the configuration iii), the effects of thickness are explored too. The electrical and mechanical measures introduced in Chapter 4 will be used to investigate the electromechanics of cultures, i.e. the action potential duration, conduction velocity, contractility and contraction force in some nodes belonging to the top layer. This study is pioneering in the literature because it is the first *in silico* analysis focusing on the problem of how properly driving the development of cardiac patches before their transplantation on the *in vivo* heart.

6.1. Introduction

As it has already been recalled in Section 1.4, cardiac cultures offer today a valid alternative to the isolation of the *in vivo* heart to perform not only different kinds of electromechanical studies but also to heal an infarcted area of the organ, if they develop into cardiac patches. During this process, a crucial issue that must be accounted for is the way cardiac cells organize their internal myofilaments to create a functional syncytium ready to be delivered on the infarcted region [26,27,218]. Moreover, they must

proliferate to a sufficient number in order to contribute significantly to the heart pumping function [27,218].

Therefore, the first aim of this study is to investigate, by a finite-element electromechanical model, if changes in the internal fiber configuration of a three-dimensional multilayered culture lead to significant differences in terms of the electrical activity and mechanical contraction. This topic has never been tackled by *in silico* studies, whereas the *in vitro* ones have only focused on the propagation of the electrical signal [12,25-27]. Thus, this lack of information in the literature is filled with the simulation results reported in this chapter.

Then, the same electromechanical model is used to check if thickness significantly changes the electrical and mechanical responses. Different thicknesses are yielded by increasing the number of cardiomyocytes layers without considering any other cell type. Again, the *in silico* results of this chapter are innovative in this field.

6.2. Methods

Since cardiac cultures may consist of cardiomyocytes derived from neonatal hearts, the bioelectrical activity and calcium dynamics model by Wang-Sobie [221] for the neonatal mouse is chosen. However, there are no models in the literature about the development of active tension in neonatal cardiomyocytes. Thus, the Wang-Sobie model is coupled with the active tension generation model by Land [133] for the adult mouse again. Then, a quasi-static finite elasticity model and a Monodomain model are added to simulate the electromechanical response of the culture.

6.2.1. The mechanical model: details and remarks

In this chapter, the isotropic strain-energy function W in [83] is adopted in order to reduce the anisotropic contribution of other structures that are not cell sarcomeres (for instance, the extracellular matrix fibers made of elastin and collagen). Moreover, like for the adult tissue in Chapter 4 and Chapter 5, the neonatal one is assumed to be a quasi-incompressible tissue. Therefore, W is given by

$$W=\frac{a}{2b}\exp(b(tr(\mathbf{C})-3)+c(J-1)^2, \tag{6.1}$$

where a, b and c are fixed parameters taken from [52,215].

As regards the contribution of sarcomeres, it must be noted the dependence in (2.52) of the active second Piola-Kirchhoff stress tensor $\mathbf{S}^{act}$ on the chosen fiber architecture by the unit vector $\widehat{\mathbf{a}_f}(\mathbf{X})$ for the local fiber direction in the reference configuration Ω_0. This is the variable stated in

different random ways at the beginning of each simulation as described later.

6.2.2. The electrophysiological model: details and remarks

Electrophysiology is modeled by the Monodomain representation coupled with the Wang-Sobie model for the neonatal mouse. As in Chapter 4, the convective term appearing in (2.88) and the i_{SAC} current are disregarded. Thus, the full Monodomain system becomes again

$$\begin{cases} c_m \dfrac{\partial V}{\partial t} - J^{-1}\mathrm{Div}(J\mathbf{F}^{-1}\mathbf{D}\mathbf{F}^{-T}\mathbf{Grad}\, V) + i_{ion}(V,\mathbf{w},\mathbf{c}) = i_{app}^m & \text{in } \Omega_0\times(0,T) \\ \dfrac{\partial \mathbf{w}}{\partial t} - \mathbf{R}(v,\mathbf{w}) = 0 & \text{in } \Omega\times(0,T) \\ \dfrac{\partial \mathbf{c}}{\partial t} - \mathbf{S}(v,\mathbf{w},\mathbf{c}) = 0 & \text{in } \Omega\times(0,T) \\ \mathbf{n}^T\mathbf{F}^{-1}\mathbf{D}\mathbf{F}^{-T}\mathbf{Grad}\, V = 0 & \text{on } \partial\Omega_0\times(0,T) \\ V(\mathbf{X},0) = V_0(\mathbf{X}) & \text{in } \Omega_0, \quad \mathbf{w}(\mathbf{x},0) = \mathbf{w_0}(\mathbf{x}), \quad \mathbf{c}(\mathbf{x},0) = \mathbf{c_0}(\mathbf{x}) \quad \text{in } \Omega, \end{cases} \tag{6.2}$$

where **w** and **c** are vectors containing the gating variables and ionic concentrations belonging to the Wang-Sobie model. The ratio χ is assumed equal to 1000 cm^{-1} and the conductivity values making up **D** are taken from [36]; in particular, the culture is assumed to be transversely isotropic, thus equal conductivities are enforced along the transverse directions to fibers. The value for i_{app}^m should be equal to zero since cardiac cultures spontaneously beat [188], but this aspect is here neglected because it does not fit the purposes of this chapter.

6.2.3. Details on the discretization and implementation of the complete model

For the electrical components of the model, a uniform mesh of 80 × 80 linear finite elements on each XY layer is employed (defining a spacing Δh_{el}=0.1 mm that is also used among layers on the Z axis) together with a constant time step Δt_{el} of 0.05 ms. For the mechanical components, instead, a uniform coarser mesh of 20 × 20 linear finite elements on each XY layer is employed (defining a spacing Δh_{mec}=0.4 mm that is also used among layers on the Z axis) together with a constant time step Δt_{mec} of 1 ms. Moreover, the time discretization is performed via a decoupled semi-implicit method.

As in Chapter 4 and Chapter 5, the numerical code for the electromechanical model is implemented in FORTRAN 90 and based on

the parallel library PETSc [100], whereas all simulations are performed on the Linux cluster of the Department of Mathematics of the University of Milan [99].

6.2.4. The geometry and electrical stimulation of the culture

With reference to Figure 6.1, the culture is modeled as a slab whose length and width are fixed (8 mm × 8 mm) and are of the order of the typical *in vitro* cultures with only cardiomyocytes. Its thickness, instead, may vary or not according to whether simulations deal with the study of the effects of thickness or the fiber architecture respectively (in the latter case, a constant value of 1.2 mm for thickness is adopted). The bottom layer is fixed in the same manner a culture is attached to a rigid substrate; this also avoids rigid motions of the whole culture.

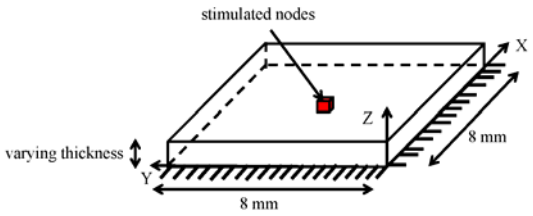

Figure 6.1: Schematic representation of the reference configuration of the culture. The culture is a slab with a fixed length and width (8 mm × 8 mm) and a varying thickness. The bottom layer is kept fixed. The current stimuli are applied to the red cluster of nodes.

For all simulations, twenty current stimuli i_{app}^{m} of amplitude 250 mA/cm^3 and duration 1 ms are delivered at a basic cycle length of 500 ms (yielding a frequency of 2 Hz, which is a typical value among the physiological ones recorded from *in vitro* cultures [54]) to a cluster of nodes central to the lowest layers (red cube in Figure 6.1), like the stimuli applied to the endocardial side of the simulated ventricular wedge in Chapter 4.

6.2.5. Bioelectrical and biomechanical measures

Sixteen points equidistant and belonging to a 4 × 4 grid central to the top layer represent the markers for results, similarly to the measures extracted from the epicardial side of the ventricular wedge in Chapter 4. In particular, the results consist of the transmembrane potential V values and (x,y,z) coordinates for all markers during the last ten beats. Then, they are postprocessed by using the same two algorithms implemented in Matlab® to derive the nodal bioelectrical and biomechanical measures listed in Chapter 4 for each of the sixteen markers, i.e. the mean action potential duration APD_{mean}, the mean conduction velocity CV_{mean}, the mean

contractility CT_{mean} and the mean contraction force CF_{mean}. Panel A of Figure 6.2 displays an example of the time evolution of the transmembrane potential from which the activation and repolarization times are computed. In particular, the threshold value for identifying the activation times is set to -50 mV, whilst the one for identifying the repolarization ones is set to the 90% repolarization value, i.e. -72 mV. Panel B, instead, shows an example of the trajectory described by each marker in the XY plane.

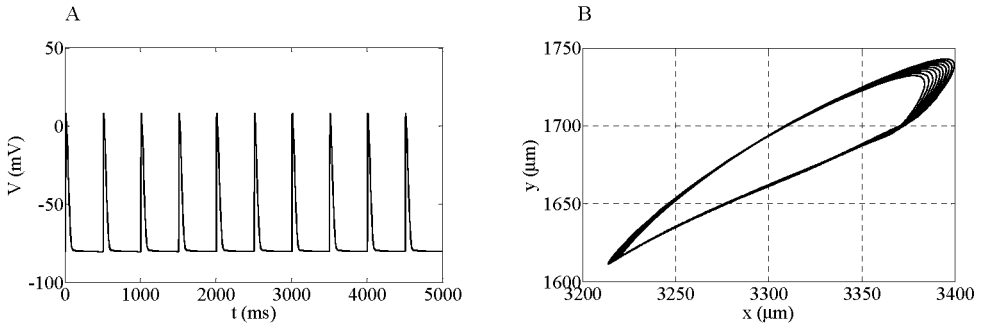

Figure 6.2: Example of simulation results for a marker: A) time evolution of the transmembrane potential V; B) trajectory in the XY plane.

6.2.6. Statistics

In a first group of simulations, four fiber architectures that may be used for an *in vitro* culture are statistically compared:

- fibers with different random directions for all nodes (in the following called random fibers RF);
- fibers with the same randomly specified direction in each XY plane but without an ordering along the Z axis (in the following called randomly rotating fibers RRF);
- fibers with the same specified direction in each XY plane determined by gradually rotating them along the Z axis from the bottom layer to the top one in a clockwise or counterclockwise fashion; the direction of fibers belonging to the top layer and the overall rotation angle from the bottom layer to the top one are randomly found (in the following called structurally rotating fibers SRF);
- parallel fibers for all layers and whose direction is randomly specified (in the following called parallel fibers PF).

In a second group of simulations, instead, the SRF configuration is selected and three increasing thicknesses are compared: 1.2 mm, 2.4 mm and 3.6 mm. In the following, they will be called TH1, TH2 and TH3, i.e. thickness 1, thickness 2 and thickness 3 respectively.

For both groups, each of the previous four or three types of simulation are repeated with five configurations randomly defined as just discussed, thus computing 16×5=80 values for the four electromechanical measures. Then, analogously to Chapter 4 and Chapter 5, in Matlab® the one-way ANOVA and LSD test are applied, choosing a significance level of 0.05.

6.3. Results and discussion

6.3.1. Effects of the fiber architecture

Panel A of Figure 6.3 shows no significant differences ($p>0.05$) among cultures in terms of their APD_{mean}. Considering CV_{mean} in panel B, instead, there are only two significant differences ($p<0.05$) between the RRF or SRF case and the PF one, whereas the remaining ones are insignificant ($p>0.05$).

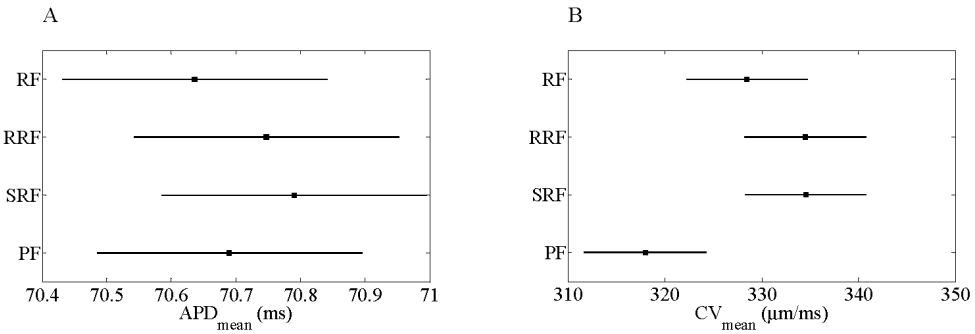

Figure 6.3: Statistical results for the bioelectrical activity of cultures when different fiber architectures are chosen: A) mean action potential duration APD_{mean}; B) mean conduction velocity CV_{mean}. The horizontal bars are the 95% confidence intervals for the differences between means according to the LSD test. Labels RF, RRF, SRF and PF stand for random, randomly rotating, structurally rotating and parallel fibers respectively.

Panel A of Figure 6.4 reports significant differences ($p<0.05$) of CT_{mean} among all cases. Note that the mean value for CT_{mean} increases by about six times from the RF case to the PF one. As regards CF_{mean} in panel B, there are significant differences ($p<0.05$) between the RF case and the SRF or PF one, between the RRF case and the PF one and between the SRF case and the PF one again; all other differences are insignificant ($p>0.05$).

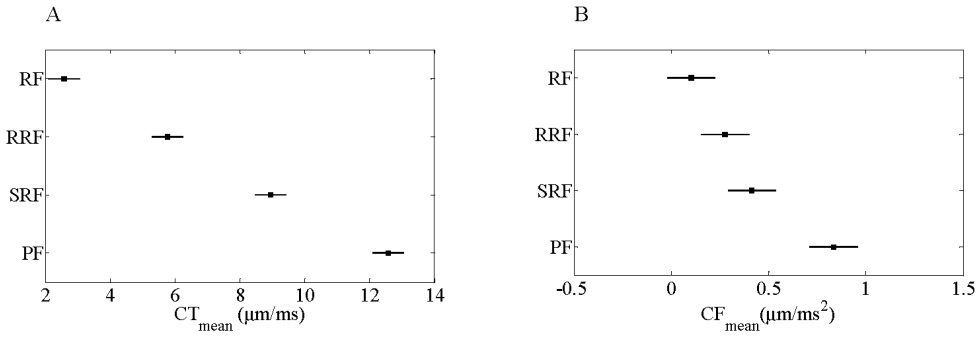

Figure 6.4: Statistical results for the biomechanical activity of cultures when different fiber architectures are chosen: A) mean contractility CT_{mean}; B) mean contraction force CF_{mean}. The horizontal bars are the 95% confidence intervals for the differences between means according to the LSD test. Labels RF, RRF, SRF and PF stand for random, randomly rotating, structurally rotating and parallel fibers respectively.

Therefore, according to the results, changing the underlying fiber architecture does not alter the action potential duration as it would be suggested by different values of APD_{mean} in panel A of Figure 6.3. This result may be due to the fact that all cells are characterized by a bioelectrical model [221] that is not affected from the mechanoelectric feedback carried out by stretch-activated channels (Chapter 2). By considering the other three measures in Figure 6.3 (panel B) and Figure 6.4 (panels A and B), instead, the optimal configuration turns out to be the culture with structurally rotating fibers because it has the highest value of electrical conduction velocity while keeping relatively high values of contractility and contraction force. Actually, a lower conduction velocity is more likely to promote arrhythmogenic mechanisms like reentries [12,26,36], whereas low mechanical performances may make the patch unable to respond to high loads after its implantation [27,174].

As a consequence, the reported results suggest that, even for a thin culture like the one here modeled, the best way to build a cardiac patch is mimicking the anisotropic and ordered architecture of the *in vivo* tissue.

6.3.2. Effects of thickness

Figure 6.5 shows significant differences ($p<0.05$) among all cases in terms of APD_{mean} (panel A) and CV_{mean} (panel B). Note that the mean value for CV_{mean} reduces by about 30% from the TH1 case to the TH3 one.

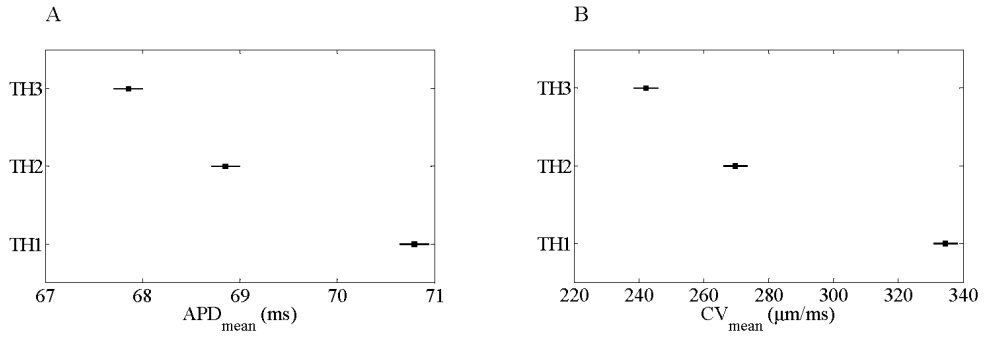

Figure 6.5: Statistical results for the bioelectrical activity of cultures when their thickness is varied: A) mean action potential duration APD_{mean}; B) mean conduction velocity CV_{mean}. The horizontal bars are the 95% confidence intervals for the differences between means according to the LSD test. Labels TH1, TH2 and TH3 stand for thickness 1, thickness 2 and thickness 3 respectively.

Panel A of Figure 6.6 reports significant differences ($p<0.05$) of CT_{mean} among all cases. As regards CF_{mean} in panel B, instead, there are significant differences ($p<0.05$) between the TH3 case and the other ones, whereas the difference between the TH1 case and the TH2 one is insignificant ($p>0.05$). Note that the mean values for CT_{mean} and CF_{mean} double at least from the TH1 case to the TH3 one.

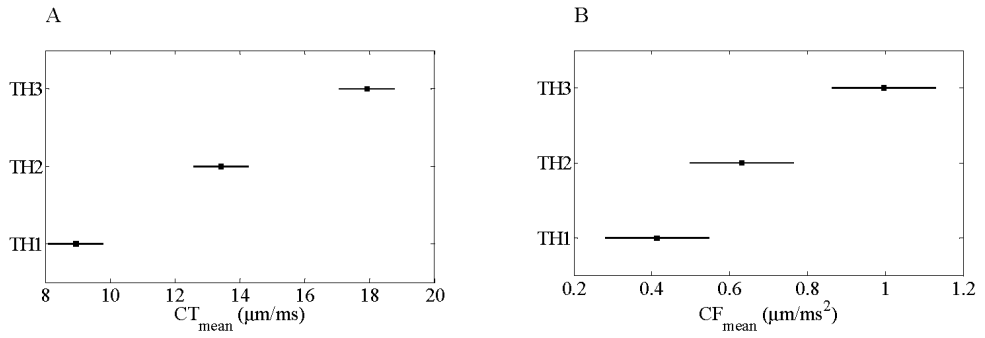

Figure 6.6: Statistical results for the biomechanical activity of cultures when their thickness is varied: A) mean contractility CT_{mean}; B) mean contraction force CF_{mean}. The horizontal bars are the 95% confidence intervals for the differences between means according to the LSD test. Labels TH1, TH2 and TH3 stand for thickness 1, thickness 2 and thickness 3 respectively.

Therefore, from panel A of Figure 6.5, the mean value for APD_{mean} slightly decreases while increasing thickness in the same manner the action potential of cells belonging to a ventricular wall shortens a little from the endocardium to the epicardium (see, e.g., [36]). Again, this result is achieved without considering the mechanoelectric feedback represented by

the stretch-activated channels on the original bioelectrical model of cells. Changes in APD_{mean} are of the order of only 1 ms; refining the mesh in time would give more accurate values for the single values of APD_{mean}, but the differences among them would be similar to the ones that have already been achieved. The other three measures in Figure 6.5 (panel B) and Figure 6.6 (panels A and B), instead, point out that an increase of thickness leads to improvements in the mechanical contraction, but it causes the electrical conduction velocity to decrease, raising the risk of inducing arrhythmogenic phenomena [36]. However, future simulations are needed to provide a thorough vision of thickness proarrhythmic effects because in this study, for example, the effects of thickness on the dynamics of the excitation wave propagation due to the increased mass of the tissue are not considered; actually, multiple wavelets favoring an arrhythmia maintenance may be harbored [173].

If only cardiomyocytes are accounted for, the thicker a culture is the more the innermost cells are likely to suffer from a lack of oxygen and nutrients because they are too far from the growth medium in bioreactors to let diffusion operate alone; they need some kind of tissue vascularization too [27,174,218]. Hence, their electrical and mechanical functionalities are reduced. At the present time, this condition is not modeled because all cardiomyocytes are assumed to be healthy even without a vascular network. Nevertheless, it is noteworthy that the results are independent of the fine configuration of these cardiomyocytes; actually, the change rate of the rotation angle for fibers among layers is randomly chosen not only inside the three groups (TH1, TH2 and TH3) but also among them.

Thus, for any fiber architecture, some attention must be paid while designing the thickness of a cardiac patch because the correct compromise between good electrical and mechanical performances must be found.

6.4. Conclusions

In the literature of *in silico* studies, the model presented in this chapter has been a first attempt to analyze the electromechanical behavior of a cardiac culture. In particular, it has focused on the interaction among the fine configuration of cardiomyocytes or thickness and the overall electrical and mechanical responses of the resultant tissue, when this last one is designed for a cardiac patch in tissue engineering. To achieve this aim, both previous responses have been made dependent on the local fiber direction, neglecting some experimental findings. For example, the electrical propagation has been modeled as transversely isotropic, though it should be fully isotropic because gap junctions develop uniformly on cell membranes both in isotropic and anisotropic cultures as a peculiar feature of neonatal cardiomyocytes [26]. Moreover, cardiomyocytes have had a mature contractile apparatus, i.e. their sarcomeres have been made of correctly-polymerized actin and myosin fibers locally oriented along a preferential direction; thus, the active tension generation model for the adult mouse

[133] has been used. This has been done even for the case of cultures with random fibers, whose internal configuration should assume a star-like pattern because of their isotropic nature [26]. At last, the lack of calibration studies in the literature aimed at defining the values of the electrical and mechanical parameters at the tissue scale for *in vitro* cardiac cultures have been bypassed since the present study has focused on cultures designed to become cardiac patches similar to the *in vivo* tissue. Therefore, some typical values retrieved in the literature of the heart tissue for the conductivity tensor **D** and the ratio χ in the Monodomain model of electrical propagation and for the parameters a, b and c in the strain energy function W have been employed. Moreover, using a Monodomain model instead of the more complex Bidomain one for the electrical current flow description has a negligible impact on the mechanical properties and action potential duration, whereas it might weakly affect the conduction velocity [36].

In the future, some other types of cells (for instance, fibroblasts and endothelial cells) may be added to cardiomyocytes in order to get closer to the *in vitro* reality of a cardiac patch. Moreover, the effects of the vascularization inside cultures and of the progressive lowering of nutrients for the innermost cells could be some other interesting topics to be studied. In doing so, it would be worth implementing the time process of growth of cardiac patches; in this way, cardiomyocytes themselves could evolve progressively from neonatal to adult cells and build their fully functional extracellular matrix.

Chapter 7

Overall conclusions

The aim of this thesis has been to get new insights into the field of cardiac modeling by studying the electromechanical effects of some factors altering the geometry and structure of the cardiac tissue. To achieve this aim, a strongly-coupled electromechanical model has been developed to take into account simultaneously both electrophysiology and mechanics and the mutual interactions between them. The first part of this dissertation has focused on hypertrophy, which is one of the most recurrent pathologies affecting the industrialized world today. More and more complex geometries have been used to investigate the effects of such a remodeling, i.e. a single one-dimensional fiber or a three-dimensional slab-shaped wedge or truncated ellipsoidal ventricle. A deep analysis on the relevance of the mechanical feedbacks has been performed too. The second part has dealt with cardiac cultures and their potential development into patches for tissue engineering purposes. In particular, the influence of two design parameters, i.e. the fiber architecture and the culture thickness, has been analyzed.

The present thesis has the following general limitations. First of all, a model is always a simplification of reality, so results are never accurate and they might not reflect the real behavior of a system. Then, the specific models employed in all chapters do not refer to the same mammalian species. This is a common drawback in cardiac modeling because the experimental data derive from studies performed on different animals according to which species the laws of a country allow to use and a research laboratory is used to handling. Thus, it adds to the already existent intrinsic variability of experimental data and testing conditions. As a consequence, there are very few cases in the literature of some cardiac models first developed independently of one another and then coupled. Due to the complexity of such models, for which the parameters calibration requires several experimental procedures that could not be performed during the last three years, and of the cardiac topics tackled, the parameters

of the employed basic models have not been redefined and the corresponding simulation results have not been quantitatively validated. Nevertheless, the developed framework has proven to be a valid tool for studying qualitatively the behavior of different cardiac tissue samples without exploiting any animal.

In the future, the reported *in silico* results might be quantitatively assessed by biological and physiological data coming from *in vivo* or *in vitro* tests applied on the same cardiac muscle preparations analyzed in this thesis. Actually, some electrical and mechanical measures that can be easily computed directly or inferred from experiments have been intentionally employed. Moreover, the general developed framework may be a useful tool for investigating other cardiac diseases, possibly together with their treatment too, or learning more about the interaction between cardiac cultures and their response to some modifications in their composition or to various physical or chemical stimuli. Last but not the least, even before the comparison with experimental data, a discussion on the sensitivity of the numerical results with respect to variations of some relevant model parameters in their own range of uncertainty should be carried out in order to test their robustness.

References

[1] Adeniran I., Hancox J.C. and Zhang H., Effect of cardiac ventricular mechanical contraction on the characteristics of the ECG: a simulation study, J Biomed Sci Eng, 2013, 6:47-60.

[2] Alastrue V., Martinez M.A. and Doblare M., Modelling adaptative volumetric finite growth in patient-specific residually stressed arteries, J Biomech, 2008, 41:1773-1781.

[3] Alford P.W., Humphrey J.D. and Taber L.A., Growth and remodeling in a thick-walled artery model: effects of spatial variations in wall constituents, Biomech Model Mechanobiol, 2008, 7:245-262.

[4] Allen D.G. and Kentish J.C., The cellular basis of the length-tension relation in cardiac muscle, J Mol Cell Cardiol, 1985, 17:821-840.

[5] Ambrosi D. and Mollica F., On the mechanics of a growing tumor, Int J Eng Science, 2002, 40:1297-1316.

[6] Ambrosi D. and Mollica F., The role of stress in the growth of a multicell spheroid, J Math Biol, 2004, 48:477-499.

[7] Ambrosi D., Guillou A. and Di Martino E.S., Stress-modulated remodelling of a non-homogeneous body, Biomech Model Mechanobiol, 2008, 7:63-76.

[8] Ambrosi D., Arioli G., Nobile F. and Quarteroni A., Electromechanical coupling in cardiac dynamics: the active strain approach, SIAM J Appl Math, 2011, 71:605-621.

[9] Ambrosi D., Ateshian G.A., Arruda E.M., Cowin S.C., Dumais J., Goriely A., Holzapfel G.A., Humphrey J.D., Kemkemer R., Kuhl E., Olberding J.E., Taber L.A. and Garikipati K., Perspectives on biological growth and remodeling, J Mech Phys Solids, 2011, 59:863-883.

[10] Ambrosi D., Preziosi L. and Vitale G., The interplay between stress and growth in solid tumors, Mech Res Commun, 2012, 42:87-91.

[11] Auricchio F., slides for the exam "Modelli costitutivi dei materiali" at the University of Pavia, 2011.

[12] Badie N. and Bursac N., Novel micropatterned cardiac cell cultures with realistic ventricular microstructure, Biophys J, 2009, 96:3873-3885.

[13] Baxy J., Barclay C.J. and Gibbs C.L., Energetics of rat papillary muscle during contractions with sinusoidal length changes, Am J Physiol Heart Circ Physiol, 2000, 278:H1545-H1554.

[14] Beeler G.W. and Reuter H., Reconstruction of the action potential of ventricular myocardial fibres, J Physiol, 1977, 268:177-210.

[15] Berberoglu E., Solmaz H.O. and Goktepe S., Computational modeling of coupled cardiac electromechanics incorporating cardiac dysfunctions, Eur J Mech A-Solids, 2014, 48:60-73.

[16] Berne R.M. and Levy M.N., Cardiovascular Physiology, Mosby, St. Louis, 2001.

[17] Bers D.M., Cardiac excitation-contraction coupling, Nature, 2002, 415:198-205.

[18] Bondarenko V.E., Szigeti G.P., Bett G.C.L., Kim S. and Rasmusson R.L., Computer model of action potential of mouse ventricular myocytes, Am J Physiol Heart Circ Physiol, 2004, 287:H1378-H1403.

[19] Bondarenko V.E., A compartmentalized mathematical model of the beta1-adrenergic signaling system in mouse ventricular myocytes, PLoS One, 2014, 9:e89113.

[20] Bovendeerd P.H., Modeling of cardiac growth and remodeling of myofiber orientation, J Biomech, 2012, 45:872-881.

[21] Brady A.J., Onset of contractility in cardiac muscle, J Physiol, 1966, 184:560-580.

[22] Braess D., Finite Elements. Theory, Fast Solvers, and Applications in Solid Mechanics, Cambridge University Press, Cambridge, 2007.

[23] Brutsaert D.L. and Sonnenblick E.H., Nature of the force-velocity relation in heart muscle, Cardiovasc Res, 1971, Suppl. 1:18-33.

[24] Brutsaert D.L., De Clerck N.M., Goethals M.A. and Housmans P.R., Relaxation of ventricular cardiac muscle, J Physiol, 1978, 283:469-480.

[25] Bursac N., Papadaki M., Cohen R.J., Schoen F.J., Eisenberg S.R., Carrier R., Vunjak-Novakovic G. and Freed L.E., Cardiac muscle tissue engineering: toward an in vitro model for electrophysiological studies, Am J Physiol, 1999, 277:H433-H444.

[26] Bursac N., Parker K.K., Iravanian S. and Tung L., Cardiomyocyte cultures with controlled macroscopic anisotropy: a model for functional electrophysiological studies of cardiac muscle, Circ Res, 2002, 91:e45-e54.

[27] Bursac N., Cardiac tissue engineering: matching native architecture and function to develop safe and efficient therapy, in: Bronzino J.D. (Ed.), The Biomedical Engineering Handbook. Tissue Engineering and Artificial Organs, CRC press, Boca Raton, 2006, 56-1-56-24.

[28] Carasso S., Yang H., Woo A., Vannan M.A., Jamorski M., Wigle E.D. and Rakowski H., Systolic myocardial mechanics in hypertrophic cardiomyopathy: novel concepts and implications for clinical status, J Am Soc Echocardiogr, 2008, 21:675-683.

[29] Caruel M., Chabiniok R., Moireau P., Lecarpentier Y. and Chapelle D., Dimensional reductions of a cardiac model for effective validation and calibration, Biomech Model Mechanobiol, 2014, 13:897-914.

[30] Casella C. and Taglietti V., Principi di Fisiologia II, La Goliardica Pavese, Pavia, 2009.

[31] Cherubini C., Filippi S., Nardinocchi P. and Teresi L., An electromechanical model of cardiac tissue: constitutive issues and electrophysiological effects, Prog Biophys Mol Biol, 2008, 97:562-573.

[32] Ciarletta P. and Ben Amar M., Papillary networks in the dermalepidermal junction of skin: a biomechanical model, Mech Res Commun, 2012, 42:68-76.

[33] Ciarletta P., Ambrosi D., Maugin G.A. and Preziosi L., Mechano-transduction in tumour growth modelling, Eur Phys J E Soft Matter, 2013, 36:23.

[34] Colli Franzone P., Guerri L., Pennacchio M. and Taccardi B., Spread of excitation in 3-D models of the anisotropic cardiac tissue. II. Effects of fiber architecture and ventricular geometry, Math Biosci, 1998, 147:131-171.

[35] Colli Franzone P., Guerri L., Pennacchio M. and Taccardi B., Anisotropic mechanisms for multiphasic unipolar electrograms: simulation studies and experimental recordings, Ann Biomed Eng, 2000, 28:1326-1342.

[36] Colli Franzone P., Pavarino L.F. and Scacchi S., Mathematical Cardiac Electrophysiology, Springer, Cham, 2014.

[37] Colli Franzone P., Pavarino L.F. and Scacchi S., Parallel multilevel solvers for the cardiac electro-mechanical coupling, Appl Numer Maths, 2015, 95:140-153.

[38] Colli Franzone P., Pavarino L.F. and Scacchi S., Joint influence of transmural heterogeneities and wall deformation on cardiac bioelectrical activity: a simulation study, Math Biosci, 2016, 280:71-86.

[39] Colli Franzone P., Pavarino L.F. and Scacchi S., Biolectrical effects of mechanical feedbacks in a strongly coupled cardiac electro-mechanical model, Math Mod Meth Appl S, 2016, 26:27-57.

[40] Cortassa S., Aon M.A., O'Rourke B., Jacques R., Tseng H., Marban E. and Winslow R.L., A computational model integrating electrophysiology, contraction, and mitochondrial bioenergetics in the ventricular myocyte, Biophys J, 2006, 91:1564-1589.

[41] Costa K.D., Hunter P.J., Wayne J.S., Waldman L.K., Guccione J.M. and McCulloch A.D., A three-dimensional finite element method for large elastic deformations of ventricular myocardium: II--Prolate spheroidal coordinates, J Biomech Eng, 1996, 118:464-472.

[42] Costa K.D., Holmes J.W. and McCulloch A.D., Modeling cardiac mechanical properties in three dimensions, Phil Trans R Soc Lond A, 2001, 359:1233-1250.

[43] Dal H., Goktepe S., Kaliske M. and Kuhl E., A fully implicit finite element method for bidomain models of cardiac electromechanics, Comput Methods Appl Mech Eng, 2013, 253:323-336.

[44] Daniels M., Noble M.I., ter Keurs H.E. and Wohlfart B., Velocity of sarcomere shortening in rat cardiac muscle: relationship to force, sarcomere length, calcium and time, J Physiol, 1984, 355:367-381.

[45] de Burgh Daly I., The second Bayliss-Starling memorial lecture. Some aspects of their separate and combined research interests, J Physiol, 1967, 191:1-23.

[46] de Tombe P.P. and ter Keurs H.E., Force and velocity of sarcomere shortening in trabeculae from rat heart. Effects of temperature, Circ Res, 1990, 66:1239-1254.

[47] Demiray H., Stresses in ventricular wall, J Appl Mech, 1976, 43:194-197.

[48] Dokos S., Smaill B.H., Young A.A. and LeGrice I.J., Shear properties of passive ventricular myocardium, Am J Physiol Heart Circ Physiol, 2002, 283:H2650-H2659.

[49] Dong S.J., MacGregor J.H., Crawley A.P., McVeigh E., Belenkie I., Smith E.R., Tyberg J.V. and Beyar R., Left ventricular wall thickness and regional systolic function in patients with hypertrophic cardiomyopathy. A three-dimensional tagged magnetic resonance imaging study, Circulation, 1994, 90:1200-1209.

[50] Ekblom B. and Hermansen L., Cardiac output in athletes, J Appl Physiol, 1968, 25:619-625.

[51] Eriksson T.S.E., Prassl A.J., Plank G. and Holzapfel G.A., Modeling the dispersion in electromechanically coupled myocardium, Int J Numer Method Biomed Eng, 2013, 29:1267-1284.

[52] Eriksson T.S.E., Prassl A.J., Plank G. and Holzapfel G.A., Influence of myocardial fiber/sheet orientations on left ventricular mechanical contraction, Math Mech Solids, 2013, 18:592-606.

[53] Faber G.M. and Rudy Y., Action potential and contractility changes in $[Na^+]_i$ overloaded cardiac myocytes: a simulation study, Biophys J, 2000, 78:2392-2404.

[54] Fassina L., Di Grazia A., Naro F., Monaco L., De Angelis M.G. and Magenes G., Video evaluation of the kinematics and dynamics of the beating cardiac syncytium: an alternative to the Langendorff method, Int J Artif Organs, 2011, 34:546-558.

[55] Fassina L., Magenes G., Gimmelli R. and Naro F., Modulation of the cardiomyocyte contraction inside a hydrostatic pressure bioreactor: in vitro verification of the Frank-Starling law, Biomed Res Int, 2015, 2015:1-7.

[56] Fawcett D.W. and McNutt N.S., The ultrastructure of the cat myocardium. I. Ventricular papillary muscle, J Cell Biol, 1969, 42:1-45.

[57] Formon R., Ford L.E. and Sonnenblick E.H., Effect of muscle length on the force-velocity relationship of tetanized cardiac muscle, Circ Res, 1972, 31:195-206.

[58] Frank O., Zur dynamik des herzmuskels, Z Biol, 1895, 32:370-437.

[59] Fuchs F. and Smith S.H., Calcium, cross-bridges, and the Frank-Starling relationship, News Physiol Sci, 2001, 16:5-10.

[60] Galerkin B.G., On electrical circuits for the approximate solution of the Laplace equation, Vestnik Inzh, 1915, 19:897-908.

[61] Gasser T.C., Ogden R.W. and Holzapfel G.A., Hyperelastic modelling of arterial layers with distributed collagen fibre orientations, J R Soc Interface, 2006, 3:15-35.

[62] Gerdes A.M., Kellerman S.E., Moore J.A., Muffly K.E., Clark L.C., Reaves P.Y., Malec K.B., McKeown P.P. and Schocken D.D., Structural remodeling of cardiac myocytes in patients with ischemic cardiomyopathy, Circulation, 1992, 86:426-430.

[63] Gerdes A.M., Cardiac myocyte remodeling in hypertrophy and progression to failure, J Card Fail, 2002, 8:S264-S268.

[64] Godunov S.K., A difference scheme for numerical solution of discontinuous solution of hydrodynamic equations, Math Sbornik, 1959, 47:271-306.

[65] Goktepe S. and Kuhl E., Electromechanics of the heart: a unified approach to the strongly coupled excitation-contraction problem, Comput Mech, 2010, 45:227-243.

[66] Goktepe S., Abilez O.J. and Kuhl E., A generic approach towards finite growth with examples of athlete's heart, cardiac dilation, and cardiac wall thickening, J Mech Phys Solids, 2010, 58:1661-1680.

[67] Goktepe S., Abilez O.J., Parker K.K. and Kuhl E., A multiscale model for eccentric and concentric cardiac growth through sarcomerogenesis, J Theor Biol, 2010, 265:433-442.

[68] Gordon A.M., Homsher E. and Regnier M., Regulation of contraction in striated muscle, Physiol Rev, 2000, 80:853-924.

[69] Griffith B.E. and Peskin C.S., Electrophysiology, Commun Pure Appl Math, 2013, 66:1837-1913.

[70] Guccione J.M., McCulloch A.D. and Waldman L.K., Passive material properties of intact ventricular myocardium determined from a cylindrical model, J Biomech Eng, 1991, 113:42-55.

[71] Guo A., Zhang C., Wei S., Chen B. and Song L., Emerging mechanisms of T-tubule remodelling in heart failure, Cardiovasc Res, 2013, 98:204-215.

[72] Harvey P.A. and Leinwand L.A., The cell biology of disease: cellular mechanisms of cardiomyopathy, J Cell Biol, 2011, 194:355-365.

[73] Healy S.N. and McCulloch A.D., An ionic model of stretch-activated and stretch-modulated currents in rabbit ventricular myocytes, Europace, 2005, 7:s128-s134.

[74] Heijman J., Volders P.G.A., Westra R.L. and Rudy Y., Local control of beta-adrenergic stimulation: effects on ventricular myocyte electrophysiology and Ca(2+)-transient, J Mol Cell Cardiol, 2011, 50:863-871.

[75] Henderson A.H., Brutsaert D.L., Parmley W.W. and Sonnenblick E.H., Myocardial mechanics in papillary muscles of the rat and cat, Am J Physiol, 1969, 217:1273-1279.

[76] Henriquez C.S., Simulating the electrical behavior of cardiac tissue using the bidomain model, Crit Rev Biomed Eng, 1993, 21:1-77.

[77] Hill A.V., The heat of shortening and dynamics constants of muscles, P R Soc B, 1938, 126:136-195.

[78] Hill J.A. and Olson E.N., Muscle. Fundamental Biology and Mechanisms of Disease, Academic Press, London, 2012.

[79] Himpel G., Kuhl E., Menzel A. and Steinmann P., Computational modelling of isotropic multiplicative growth, Comp Mod Eng Sci, 2005, 8:119-134.

[80] Hinch R., Greenstein J.L., Tanskanen A.J., Xu L. and Winslow R.L., A simplified local control model of calcium-induced calcium release in cardiac ventricular myocytes, Biophys J, 2004, 87:3723-3736.

[81] Hodgkin A.L. and Huxley A.F., A quantitative description of membrane current and its application to conduction and excitation in nerve, J Physiol, 1952, 117:500-544.

[82] Holzapfel G.A., Nonlinear Solid Mechanics: a Continuum Approach for Engineering, John Wiley & Sons, Chichester, 2000.

[83] Holzapfel G.A. and Ogden R.W., Constitutive modelling of passive myocardium: a structurally based framework for material characterization, Phil Trans R Soc A, 2009, 367:3445-3475.

[84] Horowitz A., Lanir Y., Yin F.C., Perl M., Sheinman I. and Strumpf R.K., Structural three-dimensional constitutive law for the passive myocardium, J Biomech Eng, 1988, 110:200-207.

[85] http://facweb.northseattle.edu/estavney/Bio242/Lab/Graphics%20for%20Lectures%20and%20Lab/figure_18_04e_labeled.jpg.

[86] https://ceufast.com/imgs/04_cardiac_conduction_system.jpg.

[87] http://images.slideplayer.com/24/6976511/slides/slide_35.jpg.

[88] http://ccnmtl.columbia.edu/projects/heart/exercises/MechPropHeart/Images/fig_02.gif.

[89] http://members.shaw.ca/chuangmc/module4/resources/frank-starling.jpg.

[90] http://tmedweb.tulane.edu/pharmwiki/lib/exe/fetch.php/ventricular_apd.png?w=600&tok=e64e9f.

[91] https://s-media-cache-ak0.pinimg.com/736x/21/48/e9/2148e96d4fc2d649c5163659f09498e6.jpg.

[92] https://s-media-cache-ak0.pinimg.com/736x/69/03/20/6903209c4c542c9498eb5dc793b17b34.jpg.

[93] https://classconnection.s3.amazonaws.com/682/flashcards/3453682/jpg/picture75-148552147A448E27862.jpg.

[94] https://upload.wikimedia.org/wikipedia/commons/a/a4/Sarcomere.gif.

[95] http://studydroid.com/imageCards/0r/j7/card-28942030-back.jpg.

[96] http://droualb.faculty.mjc.edu/Lecture%20Notes/Unit%203/myosin_thick_myofilaments.jpg.

[97] http://legacy.owensboro.kctcs.edu/gcaplan/anat/images/Image336.gif.

[98] http://www.nhlbi.nih.gov/health/health-topics/topics/cm.

[99] https://cluster.mat.unimi.it/.

[100] http://www.mcs.anl.gov/petsc.

[101] Hu H. and Sachs F., Stretch-activated ion channels in the heart, J Mol Cell Cardiol, 1997, 29:1511-1523.

[102] Humphrey J.D. and Yin F.C., On constitutive relations and finite deformations of passive cardiac tissue: I. A pseudostrain-energy function, J Biomech Eng, 1987, 109:298-304.

[103] Humphrey J.D., Strumpf R.K. and Yin F.C., Determination of a constitutive relation for passive myocardium: I. A new functional form, J Biomech Eng, 1990, 112:333-339.

[104] Humphrey J.D., The normal, mature heart, in: Cardiovascular Solid Mechanics. Cells, Tissues, and Organs, Springer, New York, 2001, 601-723.

[105] Hund T.J. and Rudy Y., Rate transient and regulation of action potential and calcium transient in a canine cardiac ventricular cell model, Circulation, 2004, 110:3168-3174.

[106] Hunter J.J. and Chien K.R., Signaling pathways for cardiac hypertrophy and failure, N Engl J Med, 1999, 341:1276-1283.

[107] Hunter P.J., McCulloch A.D. and ter Keurs H.E., Modelling the mechanical properties of cardiac muscle, Prog Biophys Mol Biol, 1998, 69:289-331.

[108] Hussan J., de Tombe P.P. and Rice J.J., A spatially detailed myofilament model as a basis for large-scale biological simulations, IBM J Res & Dev, 2006, 50:583-600.

[109] Huyghe J.M., van Campen D.H., Arts T. and Heethaar R.M., The constitutive behaviour of passive heart muscle tissue. A quasi-linear viscoelastic formulation, J Biomech, 1991, 24:841-849.

[110] Jafri M.S., Rice J.J. and Winslow R.L., Cardiac Ca2+ dynamics: the roles of ryanodine receptor adaptation and sarcoplasmic reticulum load, Biophys J, 1998, 74:1149-1168.

[111] Janssen P.M., Stull L.B. and Marbán E., Myofilament properties comprise the rate-limiting step for cardiac relaxation at body temperature in the rat, Am J Physiol Heart Circ Physiol, 2002, 282:H499-H507.

[112] Jie X., Gurev V. and Trayanova N., Mechanisms of mechanically induced spontaneous arrhythmias in acute regional ischemia, Circ Res, 2010, 106:185-192.

[113] Katsnelson L.B., Nikitina L.V., Chemla D., Solovyova O., Coirault C., Lecarpentier Y. and Markhasin V.S., Influence of viscosity on myocardium mechanical activity: a mathematical model, J Theor Biol, 2004, 230:385-405.

[114] Katsnelson L.B., Vikulova N.A., Kursanov A.G., Solovyova O.E. and Markhasin V.S., Electro-mechanical coupling in a one-dimensional model of heart muscle fiber, Russian J Numer Anal Math Model, 2014, 29:1-13.

[115] Keener J.P. and Sneyd J., Mathematical Physiology, Springer, New York, 2008.

[116] Keldermann R.H., Nash M.P. and Panfilov A.V., Pacemakers in a reaction-diffusion mechanics system, J Stat Phys, 2007, 128:375-392.

[117] Keldermann R.H., Nash M.P. and Panfilov A.V., Modeling cardiac mechano-electrical feedback using reaction-diffusion-mechanics systems, Physica D, 2009, 238:1000-1007.

[118] Keldermann R.H., Nash M.P., Gelderblom H., Wang V.Y. and Panfilov A.V., Electromechanical wavebreak in a model of the human left ventricle, Am J Physiol Heart Circ Physiol, 2010, 299:H134-H143.

[119] Kerckhoffs R.C., Bovendeerd P.H., Kotte J.C., Prinzen F.W., Smits K. and Arts T., Homogeneity of cardiac contraction despite physiological asynchrony of depolarization: a model study, Ann Biomed Eng, 2003, 31:536-547.

[120] Kerckhoffs R.C., Healy S.N., Usyk T.P. and McCulloch A.D., Computational methods for cardiac electromechanics, Proc IEEE, 2006, 94:769-783.

[121] Kerckhoffs R.C., Omens J. and McCulloch A.D., A single strain-based growth law predicts concentric and eccentric cardiac growth during pressure and volume overload, Mech Res Commun, 2012, 42:40-50.

[122] Kiriazis H. and Gibbs C.L., Papillary muscles split in the presence of 2,3-butanedione monoxime have normal energetic and mechanical properties, Am J Physiol, 1995, 269:H1685-H1694.

[123] Kohl P. and Sachs F., Mechanoelectric feedback in cardiac cells, Phil Trans R Soc Lond A, 2001, 359:1173-1185.

[124] Kohl P., Sachs F. and Franz M.R., Cardiac Mechano-electric Coupling & Arrhythmias, Oxford University Press, New York, 2011.

[125] Konhilas J.P., Irving T.C. and de Tombe P.P., Frank-Starling law of the heart and the cellular mechanisms of length-dependent activation, Pflügers Arch - Eur J Physiol, 2002, 445:305-310.

[126] Kroon W., Delhaas T., Arts T. and Bovendeerd P., Computational modeling of volumetric soft tissue growth: application to the cardiac left ventricle, Biomech Model Mechanobiol, 2009, 8:301-309.

[127] Kuhl E. and Steinmann P., Theory and numerics of geometrically nonlinear open systems, Int J Numer Meth Eng, 2003, 58:1593-1615.

[128] Kuhl E., Menzel A. and Steinmann P., Computational modeling of growth. A critical review, a classification of concepts and two new consistent approaches, Comput Mech, 2003, 32:71-88.

[129] Kuhl E., Maas R., Himpel G. and Menzel A., Computational modeling of arterial wall growth. Attempts towards patient-specific simulations based on computer tomography, Biomech Model Mechanobiol, 2007, 6:321-331.

[130] Kuijpers N.H., ten Eikelder H.M., Bovendeerd P.H., Verheule S., Arts T. and Hilbers P.A., Mechanoelectric feedback leads to conduction slowing and block in acutely dilated atria: a modeling study of cardiac electromechanics, Am J Physiol Heart Circ Physiol, 2007, 292:H2832-H2853.

[131] Kumar V., Abbas A.K. and Fausto N., Robbins and Cotran Pathologic Basis of Disease, Elsevier Saunders, Philadelphia, 2005.

[132] Land S., Niederer S.A. and Smith N.P., Efficient computational methods for strongly coupled cardiac electromechanics, IEEE Trans Biomed Eng, 2012, 59:1219-1228.

[133] Land S., Niederer S.A., Aronsen J.M., Espe E.K., Zhang L., Louch W.E., Sjaastad I., Sejersted O.M. and Smith N.P., An analysis of deformation-dependent electromechanical coupling in the mouse heart, J Physiol, 2012, 590:4553-4569.

[134] Langendorff O., Untersuchungen am überlebenden Säugetierherzen, Pflügers Archiv, 1898, 61:291-332.

[135] Lee L.C., Kassab G.S. and Guccione J.M., Mathematical modeling of cardiac growth and remodeling, WIREs Syst Biol Med, 2016, 8:211-226.

[136] Lee L.C., Sundnes J., Genet M., Wenk J.F. and Wall S.T., An integrated electromechanical-growth heart model for simulating cardiac therapies, Biomech Model Mechanobiol, 2016, 15:791-803.

[137] LeGrice I.J., Smaill B.H., Chai L.Z., Edgar S.G., Gavin J.B. and Hunter P.J., Laminar structure of the heart: ventricular myocyte arrangement and connective tissue architecture in the dog, Am J Physiol Heart Circ Physiol, 1995, 269:H571-H582.

[138] Li L., Niederer S.A., Idigo W., Zhang Y.H., Swietach P., Casadei B. and Smith N.P., A mathematical model of the murine ventricular myocyte: a data-driven biophysically based approach applied to mice overexpressing the canine NCX isoform, Am J Physiol Heart Circ Physiol, 2010, 299:H1045-H1063.

[139] Livshitz L.M. and Rudy Y., Regulation of Ca2+ and electrical alternans in cardiac myocytes: role of CAMKII and repolarizing currents, Am J Physiol Heart Circ Physiol, 2007, 292:H2854-H2866.

[140] Lumens J., Delhaas T., Kirn B. and Arts T., Three-wall segment (TriSeg) model describing mechanics and hemodynamics of ventricular interaction, Ann Biomed Eng, 2009, 37:2234-2255.

[141] Luo C. and Rudy Y., A model of the ventricular cardiac action potential. Depolarization, repolarization, and their interaction, Circ Res, 1991, 68:1501-1526.

[142] Luo C. and Rudy Y., A dynamic model of the cardiac ventricular action potential. I. Simulations of ionic currents and concentration changes, Circ Res, 1994, 74:1071-1096.

[143] Luo C. and Rudy Y., A dynamic model of the cardiac ventricular action potential. II. Afterdepolarizations, triggered activity, and potentiation, Circ Res, 1994, 74:1097-1113.

[144] Mahajan A., Shiferaw Y., Sato D., Baher A., Olcese R., Xie L.H., Yang M.J., Chen P.S., Restrepo J.G., Karma A., Garfinkel A., Qu Z. and Weiss J.N., A rabbit ventricular action potential model replicating cardiac dynamics at rapid heart rates, Biophys J, 2008, 94:392-410.

[145] Maron B.J., Maron M.S. and Semsarian C., Genetics of hypertrophic cardiomyopathy after 20 years: clinical perspectives, J Am Coll Cardiol, 2012, 60:705-715.

[146] McCrossan Z.A., Billeter R. and White E., Transmural changes in size, contractile and electrical properties of SHR left ventricular myocytes during compensated hypertrophy, Cardiovasc Res, 2004, 63:283-292.

[147] Mellors L.J. and Barclay C.J., The energetics of rat papillary muscles undergoing realistic strain patterns, J Exp Biol, 2001, 204:3765-3777.

[148] Mellors L.J., Gibbs C.L. and Barclay C.J., Comparison of the efficiency of rat papillary muscles during afterloaded isotonic contractions and contractions with sinusoidal length changes, J Exp Biol, 2001, 204:1765-1774.

[149] Menzel A. and Kuhl E., Frontiers in growth and remodeling, Mech Res Commun, 2012, 42:1-14.

[150] Mesin L. and Ambrosi D., Spiral waves on a contractile tissue, Eur J Phys Plus, 2011, 126:1-13.

[151] Mihl C., Dassen W.R. and Kuipers H., Cardiac remodelling: concentric versus eccentric hypertrophy in strength and endurance athletes, Neth Heart J, 2008, 16:129-133.

[152] Mozaffarian D., Benjamin E.J., Go A.S., Arnett D.K., Blaha M.J., Cushman M., Das S.R., de F.S., Despres J.P., Fullerton H.J., Howard V.J., Huffman M.D., Isasi C.R., Jimenez M.C., Judd S.E., Kissela B.M., Lichtman J.H., Lisabeth L.D., Liu S., Mackey R.H., Magid D.J., McGuire D.K., Mohler E.R., III, Moy C.S., Muntner P., Mussolino M.E., Nasir K., Neumar R.W., Nichol G., Palaniappan L., Pandey D.K., Reeves M.J., Rodriguez C.J., Rosamond W., Sorlie P.D., Stein J., Towfighi A., Turan T.N., Virani S.S., Woo D., Yeh R.W. and Turner M.B., Executive summary: heart disease and stroke statistics--2016 update: a report from the American Heart Association, Circulation, 2016, 133:447-454.

[153] Nash M.P. and Hunter P.J., Computational mechanics of the heart. From tissue structure to ventricular function, J Elasticity, 2000, 61:113-141.

[154] Nash M.P. and Panfilov A.V., Electromechanical model of excitable tissue to study reentrant cardiac arrhythmias, Prog Biophys Mol Biol, 2004, 85:501-522.

[155] Nickerson D., Smith N. and Hunter P., New developments in a strongly coupled cardiac electromechanical model, Europace, 2005, 7 Suppl 2:118-127.

[156] Niederer S.A., Hunter P.J. and Smith N.P., A quantitative analysis of cardiac myocyte relaxation: a simulation study, Biophys J, 2006, 90:1697-1722.

[157] Niederer S.A. and Smith N.P., A mathematical model of the slow force response to stretch in rat ventricular myocytes, Biophys J, 2007, 92:4030-4044.

[158] Niederer S.A. and Smith N.P., An improved numerical method for strong coupling of excitation and contraction models in the heart, Prog Biophys Mol Biol, 2008, 96:90-111.

[159] Nobile F., Quarteroni A. and Ruiz-Baier R., An active strain electromechanical model for cardiac tissue, Int J Numer Method Biomed Eng, 2012, 28:52-71.

[160] Noble D., Varghese A., Kohl P. and Noble P., Improved guinea-pig ventricular cell model incorporating a diadic space, IKr and IKs, and length- and tension-dependent processes, Can J Cardiol, 1998, 14:123-134.

[161] Noble M.I., Bowen T.E. and Hefner L.L., Force-velocity relationship of cat cardiac muscle, studied by isotonic and quick-release techniques, Circ Res, 1969, 24:821-833.

[162] Nordsletten D.A., Niederer S.A., Nash M.P., Hunter P.J. and Smith N.P., Coupling multi-physics models to cardiac mechanics, Prog Biophys Mol Biol, 2011, 104:77-88.

[163] O'Hara T., Virag L., Varro A. and Rudy Y., Simulation of the undiseased human cardiac ventricular action potential: model formulation and experimental validation, PLoS Comput Biol, 2011, 7:e1002061.

[164] Omens J.H., McCulloch A.D. and Lorenzen-Schmidt I., Mechanotransduction in cardiac remodeling and heart failure, in: Weckström M. and Tavi P. (Eds.), Cardiac Mechanotransduction, Landes Bioscience and Springer Science+Business Media, New York and Austin, 2007, 78-92.

[165] Opie L.H., Heart Physiology. From Cell to Circulation, Lippincott Williams & Wilkins, Philadelphia, 2003.

[166] Pandit S.V., Clark R.B., Giles W.R. and Demir S.S., A mathematical model of action potential heterogeneity in adult rat left ventricular myocytes, Biophys J, 2001, 81:3029-3051.

[167] Panfilov A.V., Keldermann R.H. and Nash M.P., Self-organized pacemakers in a coupled reaction-diffusion-mechanics system, Phys Rev Lett, 2005, 95:258104.

[168] Panfilov A.V., Keldermann R.H. and Nash M.P., Drift and breakup of spiral waves in reaction-diffusion-mechanics systems, Proc Natl Acad Sci USA, 2007, 104:7922-7926.

[169] Pang H., Shiwalkar A.P., Madormo C.M., Taylor R.E., Andriacchi T.P. and Kuhl E., Computational modeling of bone density profiles in response to gait: a subject-specific approach, Biomech Model Mechanobiol, 2012, 11:379-390.

[170] Pathmanathan P. and Whiteley J.P., A numerical method for cardiac mechanoelectric simulations, Ann Biomed Eng, 2009, 37:860-873.

[171] Pluim B.M., Zwinderman A.H., van der Laarse A. and van der Wall E.E., The athlete's heart. A meta-analysis of cardiac structure and function, Circulation, 2000, 101:336-344.

[172] Preziosi L. and Tosin A., Multiphase modelling of tumour growth and extracellular matrix interaction: mathematical tools and applications, J Math Biol, 2009, 58:625-656.

[173] Qu Z., Kil J., Xie F., Garfinkel A. and Weiss J.N., Scroll wave dynamics in a three-dimensional cardiac tissue model: roles of restitution, thickness, and fiber rotation, Biophys J, 2000, 78:2761-2775.

[174] Radisic M. and Christman K.L., Materials science and tissue engineering: repairing the heart, Mayo Clin Proc, 2013, 88:884-898.

[175] Rausch M.K., Dam A., Göktepe S., Abilez O.J. and Kuhl E., Computational modeling of growth: systemic and pulmonary hypertension in the heart, Biomech Model Mechanobiol, 2011, 10:799-811.

[176] Rice J.J., Winslow R.L., Dekanski J. and McVeigh E., Model studies of the role of mechano-sensitive currents in the generation of cardiac arrhythmias, J Theor Biol, 1998, 190:295-312.

[177] Rice J.J., Wang F., Bers D.M. and de Tombe P.P., Approximate model of cooperative activation and crossbridge cycling in cardiac muscle using ordinary differential equations, Biophys J, 2008, 95:2368-2390.

[178] Riemer T.L., Sobie E.A. and Tung L., Stretch-induced changes in arrhythmogenesis and excitability in experimentally based heart cell models, Am J Physiol, 1998, 275:H431-H442.

[179] Rodriguez E.K., Hoger A. and McCulloch A.D., Stress-dependent finite growth in soft elastic tissues, J Biomech, 1994, 27:455-467.

[180] Ross Jr. J., Dilated cardiomyopathy: concepts derived from gene deficient and transgenic animal models, Circ J, 2002, 66:219-224.

[181] Rossi S., Ruiz-Baier R., Pavarino L.F. and Quarteroni A., Orthotropic active strain models for the numerical simulation of cardiac biomechanics, Int J Numer Method Biomed Eng, 2012, 28:761-788.

[182] Rossi S., Lassila T., Ruiz-Baier R., Sequeira A. and Quarteroni A., Thermodynamically consistent orthotropic activation model capturing ventricular systolic wall thickening in cardiac electromechanics, Eur J Mech A-Solids, 2014, 48:129-142.

[183] Roth B.J., The electrical potential produced by a strand of cardiac muscle: a bidomain analysis, Ann Biomed Eng, 1988, 16:609-637.

[184] Rush S. and Larsen H., A practical algorithm for solving dynamic membrane equations, IEEE Trans Biomed Eng, 1978, 25:389-392.

[185] Russell W.M.S. and Burch R.L., The Principles of Humane Experimental Technique, Methuen, London, 1959.

[186] Sachs F., Modeling mechanical-electrical transduction in the heart, in: Mow V.C., Guilak F., Tran-Son-Tay R. and Hochmuth R.M. (Eds.), Cell Mechanics and Cellular Engineering, Springer-Verlag, New York, 1994, 308-328.

[187] Sainte-Marie J., Chapelle D., Cimrman R. and Sorine M., Modeling and estimation of cardiac electromechanical activity, Comput Struct, 2006, 84:1743-1759.

[188] Salameh A. and Dhein S., Culture of neonatal cardiomyocytes, in: Dhein S., Mohr F.W. and Delmar M. (Eds.), Practical Methods in Cardiovascular Research, Springer, Berlin-Heidelberg, 2005, 568-576.

[189] Sawada K. and Kawamura K., Architecture of myocardial cells in human cardiac ventricles with concentric and eccentric hypertrophy as demonstrated by quantitative scanning electron microscopy, Heart Vessels, 1991, 6:129-142.

[190] Saypol J.M. and Roth B.J., A mechanism for anisotropic reentry in electrically active tissue, J Cardiovasc Electrophysiol, 1992, 3:558-566.

[191] Schmid H., Nash M.P., Young A.A. and Hunter P.J., Myocardial material parameter estimation-a comparative study for simple shear, J Biomech Eng, 2006, 128:742-750.

[192] Schmitt O.H., Biological information processing using the concept of interpenetrating domains, in: Leibovich K.N. (Ed.), Information Processing in the Nervous System, Springer-Verlag, New York, 1969, 325-331.

[193] Schneider N.S., Shimayoshi T., Amano A. and Matsuda T., Mechanism of the Frank-Starling law--a simulation study with a novel cardiac muscle contraction model that includes titin and troponin I, J Mol Cell Cardiol, 2006, 41:522-536.

[194] Schuss Z., Nadler B. and Eisenberg R.S., Derivation of Poisson and Nernst-Planck equations in a bath and channel from a molecular model, Phys Rev E, 2001, 64:036116-1-036116-14.

[195] Seidel T., Salameh A. and Dhein S., A simulation study of cellular hypertrophy and connexin lateralization in cardiac tissue, Biophys J, 2010, 99:2821-2830.

[196] Sekine H., Shimizu T. and Okano T., Myocardial tissue engineering: toward a bioartificial pump, Cell Tissue Res, 2012, 347:775-782.

[197] Shannon T.R., Wang F., Puglisi J., Weber C. and Bers D.M., A mathematical treatment of integrated Ca dynamics within the ventricular myocyte, Biophys J, 2004, 87:3351-3371.

[198] Shaw R.M. and Rudy Y., Ionic mechanisms of propagation in cardiac tissue. Roles of the sodium and L-type calcium currents during reduced excitability and decreased gap junction coupling, Circ Res, 1997, 81:727-741.

[199] Shiels H.A. and White E., The Frank-Starling mechanism in vertebrate cardiac myocytes, J Exp Biol, 2008, 211:2005-2013.

[200] Smith N.P., Buist M.L. and Pullan A.J., Altered T wave dynamics in a contracting cardiac model, J Cardiovasc Electrophysiol, 2003, 14:S203-S209.

[201] Socci L., Pennati G., Gervaso F. and Vena P., An axisymmetric computational model of skin expansion and growth, Biomech Model Mechanobiol, 2007, 6:177-188.

[202] Solaro R.J. and Rarick H.M., Troponin and tropomyosin: proteins that switch on and tune in the activity of cardiac myofilaments, Circ Res, 1998, 83:471-480.

[203] Sonnenblick E.H., Force-velocity relations in mammalian heart muscle, Am J Physiol, 1962, 202:931-939.

[204] Starling E.H. and Visscher M.B., The regulation of the energy output of the heart, J Physiol, 1927, 62:243-261.

[205] Taber L.A., Biomechanics of growth, remodeling and morphogenesis, Appl Mech Rev, 1995, 48:487-545.

[206] Taylor R.E., Zheng C., Jackson R.P., Doll J.C., Chen J.C., Holzbaur K.R., Besier T. and Kuhl E., The phenomenon of twisted growth: humeral torsion in dominant arms of high performance tennis players, Comput Methods Biomech Biomed Engin, 2009, 12:83-93.

[207] ten Tusscher K.H., Noble D., Noble P.J. and Panfilov A.V., A model for human ventricular tissue, Am J Physiol Heart Circ Physiol, 2004, 286:H1573-H1589.

[208] Tepole A.B., Ploch C.J., Wong J., Gosain A.K. and Kuhl E., Growing skin: a computational model for skin expansion in reconstructive surgery, J Mech Phys Solids, 2011, 59:2177-2190.

[209] Tezuka F., Muscle fiber orientation in normal and hypertrophied hearts, Tohoku J Exp Med, 1975, 117:289-297.

[210] Toko H., Shiojima I. and Komuro I., The gene expression profiling of concentric and eccentric cardiac hypertrophy, Hypertens Res, 2006, 29:941-942.

[211] Tran K., Smith N.P., Loiselle D.S. and Crampin E.J., A metabolite-sensitive, thermodynamically constrained model of cardiac cross-bridge cycling: implications for force development during ischemia, Biophys J, 2010, 98:267-276.

[212] Trayanova N.A., Constantino J. and Gurev V., Models of stretch-activated ventricular arrhythmias, J Electrocardiol, 2010, 43:479-485.

[213] Tseng W.Y., Dou J., Reese T.G. and Wedeen V.J., Imaging myocardial fiber disarray and intramural strain hypokinesis in hypertrophic cardiomyopathy with MRI, J Magn Reson Imaging, 2006, 23:1-8.

[214] Valentin A., Humphrey J.D. and Holzapfel G.A., A finite element-based constrained mixture implementation for arterial growth, remodeling, and adaptation: theory and numerical verification, Int J Numer Method Biomed Eng, 2013, 29:822-849.

[215] Vetter F.J. and McCulloch A.D., Three-dimensional stress and strain in passive rabbit left ventricle: a model study, Ann Biomed Eng, 2000, 28:781-792.

[216] Vetter F.J. and McCulloch A.D., Mechanoelectric feedback in a model of the passively inflated left ventricle, Ann Biomed Eng, 2001, 29:414-426.

[217] Vikulova N.A., Katsnelson L.B., Kursanov A.G., Solovyova O. and Markhasin V.S., Mechano-electric feedback in one-dimensional model of myocardium, J Math Biol, 2016, 73:335-366.

[218] Vunjak-Novakovic G., Tandon N., Godier A., Maidhof R., Marsano A., Martens T.P. and Radisic M., Challenges in cardiac tissue engineering, Tissue Eng Pt B Rev, 2010, 16:169-187.

[219] Waffenschmidt T., Menzel A. and Kuhl E., Anisotropic density growth of bone. A computational micro-sphere approach, Int J Solids Struct, 2012, 49:1928-1946.

[220] Wang H.M., Gao H., Luo X.Y., Berry C., Griffith B.E., Ogden R.W. and Wang T.J., Structure-based finite strain modelling of the human left ventricle in diastole, Int J Numer Method Biomed Eng, 2013, 29:83-103.

[221] Wang L.J. and Sobie E.A., Mathematical model of the neonatal mouse ventricular action potential, Am J Physiol Heart Circ Physiol, 2008, 294:H2565-H2575.

[222] Weise L.D. and Panfilov A.V., A discrete electromechanical model for human cardiac tissue: effects of stretch-activated currents and stretch conditions on restitution properties and spiral wave dynamics, PLoS One, 2013, 8:e59317.

[223] Whiteley J.P., Bishop M.J. and Gavaghan D.J., Soft tissue modelling of cardiac fibres for use in coupled mechano-electric simulations, Bull Math Biol, 2007, 69:2199-2225.

[224] Williams C.D., Regnier M. and Daniel T.L., Axial and radial forces of cross-bridges depend on lattice spacing, PLoS Comput Biol, 2010, 6:e1001018.

[225] Winslow R.L., Rice J., Jafri S., Marban E. and O'Rourke B., Mechanisms of altered excitation-contraction coupling in canine tachycardia-induced heart failure, II: model studies, Circ Res, 1999, 84:571-586.

[226] Yin F.C., Ventricular wall stress, Circ Res, 1981, 49:829-842.

[227] Zabel M., Koller B.S., Sachs F. and Franz M.R., Stretch-induced voltage changes in the isolated beating heart: importance of the timing of stretch and implications for stretch-activated ion channels, Cardiovasc Res, 1996, 32:120-130.

[228] Zeng T., Bett G.C.L. and Sachs F., Stretch-activated whole cell currents in adult rat cardiac myocytes, Am J Physiol Heart Circ Physiol, 2000, 278:H548-H557.

[229] Zhang Y.H., Youm J.B., Sung H.K., Lee S.H., Ryu S.Y., Ho W.K. and Earm Y.E., Stretch-activated and background non-selective cation channels in rat atrial myocytes, J Physiol, 2000, 523:607-619.

[230] Zimmer H.G., Who discovered the Frank-Starling mechanism?, News Physiol Sci, 2002, 17:181-184.

[231] Zollner A.M., Buganza T.A. and Kuhl E., On the biomechanics and mechanobiology of growing skin, J Theor Biol, 2012, 297:166-175.

[232] Zollner A.M., Tepole A.B., Gosain A.K. and Kuhl E., Growing skin: tissue expansion in pediatric forehead reconstruction, Biomech Model Mechanobiol, 2012, 11:855-867.